AFAPL-TR-79-2048

LEVEL II ②

AD A072442

EXPERIMENTAL INVESTIGATION OF ANNULAR CASCADE PERFORMANCE

VEHICLE POWER BRANCH
AEROSPACE POWER DIVISION

MAY 1979

TECHNICAL REPORT AFAPL-TR-79-2048
FINAL REPORT FOR PERIOD 1 JANUARY 1974 - 31 JULY 1978

Approved for public release; distribution unlimited

AIR FORCE AERO PROPULSION LABORATORY
AIR FORCE WRIGHT AERONAUTICAL LABORATORIES
AIR FORCE SYSTEMS COMMAND
WRIGHT-PATTERSON AIR FORCE BASE, OHIO 45433

79 08 06 078
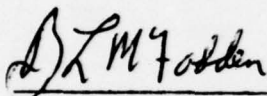
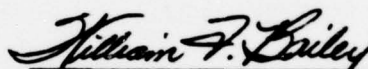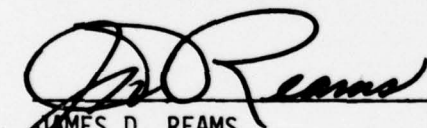This technical report has been reviewed and is approved for publication.

B. L. MCFADDEN
Technical Area Manager

WILLIAM F. BAILEY, Major, USAF
Chief, Vehicle Power Branch

FOR THE COMMANDER

JAMES D. REAMS
Chief, Aerospace Power Division

SECURITY CLASSIFICATION OF THIS PAGE *(When Data Entered)*

REPORT DOCUMENTATION PAGE		READ INSTRUCTIONS BEFORE COMPLETING FORM
1. REPORT NUMBER AFAPL-TR-79-2048	**2. GOVT ACCESSION NO.**	**3. RECIPIENT'S CATALOG NUMBER**
4. TITLE (and Subtitle) EXPERIMENTAL INVESTIGATION OF ANNULAR CASCADE PERFORMANCE.		**5. TYPE OF REPORT & PERIOD COVERED** Final Technical Report 1 Jan 74 - 31 Jul 78
		6. PERFORMING ORG. REPORT NUMBER
7. AUTHOR(s) B. L. McFadden		**8. CONTRACT OR GRANT NUMBER(s)**
9. PERFORMING ORGANIZATION NAME AND ADDRESS Air Force Aero Propulsion Laboratory (POP-1) AF Wright Aeronautical Laboratories, AFSC Wright-Patterson AFB OH 45433		**10. PROGRAM ELEMENT, PROJECT, TASK AREA & WORK UNIT NUMBERS** Program Element 62203F Project 3145, Task 314501 Work Unit 31450125
11. CONTROLLING OFFICE NAME AND ADDRESS Air Force Aero Propulsion Laboratory (PO) AF Wright Aeronautical Laboratories, AFSC Wright-Patterson AFB OH 45433		**12. REPORT DATE** May 1979
		13. NUMBER OF PAGES 232
14. MONITORING AGENCY NAME & ADDRESS(if different from Controlling Office)		**15. SECURITY CLASS. (of this report)** UNCLASSIFIED
		15a. DECLASSIFICATION/DOWNGRADING SCHEDULE

16. DISTRIBUTION STATEMENT (of this Report)

Approved for public release; distribution unlimited.

17. DISTRIBUTION STATEMENT (of the abstract entered in Block 20, if different from Report)

18. SUPPLEMENTARY NOTES

19. KEY WORDS (Continue on reverse side if necessary and identify by block number)

Radial Equilibrium
Annular Cascade
Flow Angle Measurement
Viscous Effects

20. ABSTRACT (Continue on reverse side if necessary and identify by block number)

The purpose of this experiment was to verify the analysis of radial equilibrium for compressible flow through a stationary cascade, where radial equilibrium is defined as uniform axial mass flow. Experimental determination of the effect of compressibility on analytical predictions of flow angle was of primary importance. Previous analytical work is summarized and those results shown.

A specially designed annular flow test apparatus was constructed for this work and its features are described in detail.

DD FORM 1473 EDITION OF 1 NOV 65 IS OBSOLETE
1 JAN 73

SECURITY CLASSIFICATION OF THIS PAGE *(When Data Entered)*

Finally, the results of detailed flow field surveys using three different blade angle settings are summarized and compared with both the free vortex and the Engelman analysis. In order to aid visualization of the real flow field as measured, various computerized graphical presentations of the data are shown. In addition, these survey results are compared with analytical predictions from a two-dimensional computer program developed by the General Electric Company and a three-dimensional computer program developed by AiResearch Manufacturing Company of Arizona.

FOREWORD

This report describes an experiment to investigate the performance of an annular cascade. These results were then compared with computer predictions of flow angle generated from existing codes using both two-dimensional and three-dimensional flow models. The work was performed in the Aerospace Power Division of the Air Force Aero Propulsion Laboratory under Project 3145, Task 01, and Work Unit 25. The work was conducted by B. L. McFadden, AFAPL/POP-1, during the period 1 January 1974 to 31 July 1978. In addition, the following members of the Laboratory made significant contributions which are acknowledged here: Gretchen Henrich, Margaret Weber, Nick Goggin, Maj. William Bailey, Lt. Dan Gurecki, Dr. Kervyn Mach, Joseph Gottschlich, and Karen Draper.

Accession For	
NTIS GRA&I	☑
DDC TAB	☐
Unannounced	☐
Justification	
By	
Distribution/	
Availability Codes	
Dist	Avail and/or special

iii

TABLE OF CONTENTS

LIST OF ILLUSTRATIONS

viii

ix

xi

LIST OF TABLES

LIST OF SYMBOLS

p   Pressure lbf/ft^2, absolute

T   Temperature (°R)

P   Pressure Ratio $\left(\dfrac{p_s}{p_t}\right)$

M   Mach number

V   Velocity ft/sec

X   Axial dimension in inches from blade trailing edge plane

Z   Dimensionless Axial Location $\left(\dfrac{X}{\text{Blade Chord}}\right)$

r   Radius from test apparatus centerline

k   Ratio of specific heats

g_c Gravitational Acceleration Constant (32.2 ft-lbm/lbf-sec^2)

ρ density (lbm/ft^3)

θ Circumferential position angle (0° = vertical reference)

ϕ Flow angle relative to test apparatus centerline

$\mathcal{C}_L$ Centerline

β Exit blade angle (pressure side)

(SUBSCRIPTS)

t   Total

s   Static

*   Condition at Mach number = 1.0

BRIEF SUMMARY

The purpose of this experiment was to verify the analysis of radial equilibrium for compressible flow through a stationary cascade, where radial equilibrium is defined as uniform axial mass flow. Experimental determination of the effect of compressibility on analytical predictions of flow angle was of primary importance. Previous analytical work is summarized and those results shown.

A specially designed annular flow test apparatus was constructed for this work and its features are described in detail.

Finally, the results of detailed flow field surveys using three different blade angle settings are summarized and compared with both the free vortex and the Engelman analysis. In order to aid visualization of the real flow field as measured, various computerized graphical presentations of the data are shown. In addition, these survey results are compared with analytical predictions from a two-dimensional computer program developed by the General Electric Company and a three-dimensional computer program developed by AiResearch Manufacturing Company of Arizona.

CHAPTER I

INTRODUCTION

The high output of turbine engines depends on many factors. One of the more significant ones is predicting the flow characteristics through an annular cascade. Any improvement in accuracy of the methods available would contribute greatly to the design of such engines.

Traditionally, in the early 1900's, the design of compressor or turbine stages was based on the pitch-line calculation using the mean camberline as the reference for the inlet and exit angles. Later, as the rotational speed and loading per blade increased, two additional important factors were included in the design. These are the influence of the centripetal force and the effect of the finite thickness of the blade airfoil.

The effect of high rotational speed is to cause the flow to gravitate toward the shroud area of the blade, thus, starving the hub area of the blade. The net result is the undesirable effect of not fully utilizing the entire span of the blade. To overcome this maldistribution, the concept of designing the blade profile to reach a radial equilibrium was evolved in the 1930's. Radial equilibrium means that no radial flow exists in the flowpath and, therefore, there exists uniform axial mass flow. The basic idea is simply to "underexpand" the flow near the tip section and to "overexpand" near the hub section. This controlled

2

expansion creates an increasing pressure distribution, along the radial direction, which is utilized to maintain uniformity of the mass flow in the axial direction. In this manner, the loading of the blade in the span direction is kept uniform, at least from a design viewpoint. The calculation of the necessary twist of the blade along the spanline direction is designated, generally speaking, the radial equilibrium theory. Among those who have contributed greatly are Wu and Wolfenstein[1]*, Wu[2], Wu[3], Stanitz[4], Wu and Brown[5], Huppert and MacGregor[6], Smith and Traugott[7], Shepherd[8], Giamati and Finger[9], Mereiros and Hood[10], Herzig and Hansen[11], Smith[12], Hawthorne and Horlock[13], and Hawthorne and Ringrose[14]. These are but a few of the possible citations, and Marble[15, pp. 83-164] develops the entire three-dimensional flow treatment in great detail.

A second advancement in the design procedure is the use of a mapping technique in conjunction with the potential flow theory to calculate the streamlines through a cascade. The turning of flow can thus be more realistically assessed with the airfoil thickness taken into account. A drawback is that such a flow calculation is restricted to a two-dimensional or linear cascade. For an annular cascade, however, there has been, up to the present, no theory advanced to account for the curvature effect. Consequently, a compromise procedure is to calculate the flow characteristics at various radial lines for an annular cascade. The resultant flow distributions are stacked upon each other to form, at least as a first order solution, a composite picture for an annular cascade.

*Numbers in parentheses (N,p.M) refers to item number (N) in the bibliography and the specific page (M) of that reference as appropriate

3

More recently, attempts have been made by Dodge[16] to use a numerical scheme to calculate the flow distribution in a channel formed by two adjacent blades and an upper wall representing the shroud and a lower wall representing the hub. This numerical scheme takes into account the effect of viscosity, wall roughness, etc., and its development is still in progress.

The performance improvement due to the present design capability to include all these considerations for both compressor and turbines stages has been demonstrated, in a general sense, by increased propulsive efficiency. For gas turbine units of small size such as Auxiliary Power Units (APU), these modern tools are yet to be fully incorporated into their design. This is due partly to a size limitation and partly to the greatly increased cost versus possible gains in their efficiency. For the reasons of ascertaining the usefulness of the concepts of radial equilibrium the two-dimensional cascade flow theory, and the three-dimensional viscous calculations, the present investigation was undertaken in part to determine the extent to which they can or should be applied to the design of small units. For economical reasons, the blades of the annular cascade in this investigation were chosen straight so as to ascertain the flow departure from that of radial equilibrium. In addition, a major goal of this investigation was to verify Engelman's analysis of radial equilibrium in compressible flow.

It has been concluded by several authors, Binder[17, p. 191] and Shepherd[8, p. 205, 424], that radial equilibrium is a desirable condition to achieve with the machine and blade designs.

Using the proper assumptions to simplify the basic mathematical description of the physical situation, the calculation of radial

4

distribution of flow can be reduced to one basic equation:

$$\frac{dr}{r} = g_c \frac{dp}{\rho V^2}$$

As is well known, e.g. see Velkoff[18, p. 223], the simplest and therefore most used solution scheme is to make the assumption that between blade rows, the actual flow can be represented by a free vortex flow. However, such an assumed flow field will not always produce radial equilibrium and Professor H. W. Engelman[19] has suggested that two solutions are appropriate; i.e., one for incompressible flow and another for compressible flow. In his derivation and proposed solutions, the achievement of radial equilibrium is the primary condition and the assumptions made are:

      (1)   constant enthalpy

      (2)   constant entropy

      (3)   mass is conserved

The only difference between the two solutions is that in one case the fluid is assumed to be incompressible, while in the other the fluid is considered as an ideal compressible gas.

A dimensionless solution was derived by Engelman and numerical solution of the resulting equations was carried out by Bogus[20]. The result for the incompressible fluid is a free vortex, while the result for the compressible fluid is very different in the transonic and supersonic regimes. A final observation is that the compressible result is very close to a free vortex in the low subsonic range.

Complete derivations of the basic equation, and the numerical solutions are included in Appendix A.

5

In an attempt to obtain experimental verification of these analytical results, a small rig was fabricated and tested at Robinson Laboratory by Bogus[20] in 1970. Due to the channel configuration and size relative to the available measurement system, the results were inconclusive.

In summary, the primary purpose of this investigation was to obtain sufficient experimental data to either prove or disprove the validity of the Engelman radial equilibrium analysis.

CHAPTER II
EXPERIMENT

Design of Test Apparatus

Since no existing test configuration was available which could be used for this purpose, an entirely new apparatus had to be designed and built. As a starting point, it was clear from the previous attempt by Bogus[20] that at least a 12-inch outer diameter annulus would be required. This was considered necessary to prevent probe and endwall effects from dominating the results. Such a large channel would, of course, require a significant increase in facility pumping capacity compared to the Ohio State University capability. The test facilities of the Air Force Aero Propulsion Laboratory at Wright-Patterson Air Force Base include altitude chambers capable of handling the through flow of J-85 class engines up to approximately 50,000 feet. Thus the operation of an annular flow cascade in this class was considered feasible and a preliminary design layout was made.

The parameters of interest which were to be measured at various points in the channel were total and static pressures, total temperature, and flow angle. To measure these, a wedge probe was chosen and was used for all measurements. This probe provides three pressure taps; one total pressure and two static pressures, one in each face of the wedge. The flow angle was measured by rotating the probe until the two wedge face

7

tap pressures balanced each other. A checkout setup was fabricated to assure the accuracy of this probe for use in measuring flow angle. The details of this checkout are described in Appendix B.

An atmospheric inlet was chosen; its design therefore required some form of bellmouth to assure a uniform axial flow field. Fortuitously, there existed a surplus J-85 engine test bellmouth with a 16-inch inside diameter and preliminary calculations indicated that, with a reasonable hub-tip ratio, the laboratory air supply system could handle the resulting flow. Therefore, the preliminary layout was based on a 16-inch channel outer diameter with an 11-inch centerbody outer diameter thus giving a 2 1/2-inch blade height and a 0.6875 hub to tip ratio.

In order to produce the whirling flow field required for this experiment, nontapered, nontwisted blades were desired. This would produce a flow field which was not specifically tailored to fit a certain radial equilibrium model or theory, but rather one which could then be surveyed to ascertain its characteristics. In addition, of course, the Engelman analysis predicts that such blading will produce uniform axial mass flow distribution at high Mach numbers and verification would then be a straightforward experiment. After giving brief consideration to designing and fabricating a special blade, it was concluded that surely some existing blade could be found which would perform adequately. As a result of work sponsored at Teledyne CAE[21, 22] by the U. S. Army, an extruded aluminum blade design existed which was considered quite satisfactory for the intended purpose. A closeup of this contour is shown in Figure 1 and the profile coordinates are given in Figure 2. Permission was obtained from the Army to use the extrusion die to produce enough

8
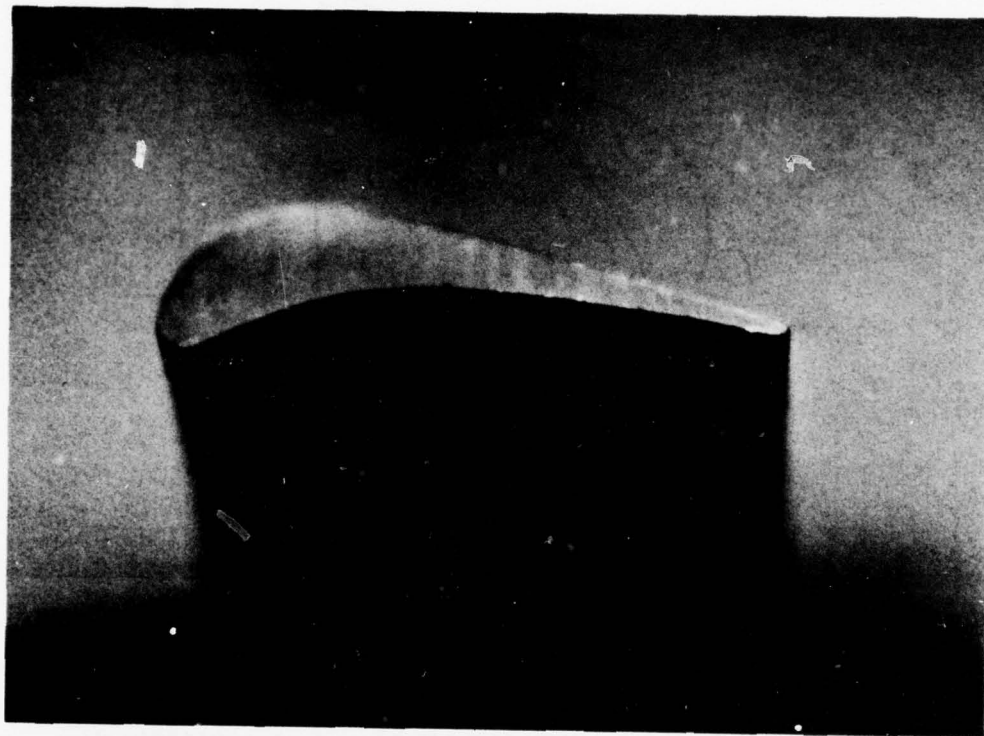
Figure 1   Closeup of Airfoil Section
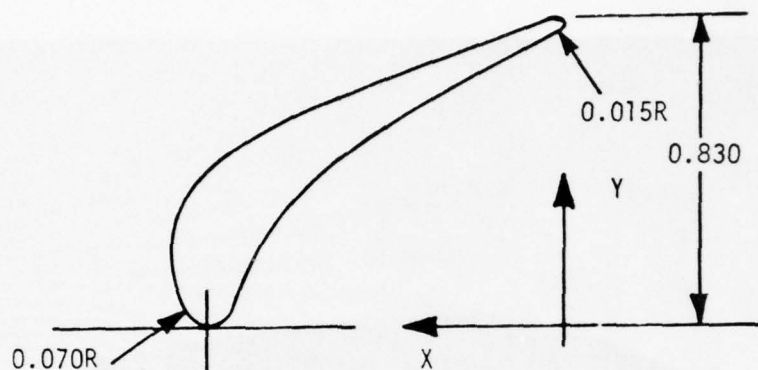
Y COORDINATES	X PRESSURE COORDINATES	X SUCTION COORDINATES
0.0	0.10282000D 01	0.10282000D 01
0.50000000D-01	0.96110000D 00	0.10980000D 01
0.10000000D 00	0.94190000D 00	0.11195000D 01
0.15000000D 00	0.92000000D 00	0.11300000D 01
0.20000000D 00	0.89500000D 00	0.11350000D 01
0.25000000D 00	0.86440000D 00	0.11295000D 01
0.30000000D 00	0.82710000D 00	0.11124000D 01
0.35000000D 00	0.78500000D 00	0.10845000D 01
0.40000000D 00	0.73400000D 00	0.10430000D 01
0.45000000D 00	0.67310000D 00	0.98980000D 00
0.50000000D 00	0.60300000D 00	0.91730000D 00
0.55000000D 00	0.52760000D 00	0.81400000D 00
0.60000000D 00	0.44500000D 00	0.69590000D 00
0.65000000D 00	0.35540000D 00	0.56500000D 00
0.70000000D 00	0.26420000D 00	0.43150000D 00
0.75000000D 00	0.16700000D 00	0.29800000D 00
0.80000000D 00	0.67500000D-01	0.16250000D 00
0.83000000D 00	0.72000000D-01	0.72000000D-01

NOTE: All dimensions in inches

Figure 2 Vane Coordinates

10

strip stock for three rows of blades. The design point blade angle for this profile was 69.7° and one blade row was set at this angle. Two more rows were fabricated with settings of 65° and 60° to provide options for a broad range of test conditions. Pictures of the blade rows are shown as Figures 3, 4, 5, and 6 with engineering drawings shown in Figures 7 through 12. Tables 1, 2, and 3 show the geometric and aerodynamic design data.

Having established the channel cross sectional configuration, only channel length remained to be set. The goal was at least 24 inches with as many axial measurement stations as practical. As shown in Figure 13, the final as-built channel length was approximately twenty-eight inches and eleven measurement stations were incorporated at two inch centerline-to-centerline spacing. Figure 14 shows the numbering system used for stations and centerbody static pressure taps.

Also shown in Figure 13 are the remaining construction details of the assembly, including two unique and patented features. The first was devised to permit circumferential traversing of the probe with minimum aerodynamic disturbance and the second relates to the automatic wrenchless coupling/decoupling of centerbody static pressure tap readout lines.

In order to move the probe circumferentially, slots would, of course, be required in the channel wall. Cutting such slots would seriously interrupt the channel boundary and create undesirable leakage flows. So after making many preliminary sketches and reviewing conceptual ideas, it was decided to make a liner for the rig which would serve as the channel outer wall and which could rotate inside the slotted outer structure. This can be seen in Figures 15 and 16. In this way, only simple radial

11
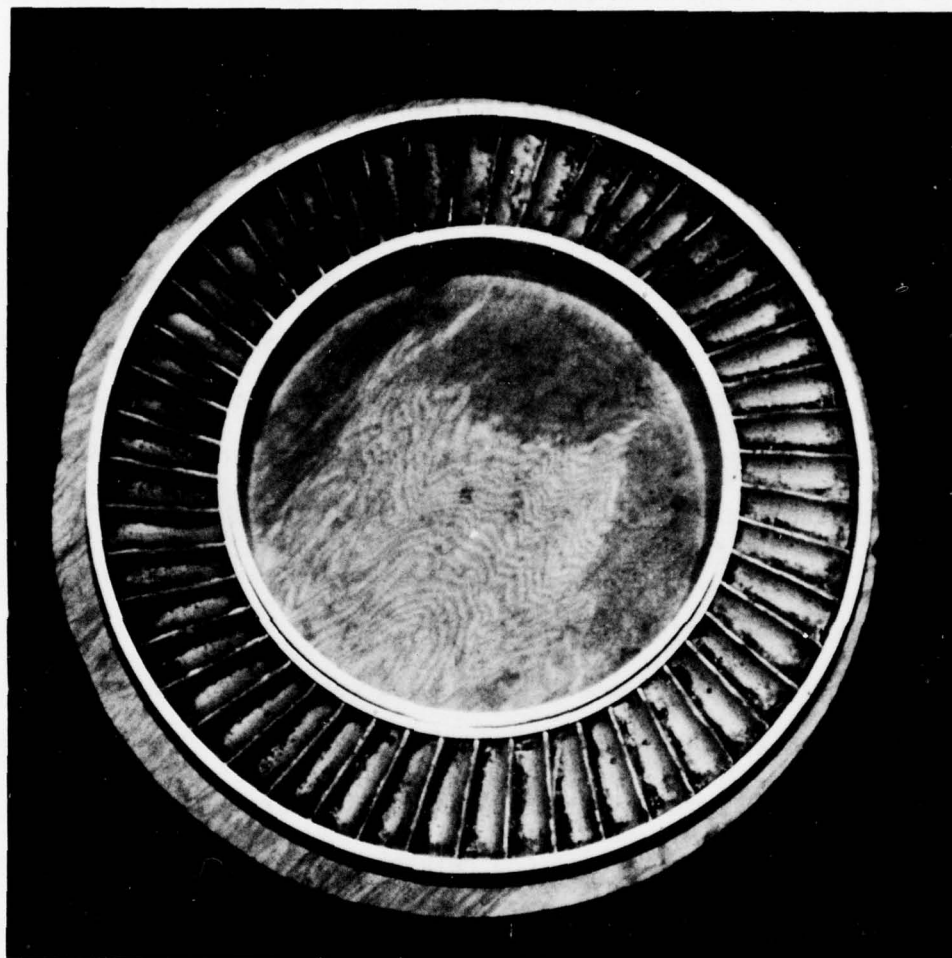
Figure 3 69.7° Blade Row Entrance Side
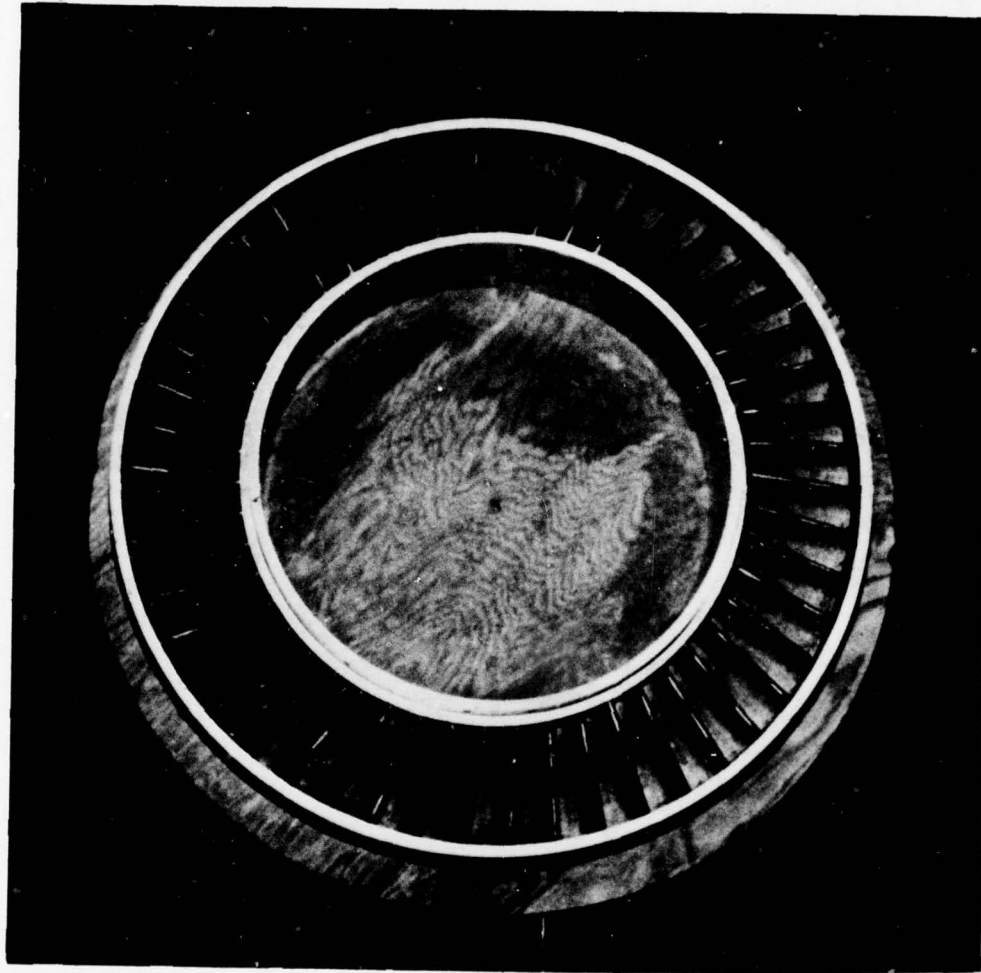
Figure 4   65° Blade Row Entrance Side
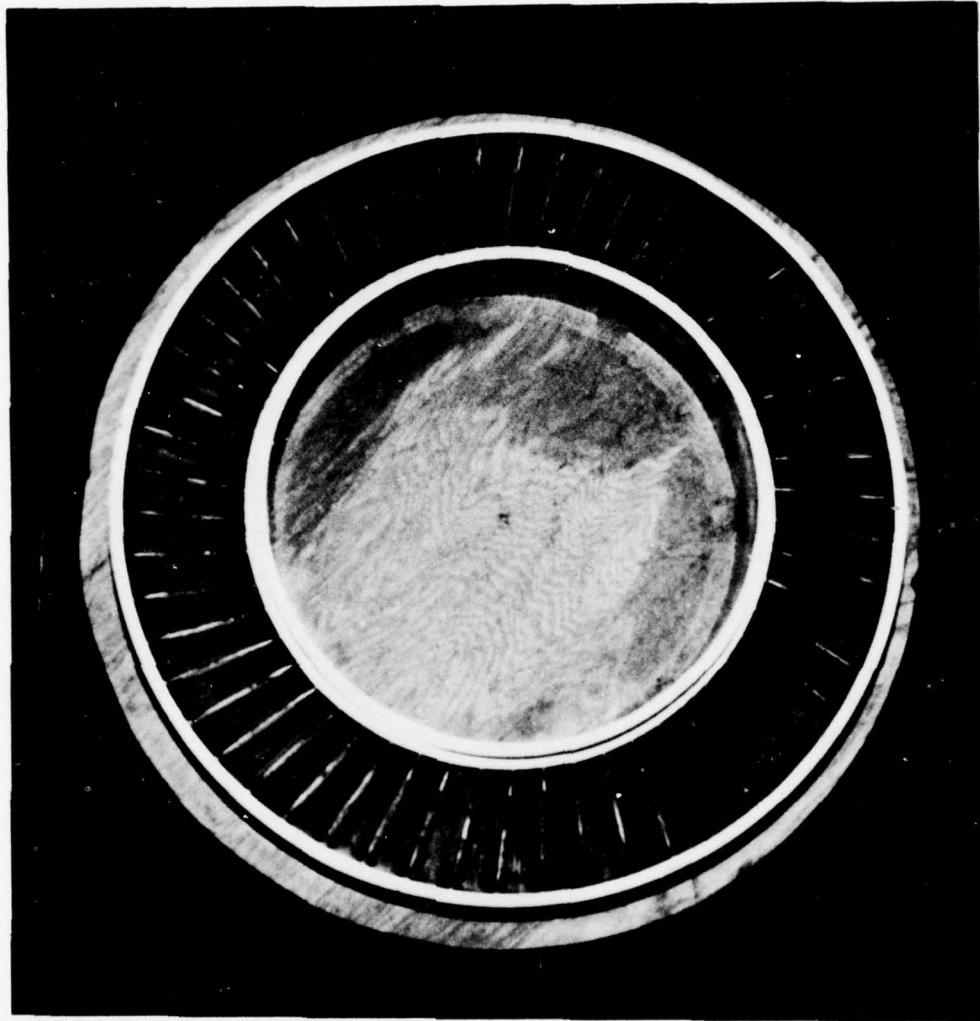
Figure 5   60° Blade Row Entrance Side

14
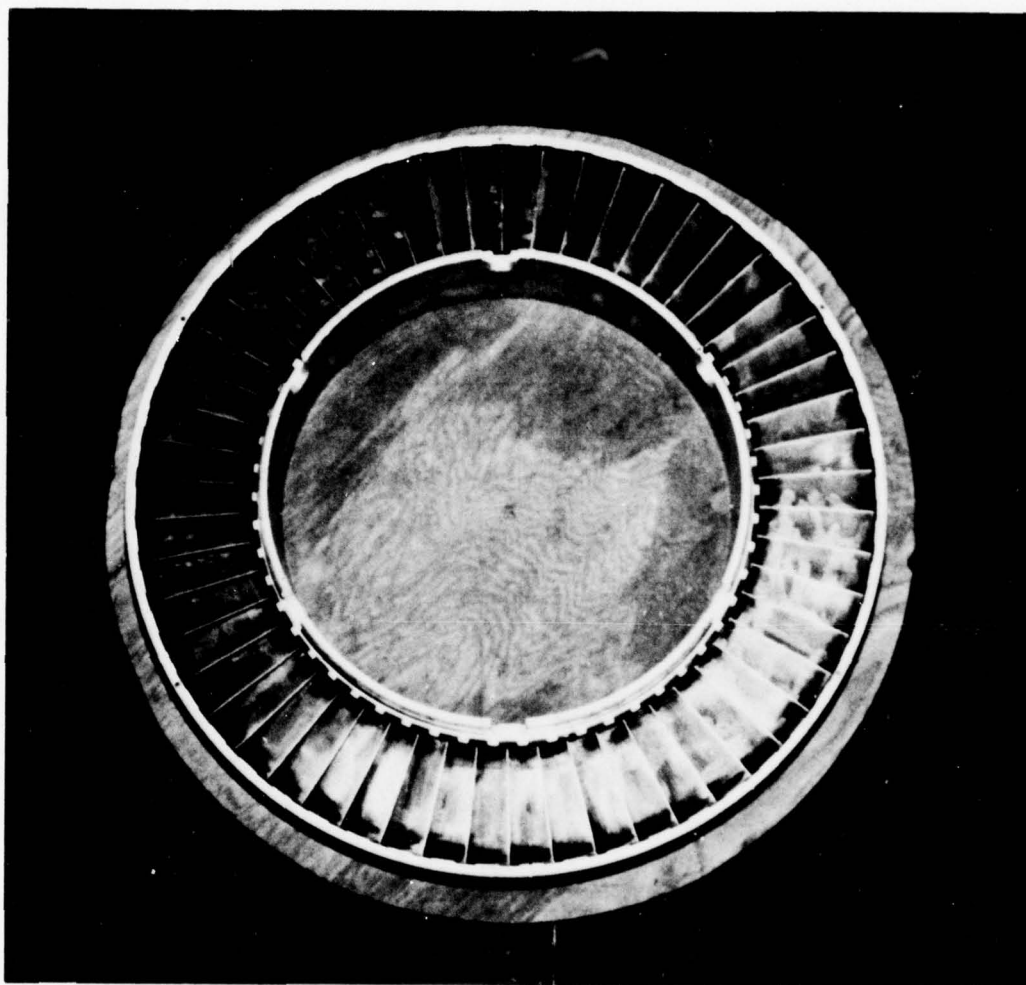
Figure 6 60° Blade Row Exit Side

BLADE SECTION G.F.E.

FLOW

SEE VIEW C

.25

40°42'(REF)

.32(REF)

SECTION A-A
TYP 48 PLACES

.340(REF)

.05 ON ₵

B

B

A

.12 ON ₵

A

T.E. OF BLADE
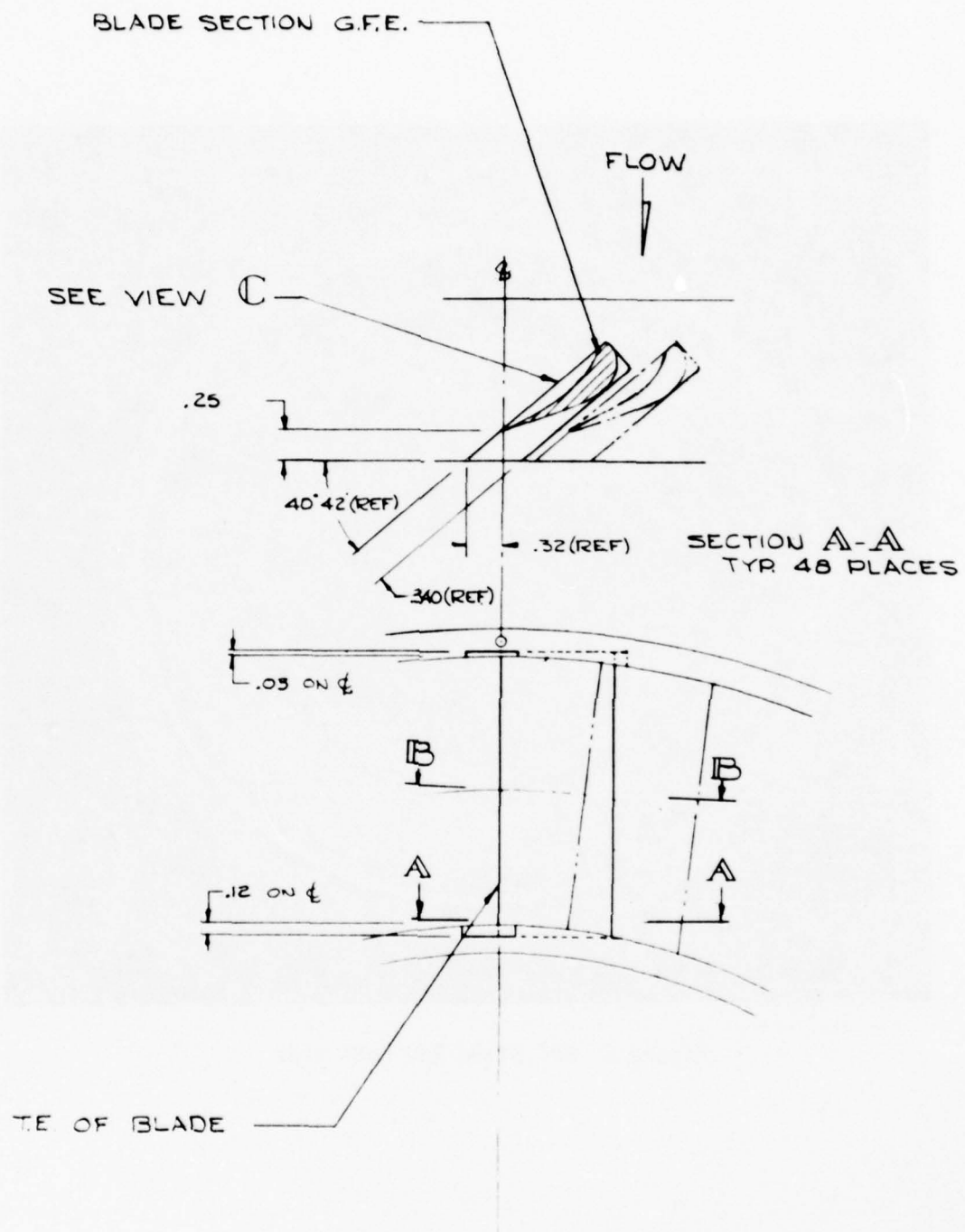
Figure 7 69.7° Blade Row Detail

16

CONTOUR AT VERTICAL ₵

CONTOUR AT 11.00 DIA.

CONTOUR AT 13.50 DIA

CONTOUR AT 16.00 DIA

.023
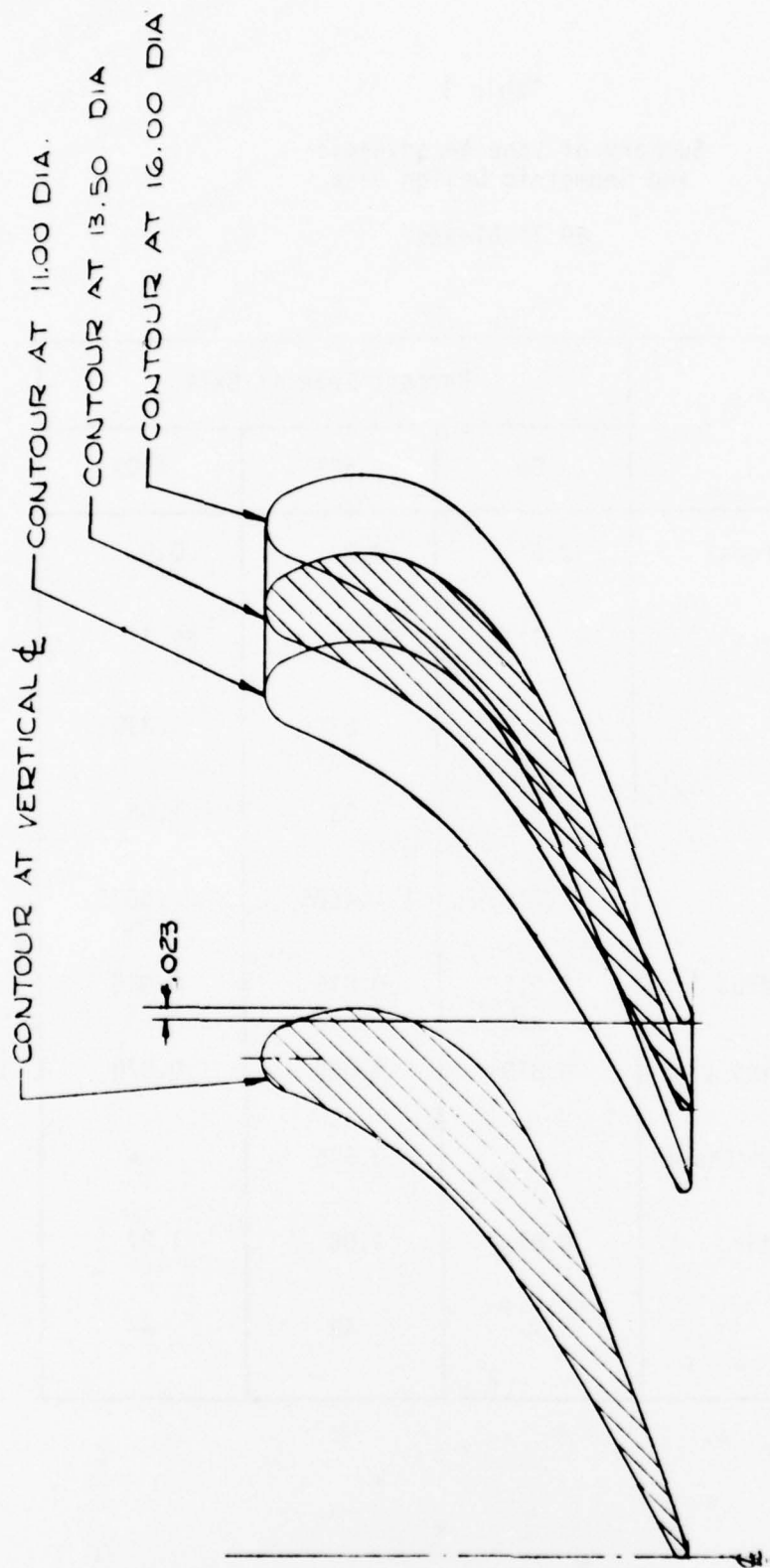
SECTION B-B
4× SIZE

Figure 8 69.7° Blade Row Sections

17

Table 1

Summary of Vane Aerodynamic
and Geometric Design Data

69.7° Blades

Parameter	Percent Span at Exit		
	0%	50%	100%
Inlet Angle (degrees)	0.0	0.0	0.0
Exit Angle (degrees) (Pressure Side)	69.7°	69.7°	69.7°
Axial Chord (in)	.830	.830	.830
Spacing (in)	0.72	0.88	1.05
Throat (in)	.2125	.4625	.5875
Trailing Edge Radius (in)	0.015	0.015	0.015
Leading Edge Radius (in)	0.070	0.070	0.070
Aspect Ratio (Span/Chord)	--	0.576	--
Spacing/Chord Ratio	0.87	1.06	1.27
Number of Vanes	--	48	--

BLADE SECTION G.F.E.

SEE VIEW C

FLOW

.250

45° 35'

.264 (REF.)

.340 (REF.)

SECTION A-A
TYP. 50 PLACES

.030 ON ℄

B

B

A

A

.120 ON ℄

T.E. OF BLADE

℄ VERTICAL
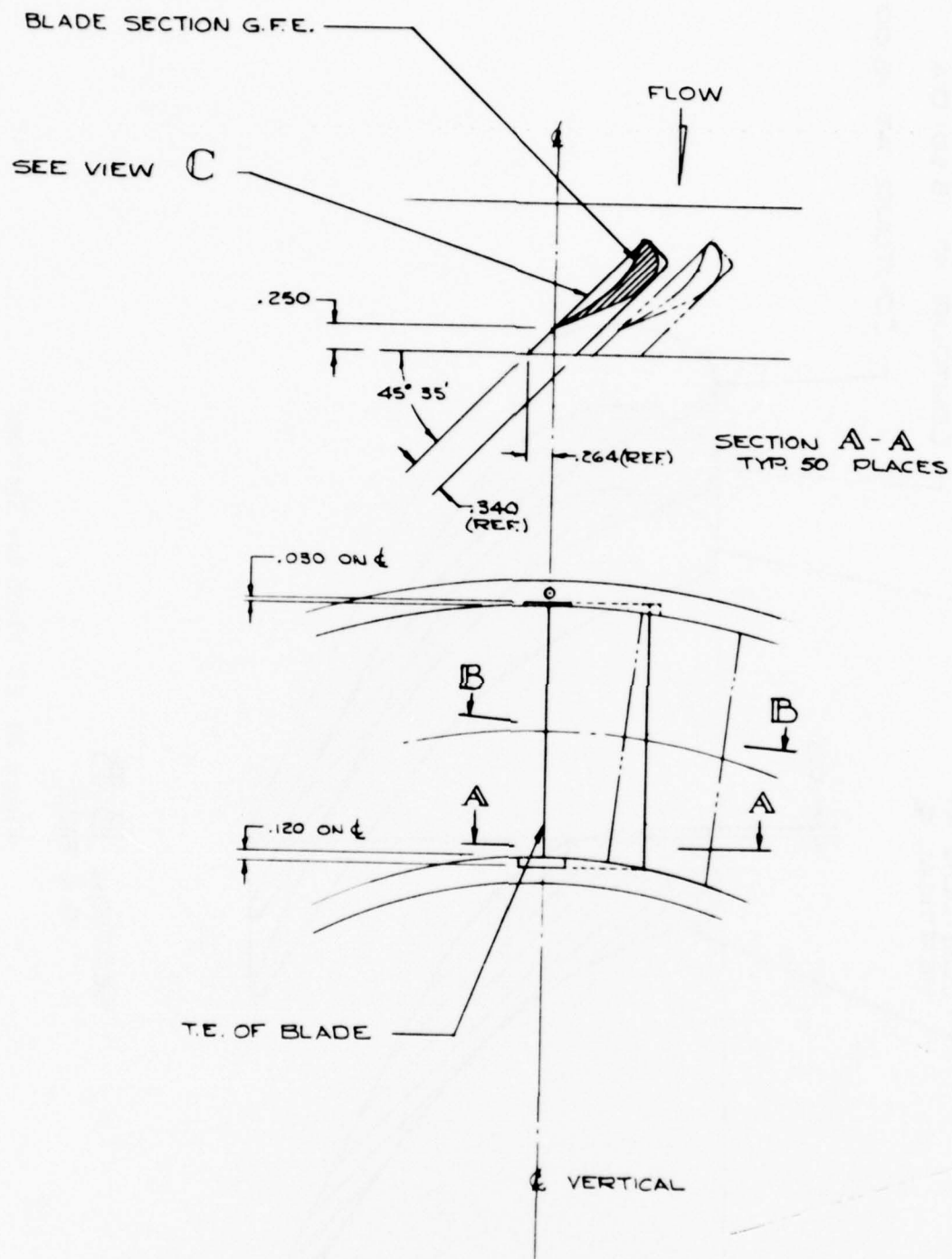
Figure 9 65° Blade Row Detail

19

CONTOUR AT 11.00 DIA.

CONTOUR AT 13.50 DIA

CONTOUR AT 16.00 DIA

CONTOUR AT VERTICAL ℄

.015
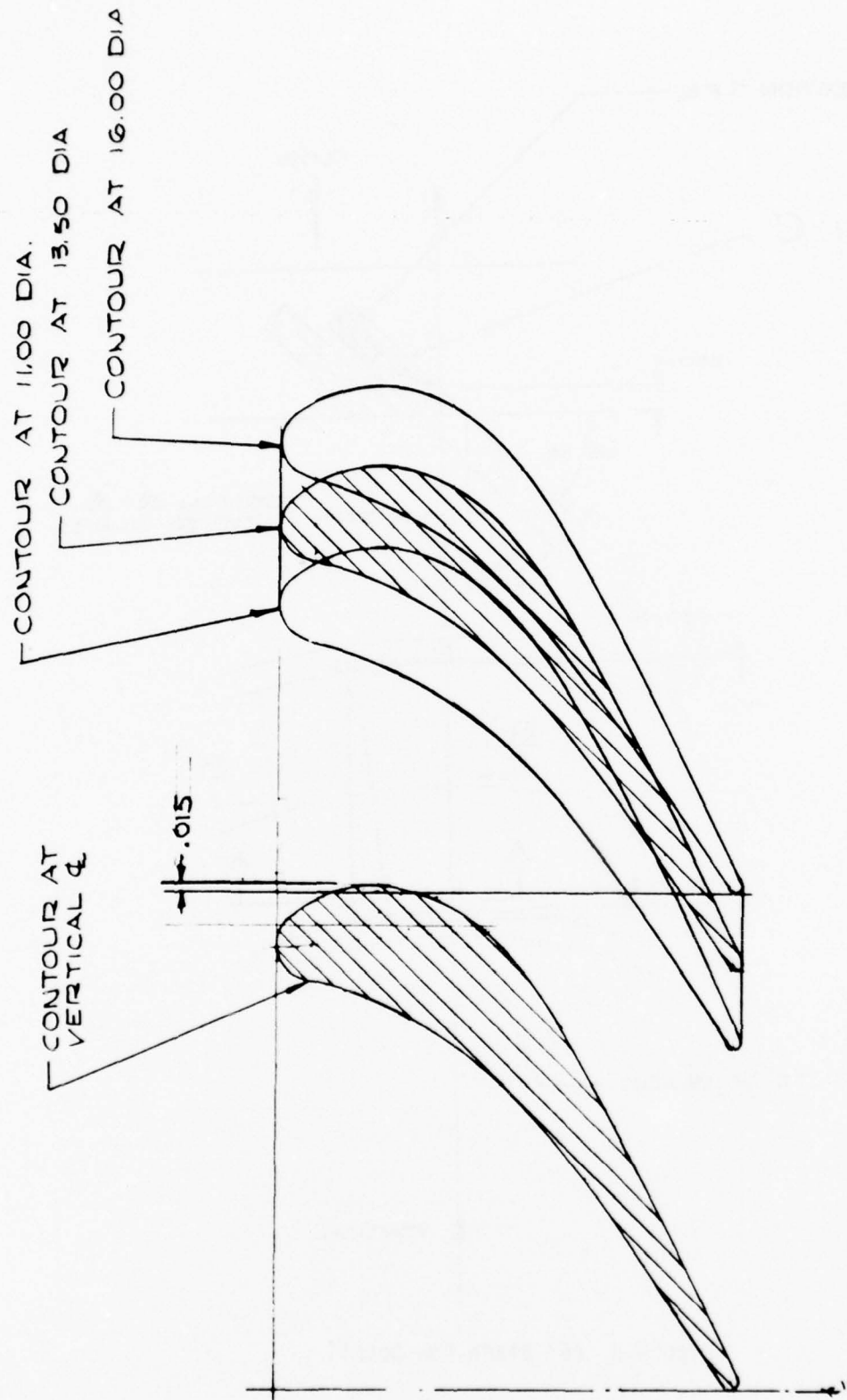
SECTION B-B
4 x SIZE

Figure 10   65° Blade Row Sections

20

Table 2

Summary of Vane Aerodynamic
and Geometric Design Data

65° Blades

Parameter	Percent Span at Exit		
	0%	50%	100%
Inlet Angle (degrees)	4.9°	4.9°	4.9°
Exit Angle (degrees)	65°	65°	65°
Axial Chord (in)	.905	.905	.905
Spacing (in)	0.691	.85	1.01
Throat (in)	0.266	0.356	0.438
Trailing Edge Radius (in)	0.015	0.015	0.015
Leading Edge Radius (in)	0.070	0.070	0.070
Aspect Ratio	--	0.576	--
Spacing/Chord Ratio	0.764	0.939	1.116
Number of Vanes	--	50	--
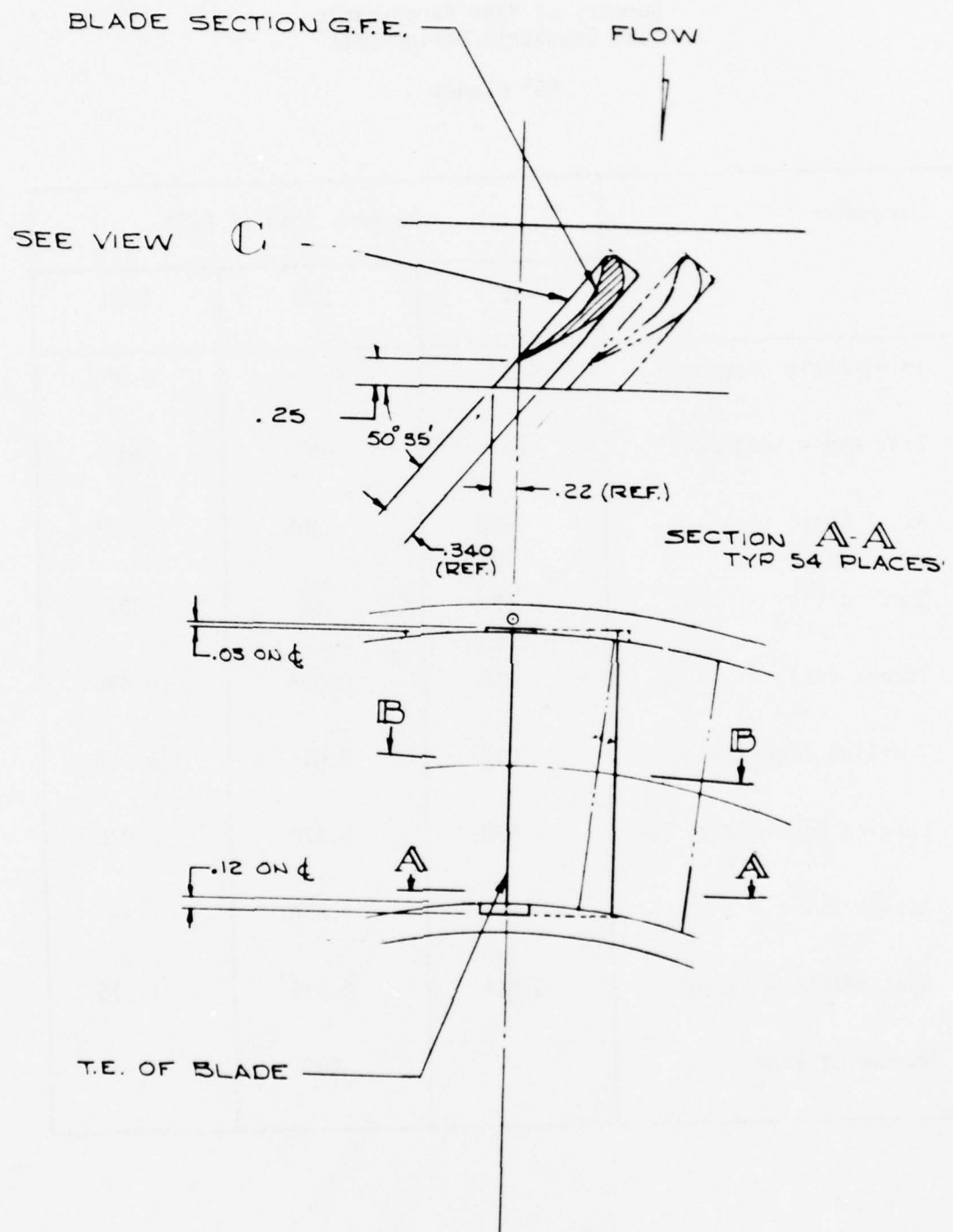
Figure 11 60° Blade Row Detail

CONTOUR AT 11.00 DIA.

CONTOUR AT 13.50 DIA.

CONTOUR AT 16.00 DIA.

CONTOUR AT VERTICAL ℄

.039
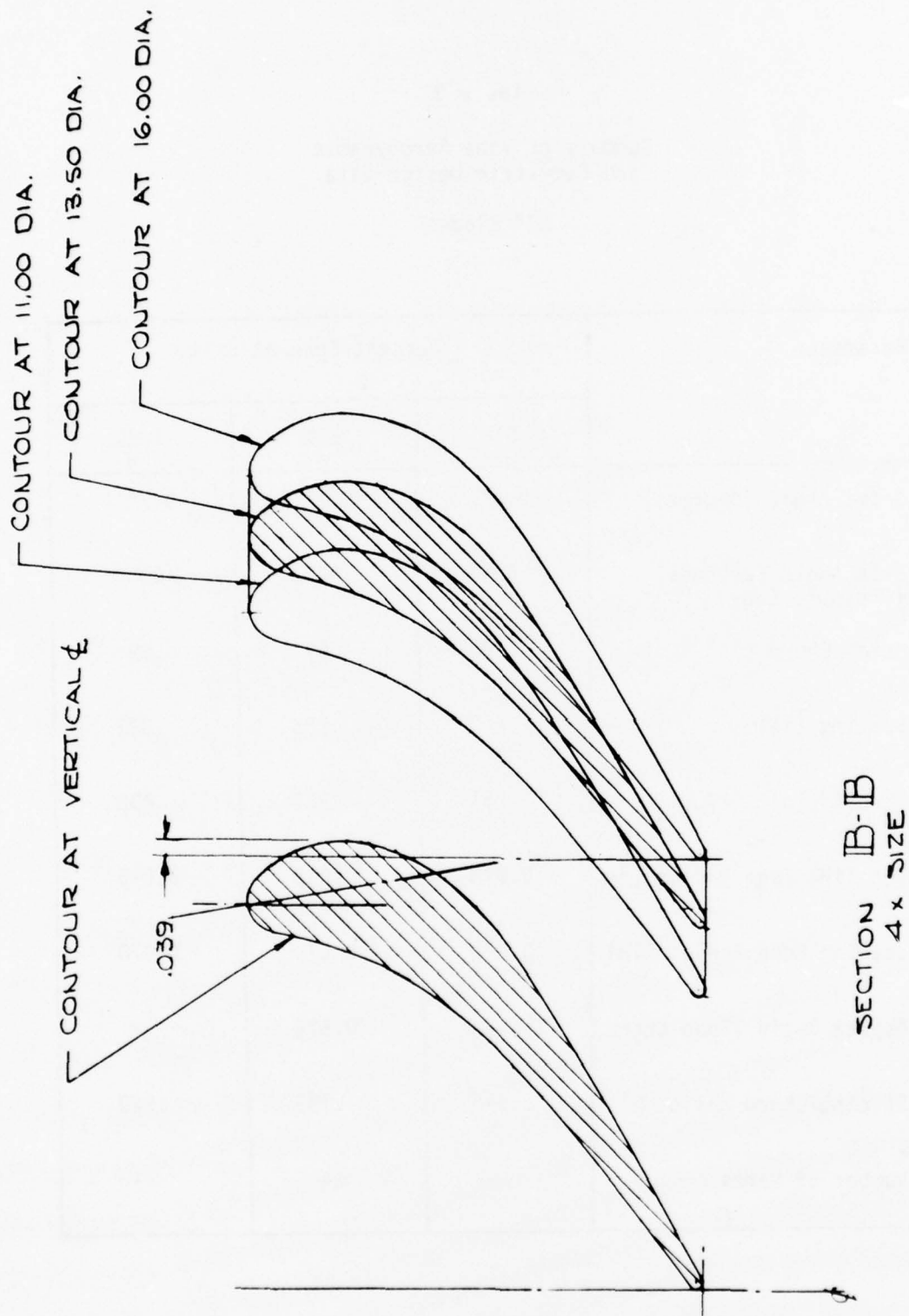
SECTION B-B
4× SIZE

Figure 12 60° Blade Row Sections

23

Table 3

Summary of Vane Aerodynamic
and Geometric Design Data

60° Blades

Parameter	Percent Span at Exit		
	0%	50%	100%
Inlet Angle (degrees)	9.7°	9.7°	9.7°
Exit Angle (degrees) (Pressure Side)	60°	60°	60°
Axial Chord (in)	.99	.99	.99
Spacing (in)	.640	.785	.931
Throat (in)	.281	.356	.438
Trailing Edge Radius (in)	0.015	0.015	0.015
Leading Edge Radius (in)	0.070	0.070	0.070
Aspect Ratio (Span Chord)	--	0.576	--
Spacing/Chord Ratio	.646	.793	.940
Number of Vanes	--	54	--

Figure 13 Assembly of Test Apparatus

STATIONS

① ② ③ ④ ⑤ ⑥ ⑦ ⑧ ⑨ ⑩ ⑪

2.00"
0.75"

INNER BODY STATIC PRESSURE TAPS

BLADE GEOMETRIC CHORD=1.293"
BLADE AXIAL CHORD=0.830" FOR 69.7° BLADES
=0.903" FOR 65.0° BLADES
=0.990" FOR 60.0° BLADES

2.50"

8.00"
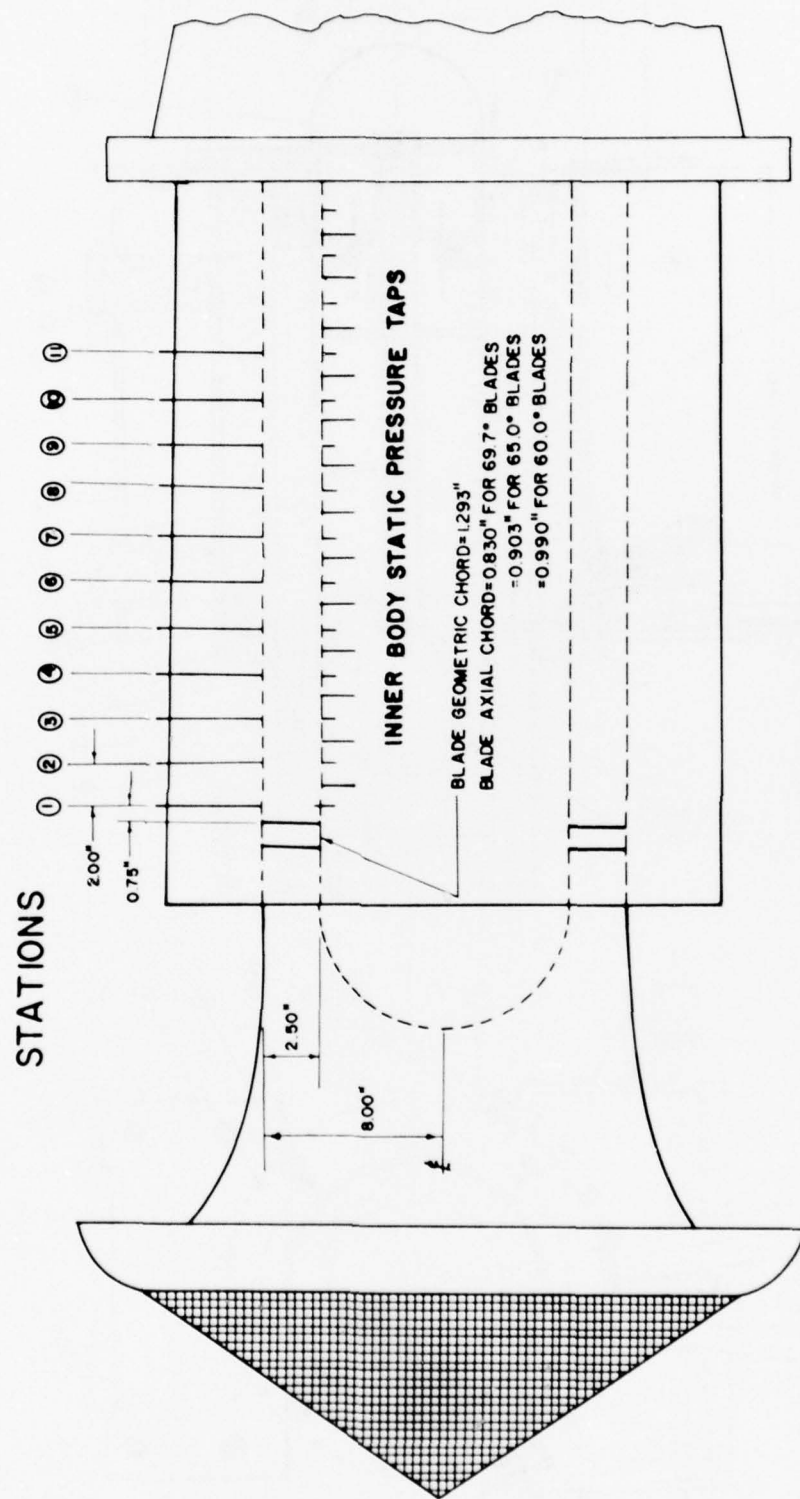
Figure 14   MEASUREMENT LOCATIONS

26
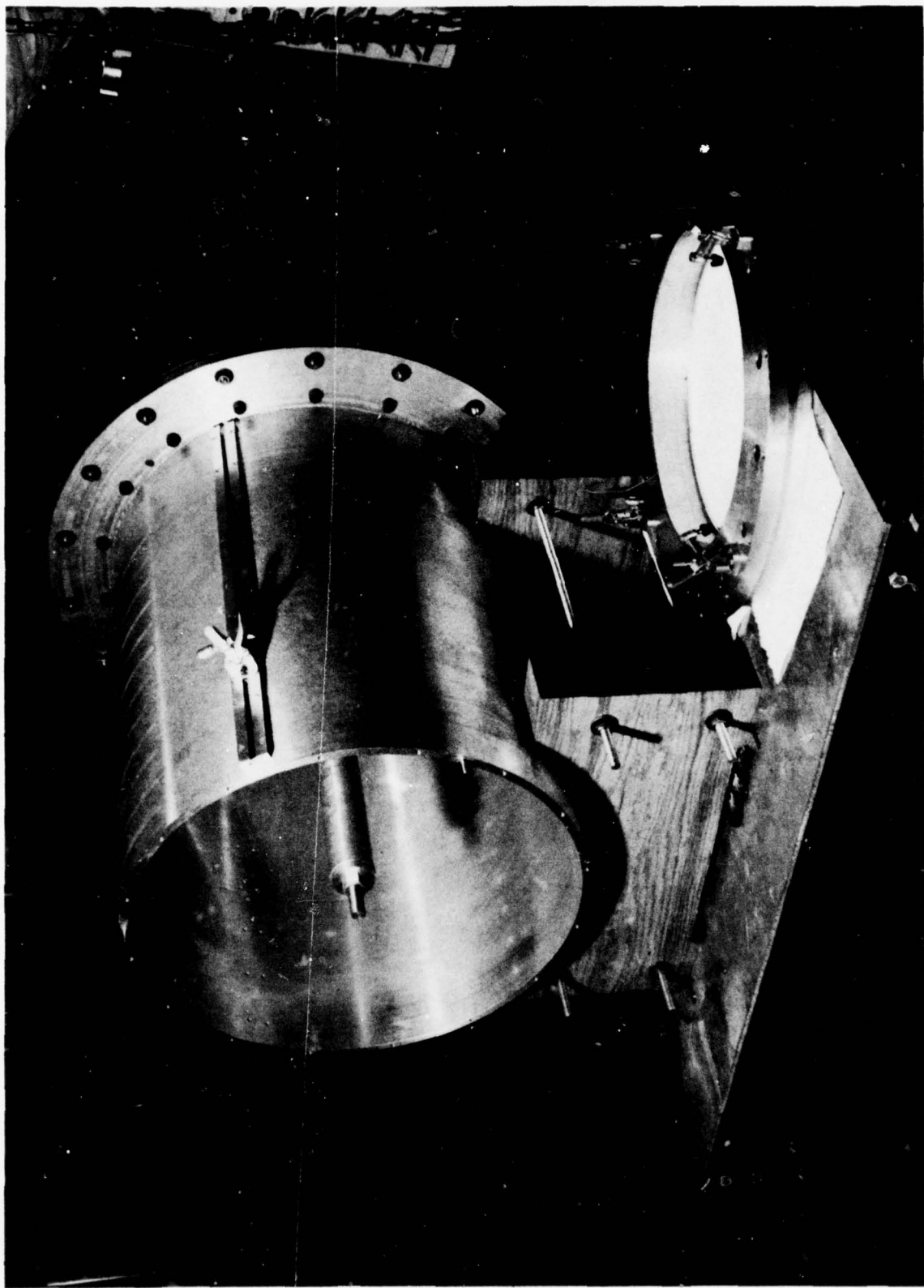
Figure 15 Outer Shell With Wood Liner Removed

27
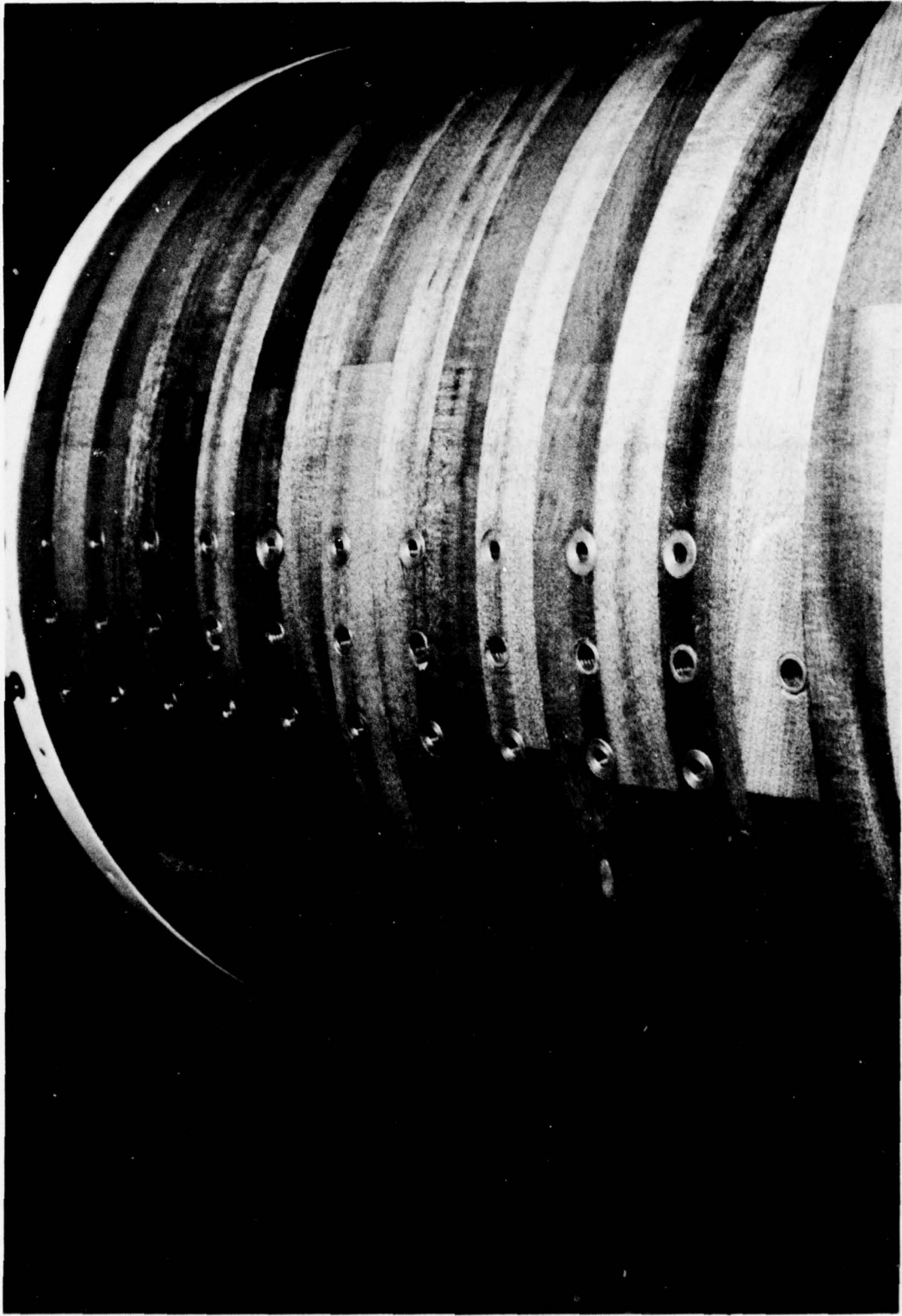
Figure 16 Wood Liner Probe Penetrations

28

holes were required in the liner to permit probe penetration and those
not in use could be plugged with simple, nonflow-interfering slugs. This
design concept was awarded United States Patent No. 4,031,749 on
28 June 1977. The liner, Figure 16, was made of laminated mahogany for
dimensional stability and was approximately three and one half inches
thick to permit flexibility in channel wall contour, if later required.
The penetrations through the liner consisted of metal inserts in the wood
which were drilled large enough to provide clearance for the probes.
In addition, the flow channel side was tapped for either a probe support/
seal bushing or a solid cylindrical plug. These were made of teflon to
reduce friction on the probe, and a typical one is shown in Figure 17.
The liner was sealed to the outer structure at each end with an O-ring
made of hollow plastic tubing.

With regard to the wrenchless static pressure line connections,
this was achieved by putting an elastomeric O-ring around each line to
act as a static seal as the line crossed a bulkhead in the rear center-
body support assembly. This bulkhead is shown in Figure 18. To allow
for any slight misalignment due to fabrication tolerance or temperature
changes during a test run, each O-ring was contained in a spring-loaded
carrier which permitted slight axial and radial displacements. This
connection concept was awarded United States Patent No. 4,111,463 on
5 September 1978.

The entire assembly was designed for easy teardown and quick access
to the flow channel and all instrumentation. Standard tooling toggle
clamps were used to retain both the bellmouth and the circumferential
saddle. Thus, without any wrenches, the axial saddle station could be

29
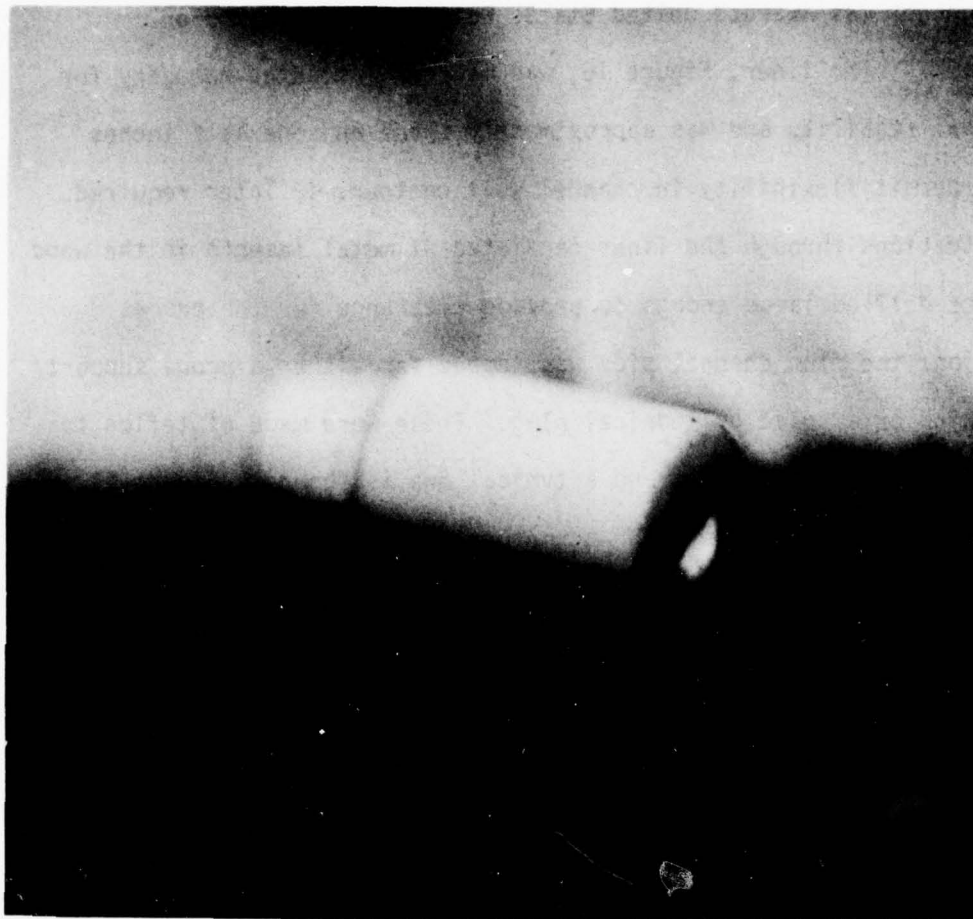
Figure 17   Closeup of Typical Probe Teflon Bushing

Figure 18 Rear Centerbody Support - Upstream View

31

changed and the inlet bellmouth assembly removed. Once the bellmouth assembly was off the main assembly, the blade row could be slipped out, again without tools. This gave access to the channel and probe. Then, with only the removal of one hex nut, the entire centerbody assembly could be removed. As described above, the static pressure lines were automatically broken at the rear of the centerbody without any requirement for tools. These details are shown in Figures 19 through 26.

The centerbody static pressure line installation is shown in Figure 24. All wall static pressure taps used in this experiment were machined in accordance with the recommendations of Rayle[23] as reported by Dean[24, pp. 59, 60]. The centerbody taps are shown in Figure 27. The first thirteen are spaced one-half inch apart and the others are spaced one inch apart. A closeup of a typical outer wall static tap is shown in Figure 28. The teflon bushing adapts the metal pressure tap to the liner penetration ports in a manner similar to that used for the wedge probe. and these are shown as installed in Figure 29.

The circumferential saddle assembly shown in Figures 30 and 31 was designed to permit mounting two probe actuators manufactured by Northern Research Company. These actuators are hydraulic servo positioning mechanisms which can be remotely set from the test cell control room. They accurately and repeatably set the radial and angular positions of any probe inserted in their collet assembly. Details of the calibration procedures used on the actuator are contained in Appendix C. A three-channel system was purchased since no similar equipment existed in the Laboratory, and the flexibility for future use was considered worth the extra cost. In the final arrangement for this experiment, only one

32
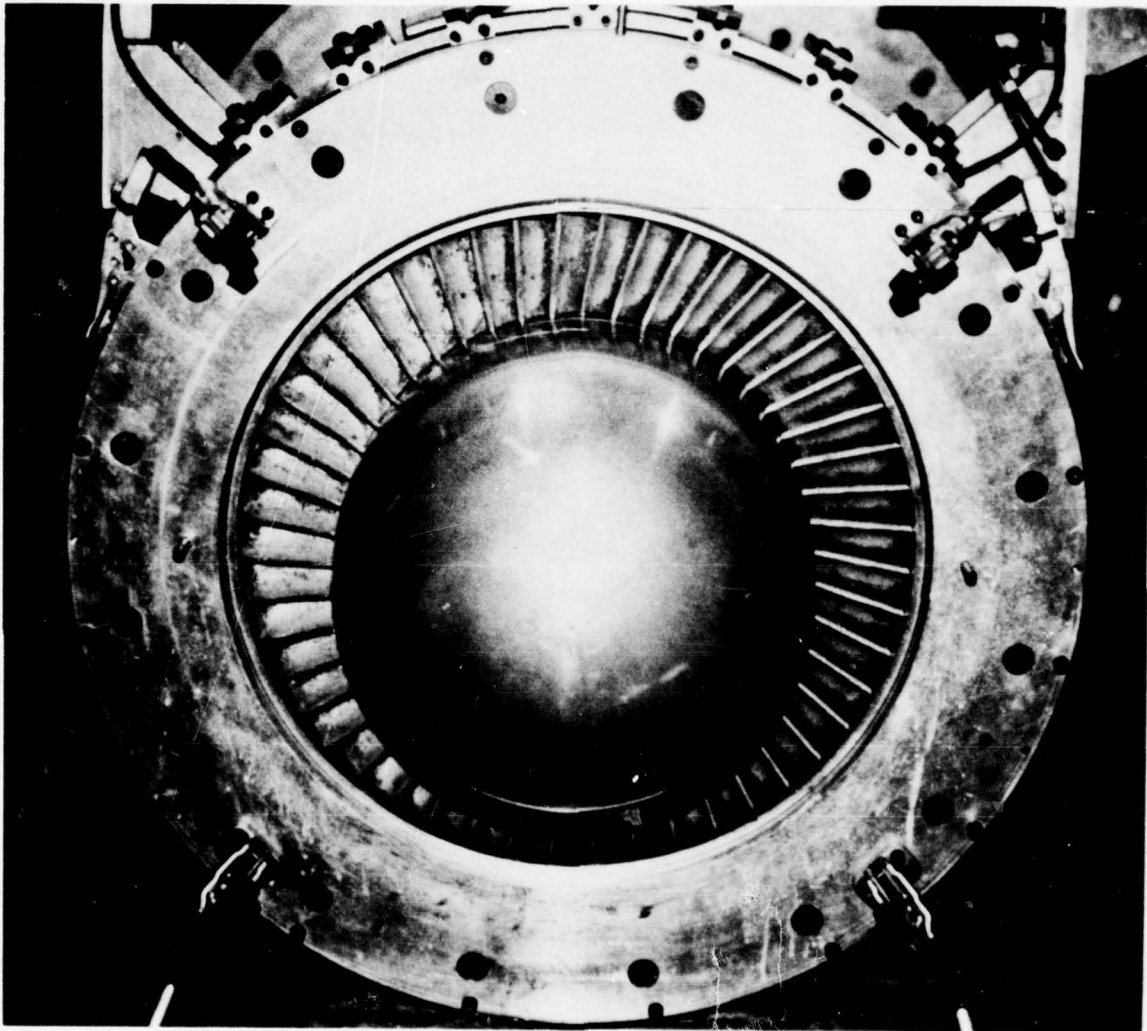
Figure 19 Inlet With Bellmouth Removed
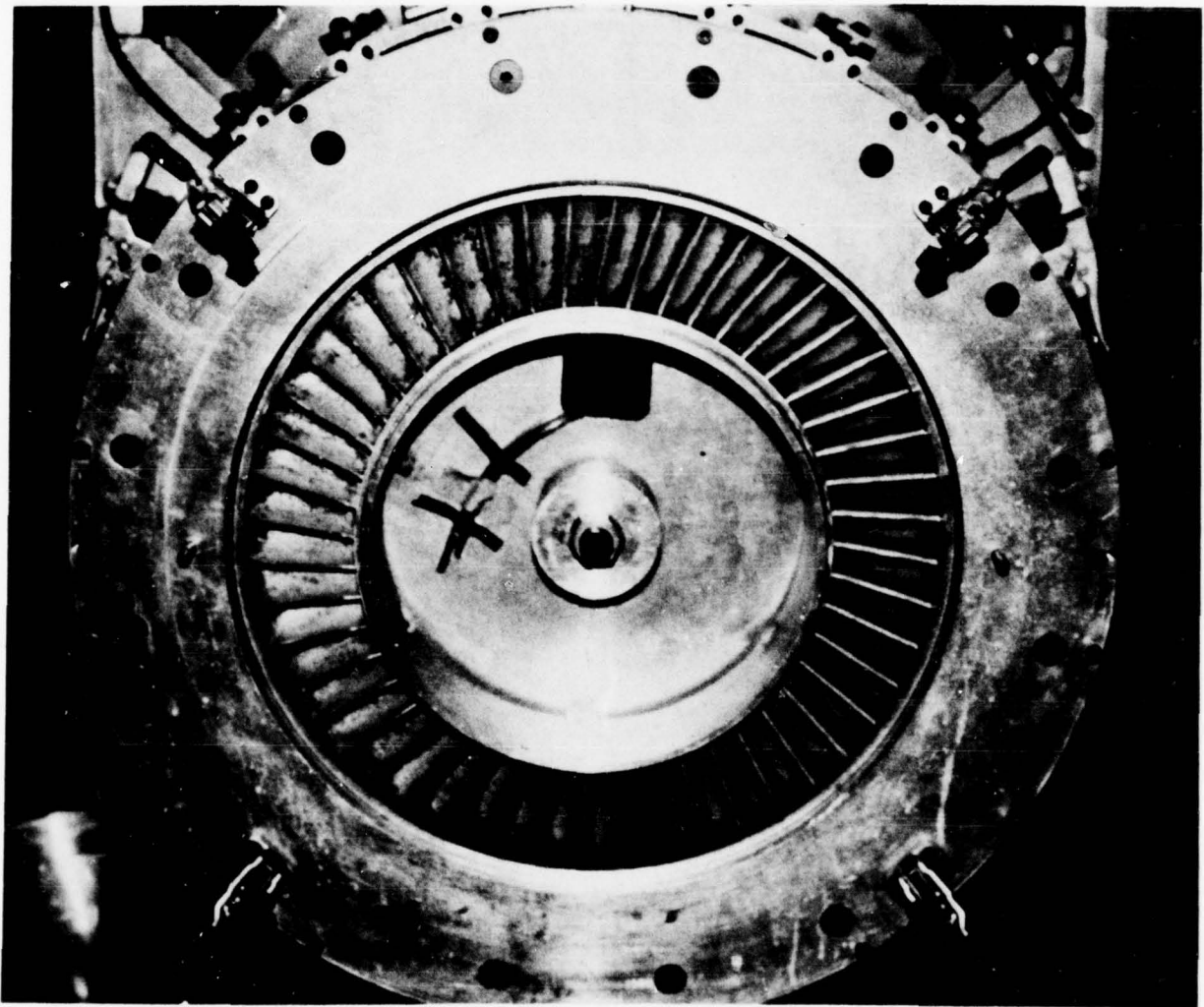
Figure 20   Inlet With Centerbody Fairing Removed
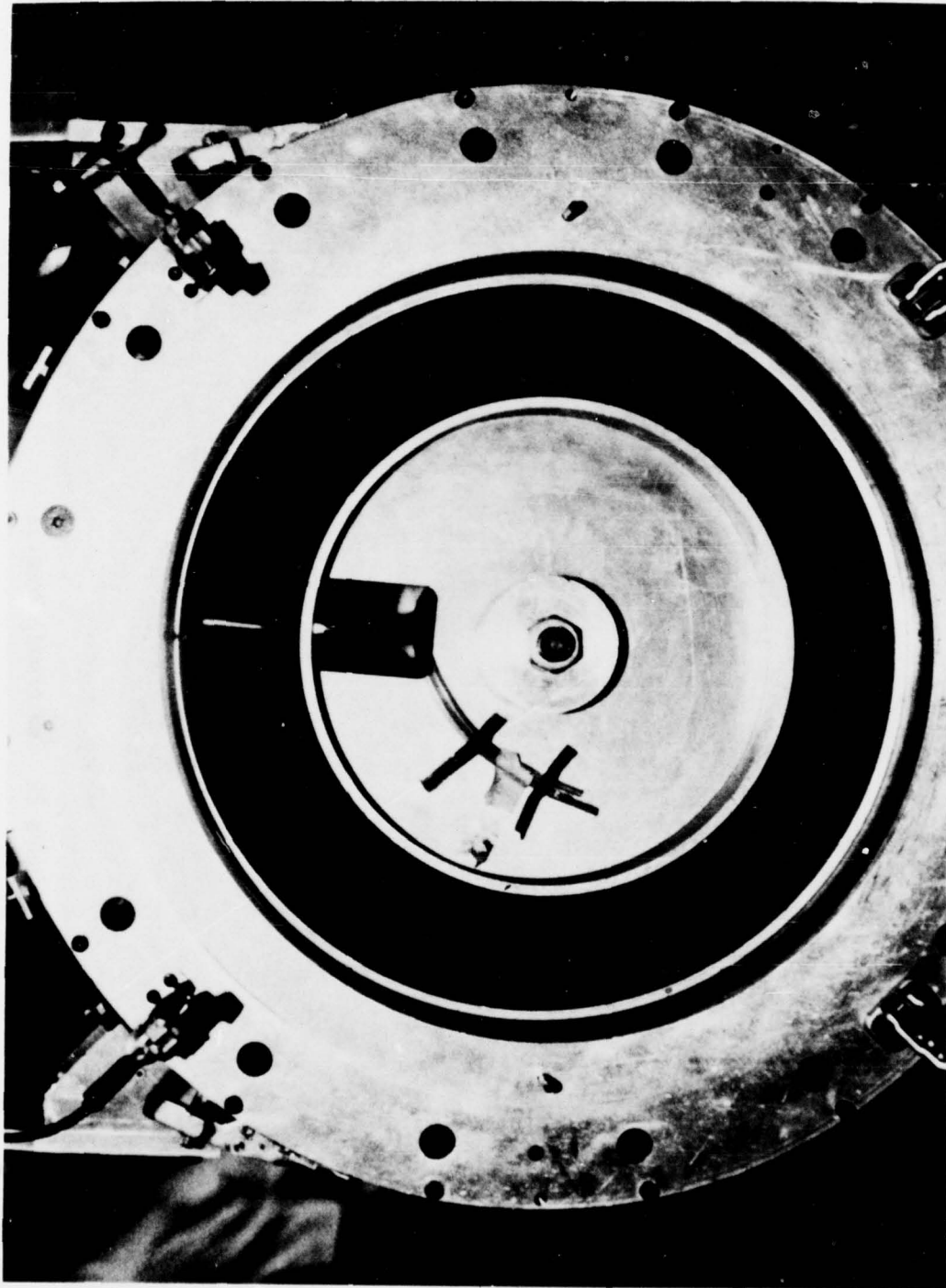
Figure 21 Test Apparatus Less Blade Row
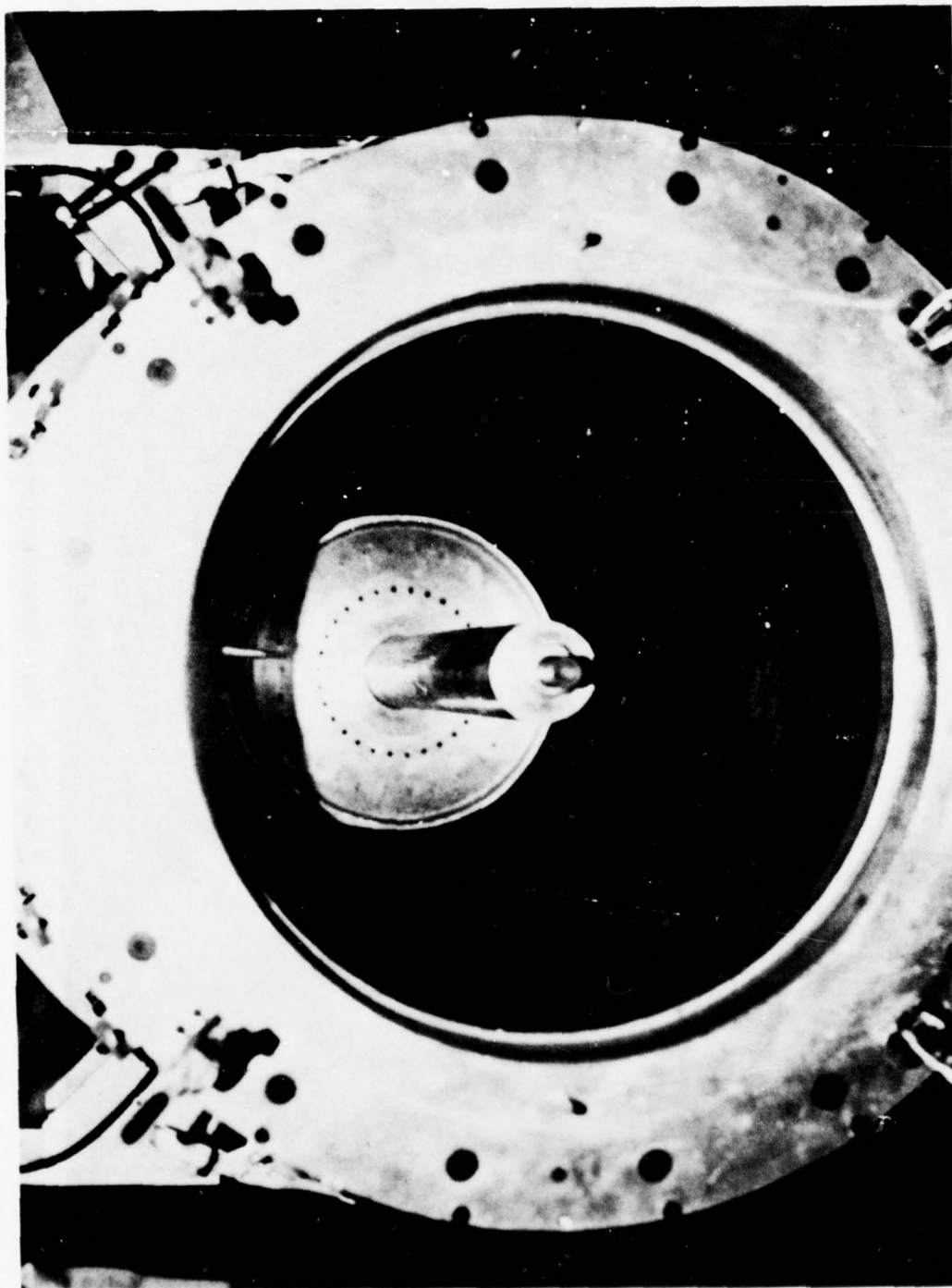
Figure 22 Centerbody Removed

Figure 23 Centerbody Guide Tube Removed

37
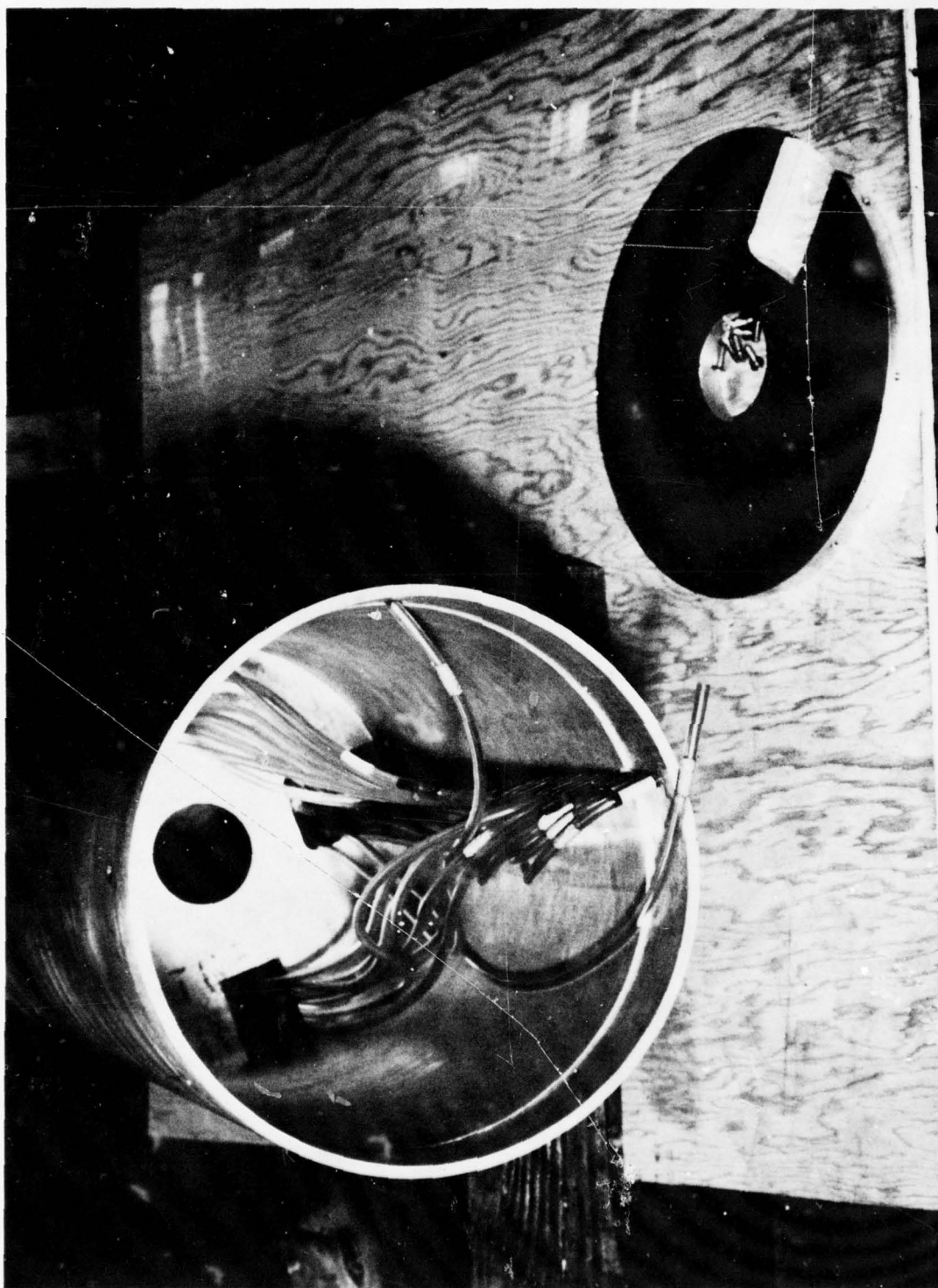
Figure 24. Centerbody Static Pressure Lines
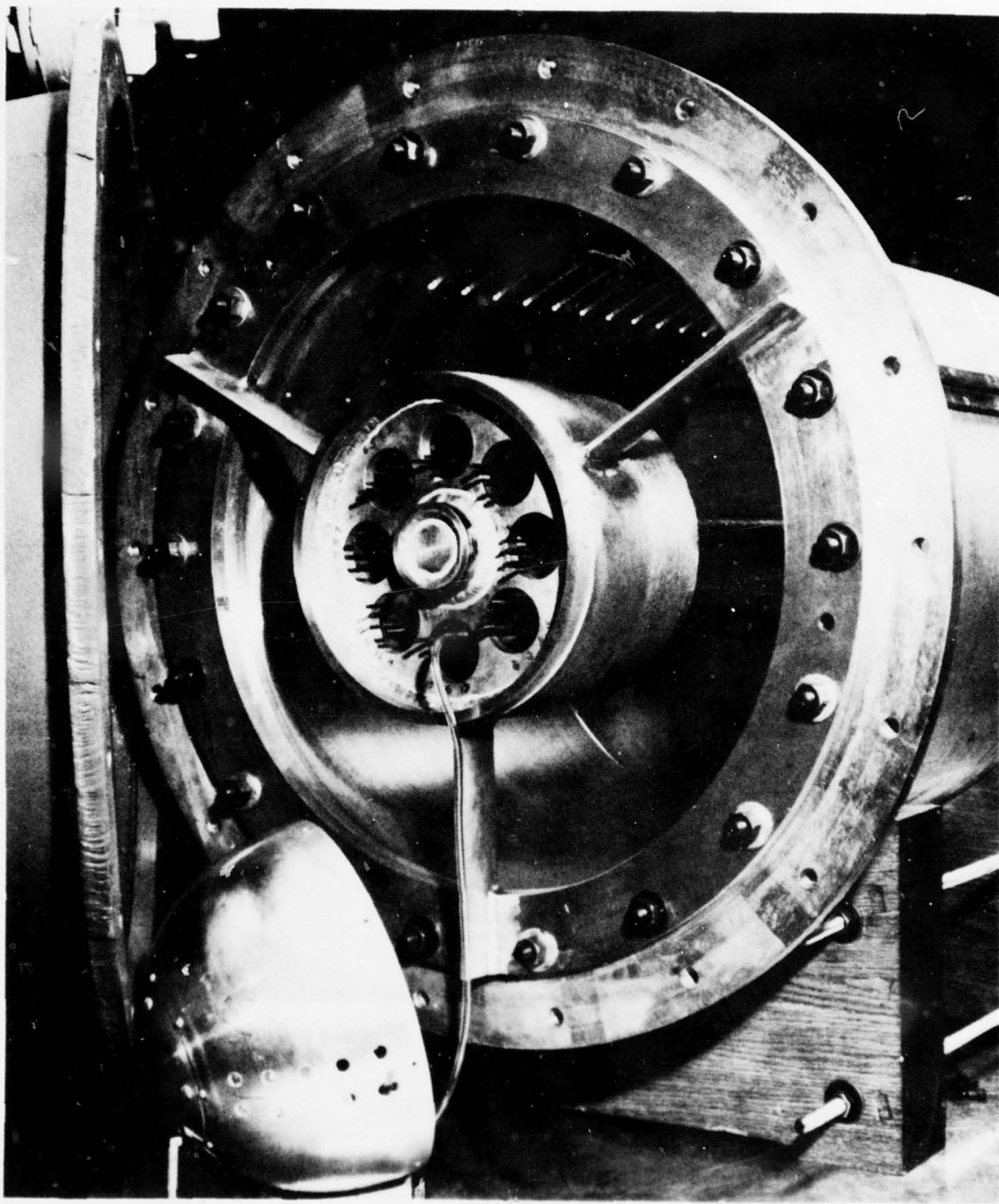
Figure 25 Rear Centerbody Support - Downstream View

39
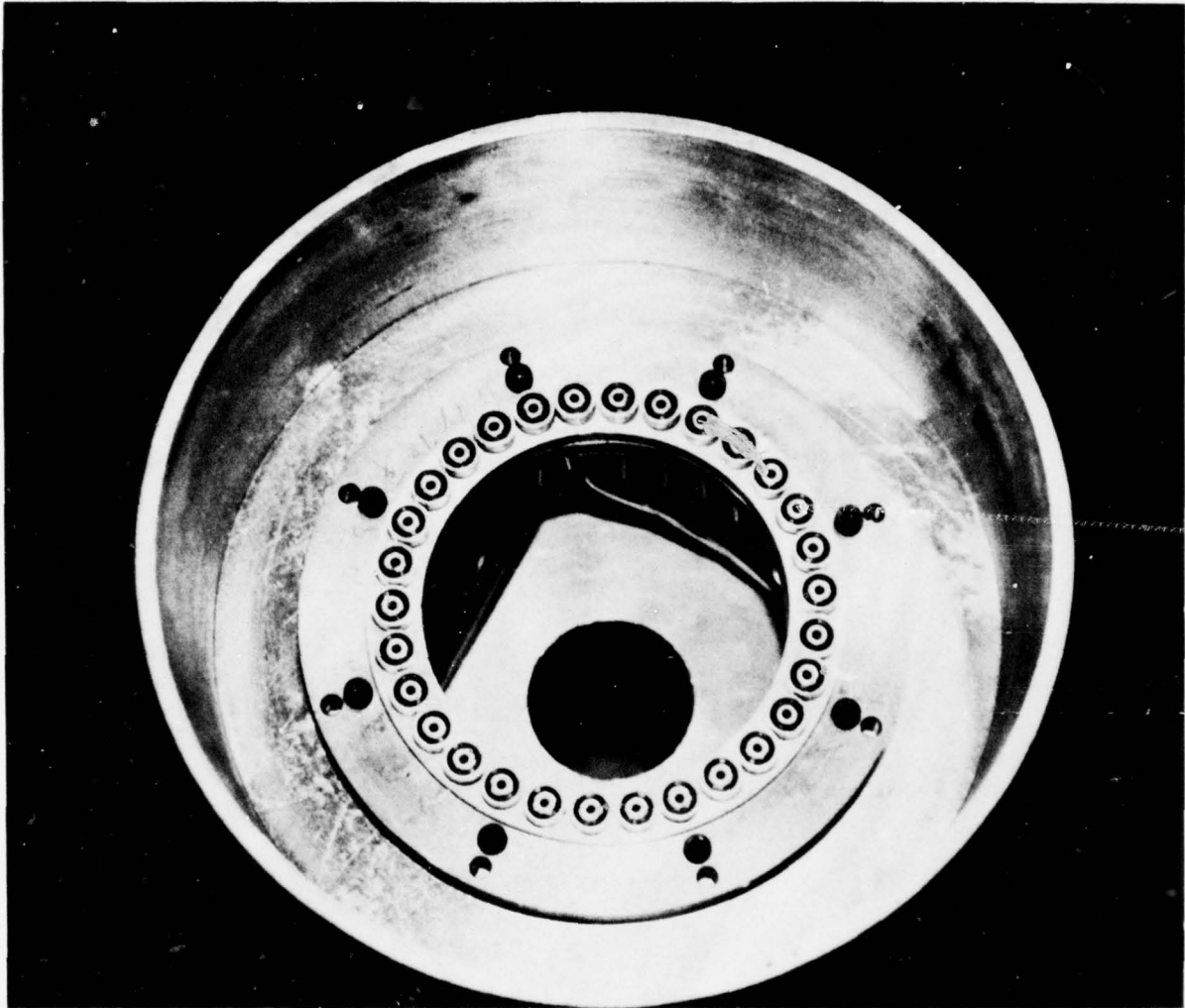
Figure 26   Centerbody Wrenchless Pressure Connection

40
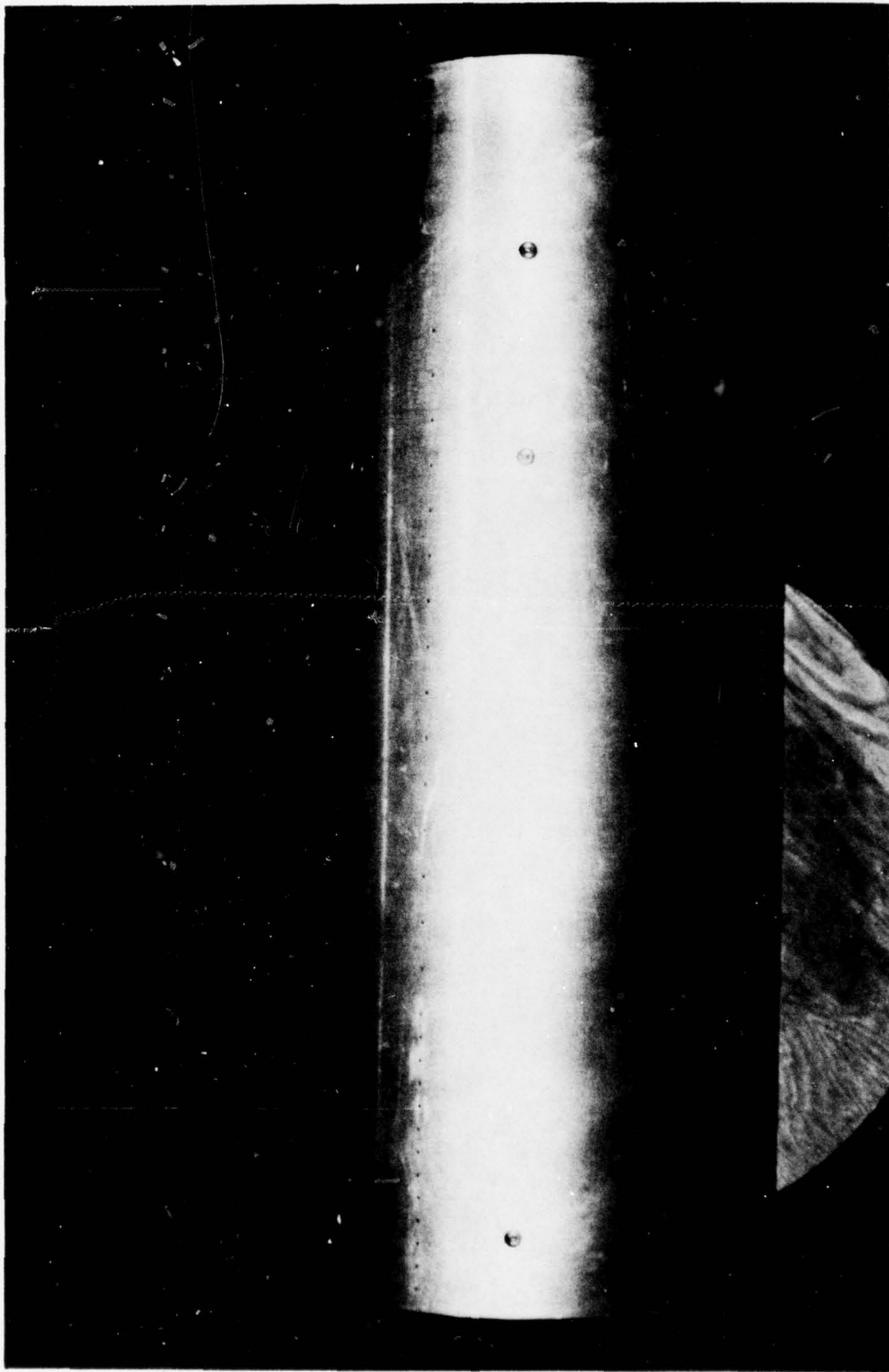
Figure 27 Centerbody Static Pressure Taps
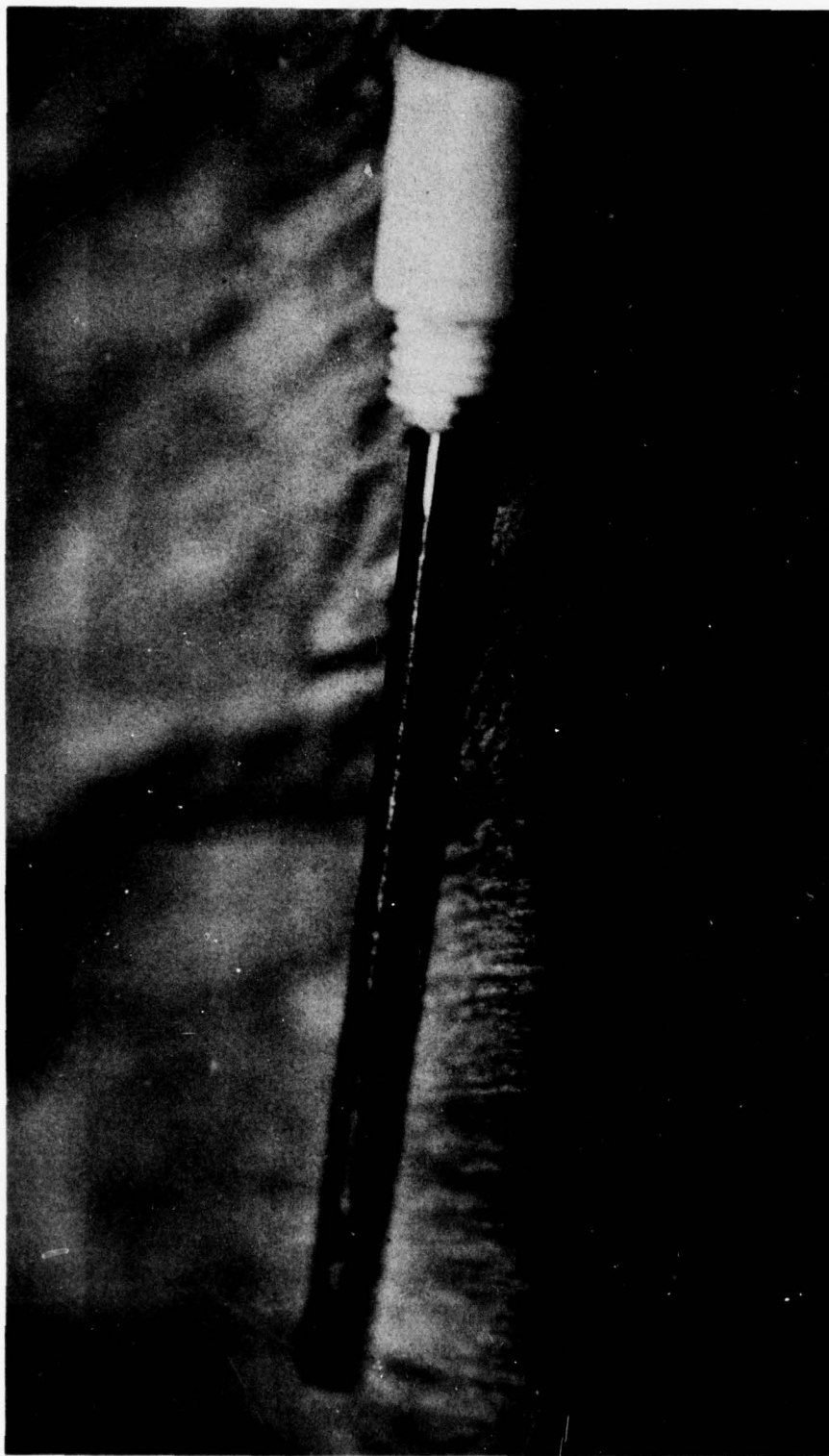
Figure 28 Closeup of Outer Wall Static Pressure Tap
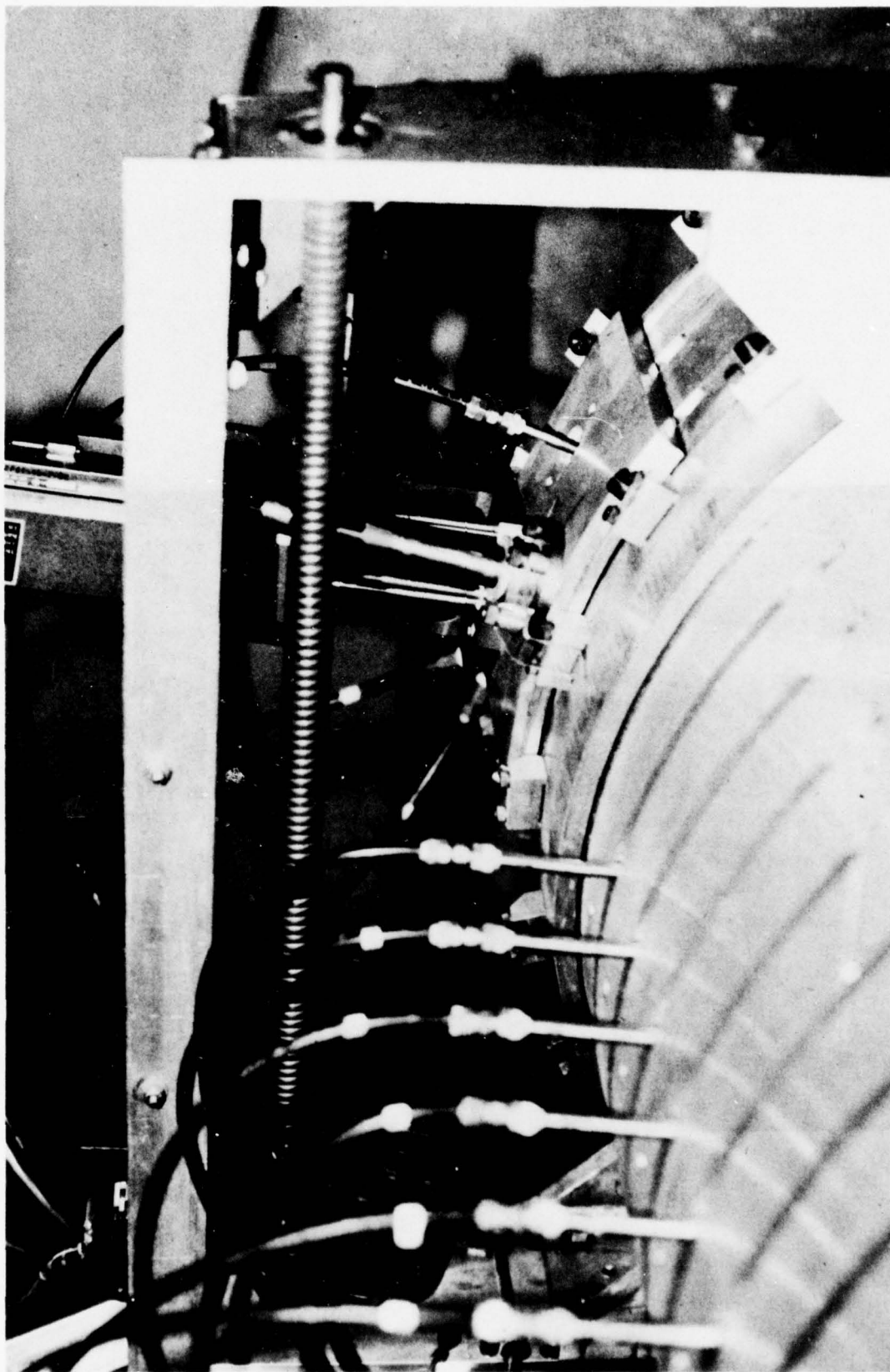
Figure 29 Outer Wall Static Taps

43
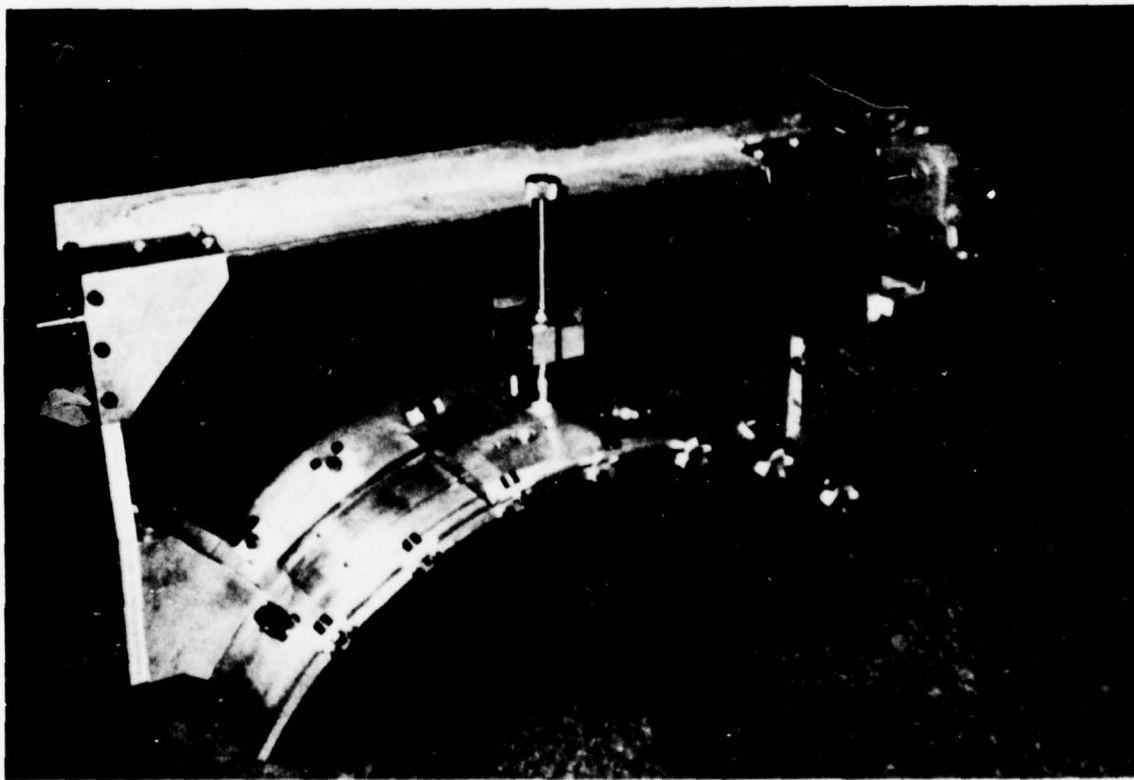
Figure 30   Circumferential Saddle Assembly

44
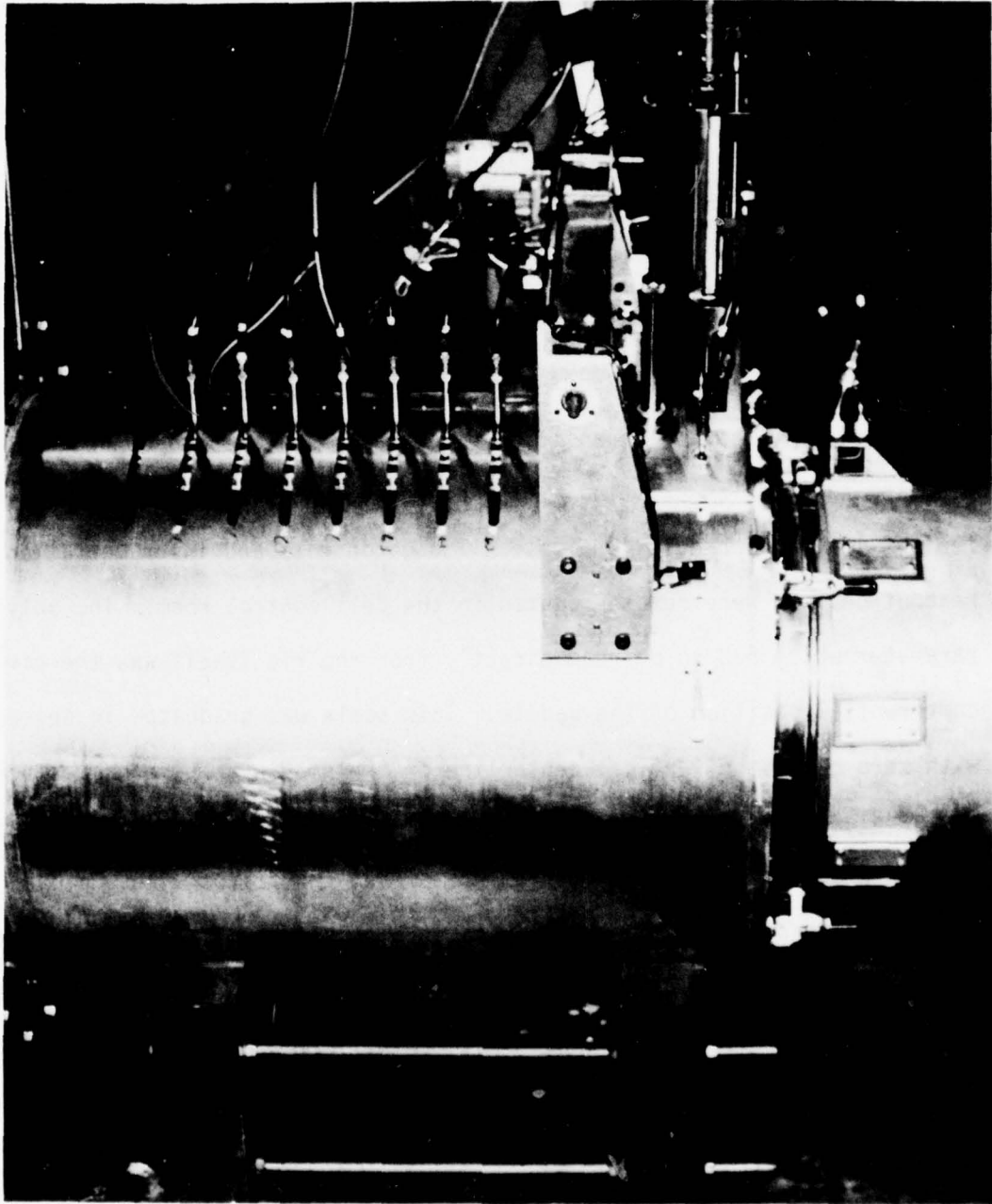
Figure 31 Actuator Installation on Saddle

45

actuator was used. The system consists of the actuators, a hydraulic power supply, and a remote control/readout panel. These are shown in a bench functional checkout setup in Figure 32. The actuator is shown as mounted on the circumferential saddle assembly on the rig in Figures 31 and 33. A complete numerical index of all rig fabrication drawings is shown in Appendix D.

Experimental Setup

The entire test assembly with probe installed is shown in Figures 34 and 35 as set up in Cell 24 of Building 18E at Wright-Patterson Air Force Base, Area B. A conical transition piece was fabricated to connect the test apparatus to an existing altitude engine stand via approximately 18 feet of 16-inch Schedule 40 pipe. All rig controls and instrumentation readout devices were remote mounted in the cell control room. The only parameter which had to be read directly from the rig itself was the circumferential position of the saddle. This scale was graduated in degrees with zero being the vertical centerline of the saddle. Therefore, since the saddle contains two actuator pads, the actual circumferential position of each probe radial line of action was offset from zero. These pads were machined as close together as possible; but due to the actuator size, each had to be offset 7 1/2 degrees; i.e., there was a 15-degree included angle between probe radial paths. These details are shown in Figure 13. The relative location of the probe and blade row with probe installed at station one is described in Figures 36 and 37.

Except for total temperature readout from the probe, the control room arrangement is shown in Figure 38, while Figure 39 shows the Brown recorder used for temperature readout and recording. All probe pressures

46
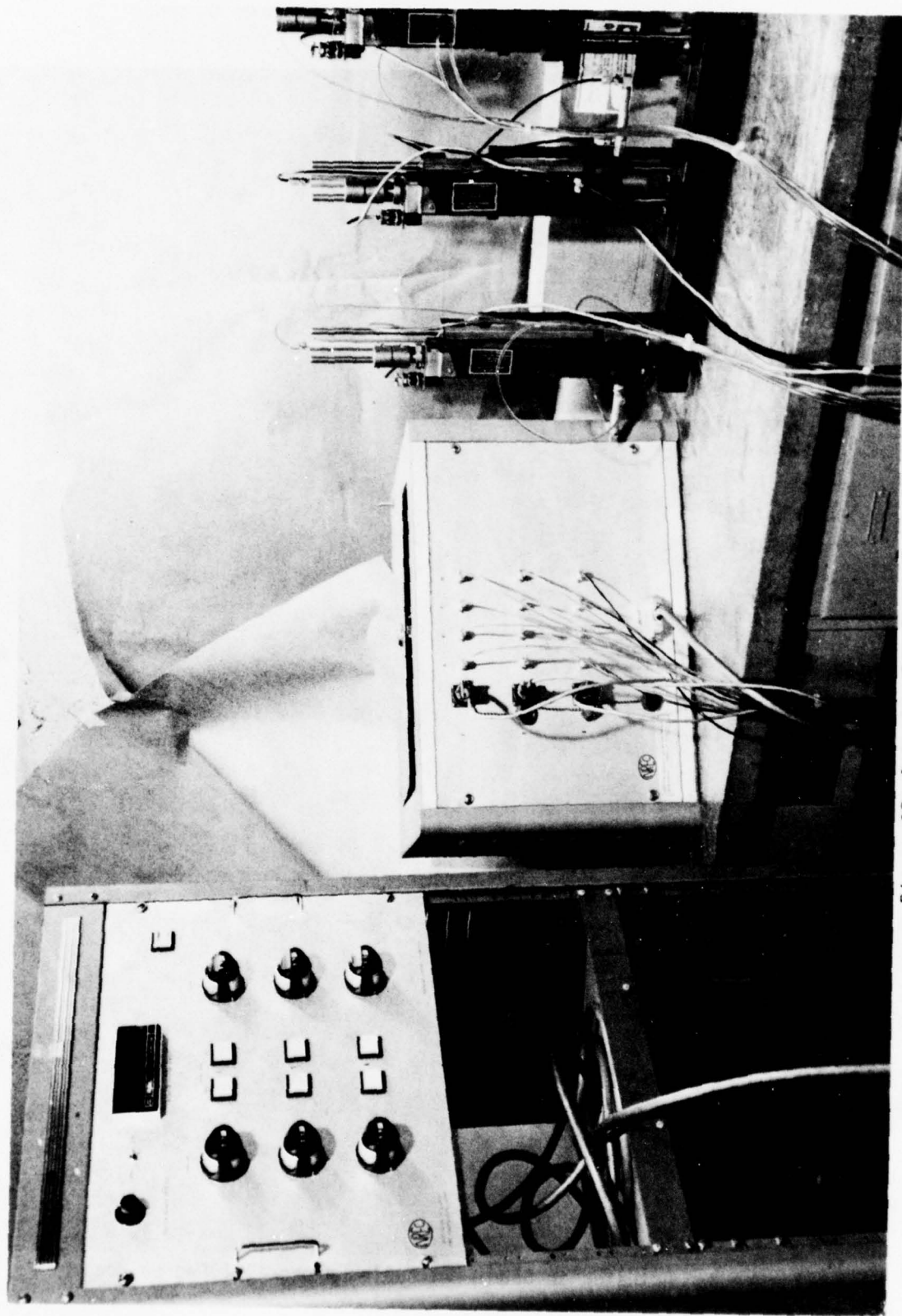
Figure 32 Actuator Bench Checkout Setup

47
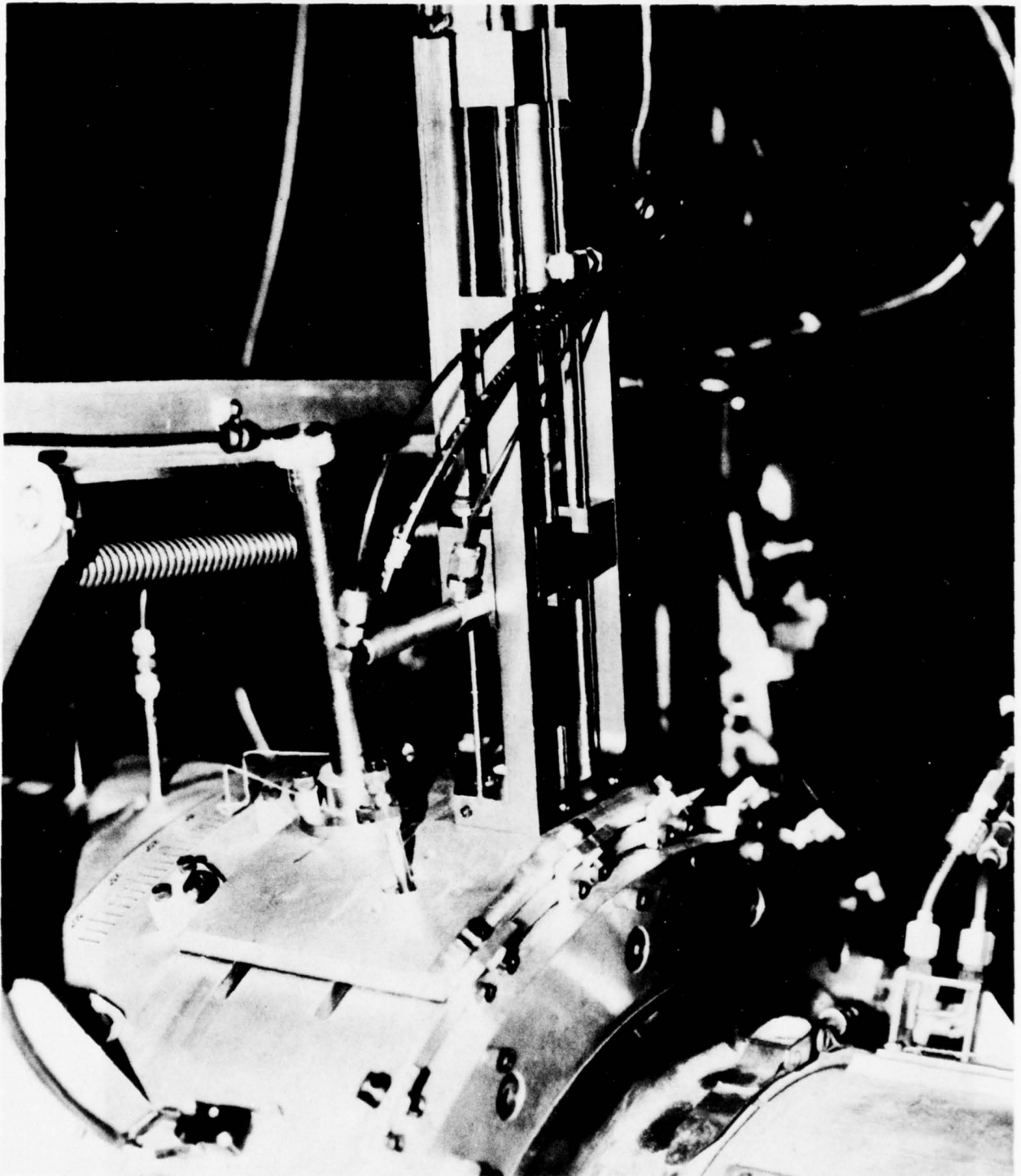
Figure 33 Actuator on Saddle with Circumferential Degree Scale

48
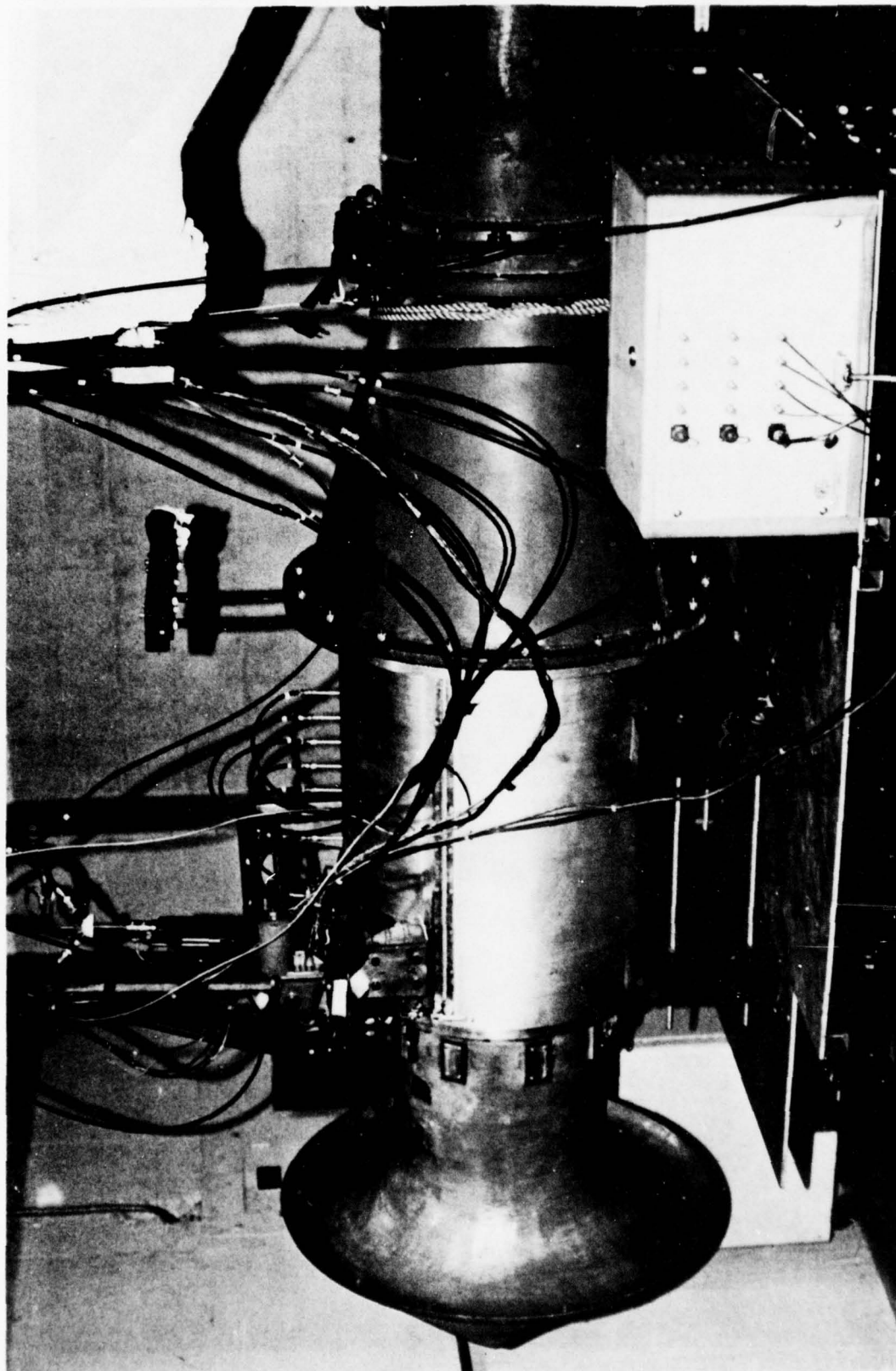
Figure 34 Test Assembly Installation - Right Side
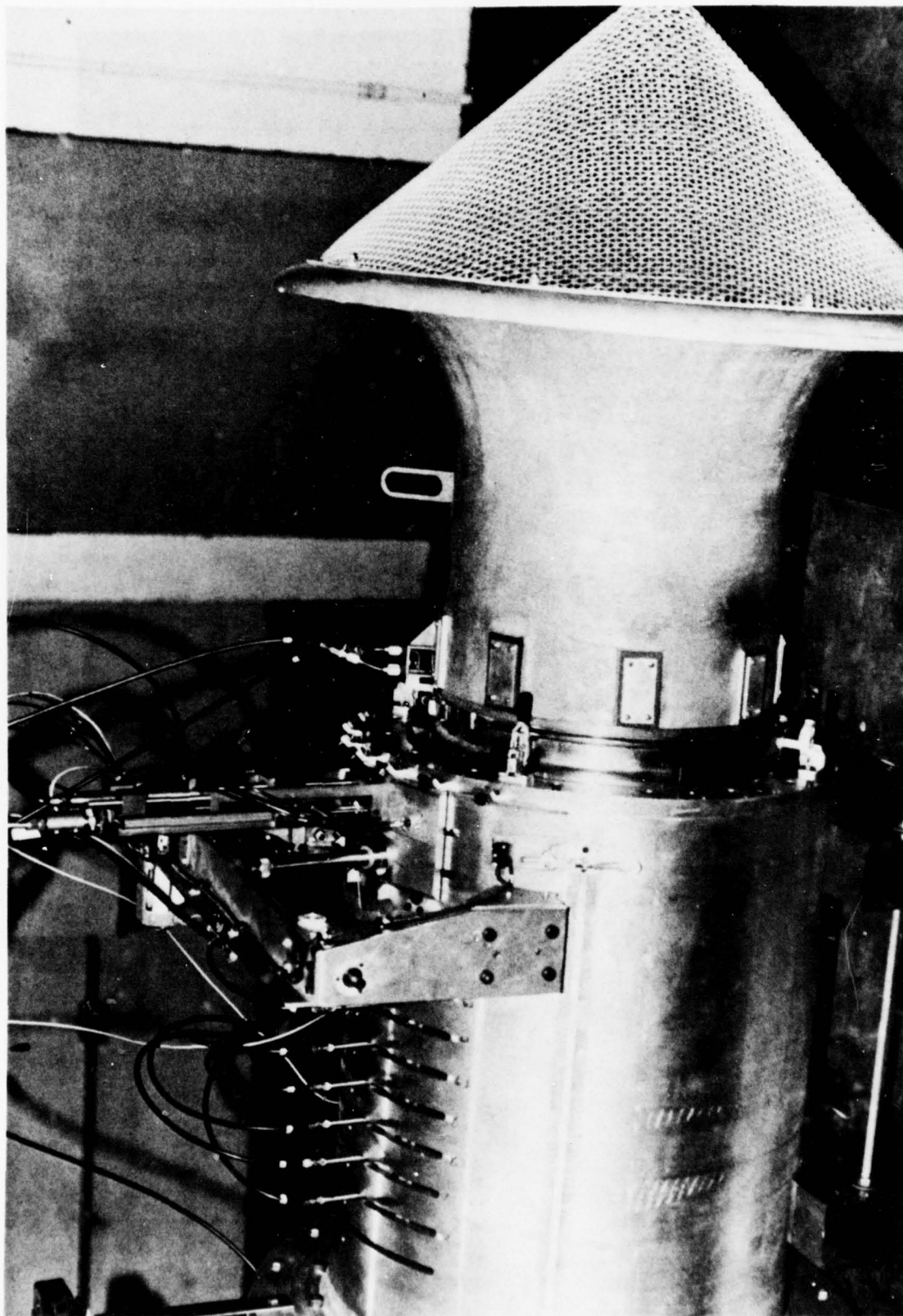
Figure 35 Test Assembly Installation – Left Side

BLADE
EXIT
PLANE

STATION

0.75"

BLADE
ANGLE

FLOW
ANGLE
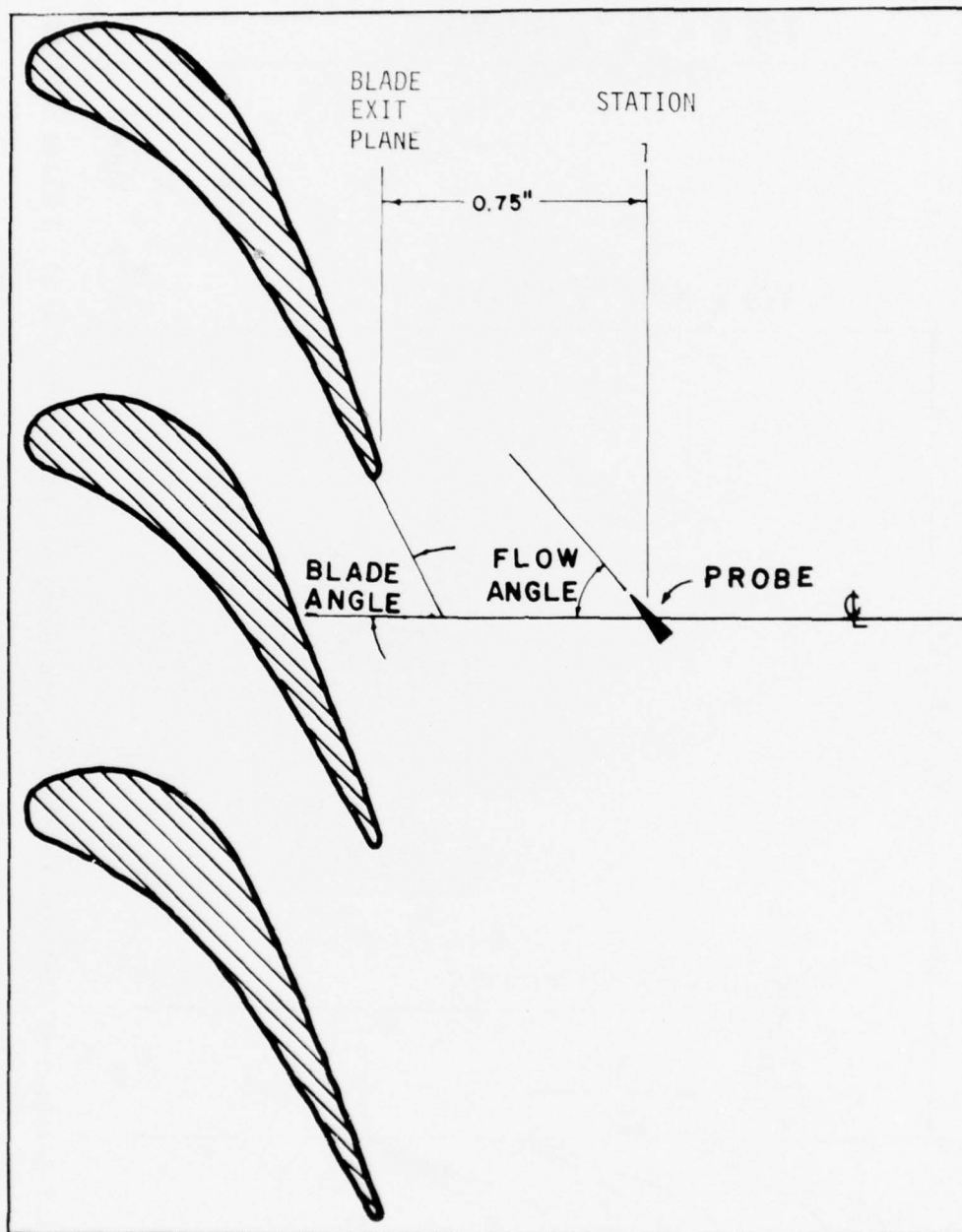
PROBE

Figure 36 **PROBE - CHANNEL**
REFERENCE

51

STATION 7, Z_7 = 9.861

STATION 3, Z_3 = 3.674

NOTE:

$$Z_I = \frac{X_I}{CHORD}$$

X_7 = 12.75"

X_3 = 4.75"

β	PITCH, TIP
69.7°	1.0472"
65.0°	1.0053"
60.0°	0.9308"

STATION 1, Z_1 = 0.58

X_1 = 0.75"

PITCH

CHORD = 1.293"

β
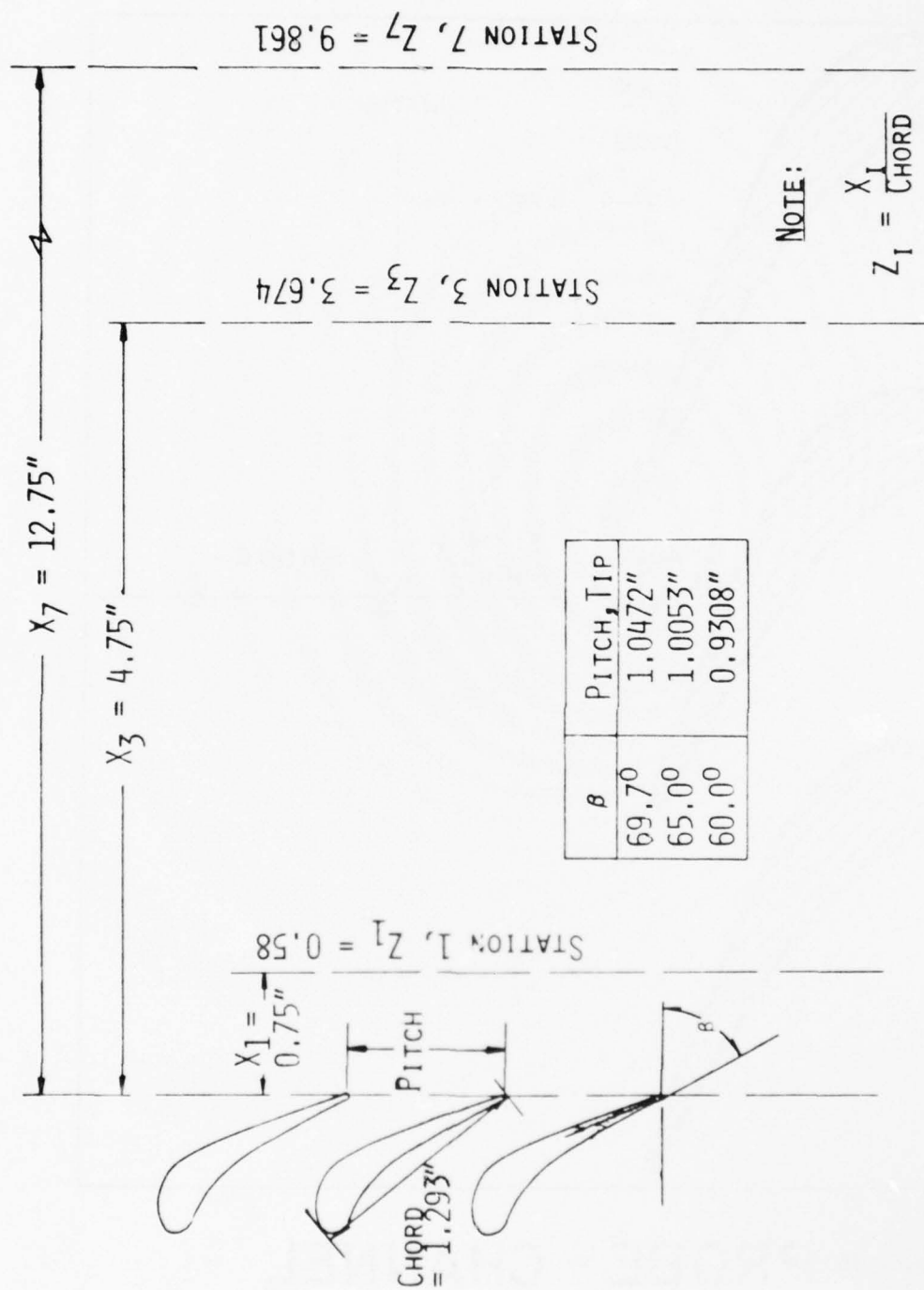
Figure 37 Spatial Relation of Stations to Blading, and Geometric Parameters for the 3 Blade Settings Used

52
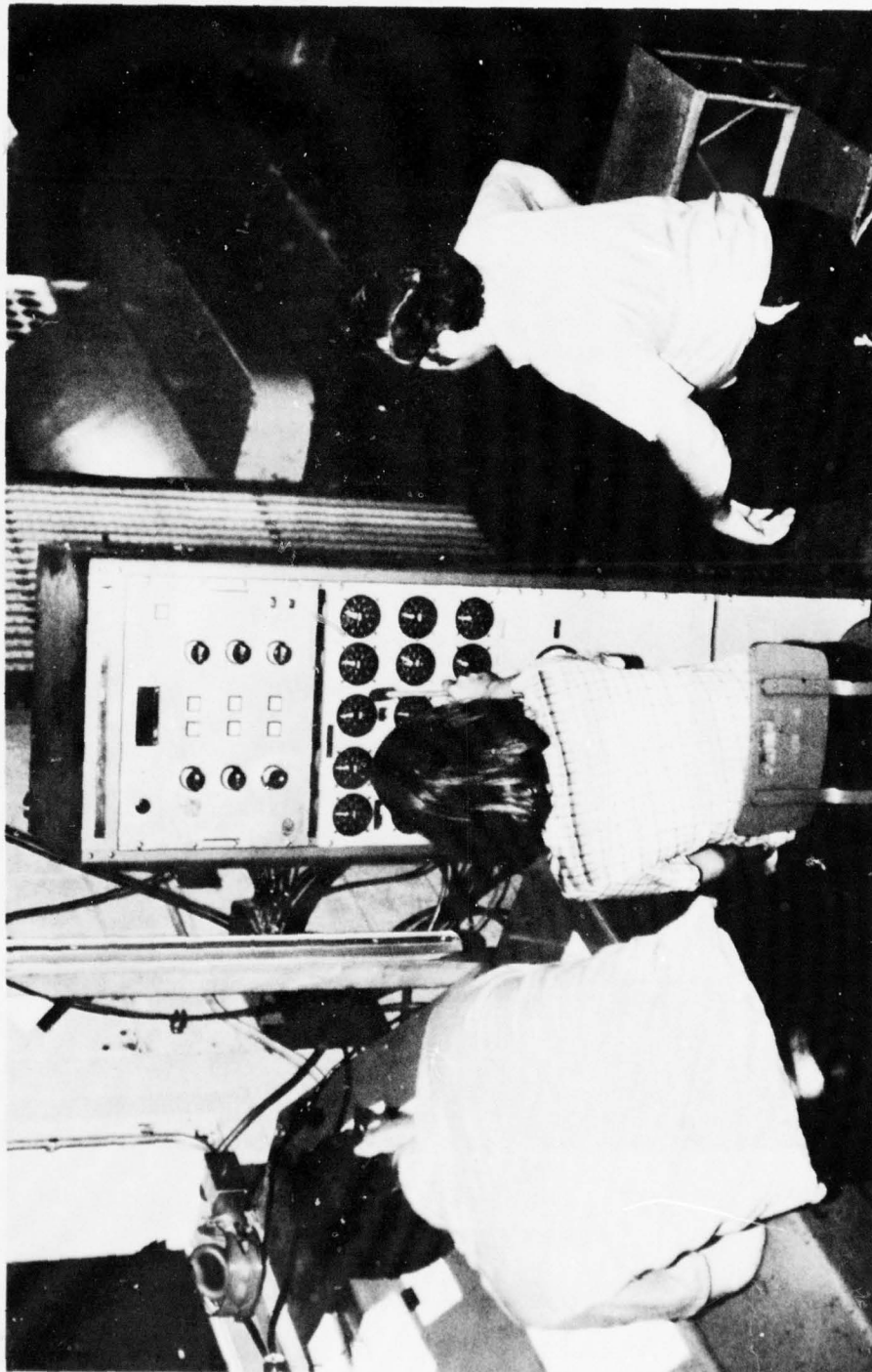
Figure 38 Control Room Operation and Readout Equipment
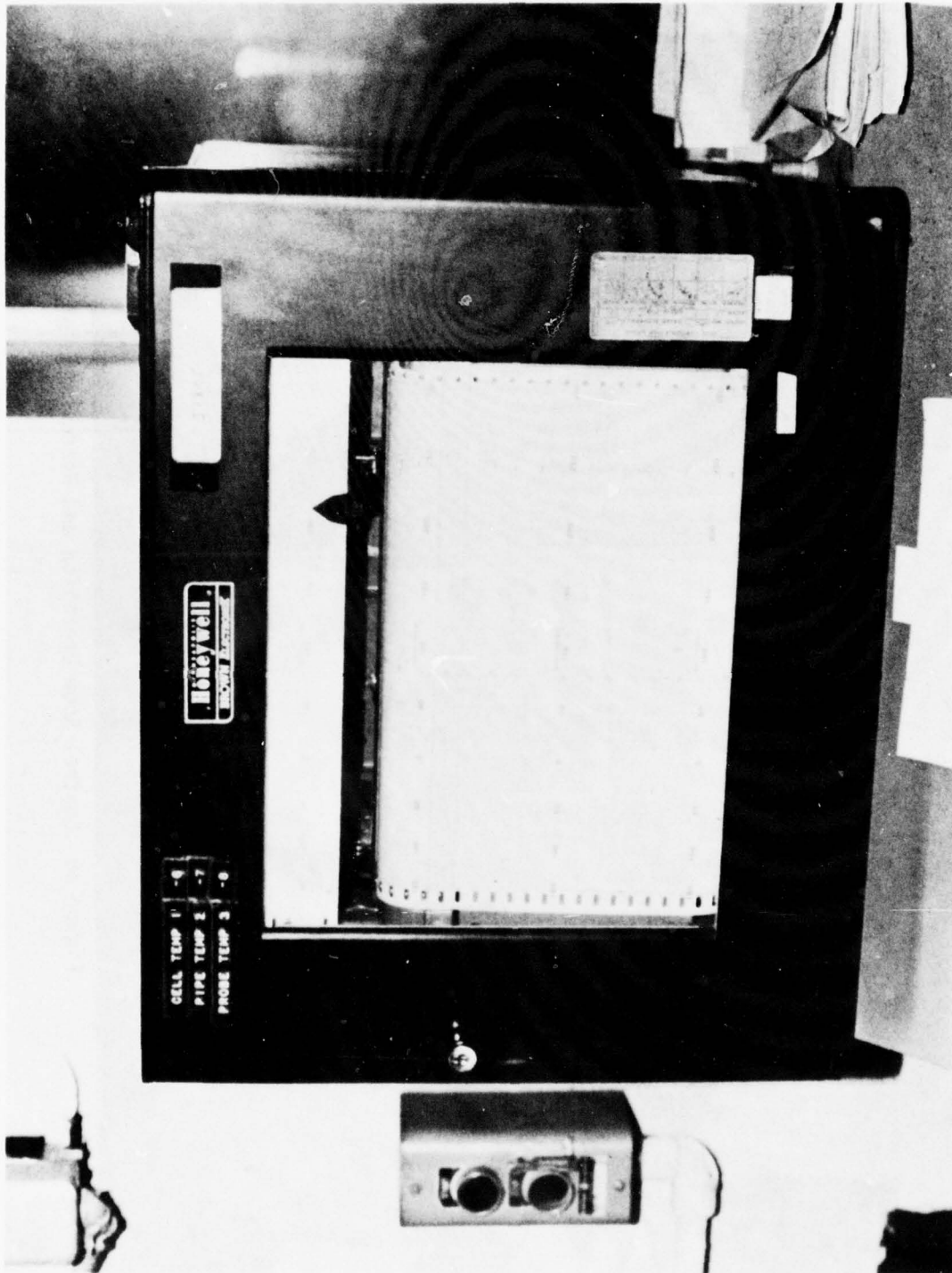
Figure 39 Temperature Recorder

54

were read on Kollsman aneroid gages graduated in inches of water which were calibrated by the Base PME (Precision Measuring Equipment) Shop. The remaining gages on the panel were used for outer channel wall static readings, while the inner wall static taps were connected to a manometer board also shown in Figure 38.

The probe angular and radial (linear) positions were read from a digital voltmeter which was part of the actuator package. Using the calibration table in Appendix C, the actual geometrical position could be determined or set.

Data Acquisition Technique

The raw data taken at each circumferential position consisted of:

Wedge Probe

$$P_{total}$$

$$\Delta P = P_{total} - P_{static}$$

$$T_{total}$$

Flow Angle

Radial Position

Wall Static Pressures (both inner and outer)

Chamber (Receiver) Pressure

Cell (Air Inlet) Temperature

As stated before, it was not considered cost or time effective to install and checkout the required data automation equipment on such a relatively simple, steady-state experiment. Therefore, all data were recorded by hand on prepared data sheets, and two sample complete runs are shown in Appendix E. These sample data sheets show the total scheme

55

used for recording all data taken. Note that, on the data sheets $P_t = P_1$; P_2 and P_3 are the wedge face taps.

The standard nomenclature for probe circumferential location used for all data taken during this experiment is shown in Figure 40 and is described below.

As shown in Figures 7, 9, and 11, each of the three cascades was located by a dowel pin such that a trailing edge was always on the vertical centerline of the test assembly. In addition, the circumferential "saddle" zero reference was located on the vertical centerline. Now, since the saddle was designed and machined to permit simultaneous mounting of two probe actuators, the included angle between probe lines of action was 15 degrees. Therefore, when the saddle circumferential position indicating pointer is set at zero, the actual probe positions are 7 1/2° right or left from zero. Finally, right and left were established as seen when facing the cascade inlet. So, during data taking, the circumferential position was always read directly from the scale and a proper allowance was made for actual probe locations during data reduction. For all runs conducted, the wedge probe actuator was mounted on the right saddle pad so that the following conversion was applicable to the raw data sheets: 0° indicated $\equiv$ 7 1/2° right.

The procedure used during a run at a given circumferential position was to set the desired radial traverse position and then rotate the wedge probe until the pressure difference between the two side static taps was zero. At this point, the flow angle was recorded and all other readings taken in sequence. The standard radial traverse positions used are shown in Table 4. A "short" traverse was also developed later as data became available, and comparative plots made which showed little

56
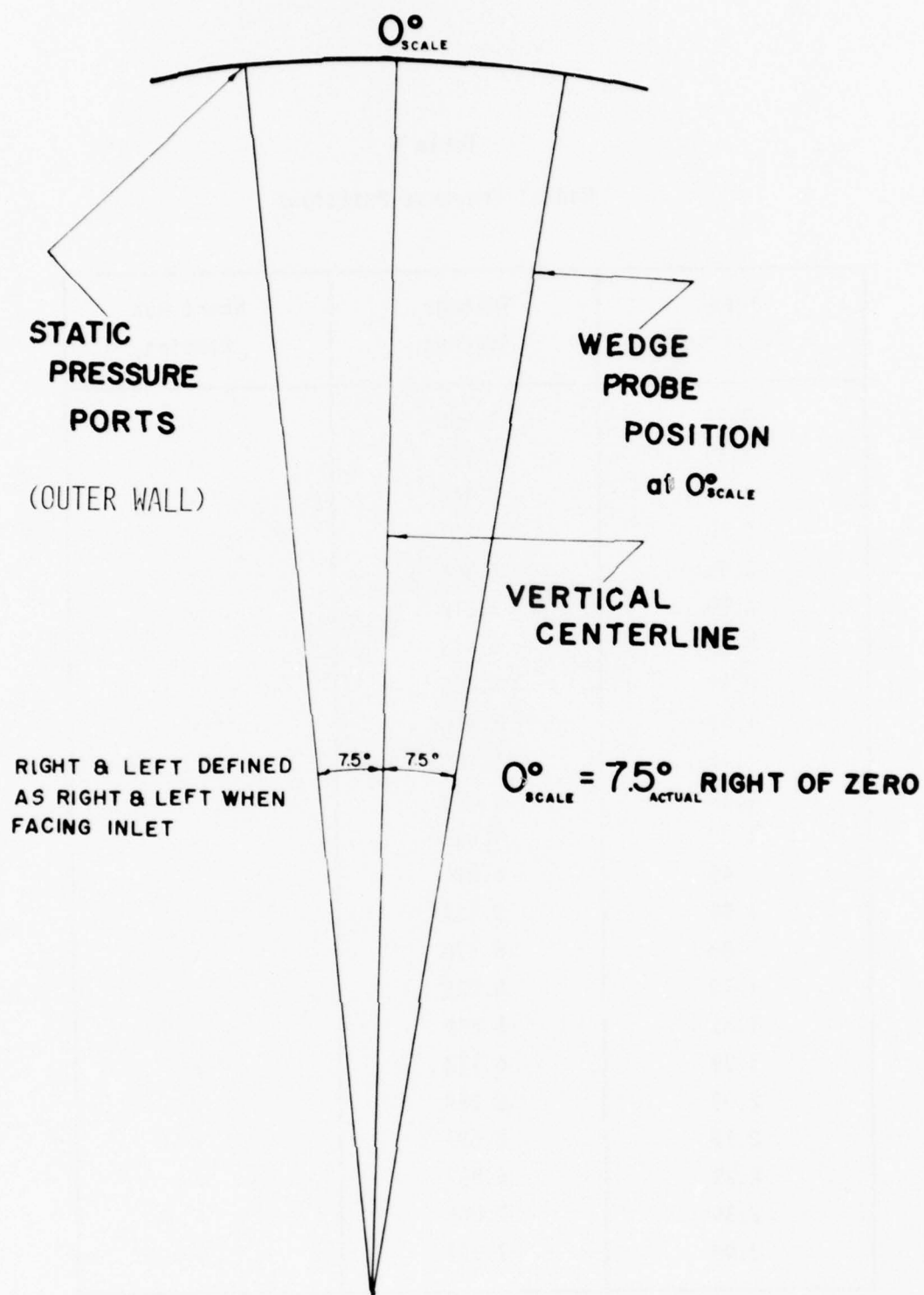
Figure 40   Probe Circumferential Location Nomenclature

Table 4

Radial Traverse Positions

Linear Position	Voltage Reading	Short Run Reading
0.29	1.956	✓
0.39	2.193	✓
0.49	2.444	✓
0.59	2.701	✓
0.69	2.966	✓
0.79	3.218	✓
0.89	3.448	
0.99	3.686	
1.09	3.916	✓
1.19	4.160	
1.29	4.398	
1.39	4.642	✓
1.49	4.894	
1.59	5.133	
1.69	5.378	✓
1.79	5.625	
1.89	5.866	
1.99	6.113	✓
2.09	6.358	✓
2.19	6.627	✓
2.29	6.857	✓
2.39	7.066	✓
2.49	7.227	✓

need for the close spacing in the center of the flow channel. A sample
of these plots is shown in Appendix F.

During the trial runs, it was observed that total pressure readings
across the channel were not uniform and that recirculation was apparently
occurring inside the channel due to exit conditions. Considerable effort
was then expended to eliminate this characteristic with the final result
being a "backflow plate" or flow fence installed at the outer diameter
of the channel exit. The proper plate bore for each blade row was deter-
mined by an experimental trial-and-error procedure. Plots of total
pressure and flow angle vs probe position as a function of backflow
plate bore are shown in Appendix G. As can be seen from these data,
a slight fence height change makes a very significant difference in the
pressure profile. For the 60° blade cascade, no plate was required.

Once this was settled, actual traverse data were taken over a wide
range of receiver pressures (flow rates) and at many axial and circumfer-
ential positions in the channel. All three blade cascades were even-
tually tested and the results are presented in Chapter III.

CHAPTER III

RESULTS

The experimental results obtained are summarized and discussed in this section. An analysis of experimental error associated with the instrumentation and procedures used is presented in Appendix L. Data was taken for all three blade angle settings: 60°, 65°, and 69.7°. Computer-generated plots of the basic data are shown for selected representative runs in Figures 41-43, 45-47, 49-51, 53-55, 57-59, and 61-63. The curve fitting method was a spline technique. To serve as a guide to the range of profiles covered, the following tabulation organizes the entire set of six samples with respect to probe circumferential location. Recall that the circumferential location is specified in degrees right or left when facing the inlet to the cascade and that the zero reference is the cascade vertical centerline which always has a blade trailing edge indexed on it by means of a dowel pin.

Table 5

Circumferential Location of Sample Traverses

Blade Angle (degrees)	Station No	
	1	3
69.7	2.5°L	0°
65	10°R	7.5°R
60	2.5°R	5.5°R

60

Blade Angle 69.7°
Station 1

Figure 41 P_{total} VS Probe Position

61

Figure 42 ΔP VS Probe Position

Blade Angle 69.7°
Station 1

Figure 43 Flow Angle VS Probe Position

63

Table 6

Mass Flow Calculation - Station 1, 69.7°

DATE 14/ 7/77   POSITION: 10.00 DEGREES LEFT OF ZERO   SADDLE STATION 1
CHAMBER PRESSURE 8.45 IN HG   BLADE ANGLE 69.70 DEGREES
ACTUAL PROBE POSITION: 2.5° LEFT OF T.E.

AREA FT**2	FLOW ANGLE DEGREES	MACH NUMBER	MACH NUMBER-AXIAL	DENSITY LB/FT**3	FLOW RATE LB/SEC	FLOW RATE/AREA LB/SEC/FT**2	VELOCITY-AXIAL FT/SEC	PS/PT
.084116	57.28	.67950310	.36723454	.049620	1.732693	20.59885750	415.1350	.734064
.025700	57.65	.63283549	.36537828	.049490	.525744	20.45697257	413.3580	.731933
.026136	58.28	.68024050	.35764909	.049709	.525677	20.11312160	404.6139	.733593
.026573	58.67	.69441751	.36107379	.043545	.537795	20.23840700	408.4883	.724505
.027009	59.26	.70198863	.35861662	.049673	.544607	20.16391596	405.9347	.719636
.027445	59.49	.71016162	.36054105	.049728	.556673	20.28302444	407.8856	.714368
.027882	60.01	.70701483	.35340054	.049856	.555765	19.93275456	399.8074	.716398
.028318	60.41	.71256563	.35196772	.049982	.563954	19.91503722	398.4475	.712804
.028754	60.66	.70493111	.34541000	.050000	.562333	19.55668988	391.1349	.711741
.029190	61.33	.69745884	.33461575	.050256	.555850	19.04247267	378.9118	.722551
.029633	61.82	.70201160	.33152013	.050420	.560895	18.92804778	375.4063	.719621
.030058	62.26	.68639732	.31940051	.050603	.550282	18.30733406	361.7843	.729651
.030499	62.52	.68247378	.31491998	.050804	.552554	18.11711825	356.6087	.732164
.030936	62.59	.70399156	.32408584	.053800	.577280	18.66044735	367.3322	.718346
.031373	62.69	.71906501	.32991953	.050869	.597339	19.03990001	374.2946	.708605
.031808	62.70	.72257042	.33140659	.050792	.608000	19.11469767	376.3331	.706351
.032245	62.76	.72376380	.33129025	.050865	.617000	19.13475458	376.1896	.705578
.032682	62.89	.72252719	.32925583	.050974	.622873	19.05858945	373.8907	.706379
.033117	62.93	.71762810	.32657728	.051228	.629153	18.95789065	370.8491	.709547
.033554	62.92	.70525873	.32105784	.051791	.633573	18.86218783	364.5814	.717530
.033990	62.38	.68399181	.31710226	.052594	.644928	18.97405325	360.7612	.731192
.027507	60.80	.67783627	.33068896	.052656	.544413	19.79181569	375.8685	.735130
.027785	59.47	.65927335	.33490389	.053164	.562296	20.23740261	380.6593	.746948

TOTAL FLOW RATE IS   14.361678 LB/SEC

Blade Angle 69.7°
Station 1

FLOW/AREA (LB/SEC/FT**2)

PROBE POSITION (IN FROM CENTERBODY)

LEGEND
o - 2.5 DEG LEFT OF T.E.
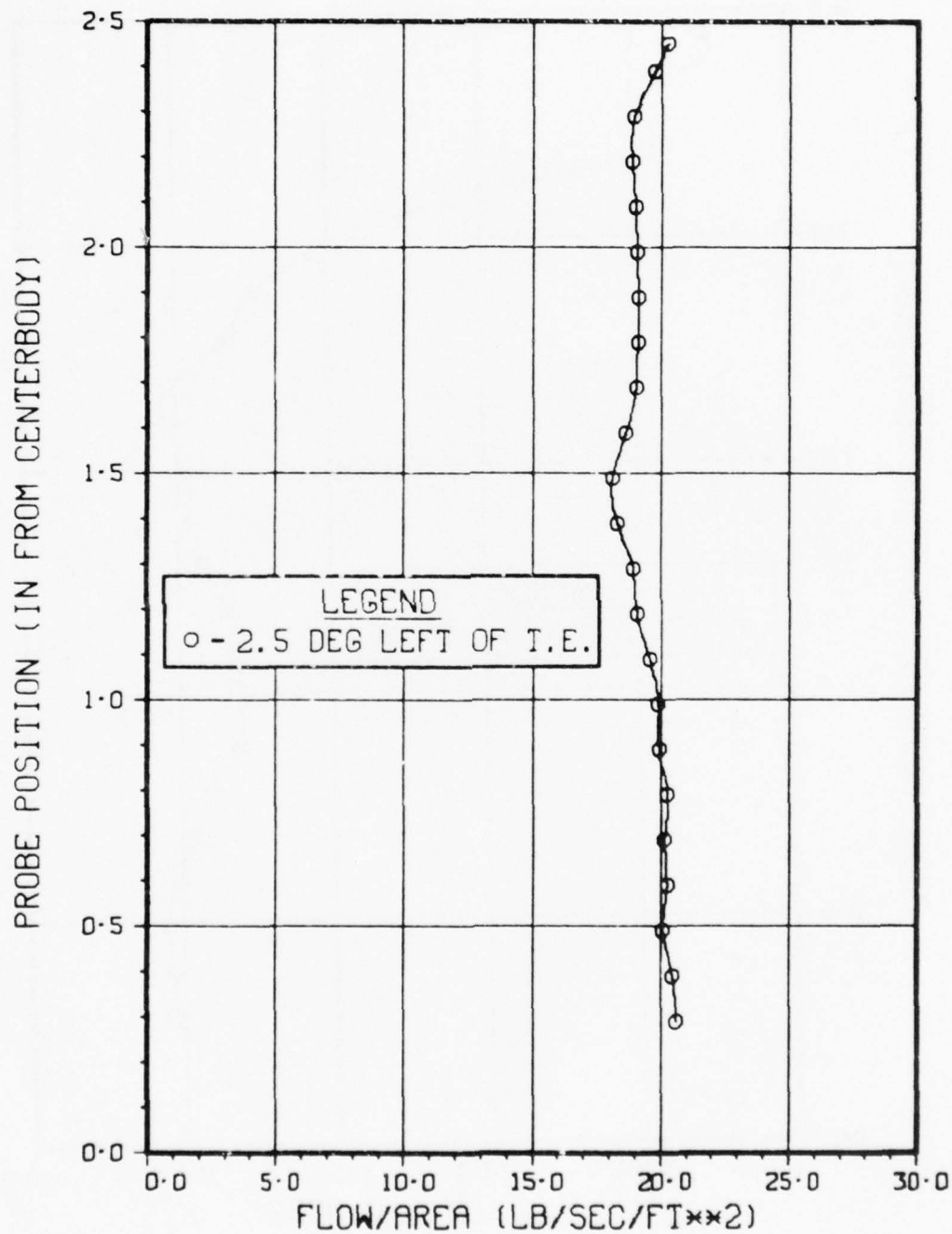
Figure 44 Flow VS Probe Position

65

Blade Angle 65.0°
Station 1
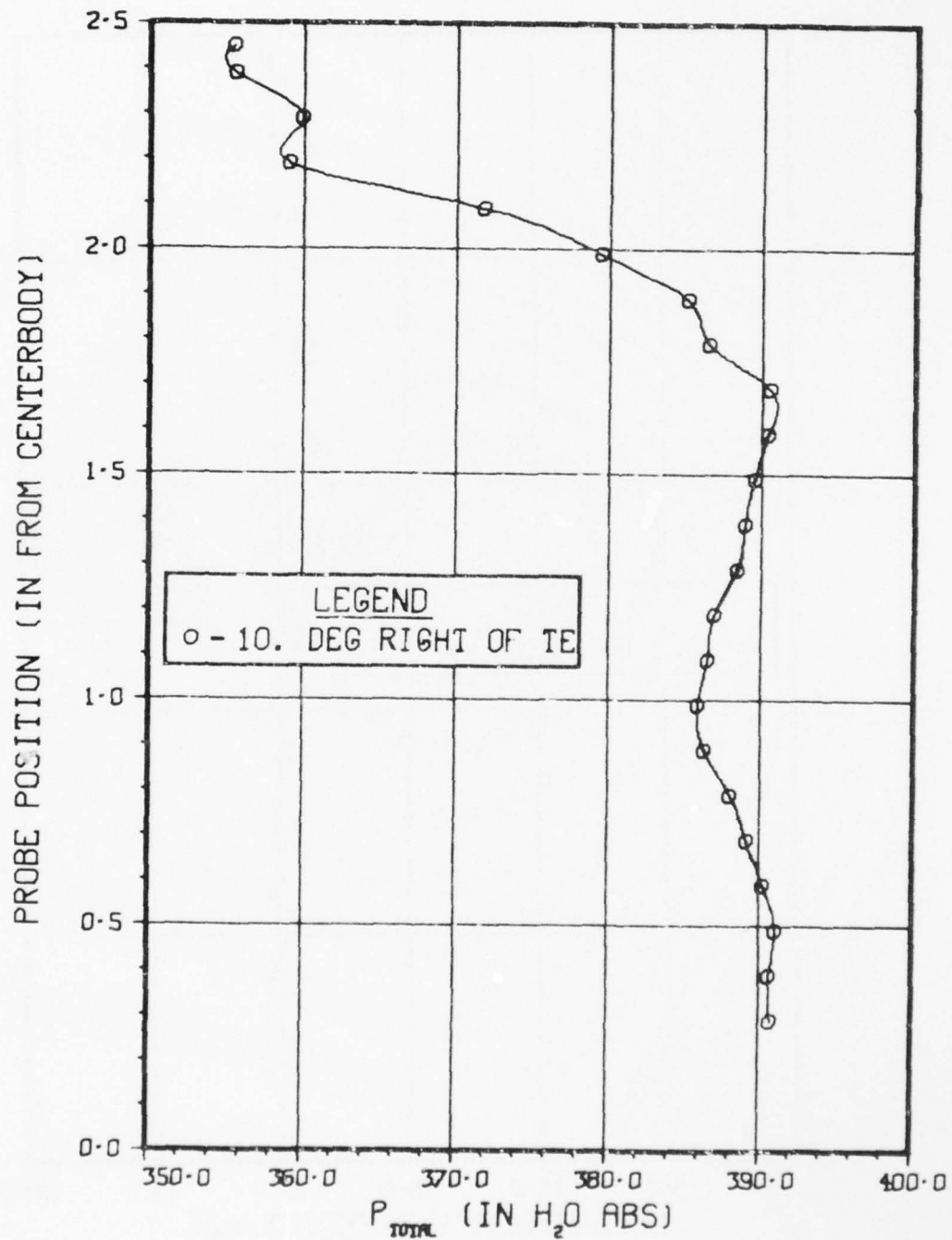
Figure 45 P_{total} VS Probe Position
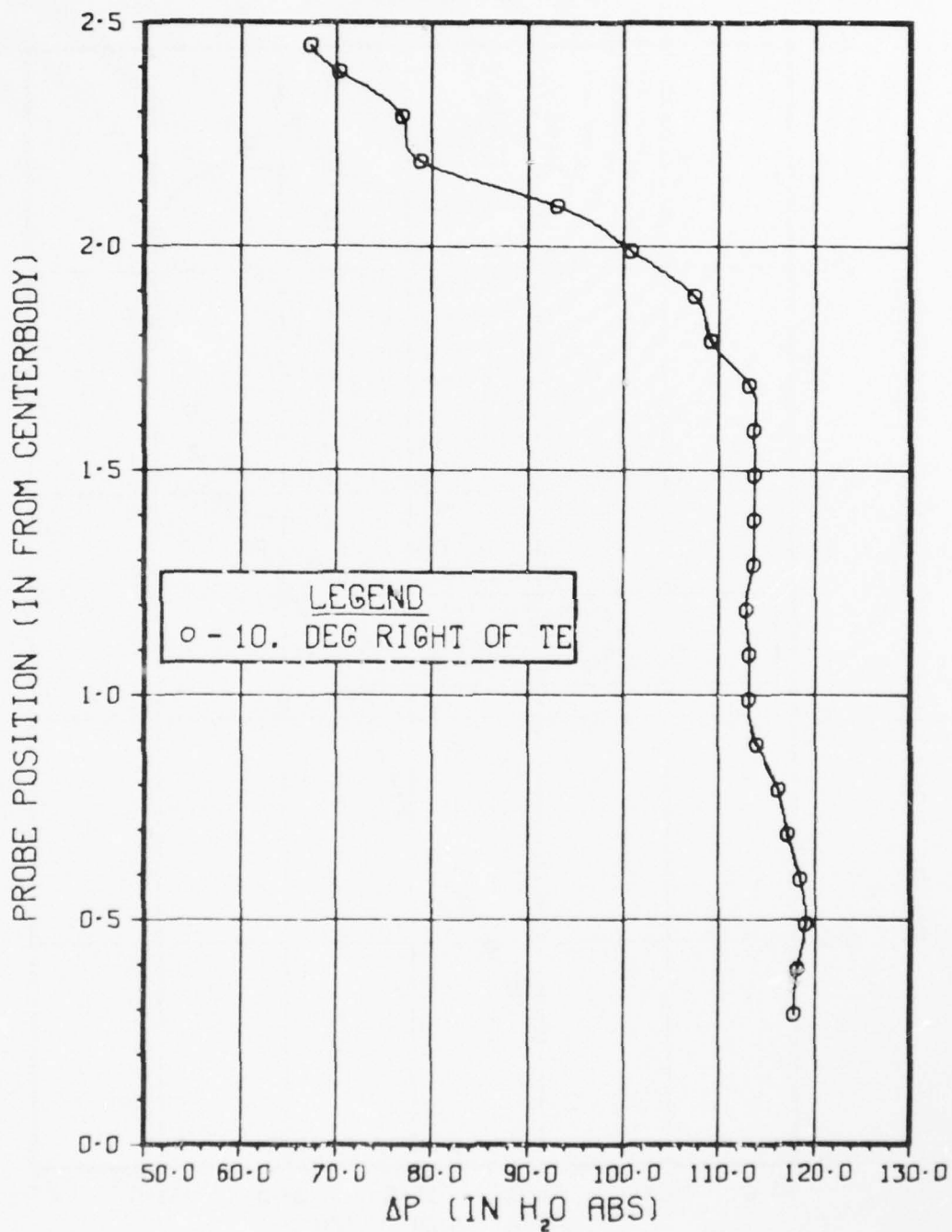
Figure 46   ΔP VS Probe Position

Blade Angle 65.0°
Station 1
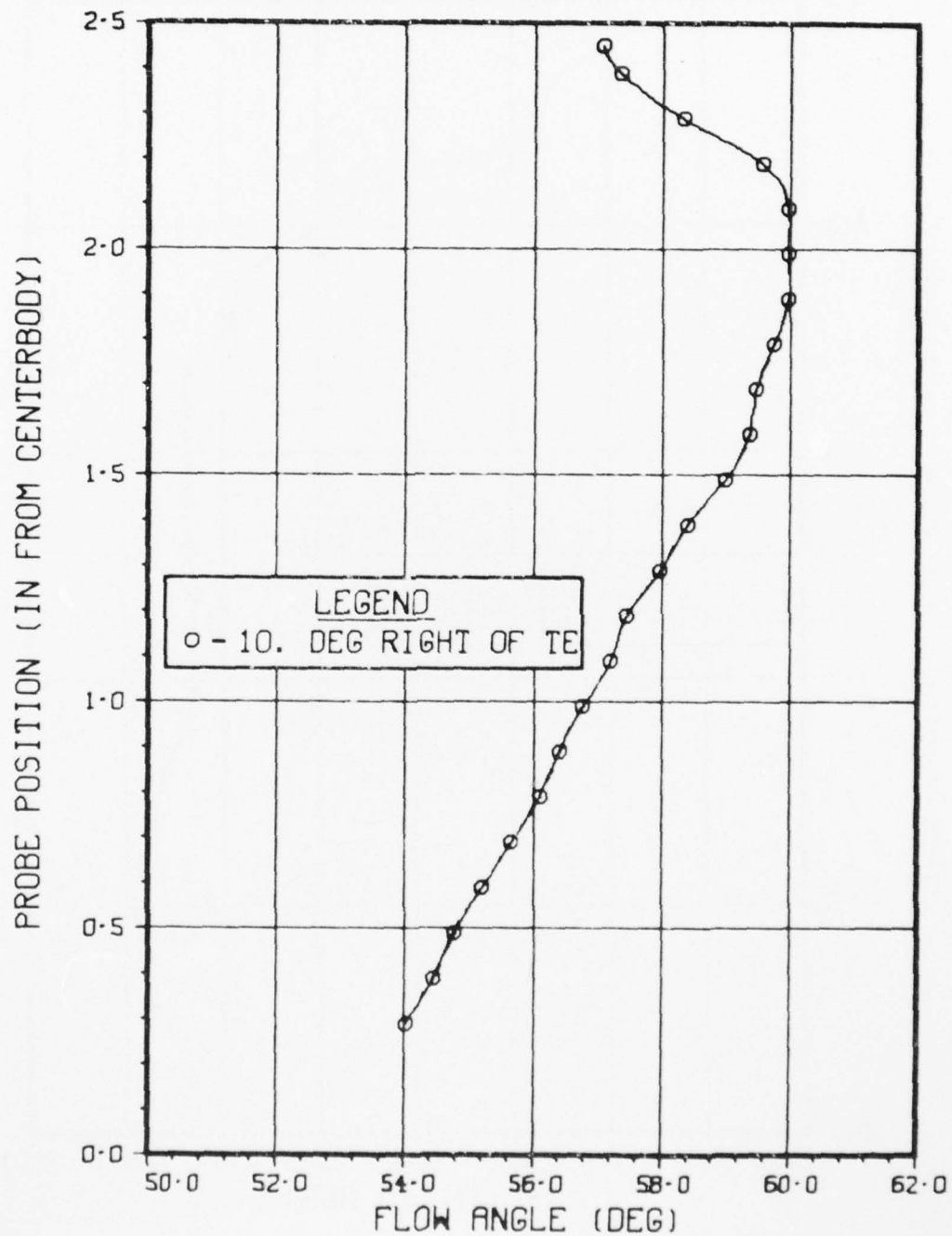
Figure 47   Flow Angle VS Probe Position

68

Table 7

Mass Flow Calculation - Station 1, 65°

DATE 22/ 4/77   POSITION: 2.50 DEGREES RIGHT OF ZERO   SADDLE STATION 1
CHAMBER PRESSURE 9.70 IN HG   BLADE ANGLE 65.00 DEGREES
ACTUAL PROBE POSITION: 10° RIGHT OF T.E.

AREA FT**2	FLOW ANGLE DEGREES	MACH NUMBER- BLADE EXIT	MACH NUMBER- AXIAL	DENSITY LB/FT**3	FLOW RATE LB/SEC	FLOW RATE/AREA LB/SEC/FT**2	VELOCITY-AXIAL FT/SEC	PS/PT
.084116	54.01	.73466967	.43172425	.050733	2.068546	24.59158201	434.7277	.698513
.025700	54.44	.73636750	.42823832	.050640	2.065752	24.34833198	460.8138	.697412
.026136	54.77	.73904375	.42632484	.050565	.632594	24.20394674	478.6654	.695676
.026573	55.21	.73893061	.42109830	.050510	.674586	23.88085250	472.7972	.696333
.027009	55.67	.73420353	.41406033	.050644	.635292	23.52147532	464.4511	.698815
.027445	56.10	.73114762	.40794400	.050741	.636346	23.18769747	456.9844	.700796
.027882	56.41	.72478799	.40099617	.050718	.636052	22.81227993	449.7858	.704915
.028318	56.78	.72165682	.39536349	.050909	.638721	22.55528662	443.0544	.706942
.028754	57.21	.72135352	.39065723	.050904	.641395	22.30627441	438.1999	.707138
.029190	57.46	.71928686	.38689596	.050956	.646121	22.13439931	434.3958	.708474
.029633	57.99	.72073086	.38203583	.051086	.649341	21.91275513	428.9390	.707541
.030058	58.40	.72014950	.37734818	.051179	.651755	21.68325852	423.6758	.707917
.030499	58.99	.71945375	.37065369	.051193	.650380	21.32464135	416.5566	.708366
.030936	59.36	.71881012	.36633597	.051439	.654529	21.15751006	411.3116	.708783
.031373	59.48	.71571392	.36397534	.051551	.660927	21.06675133	408.6612	.710138
.031808	59.74	.70492461	.35522894	.051373	.652979	20.52876223	399.3932	.717745
.032245	59.98	.69966266	.35004281	.051527	.653613	20.27021888	392.3932	.721133
.032682	59.98	.67944654	.33994865	.051577	.644607	19.72350524	382.4129	.734075
.033117	59.98	.65506277	.32772938	.051614	.630160	19.02836479	368.6672	.749617
.033554	59.57	.60564543	.30675050	.051892	.630821	17.90609619	345.0678	.786520
.033990	58.33	.59661851	.31324028	.052491	.528091	18.47868616	352.0329	.786970
.027507	57.35	.57041000	.30773947	.052900	.503250	18.29574509	345.8509	.801986
.027785	57.07	.55638726	.30245990	.053438	.504697	18.16435615	339.9175	.810371

TOTAL FLOW RATE IS   15.86059. LB/SEC

69
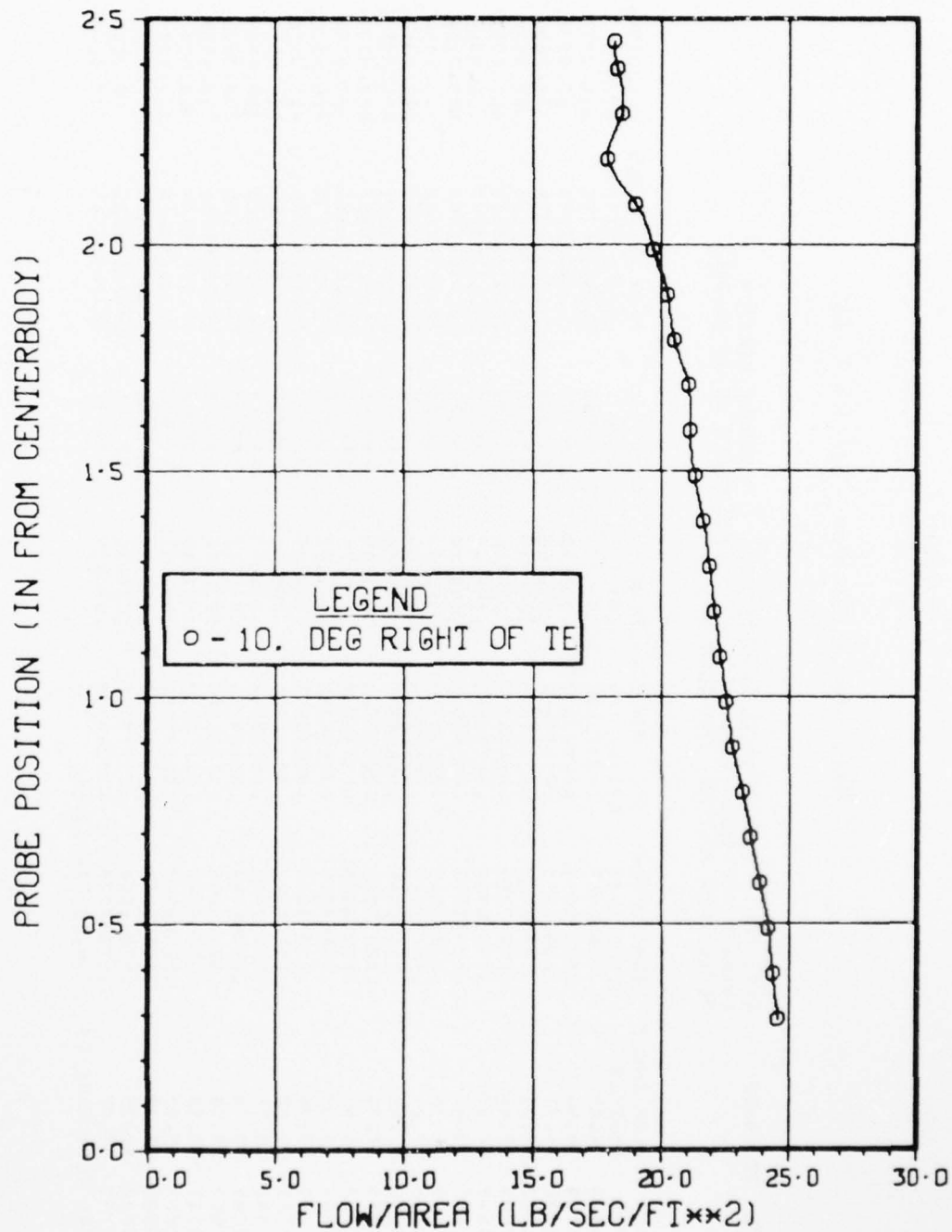
Figure 48   Flow VS Probe Position

Blade Angle 60.0°
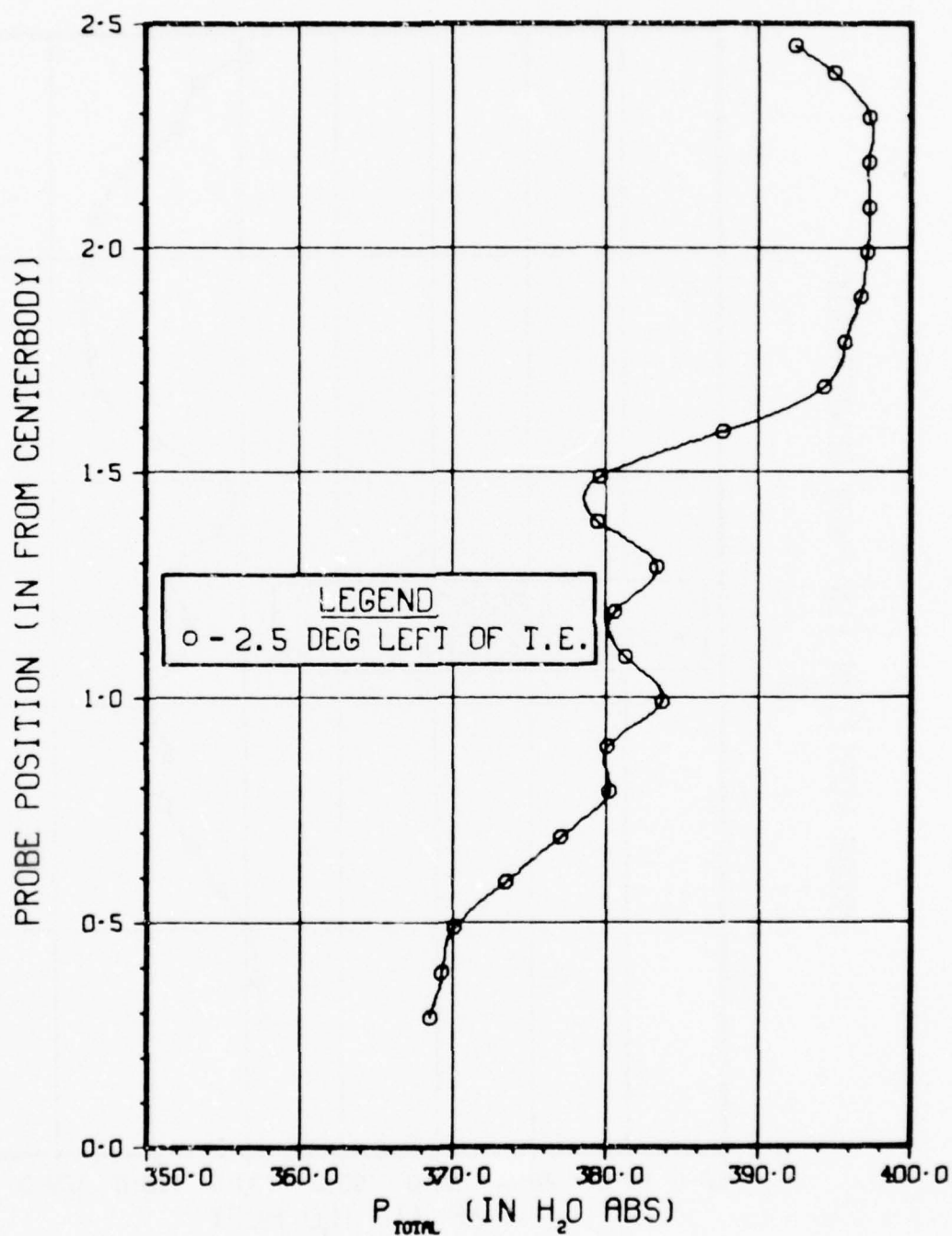## Station 1

Figure 49 P_{total} VS Probe Position
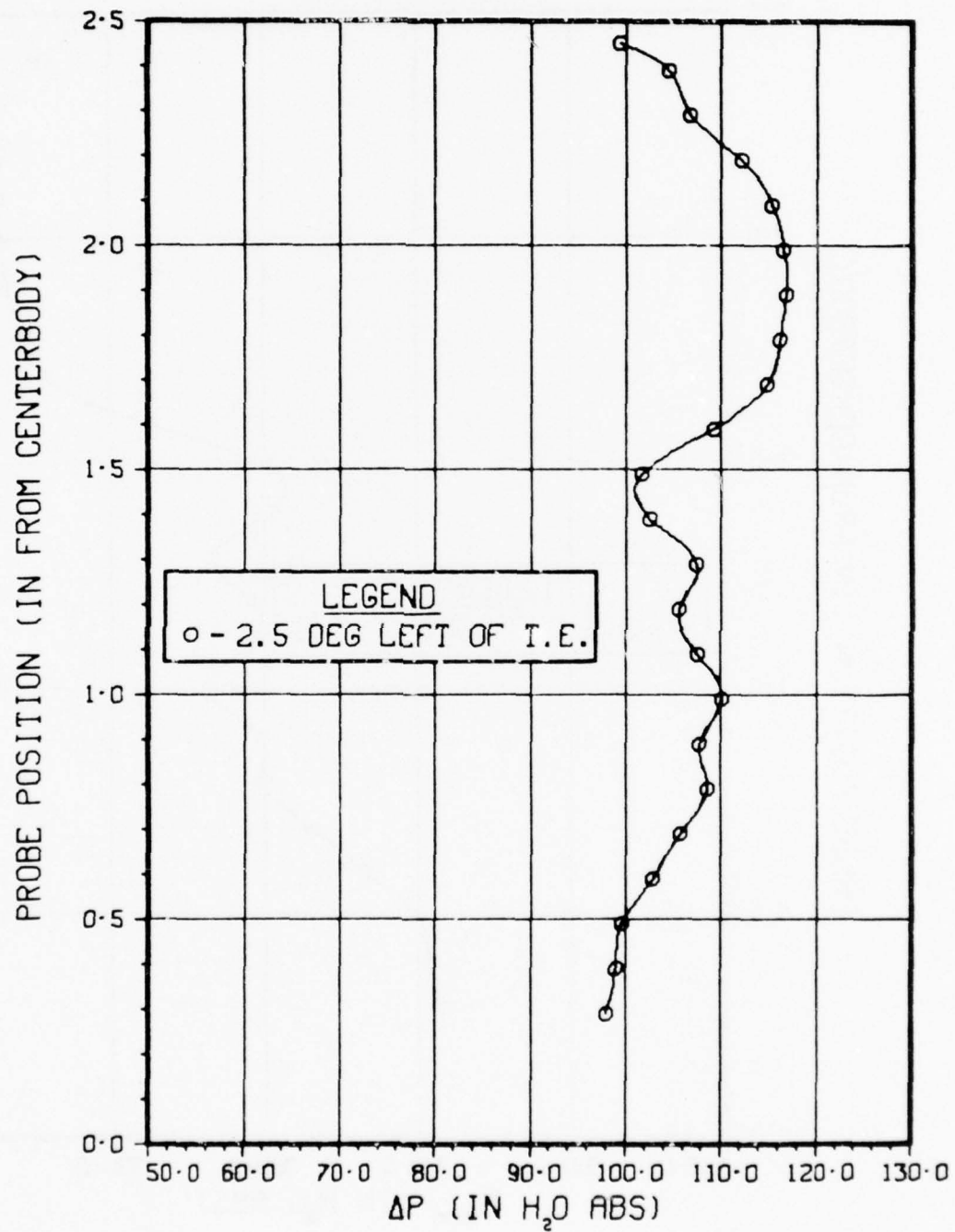
Blade Angle 60.0°
Station 1

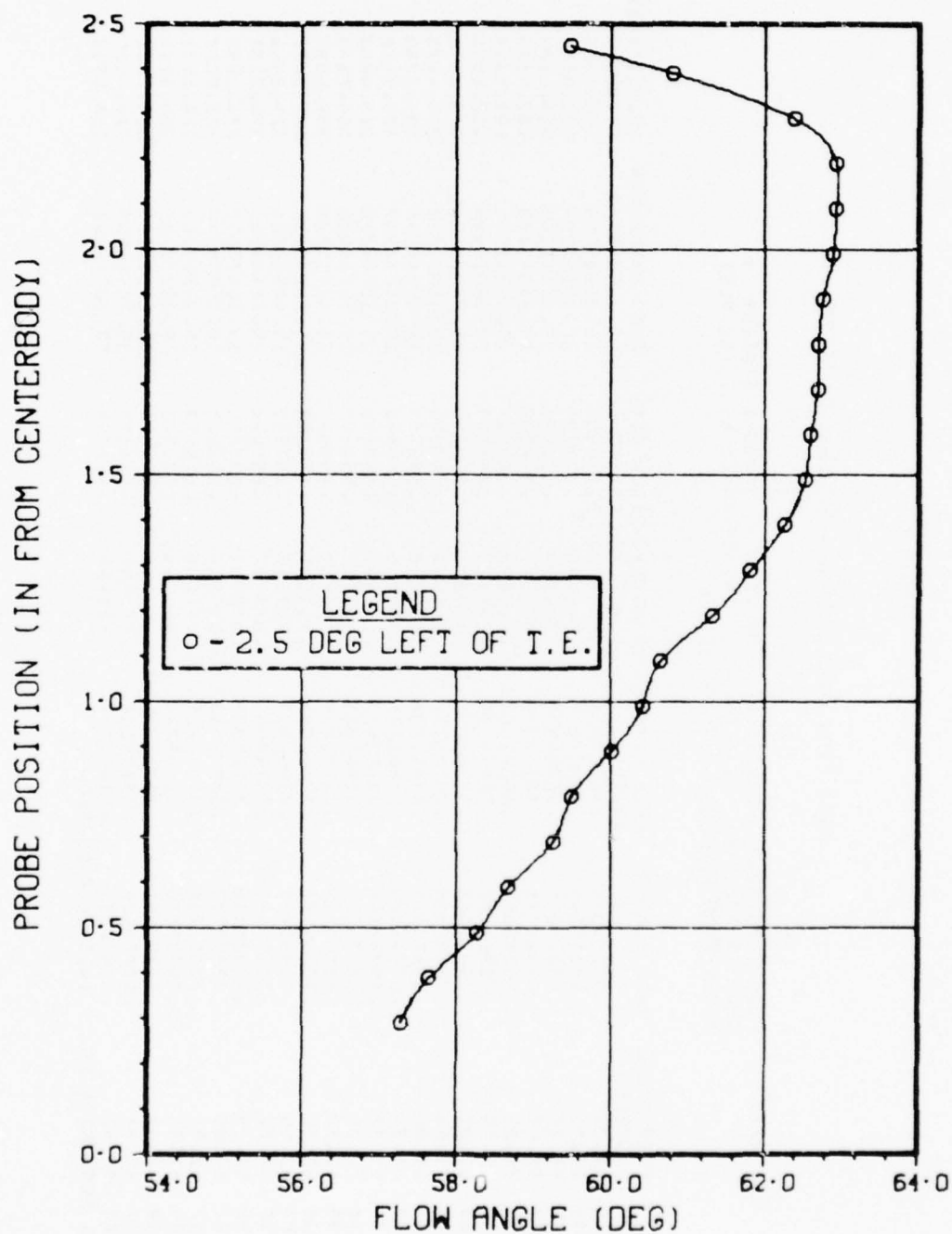Figure 50 ΔP VS Probe Position

Blade Angle 60.0°
Station 1

Figure 51   Flow Angle VS Probe Position

73

Table 8

Mass Flow Calculation - Station 1, 60°

DATE 15/ 8/77

POSITION: 5.00 DEGREES LEFT OF ZERO   SADDLE STATION 1
CHAMBER PRESSURE 9.50 IN HG   BLADE ANGLE 60.00 DEGREES
ACTUAL PROBE POSITION: 2.5° RIGHT OF T.E.

AREA FT**2	FLOW ANGLE DEGREES	MACH NUMBER	MACH NUMBER- AXIAL	DENSITY LB/FT**3	FLOW RATE LB/SEC	FLOW RATE/AREA LB/SEC/FT**2	VELOCITY-AXIAL FT/SEC	PS/PT
.084116	52.26	.64877242	.39710014	.054706	2.067263	24.57633729	449.2455	.753594
.025700	52.72	.64737741	.39212341	.054797	.624740	24.30893957	443.6152	.754474
.026136	53.11	.64248056	.38566864	.055035	.627594	24.01263540	436.3128	.757560
.026573	53.35	.63767052	.38064162	.055255	.632285	23.79425060	430.6257	.760585
.027009	53.85	.63244636	.37308088	.055493	.632607	23.42207972	422.0721	.763861
.027445	54.10	.62882122	.37094241	.055658	.641032	23.35657496	419.6528	.766129
.027882	54.40	.62357227	.36564554	.055896	.644685	23.12150443	413.6604	.769405
.028318	54.68	.61840000	.35998464	.056116	.647163	22.85342049	407.2564	.772624
.028754	54.68	.61271127	.35423440	.056372	.649584	22.59107770	404.7508	.776153
.029190	55.60	.60741127	.34316732	.056610	.641529	21.97768420	386.2304	.779430
.029633	56.00	.60118458	.33617837	.056903	.641302	21.64149696	380.3237	.783266
.030058	56.23	.59872363	.33280677	.057013	.645219	21.46561018	376.5094	.784778
.030499	56.30	.59296465	.37900313	.057269	.650113	21.31588133	372.2063	.788306
.030936	56.40	.58883711	.32585747	.057452	.655211	21.17957048	368.6475	.790827
.031373	56.43	.58469748	.32331160	.057635	.661376	21.08106426	365.7674	.793347
.031808	56.63	.57929728	.31863872	.057873	.663584	20.86217405	360.4809	.796623
.032245	56.90	.57605318	.31458376	.057855	.663930	20.59016885	355.8934	.792585
.032682	57.18	.57144243	.30722270	.058056	.664836	20.34256909	350.3940	.801365
.033117	57.17	.55862316	.30285657	.058331	.661866	19.98569648	342.6263	.809040
.033554	56.98	.49809705	.27142889	.058477	.602520	17.95674064	307.0717	.844080
.033990	56.00	.49049702	.27450613	.058880	.621521	18.28540592	310.5530	.848101
.027507	56.11	.44026972	.24550509	.058496	.446901	16.24660179	277.7437	.875342
.027785	54.80	.31925361	.18402810	.057287	.331388	11.92666263	208.1938	.931805

TOTAL FLOW RATE IS 15.718250 LB/SEC

74

Blade Angle 60.0°
Station 1

FLOW/AREA (LB/SEC/FT**2)

PROBE POSITION IN FROM CENTERBODY)

LEGEND
○ - 2.5 DEG RIGHT OF TE
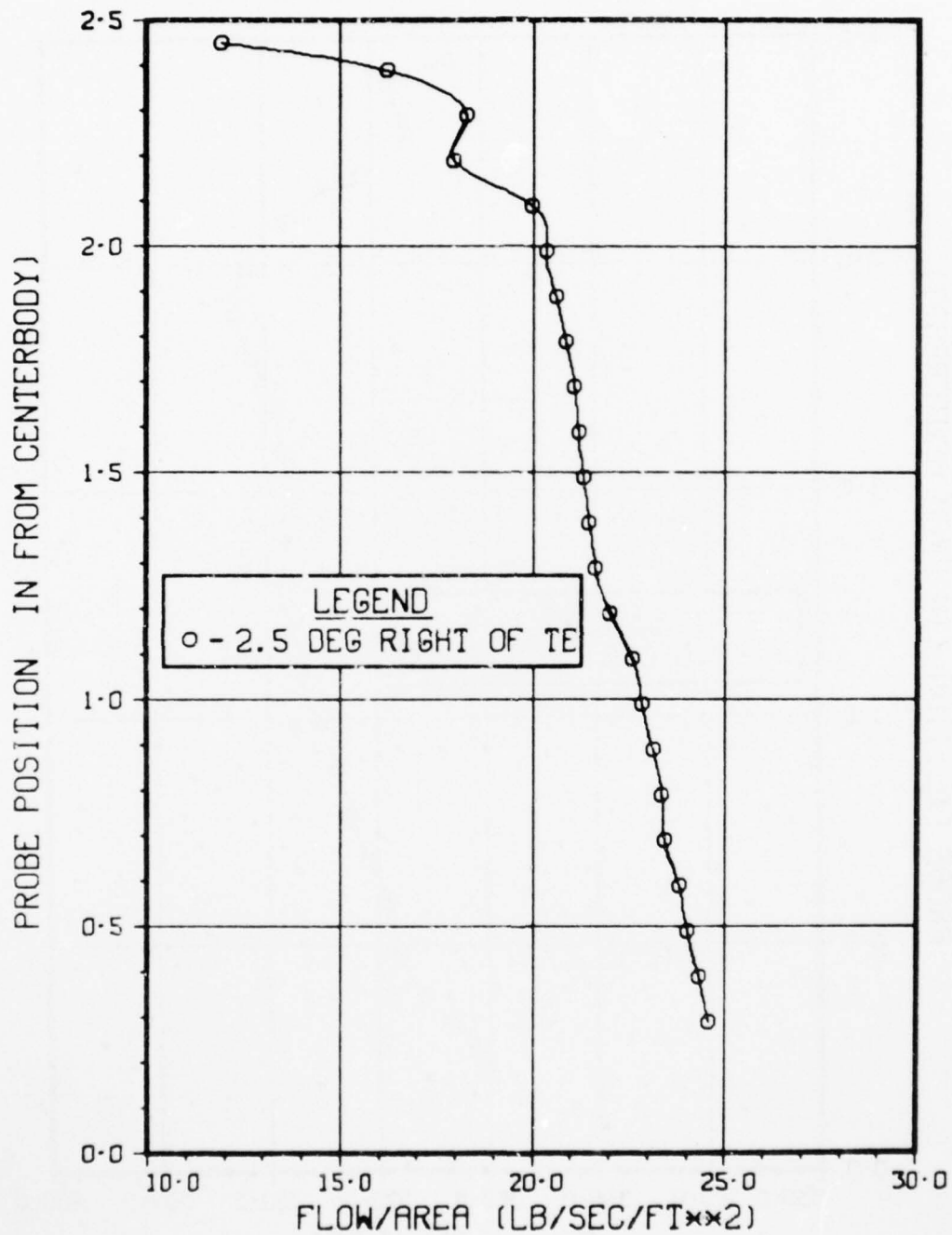
Figure 52 Flow VS Probe Position

75

Blade Angle 69.7°
Station 3
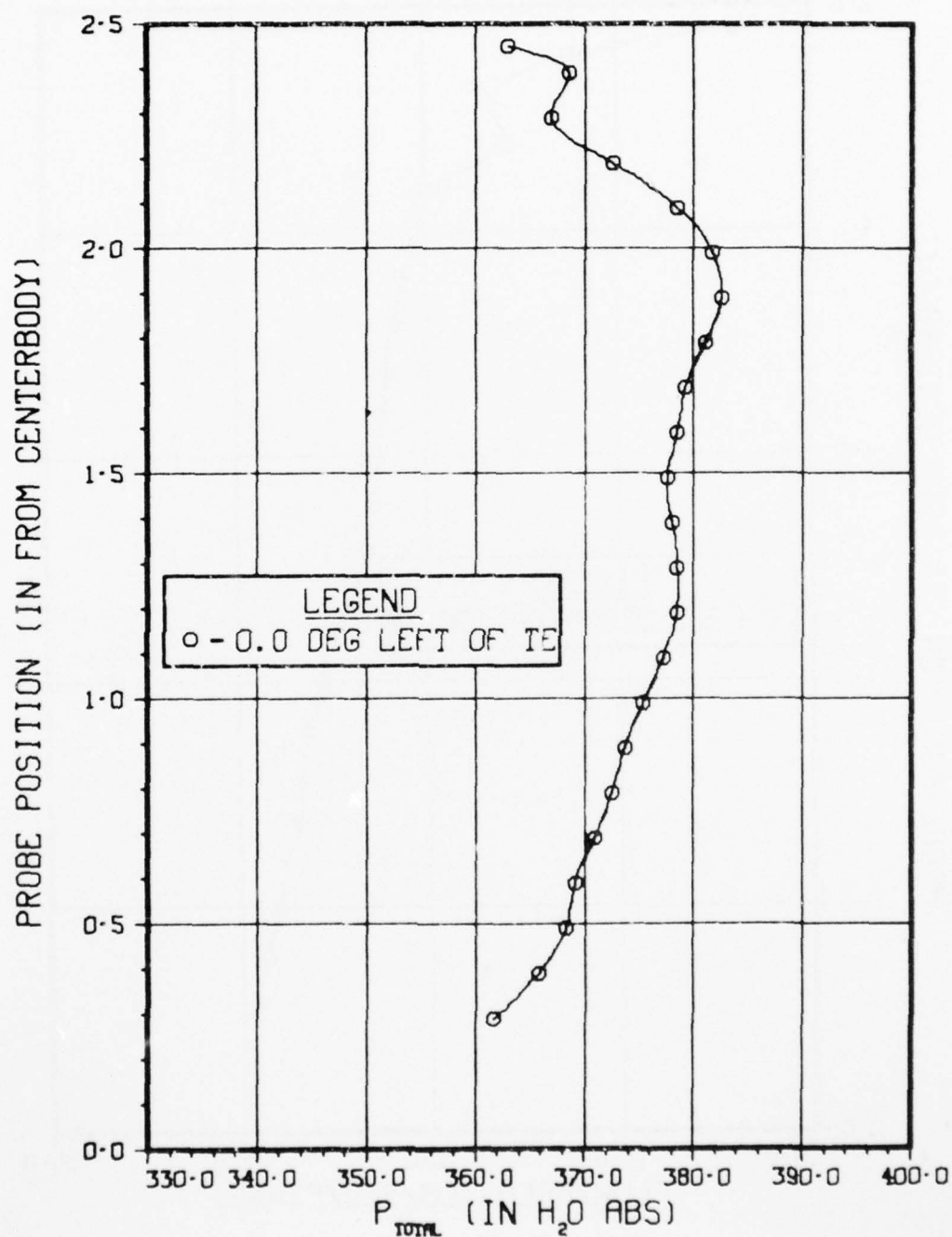
Figure 53 P_{total} VS Probe Position

76

Blade Angle 69.7°
Station 3

Figure 54   ΔP VS Probe Position

77
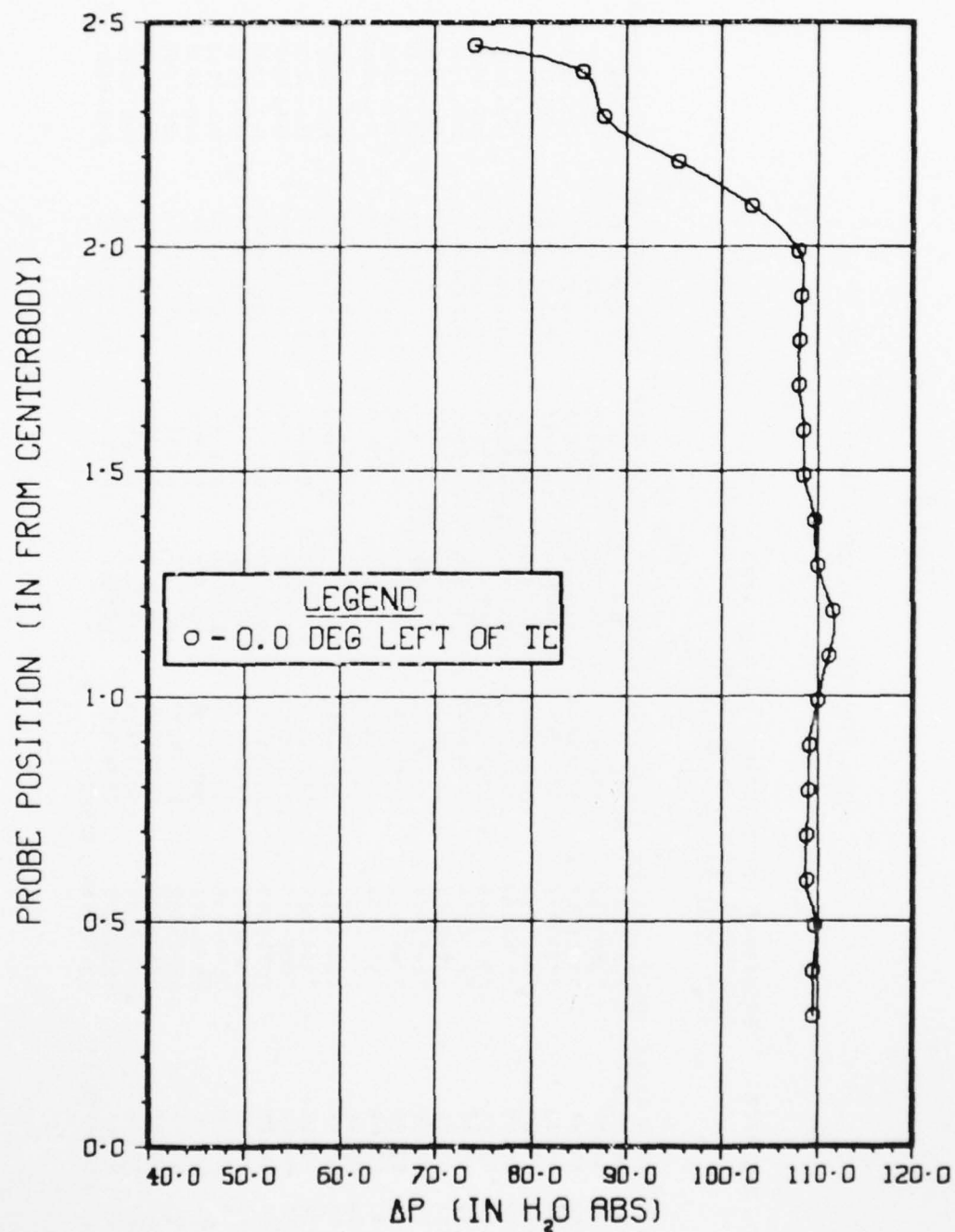
Table 9

Mass Flow Calculation - Station 3, 69.7°

DATE 30/ 6/77   POSITION: 7.50 DEGREES LEFT OF ZERO   SADDLE STATION 3
CHAMBER PRESSURE 8.65 IN HG   BLADE ANGLE 69.70 DEGREES
ACTUAL PROBE POSITION: 0° RIGHT OF T.E.

AREA FT**2	FLOW ANGLE DEGREES	MACH NUMBER- BLADE EXIT	MACH NUMBER- AXIAL	DENSITY LB/FT**3	FLOW RATE LB/SEC	FLOW RATE/AREA LB/SEC/FT**2	VELOCITY-AXIAL FT/SEC	PS/PT
.084116	58.37	.7369166	.38649136	.046601	1.705880	20.28008878	435.1827	.697020
.025700	59.07	.73186162	.37616988	.047251	.514838	20.03262337	423.9629	.700334
.026136	59.23	.7294357E	.37317405	.047694	.524270	20.05920099	420.5864	.701906
.026573	59.69	.72425438	.36551546	.047935	.525234	19.76568747	412.3449	.705261
.027009	59.99	.72246082	.36133960	.048157	.530697	19.64889170	408.0194	.706422
.027445	60.50	.72092666	.35500127	.048432	.532837	19.41473000	400.8623	.707414
.027882	60.92	.72030154	.35008840	.048616	.535956	19.21869876	395.3147	.707818
.028318	61.28	.72155051	.34672641	.048782	.540842	19.09889713	391.5184	.707010
.028754	62.06	.72430604	.33937118	.048892	.538735	18.77599724	383.2130	.705227
.029190	62.28	.72444494	.33699980	.049039	.544715	18.56101339	380.5350	.705105
.029633	62.40	.71783985	.33257235	.049538	.550234	16.56827335	374.8262	.709410
.030058	62.58	.71729668	.33028060	.050071	.557042	18.53224988	370.1209	.709819
.030499	62.87	.71329126	.32526862	.050473	.559494	18.34465750	363.4547	.712348
.030936	63.14	.71211422	.32174174	.050955	.565081	18.26612072	358.4726	.713108
.031373	64.04	.70884160	.31029084	.051003	.554255	17.66663317	346.3842	.715220
.031808	64.29	.70745389	.30690505	.051422	.559833	17.60038643	342.2735	.716115
.032245	64.45	.70665332	.30477857	.051648	.566070	17.55528197	339.9019	.716531
.032682	64.21	.70594899	.30714001	.051473	.576786	17.64841720	342.8668	.717085
.033117	64.21	.6899+981	.30017919	.051377	.572348	17.28261896	336.3885	.727374
.033554	63.61	.66404259	.29615287	.051713	.573918	17.10432335	330.7558	.743920
.033990	62.57	.63658068	.29325015	.051924	.581101	17.09622196	329.2530	.761269
.027507	60.96	.62585434	.30352558	.052449	.492600	17.90815676	341.4401	.768338
.027785	58.47	.58105425	.33285937	.053467	.507798	18.27597633	341.8155	.795558

TOTAL FLOW RATE IS   13.710464 LB/SEC

Blade Angle 69.7°
Station 3
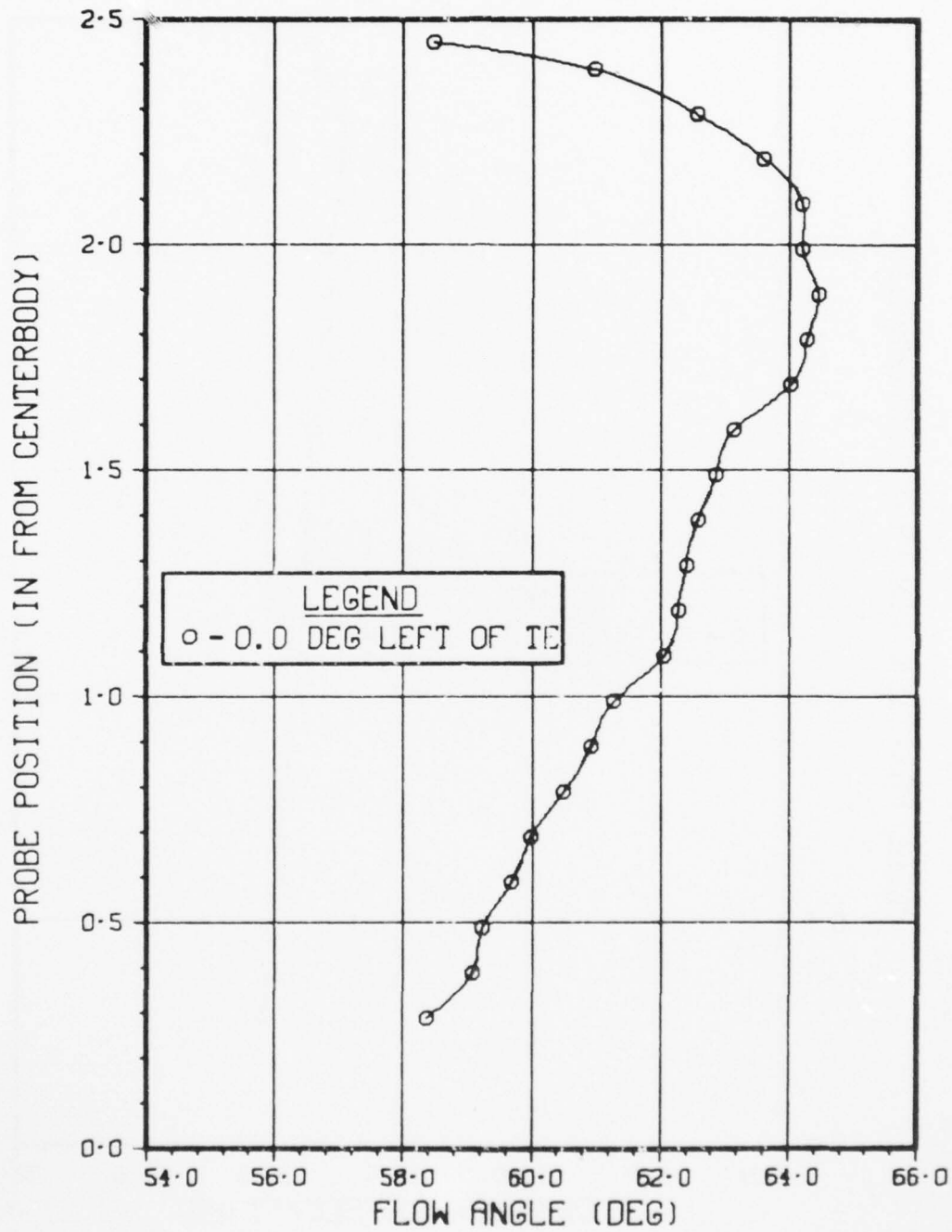
Figure 55 Flow Angle VS Probe Position

79

Blade Angle 69.7°
Station 3
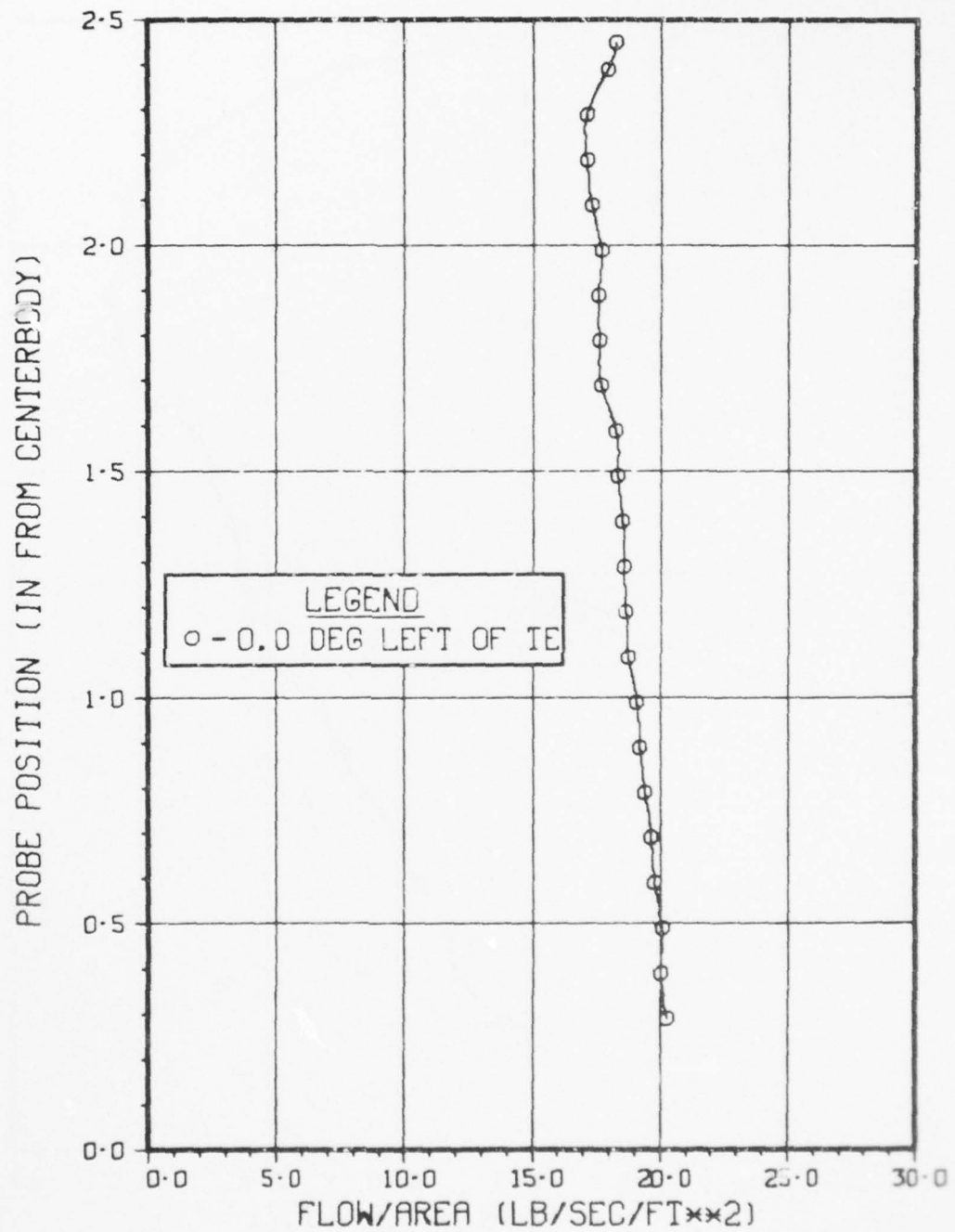
Figure 56   Flow VS Probe Position
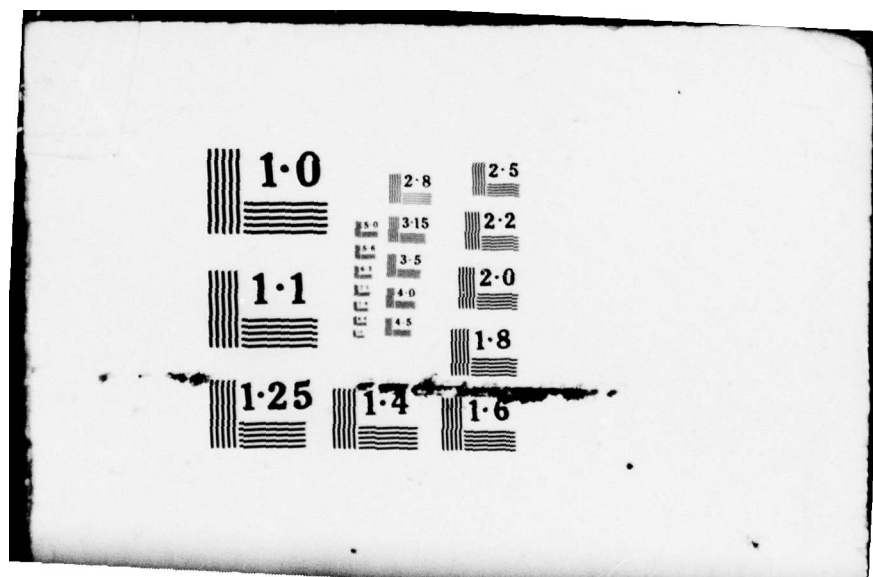
Blade Angle 65.0°
Station 3
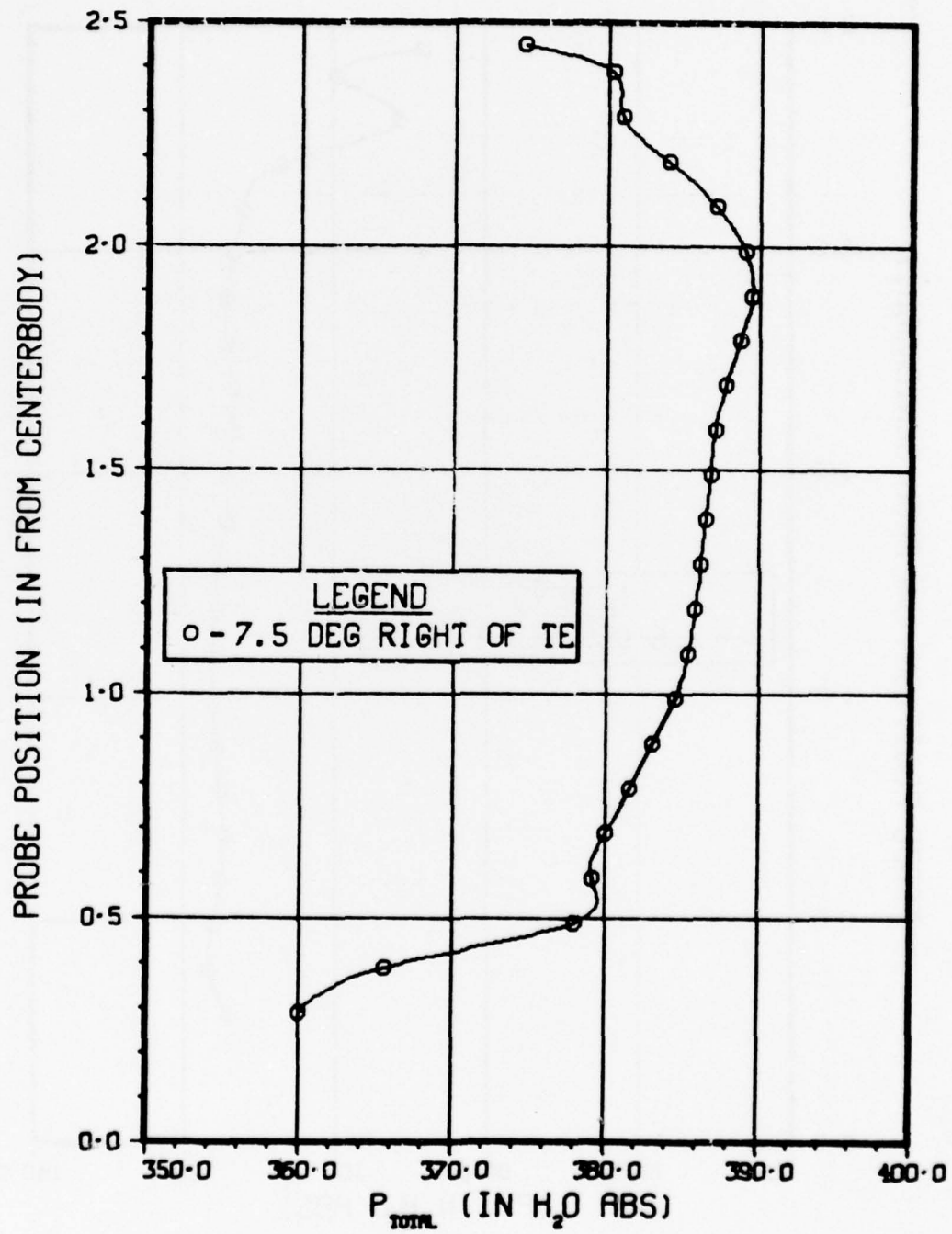
Figure 57   P$_{total}$ VS Probe Position

LEGEND
o - 7.5 DEG RIGHT OF TE

PROBE POSITION (IN FROM CENTERBODY)

P$_{TOTAL}$ (IN H$_2$O ABS)

81

Blade Angle 65.0°
Station 3

Figure 58 ΔP VS Probe Position

82
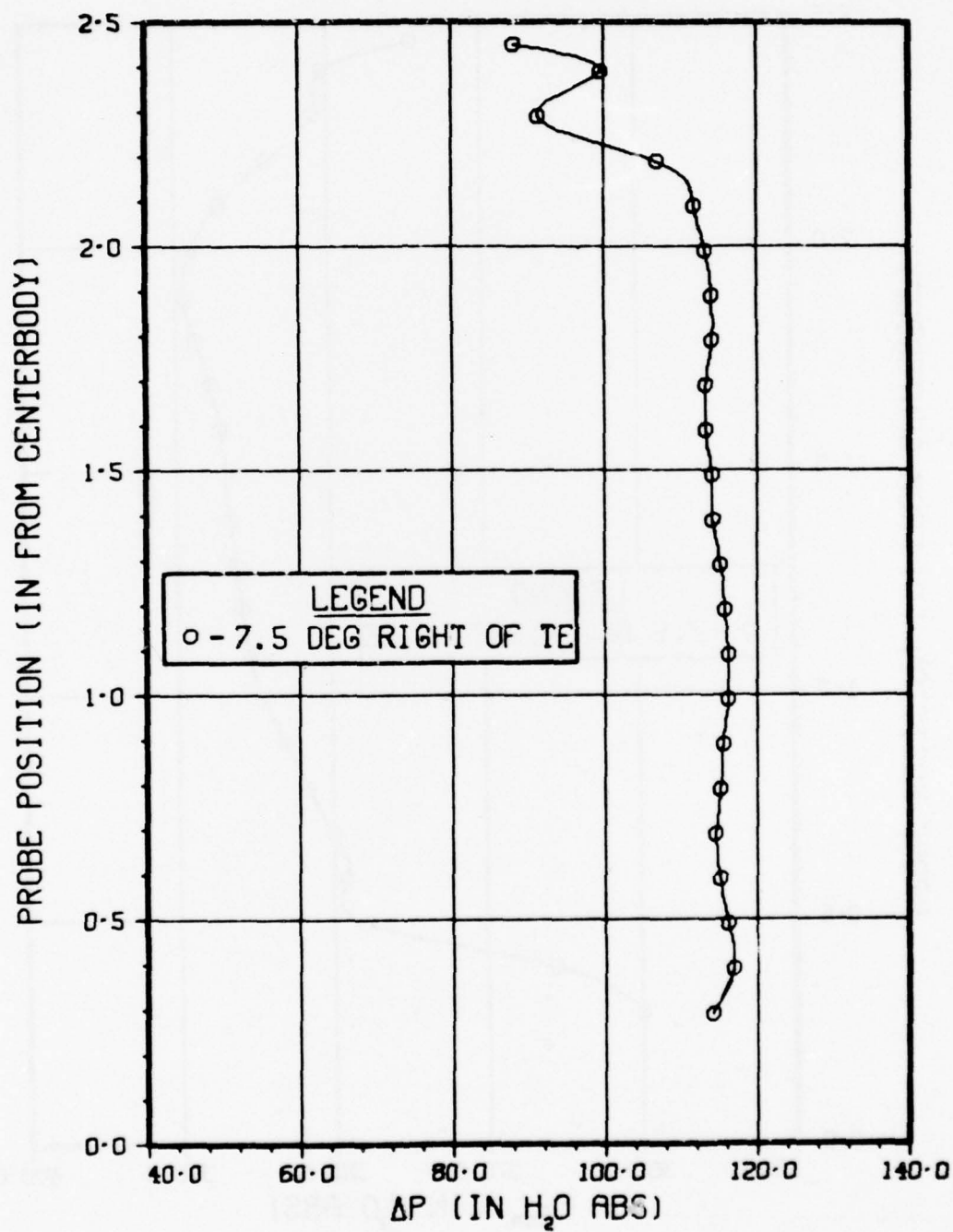
Blade Angle 65.0°
Station 3
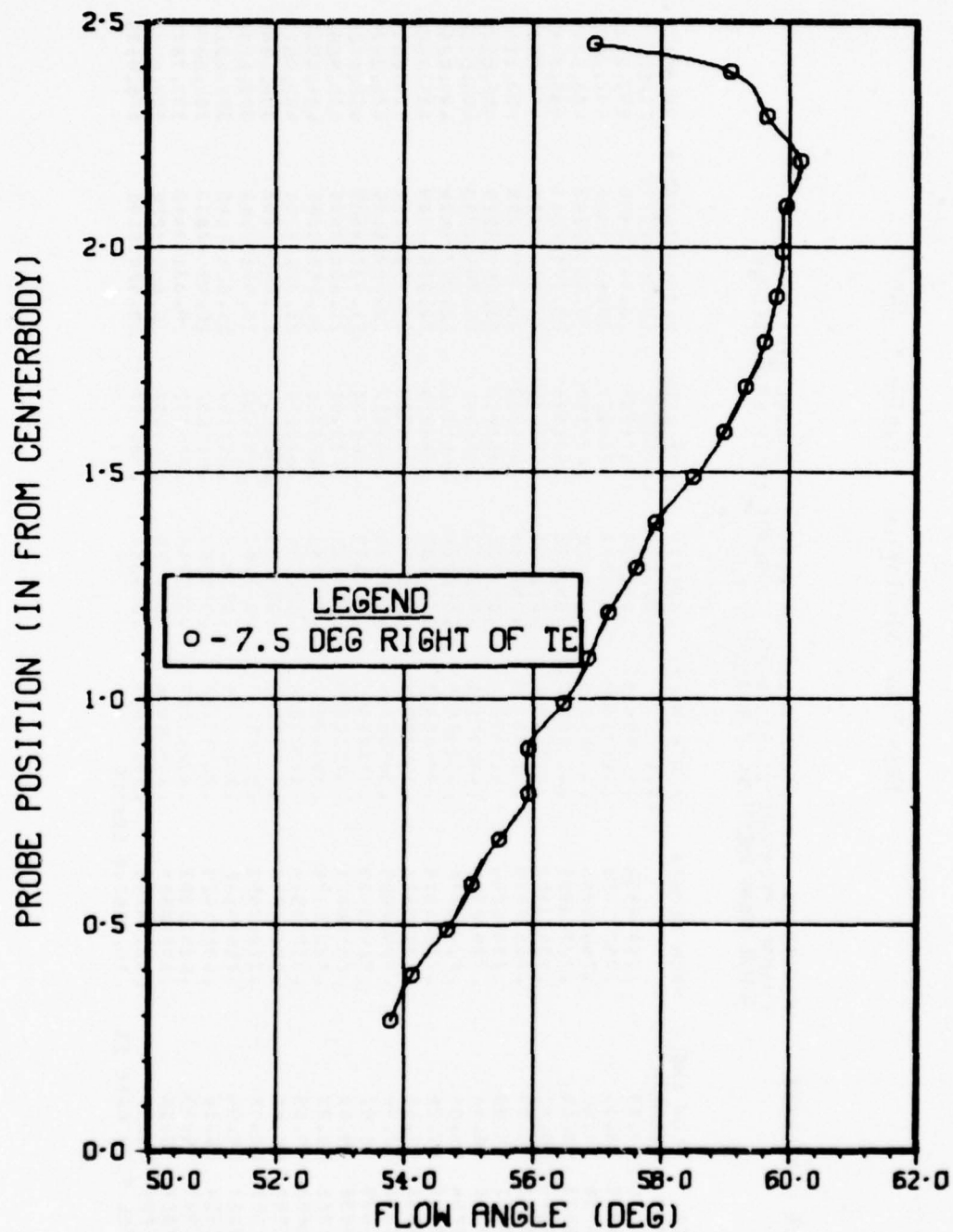
Figure 59 Flow Angle VS Probe Position

Table 10

Mass Flow Calculation - Station 3, 65°

DATE 8/ 4/77   POSITION: 0.00 DEGREES LEFT OF ZERO   SADDLE STATION 3
                   CHAMBER PRESSURE 11.50 IN HG   BLADE ANGLE 65.00 DEGREES
                   ACTUAL PROBE POSITION: 7.5° RIGHT OF T.E.

AREA FT**2	FLOW ANGLE DEGREES	MACH NUMBER	MACH NUMBER- AXIAL	DENSITY LB/FT**3	FLOW RATE LB/SEC	FLOW RATE/AREA LB/SEC/FT**2	VELOCITY-AXIAL FT/SEC	FS/PT
.024116	53.80	.75846566	.44705411	.047523	1.971765	23.44102595	493.2523	.683056
.025700	54.11	.76235491	.44691605	.048084	.608127	23.66251425	492.1093	.680525
.026136	54.60	.74420018	.43046566	.050678	.627188	23.99707743	473.5246	.692328
.026573	55.04	.73794855	.42284777	.051123	.631895	23.77957511	465.1447	.696386
.027009	55.47	.73481152	.41651884	.051497	.636638	23.57133088	457.7268	.690421
.027445	55.93	.73528620	.41191125	.051588	.641530	23.37512789	453.1143	.690113
.027882	55.93	.73479244	.41163465	.051801	.653997	23.45588515	452.8100	.690433
.028318	56.48	.73578556	.40632141	.052059	.658266	23.24550093	446.5204	.697789
.028754	56.88	.73469738	.40143449	.052026	.661260	22.99716454	442.0285	.690495
.029190	57.20	.73261614	.39079878	.052285	.666279	22.55997224	436.5620	.699044
.029633	57.62	.72973925	.39079874	.052478	.668520	22.82557749	429.8899	.701709
.030058	57.94	.72532685	.38504044	.052521	.669989	22.28988600	424.3974	.704528
.030499	58.52	.72423403	.37819566	.052618	.668960	21.93384465	416.8529	.705274
.030936	59.00	.72106621	.37138685	.053021	.670101	21.66067908	408.5362	.707311
.031373	59.33	.72026934	.36740407	.053051	.673328	21.46203380	404.5569	.707839
.031808	59.63	.72240534	.36523519	.052965	.678209	21.32155391	402.5677	.706457
.032245	59.81	.72147338	.36280666	.053225	.665624	21.26296100	399.4946	.707060
.032682	60.18	.71867550	.35748013	.053283	.685460	20.97361188	393.6294	.708740
.033117	59.94	.71509147	.35819405	.053417	.696344	21.02679642	393.6317	.711186
.033554	60.18	.69891429	.34755388	.053553	.687682	20.49477833	382.6994	.721615
.033990	59.65	.63811657	.32242810	.055748	.674072	19.83149448	355.7370	.760305
.027507	59.10	.67276867	.34549444	.054376	.568457	20.66589779	380.0538	.738364
.027785	56.97	.63144798	.34418845	.055331	.582657	20.97018196	376.9936	.764406

TOTAL FLOW RATE IS   16.366348 LB/SEC

84

Blade Angle 65.0°
Station 3
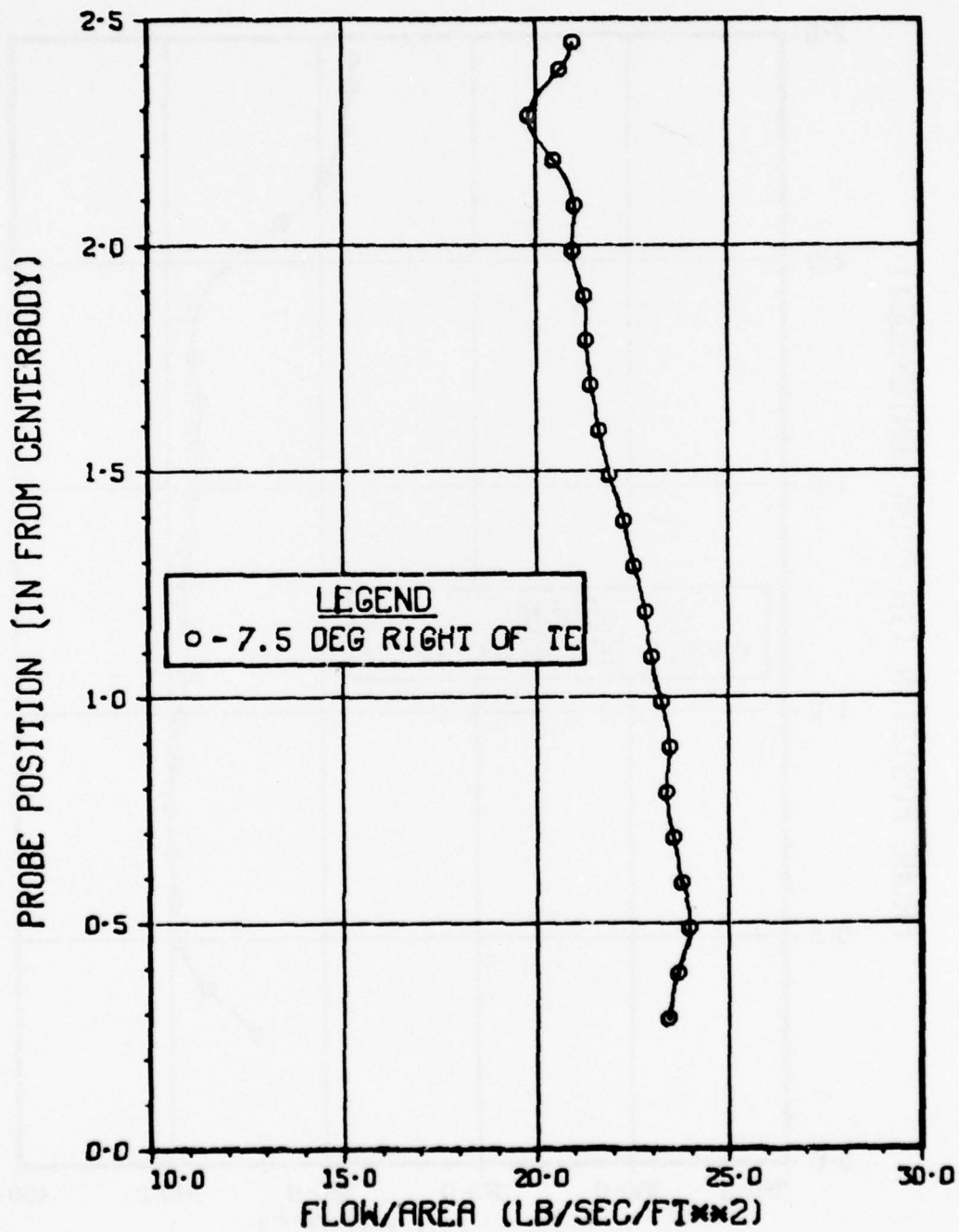
Figure 60   Flow VS Probe Position

85

Blade Angle 60.0°
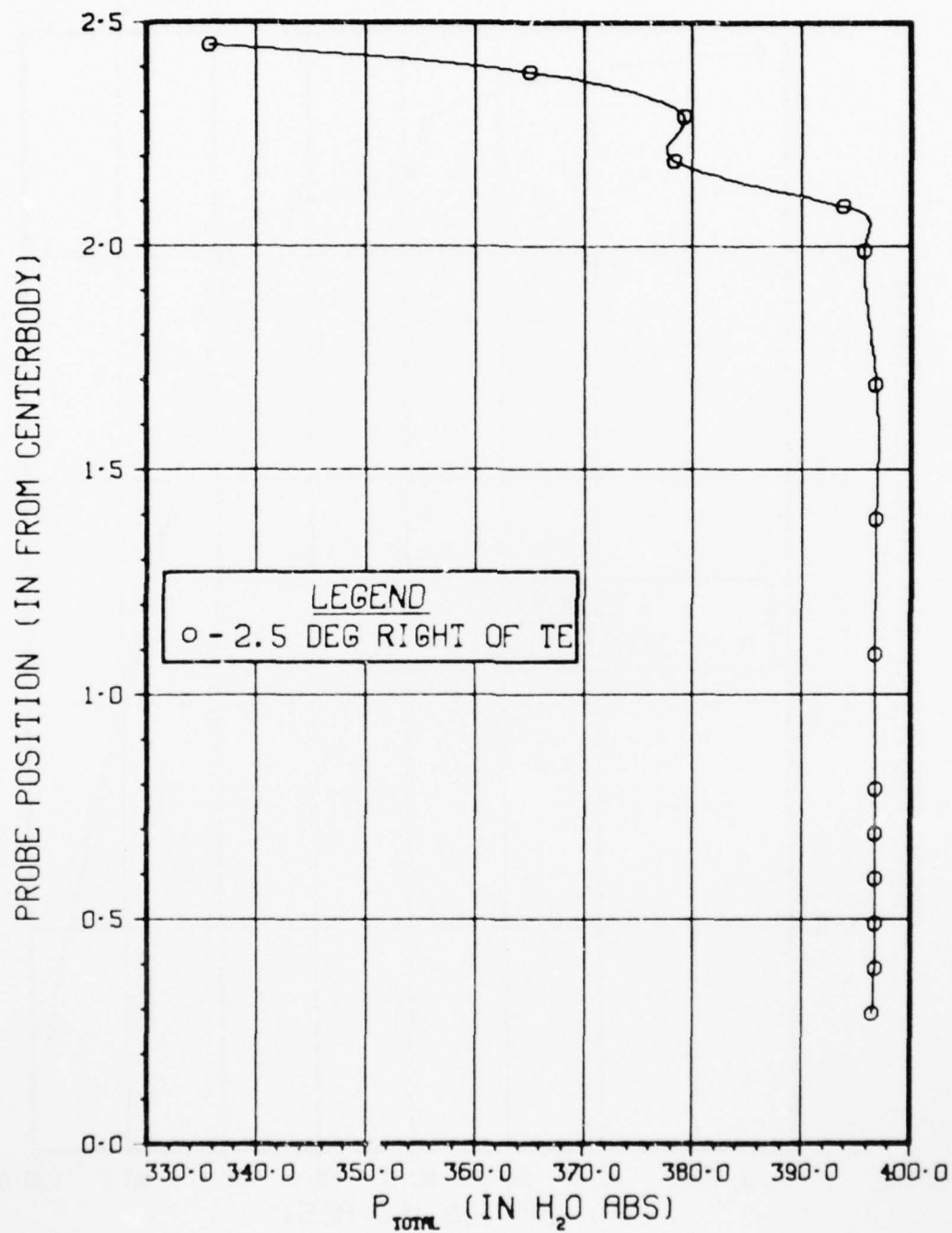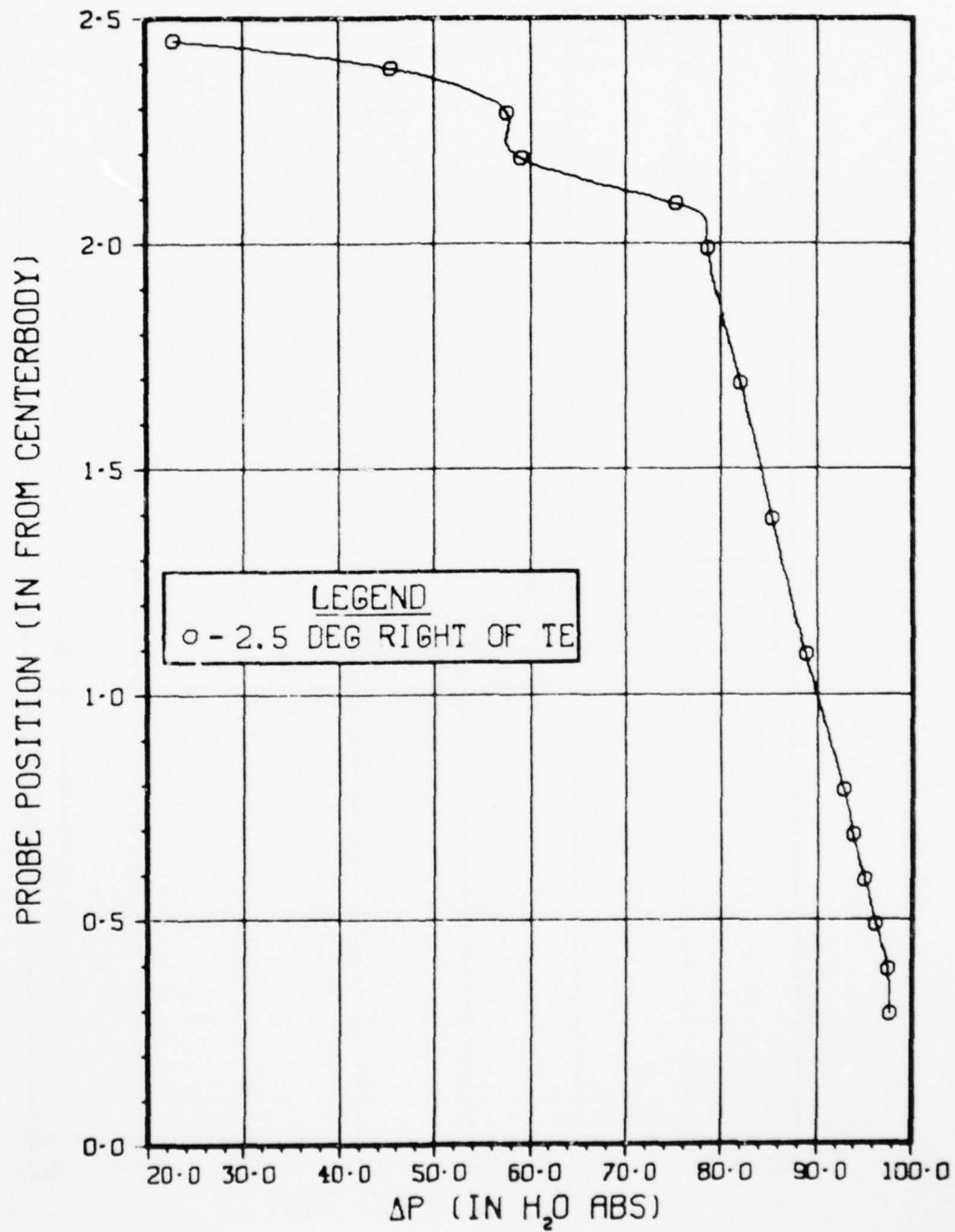## Station 3

Figure 61 P_{total} VS Probe Position

86

Blade Angle 60.0°
Station 3
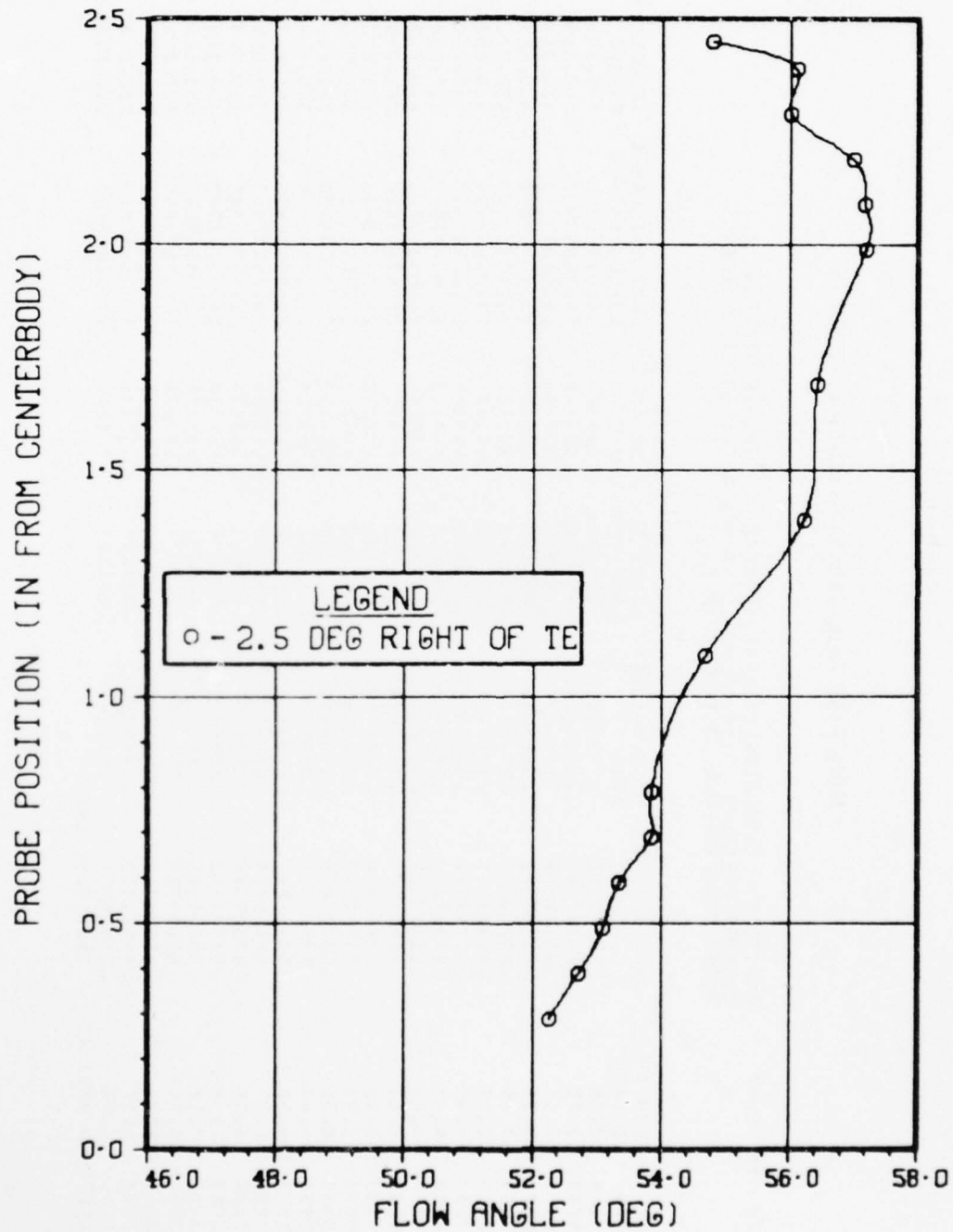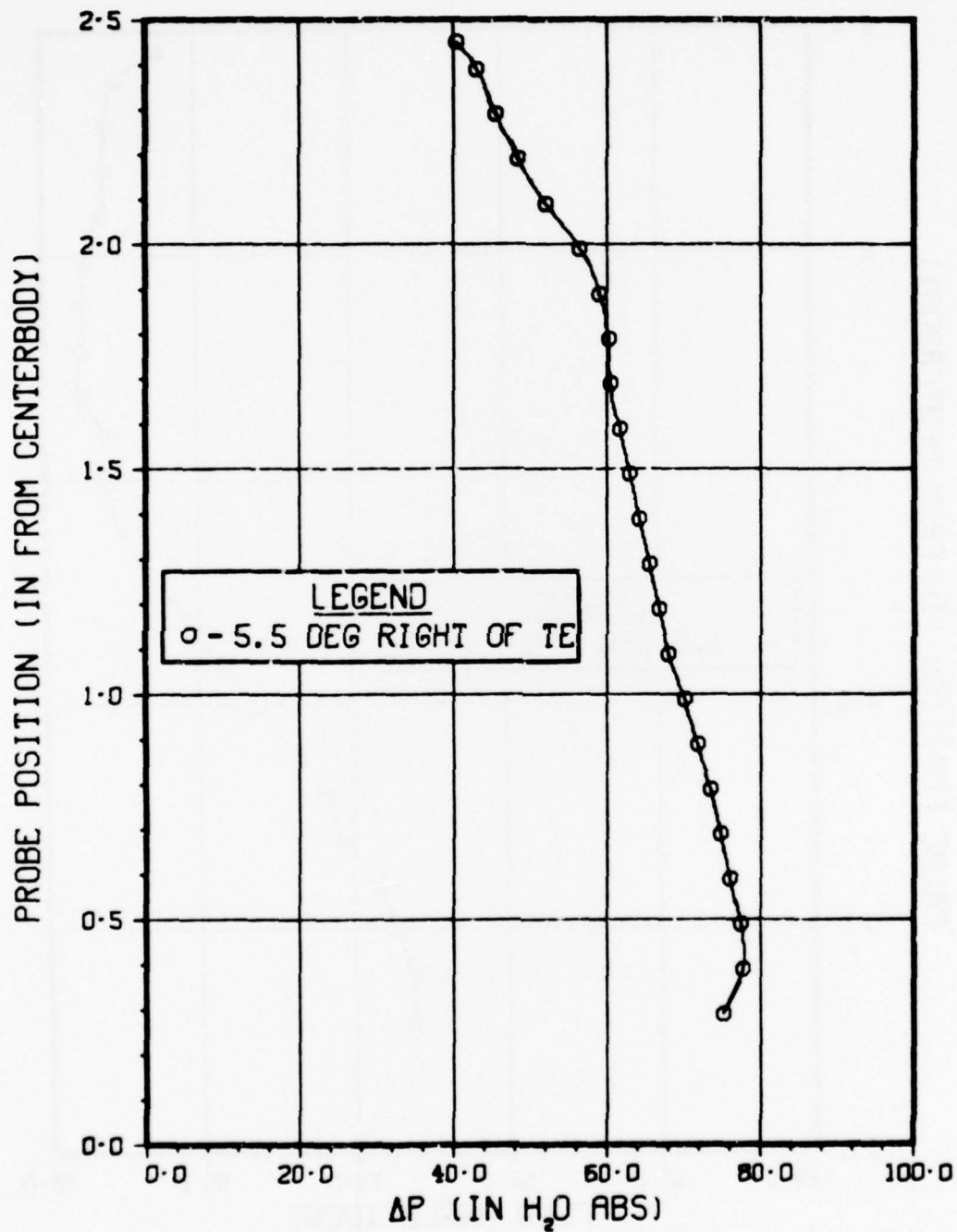

Figure 62 ΔP VS Probe Position

Blade Angle 60.0°
Station 3

Figure 63   Flow Angle VS Probe Position

88

Table 11

Mass Flow Calculation, Station 3, 60°

DATE 19/12/77   POSITION: 2.00 DEGREES LEFT OF ZERO   SADDLE STATION 3
                    CHAMBER PRESSURE 15.90 IN HG   BLADE ANGLE 60.00 DEGREES
                    ACTUAL PROBE POSITION: 5.5° RIGHT OF T.E.

AREA FT**2	FLOW ANGLE DEGREES	MACH NUMBER- BLADE EXIT	MACH NUMBER- AXIAL	DENSITY LB/FT**3	FLOW RATE LB/SEC	FLOW RATE/AREA LB/SEC/FT**2	VELOCITY-AXIAL FT/SEC	PS/PT
.024116	53.24	.5663816	.33900101	.059521	1.872592	22.26201565	374.0220	.834370
.025790	53.26	.5743922	.34376137	.059675	.581569	22.63303402	379.2742	.799567
.026136	53.45	.5715697	.34030783	.060079	.589700	22.56273773	375.5521	.801284
.026573	53.67	.5653037	.33497361	.060406	.593113	22.32013299	363.5013	.805028
.027809	54.15	.5967662	.32776730	.060676	.592631	21.94198136	361.6278	.804412
.027445	54.35	.5539877	.32285112	.050945	.595400	21.70887092	356.2037	.811795
.027802	54.74	.5455727	.31571736	.061215	.594530	21.32366277	348.3330	.816012
.028318	55.23	.5396461	.30774091	.061484	.591162	20.87584902	339.5325	.820236
.028754	55.73	.53124830	.29917307	.061773	.586293	20.38995288	330.0796	.825148
.029190	56.16	.5259292	.29285839	.062004	.584799	20.03421862	323.1126	.828233
.029633	56.65	.52712140	.28596810	.062254	.582046	19.64181468	315.5105	.831576
.030058	57.02	.5145249	.28012611	.062427	.579942	19.29410079	309.0650	.834749
.030499	57.19	.5085217	.27573151	.062639	.581184	19.05583344	304.2164	.838012
.030936	57.17	.5097973	.27273542	.062851	.585079	18.91256013	300.9119	.841278
.031373	57.52	.4977235	.26725412	.063043	.583296	18.58943645	294.8676	.844290
.031808	57.52	.4960575	.26636355	.063178	.590573	18.56661361	293.8806	.845223
.032245	57.47	.4911987	.26410981	.063351	.595249	18.46020049	291.3941	.847977
.032682	57.47	.4876199	.25853964	.063467	.591669	18.10381464	285.2485	.853703
.033117	57.24	.4616558	.24940755	.063621	.580700	17.53490842	275.6143	.864952
.033554	57.20	.4456797	.24144126	.063775	.570035	16.98857400	256.3837	.872531
.033990	57.17	.4315730	.23374485	.064121	.562072	16.53638942	257.8922	.880053
.027507	57.03	.4189527	.22801242	.064447	.445242	15.22285634	251.5675	.886243
.027785	56.48	.4051530	.22376635	.064968	.445659	16.03956378	246.8029	.893093

TOTAL FLOW RATE IS   16.475946 LB/SEC

Blade Angle 60.0°
Station 3
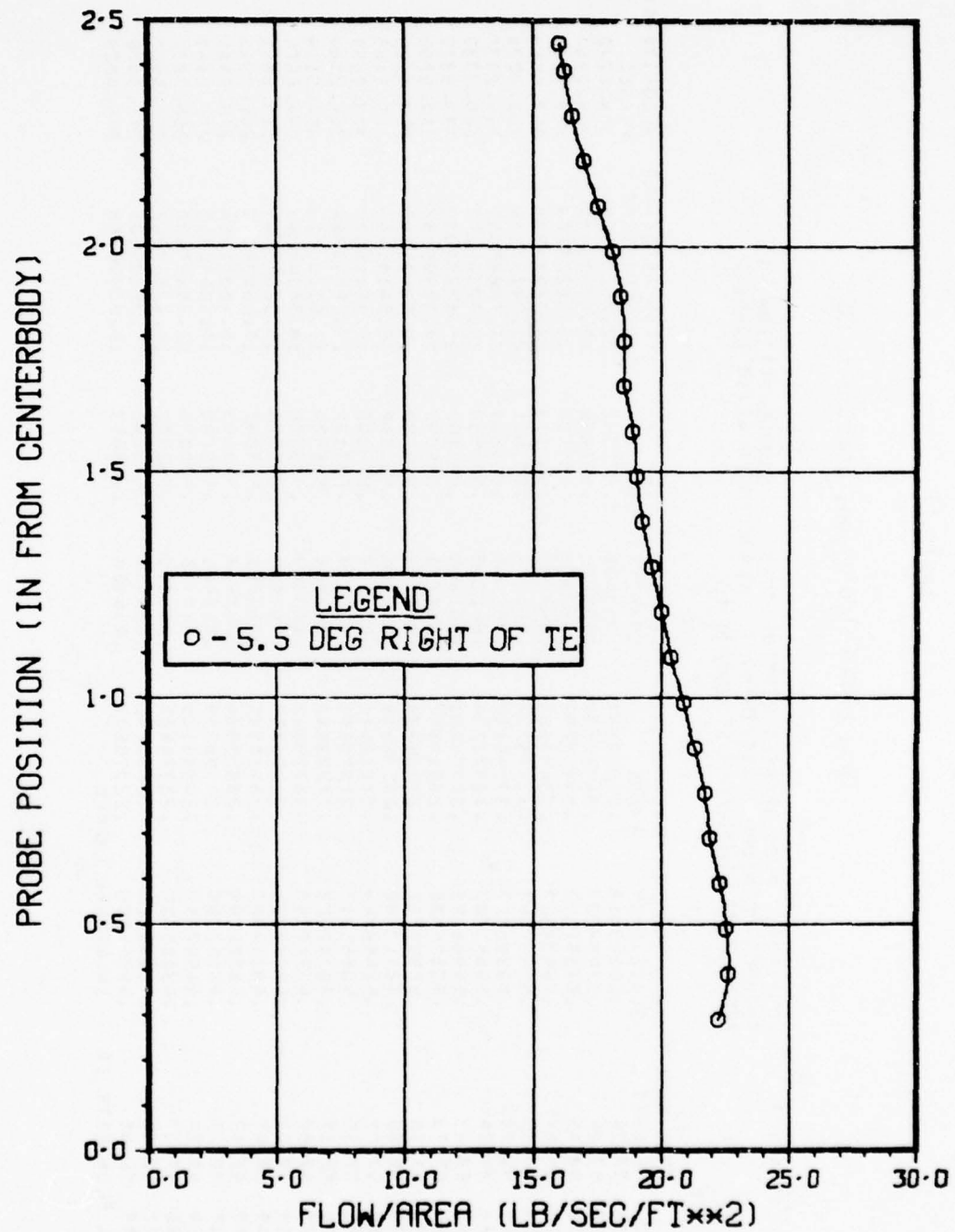
Figure 64 Flow VS Probe Position

90

Calculated results are then shown in Tables 6 through 11 with corresponding plots of mass flow distribution immediately following the tables in Figures 44, 48, 52, 56, 60, and 64. The division of the annulus area into circumferential strips for mass flow calculation is shown in Figure 65. A computer program was written to generate these answers and complete details of the calculations are shown in Appendix J. A total of one hundred eleven (111) different traverses were made during the course of this experimental program and the complete tabulation of raw data was transferred to computer cards at the Air Force Aero Propulsion Laboratory. A thorough review of all these runs and a series of repeat runs produced the conclusion that, for any given cascade, the results were both consistent and repeatable. Therefore, those shown here are deemed representative and adequate to establish the correct conclusions. In all cases, due to the location of pressure taps on the probe and the need for operating clearance between the centerbody and the end of the probe, the innermost reading was approximately 0.3 inches above the surface of the centerbody. At the outside wall, due to the liner penetration scheme, the probe could be withdrawn such that the pressure taps were physically at the wall. Thus, in all plots, the boundary layer effect at the outer wall is clearly visible while at the inner wall the thickness of the boundary layer is generally less than the 0.3 inch limit. The fact that near the outer wall there is a stronger boundary layer effect than near the hub, can be attributed to the flow path following the bellmouth entrance. The accumulated boundary layer growth along the entrance bellmouth is manifested in the greater thickness of the boundary layer. Obviously, the same effect took place near the centerbody but on a much weaker scale. So each plot

91
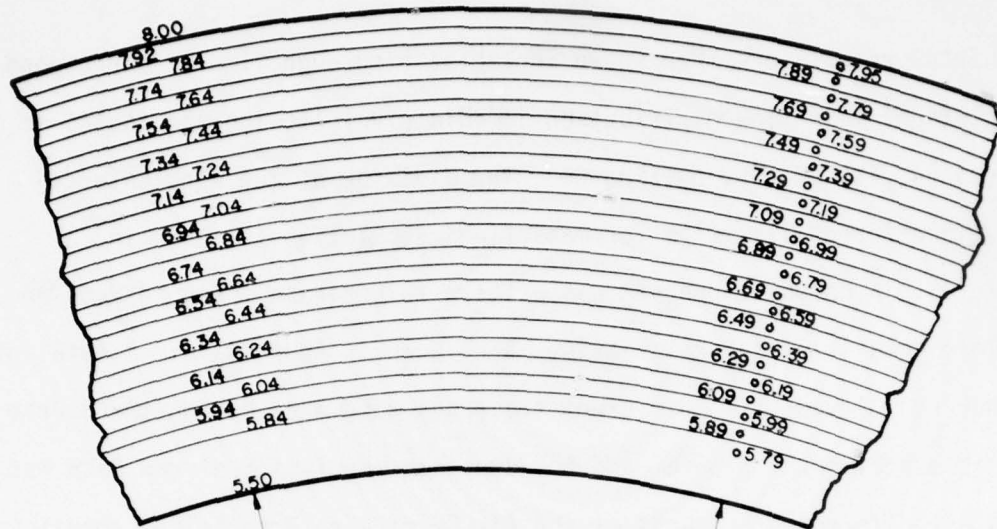
MASS FLOW
AREA DIVISION

Figure 65

can be considered as demonstrating several zones; i.e., outer wall boundary layer, fully developed channel flow, distorted flow due to the effects of increasing blade blockage at inner radii and finally inner wall boundary layer effect which could not be measured but is certainly there. As can be seen readily from the total pressure and mass flow distribution plots, uniformity across the channel has been achieved. The scales selected for these plots tend to exaggerate what in reality are relatively small percentage changes. For example, taking the worst case shown in Figure 41, there is a maximum variation of approximately 368 to 398 inches of water absolute total pressure. Therefore, the maximum change of 30 inches compared to an average value of 388 inches gives a percentage variation of $\pm$ 3.87%. These scales were consciously selected to demonstrate both the sensitivity of the instrumentation used and the repeatability of the data. A sample typical repeat run comparison is shown in Figures 66, 67, 68, and 69, for the 65° blade row. In this case, the maximum deviation between runs of total pressure is approximately 5 inches of water out of a nominal absolute value of 395. Thus, the percentage change is approximately $\pm$ 0.633%. The flow distribution comparison shown in Figure 69 indicates excellent repeatability and the legend gives the receiver pressures for the respective runs. These were run on different days and the receiver pressure was always a function of facility controls and the atmospheric pressure.

This uniformity of total pressure and flow per unit area of the channel is the essence of the proof of Engelman's analysis. Achievement of uniform axial mass flow distribution at high subsonic Mach numbers with nontapered, nontwisted blades is not predicted by the free vortex

93

Blade Angle 65.0°
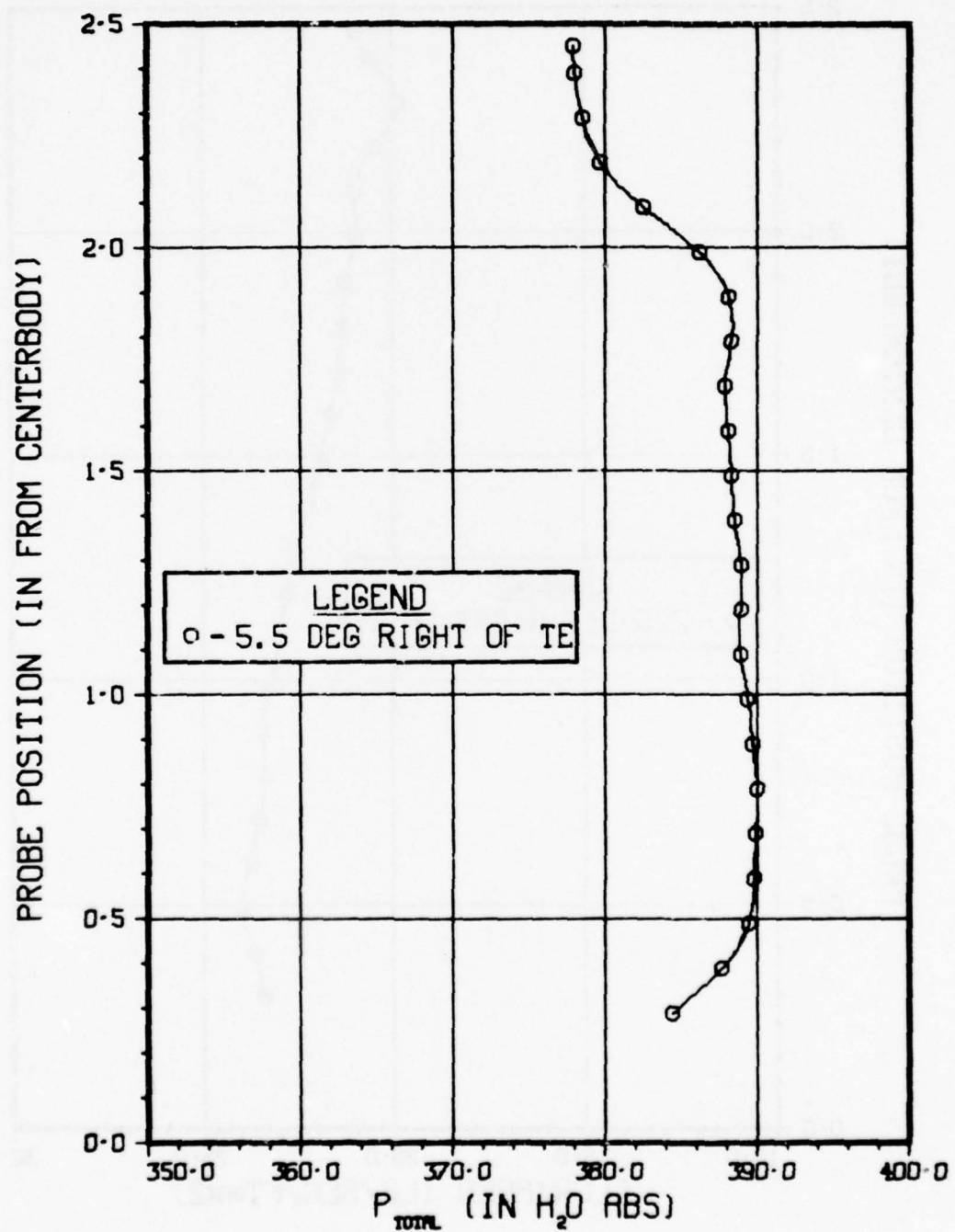## Station 1
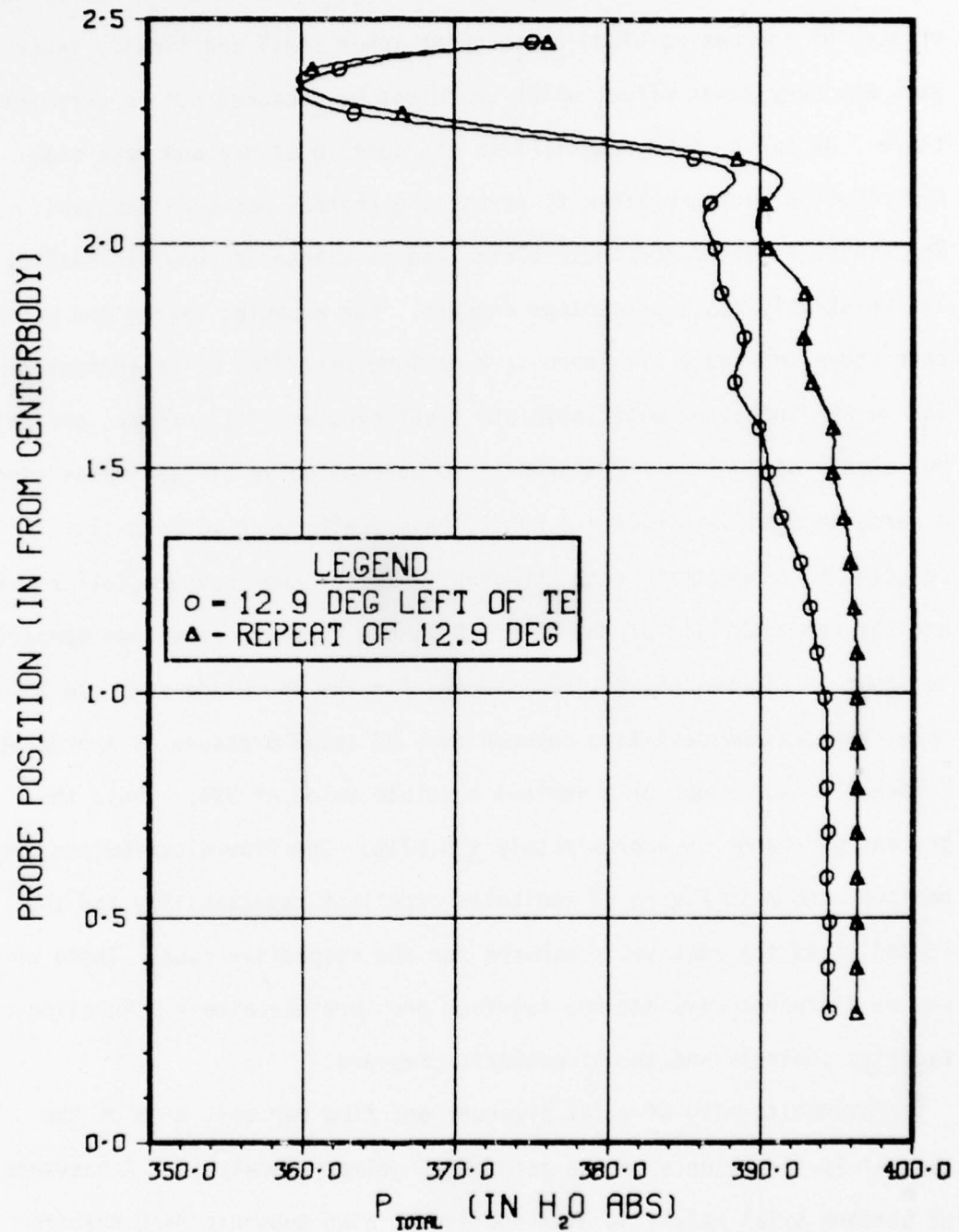
Figure 66 P_{total} VS Probe Position

Blade Angle 65.0°
Station 1

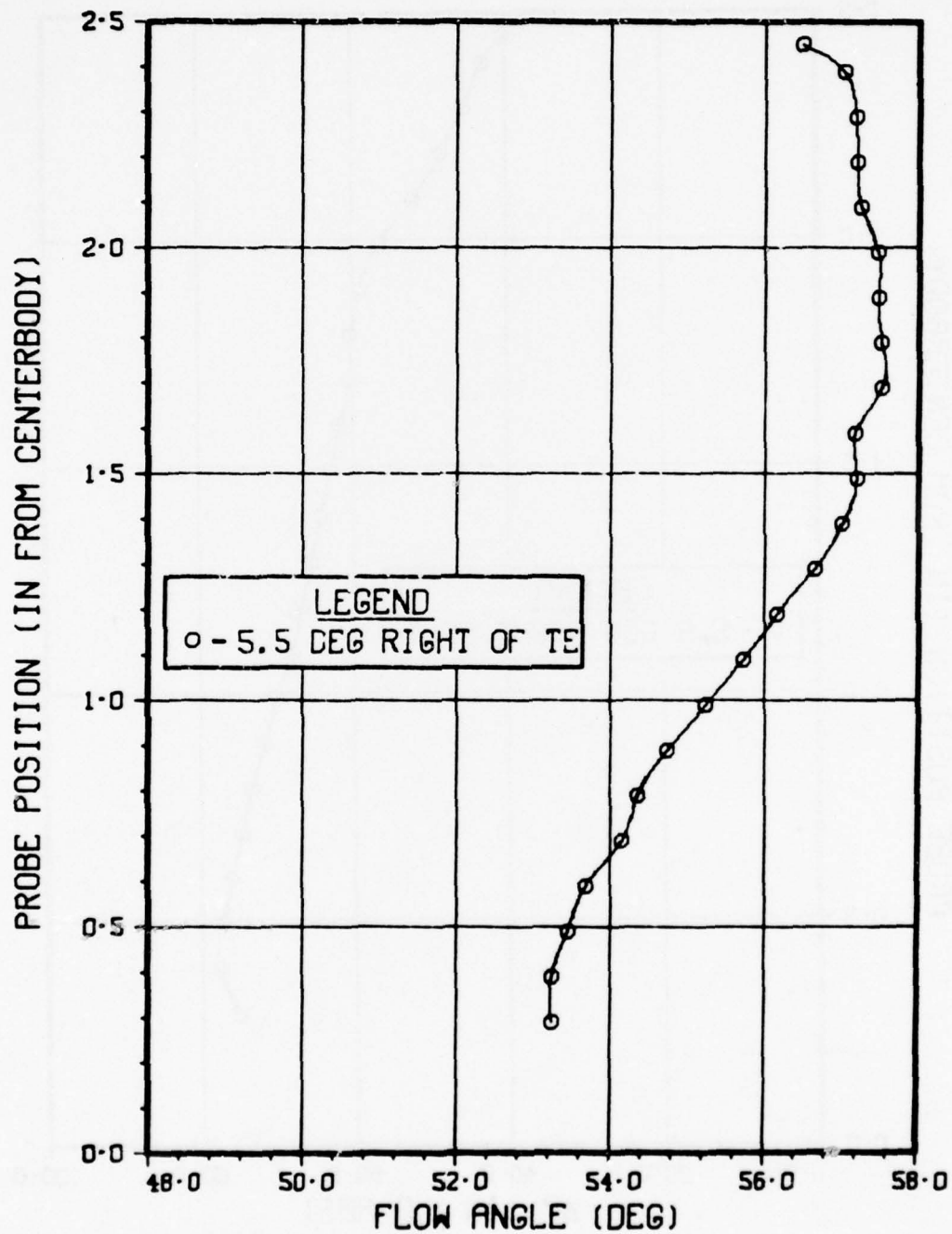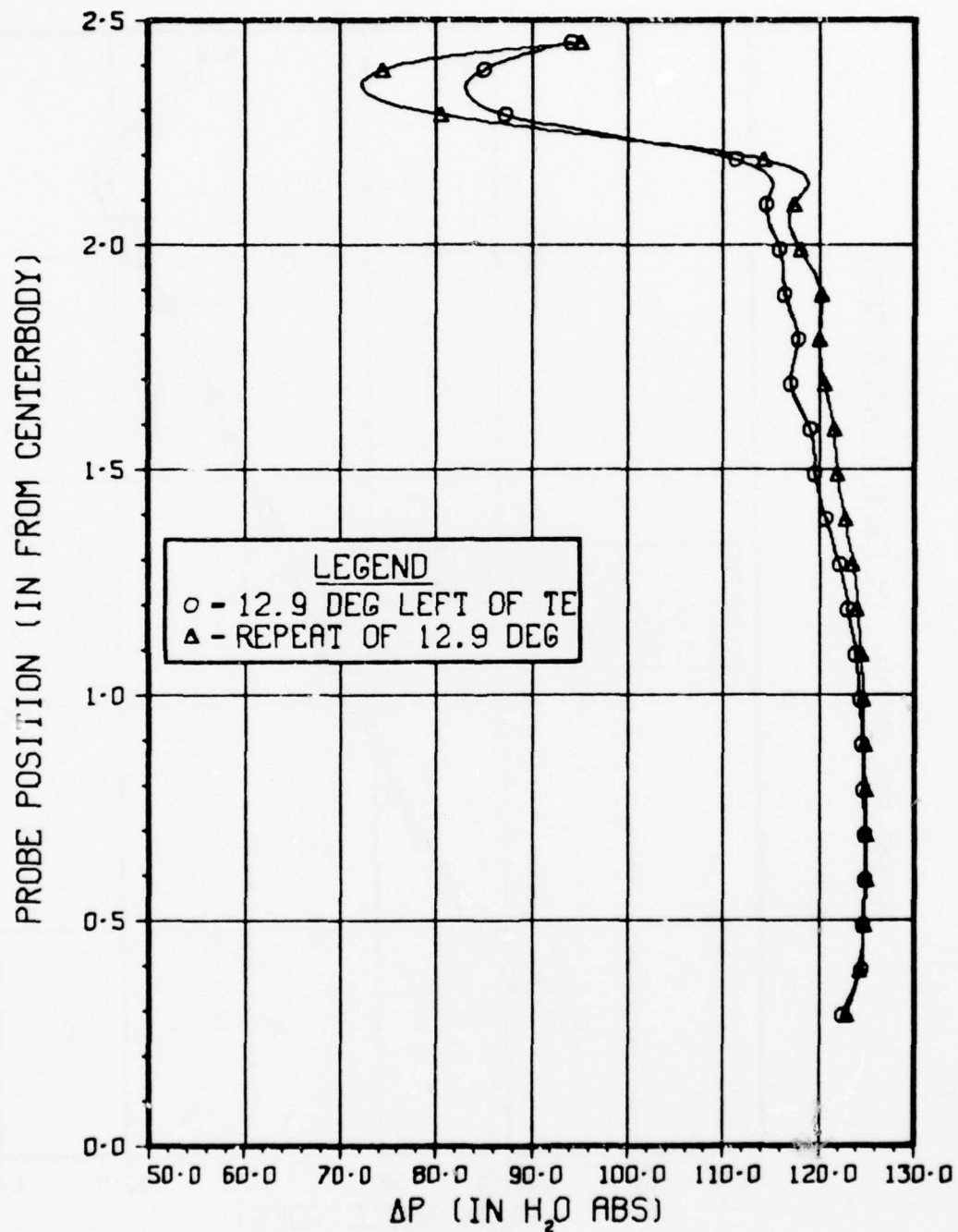Figure 67   ΔP VS Probe Position

95

Blade Angle 65.0°
Station 1
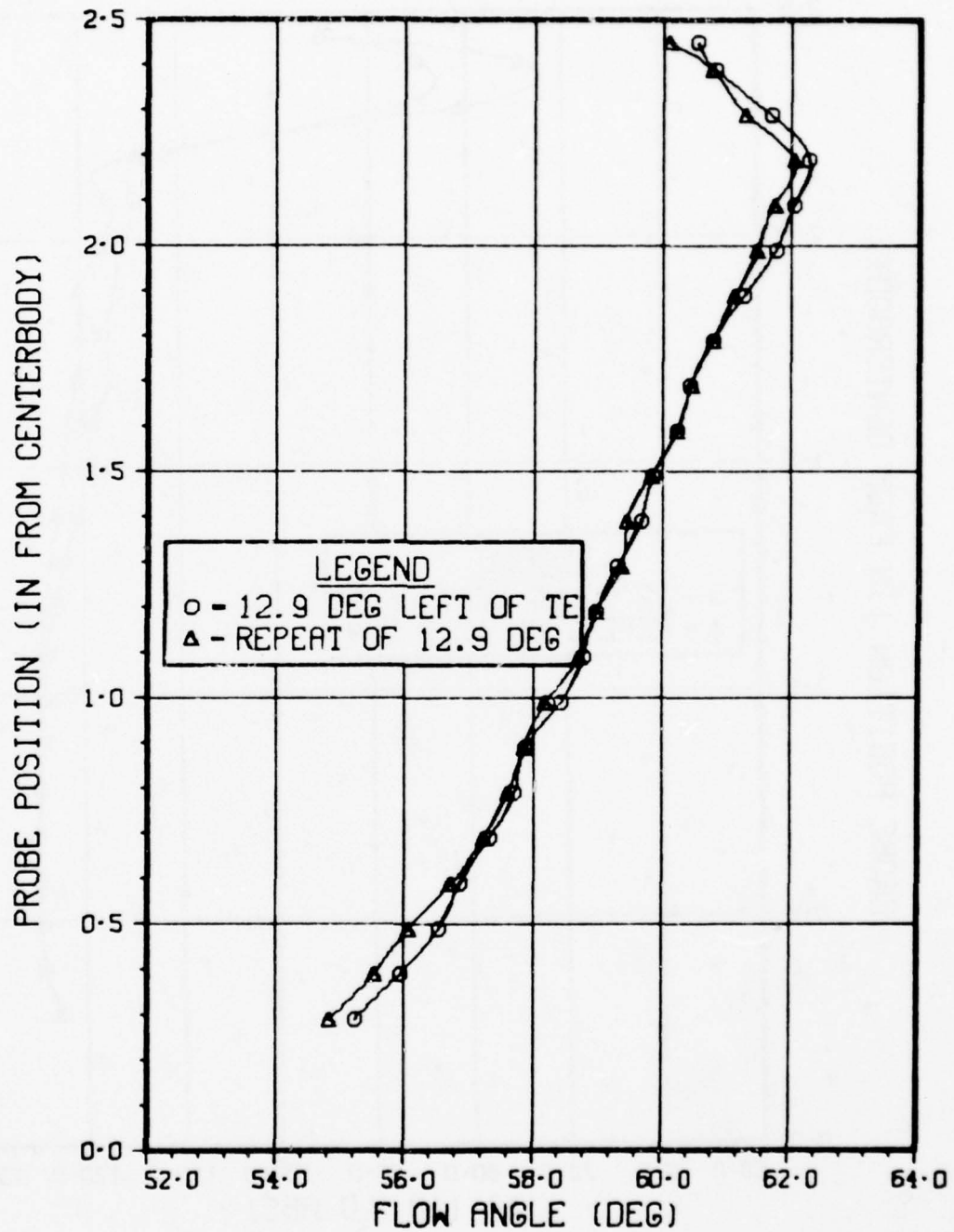
Figure 68   Flow Angle VS Frobe Position

96

Blade Angle 65.0°
Station 1
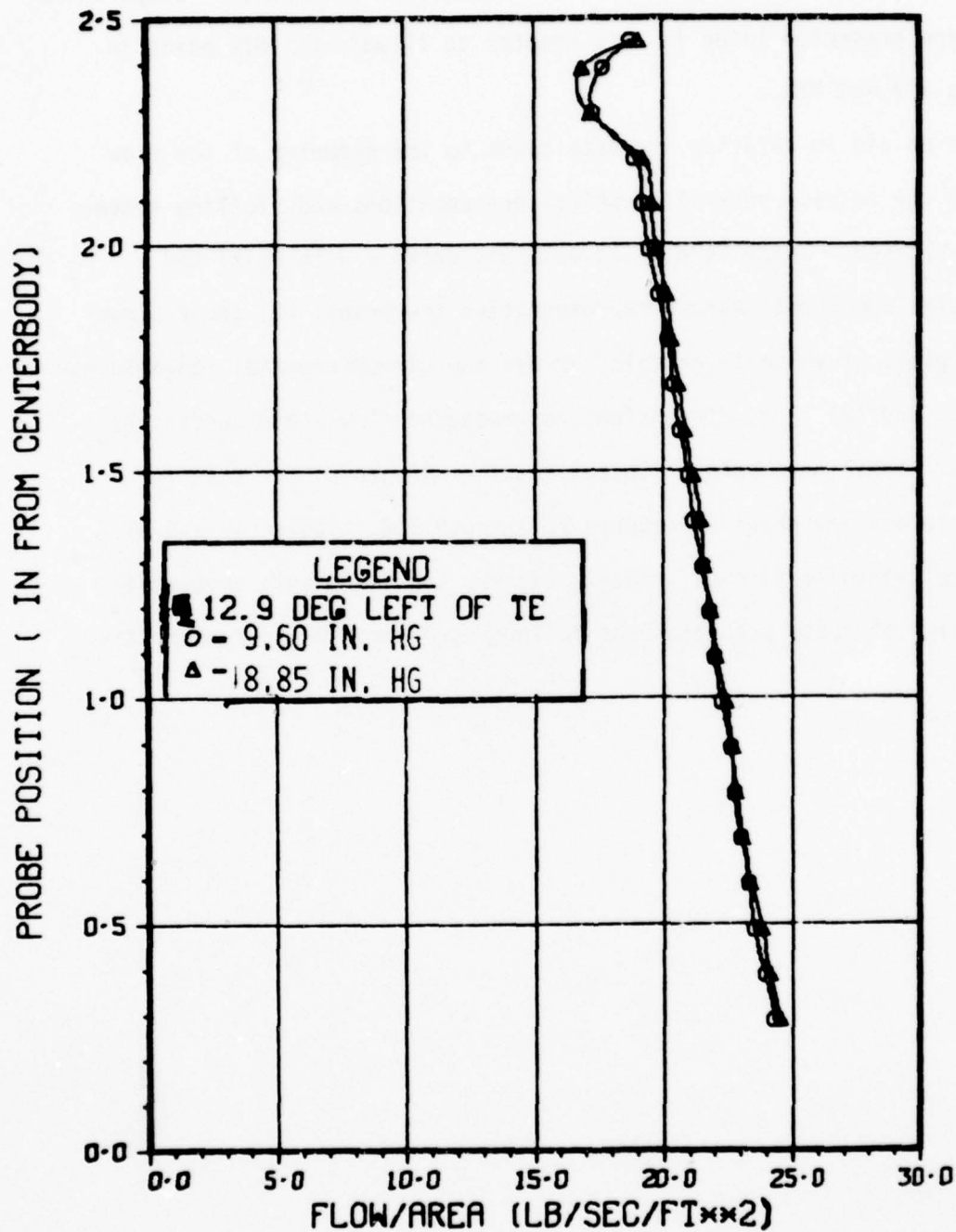
Figure 69 Flow VS Probe Position

97

theory. The compressibility effects are clearly real and the analysis by Engelman is better able to predict actual flow parameters. Comparative plots are presented later in this chapter to illuminate this point in Figures 109 and 110.

As an aid in relating the data taken to the geometry of the flow path in the cascade, several graphical presentations and plotting schemes were exercised. These were: (1) velocity vectors with axial and tangential components across representative traverses, (2) three dimensional plots of velocity profiles across the circumferential range investigated, and (3) plots of constant, as-measured flow angle across the annulus. These have been collected together in groups for ease in reference and are shown in Figures 70 through 108. Tables 12 and 13 organize the collection of velocity vectors and components presented. Discussion of these presentations follows each grouping as appropriate.

Table 12

Velocity Vectors & Components

in Selected Core Flow Regions

Blade Exit Angle	Station 1	Station 3
69.7°	2.5° Left of T.E.	0° Right of T.E.
	Figure 70	Figure 73
65.0°	10.0° Right of T.E.	7.5° Right of T.E.
	Figure 71	Figure 74
60.0°	2.5° Right of T.E.	5.5° Right of T.E. Low Flow
	Figure 72	Figure 75

99
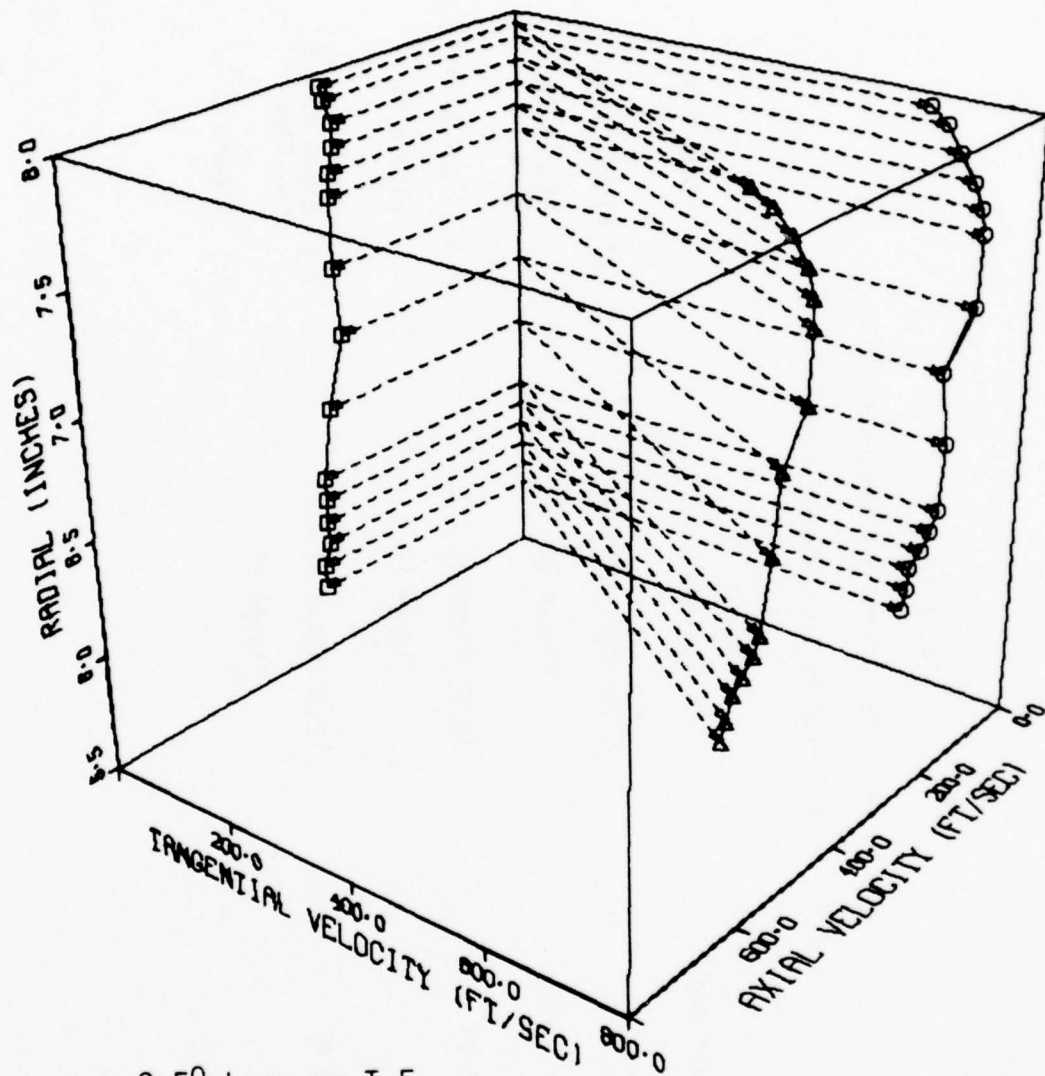
2.5° LEFT OF T.E.
69.7° BLADES
STATION 1

Figure 70   Velocity Vectors & Components

100
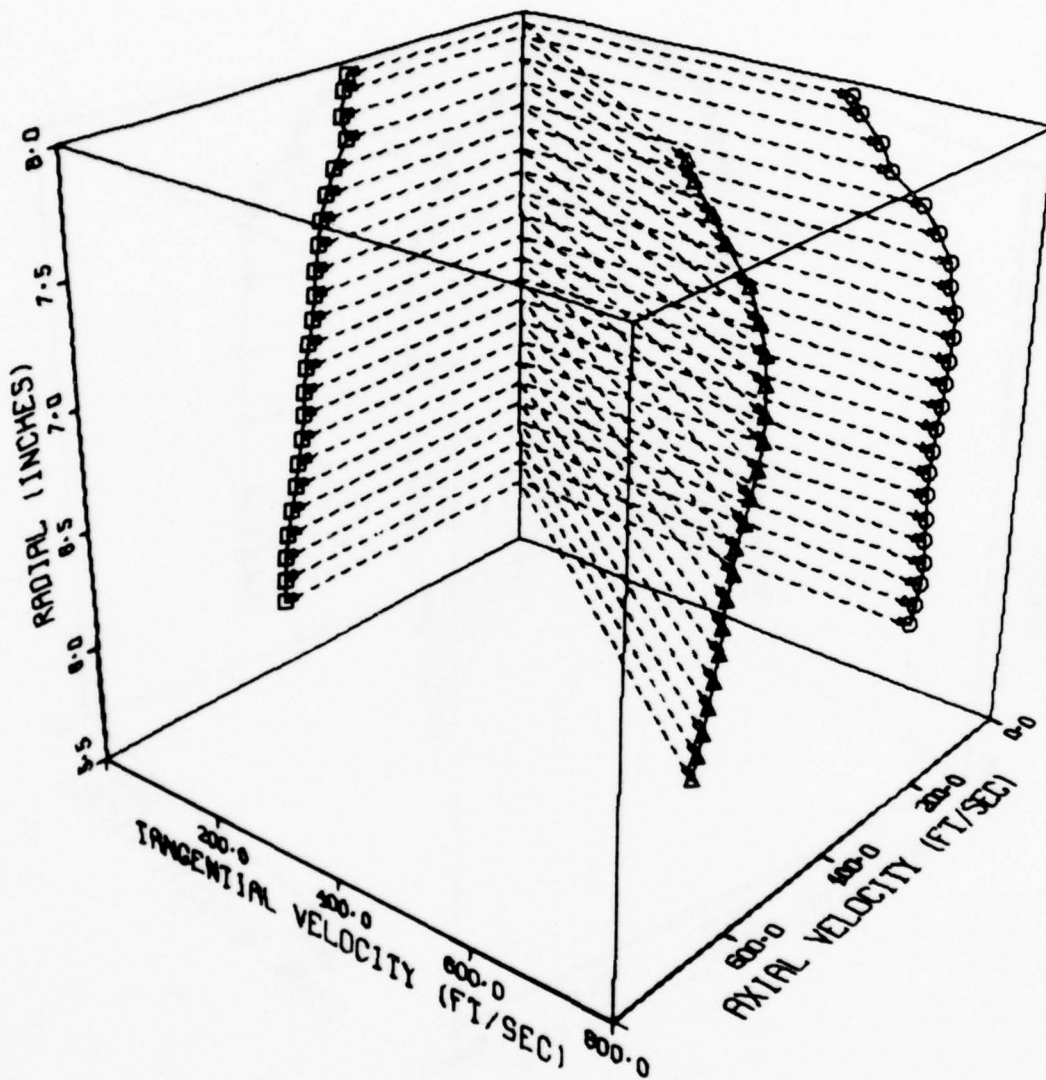
10° RIGHT OF T.E.
65° BLADES
STATION 1

Figure 71 Velocity Vectors & Components

101
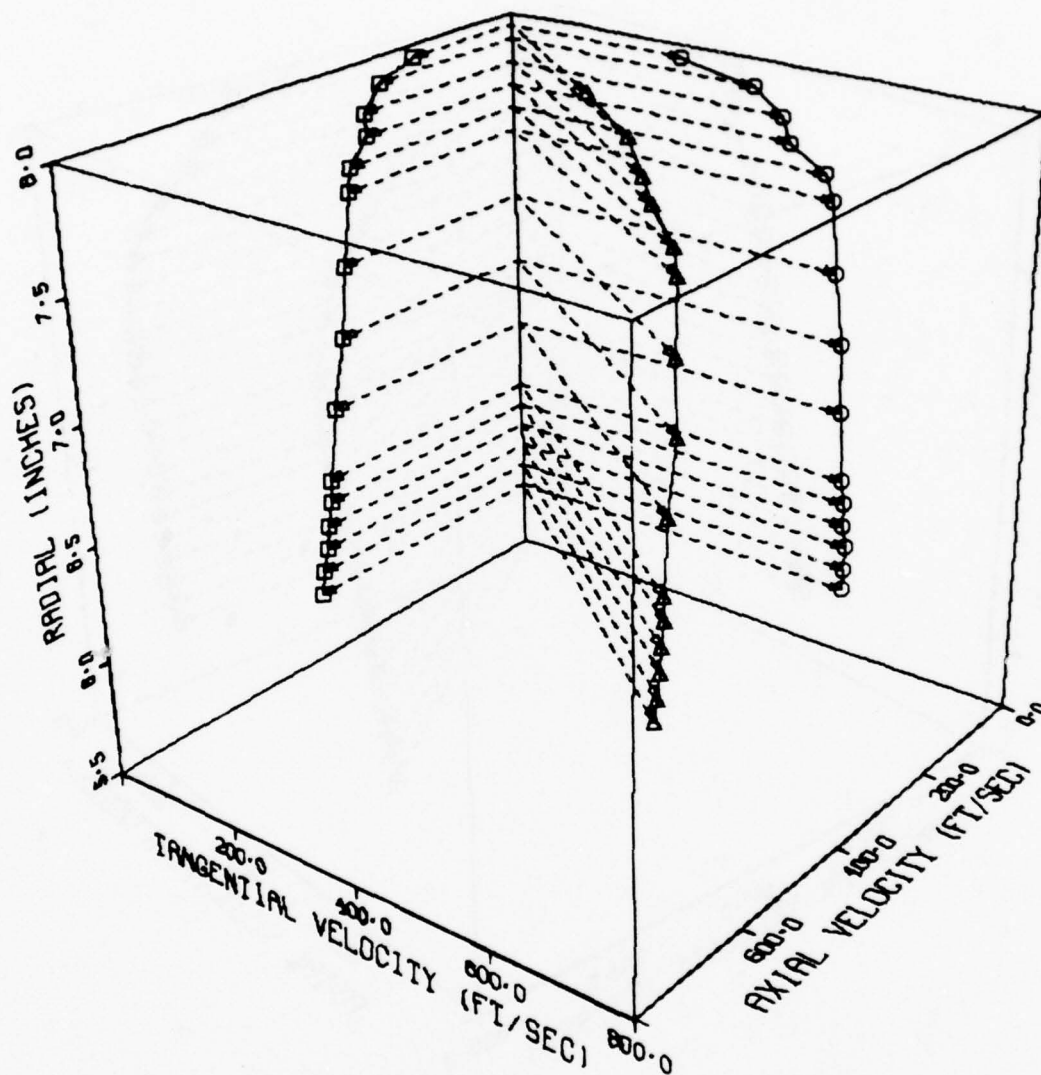
2.5° Right of T.E.
60° Blades
Station 1

Figure 72   Velocity Vectors & Components

102
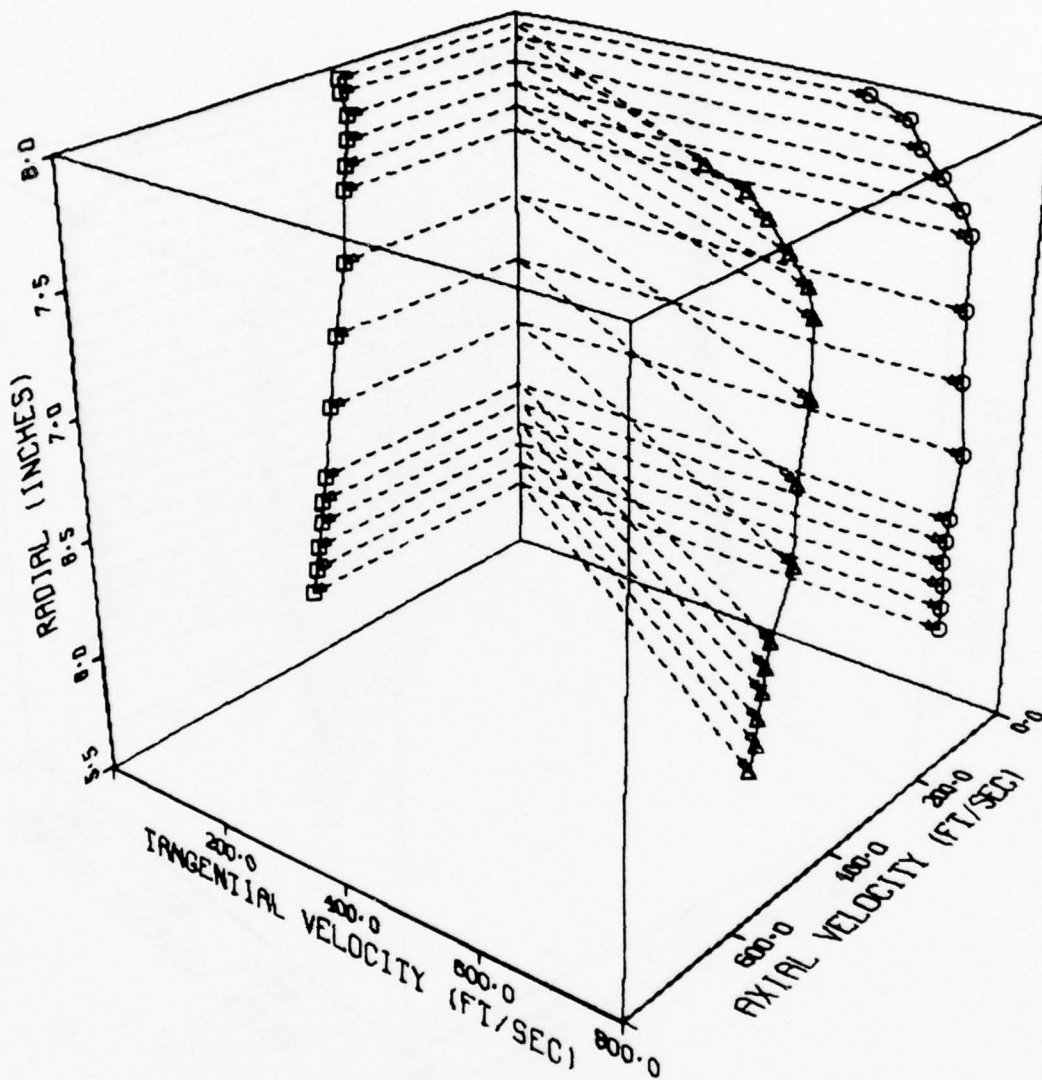
0° RIGHT OF T.F.
69.7° BLADES
STATION 3

Figure 73   Velocity Vectors & Components
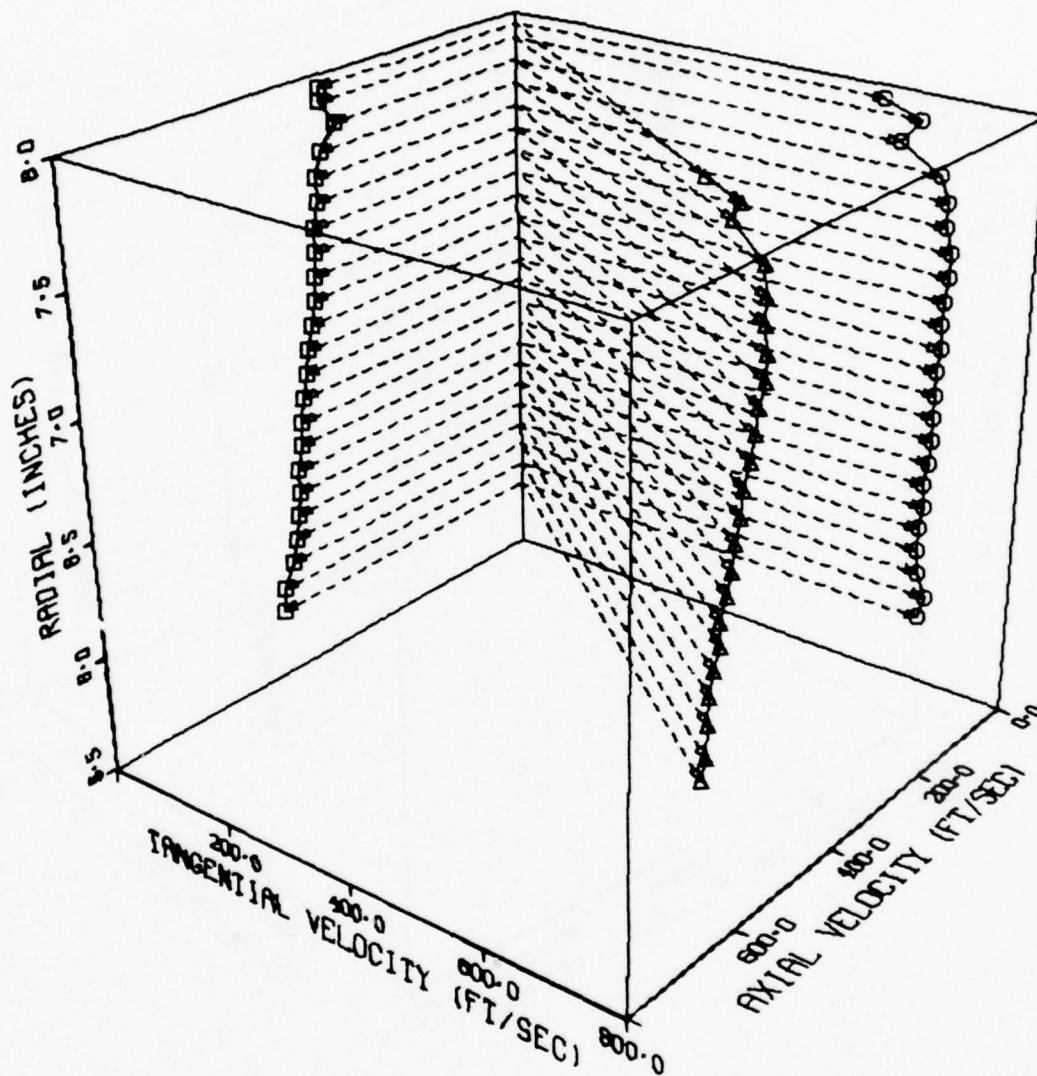
7.5° RIGHT OF T.E.
65° BLADES
STATION 3

Figure 74   Velocity Vectors & Components

104

5.5° RIGHT OF T.E.
60° BLADES
STATION 3
LOW FLOW
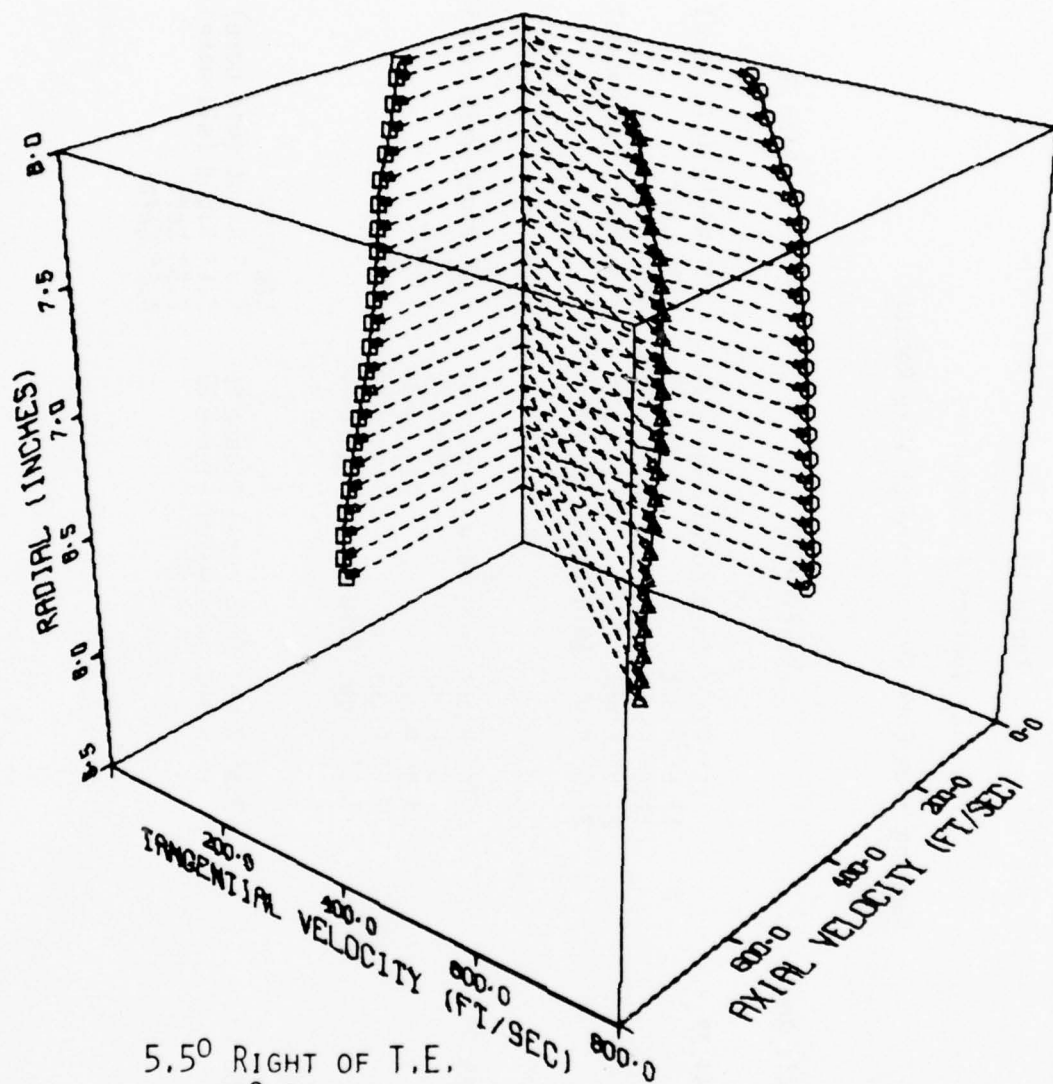
Figure 75   Velocity Vectors & Components

Table 13

Velocity Vectors & Components

Ranging from Core Region through Wake Region

Blade Exit Angle	Station 1	Station 3
69.7°	15° Right (mid core) Figure 76 17.5° Right Figure 77 19.5° Right Figure 78 21.5° Right Figure 79 23.5° Right (mid wake) Figure 80	0° Right (mid core) Figure 88 2.5° Left Figure 89 4.5° Left Figure 90 7.5° Left (mid wake) Figure 91
65.0°	10° Right (mid core) Figure 81 5° Right Figure 82 4.5° Right Figure 83 2.5° Right Figure 84 1.5° Right (mid wake) Figure 85	7.5° Right (mid core) Figure 92
60.0°	2.5° Right (mid core) Figure 86 0° Right (mid wake) Figure 87	LOW FLOW 5.5° Right (mid core) Figure 93 3.5° Right (mid wake) Figure 94 2.5° Left Figure 95 4.5° Left Figure 96
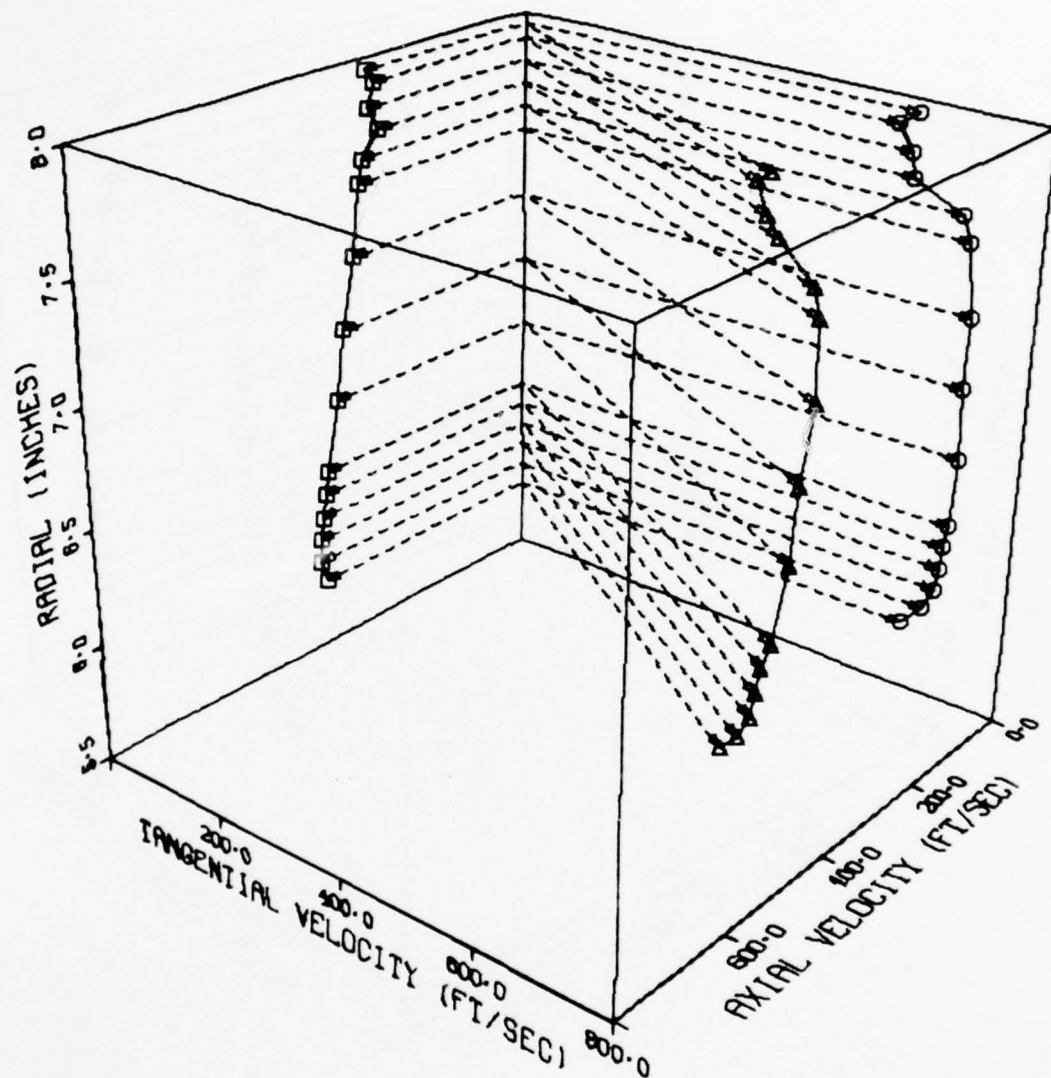
15° RIGHT OF T.E.
69.7° BLADES
STATION 1

Figure 76 Velocity Vectors & Components

107
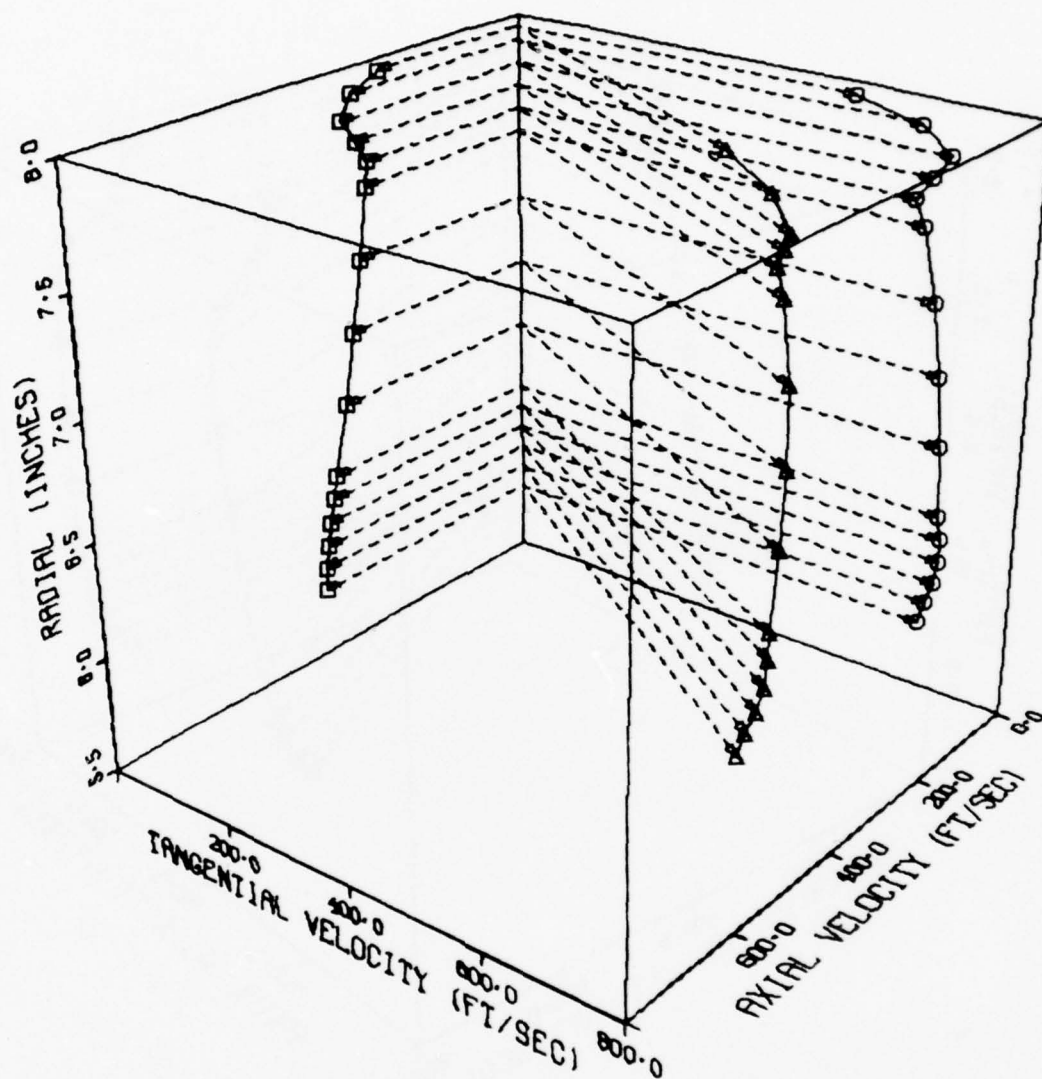
17.5° RIGHT OF T.E.
69.7° BLADES
STATION 1

Figure 77 Velocity Vectors & Components

108
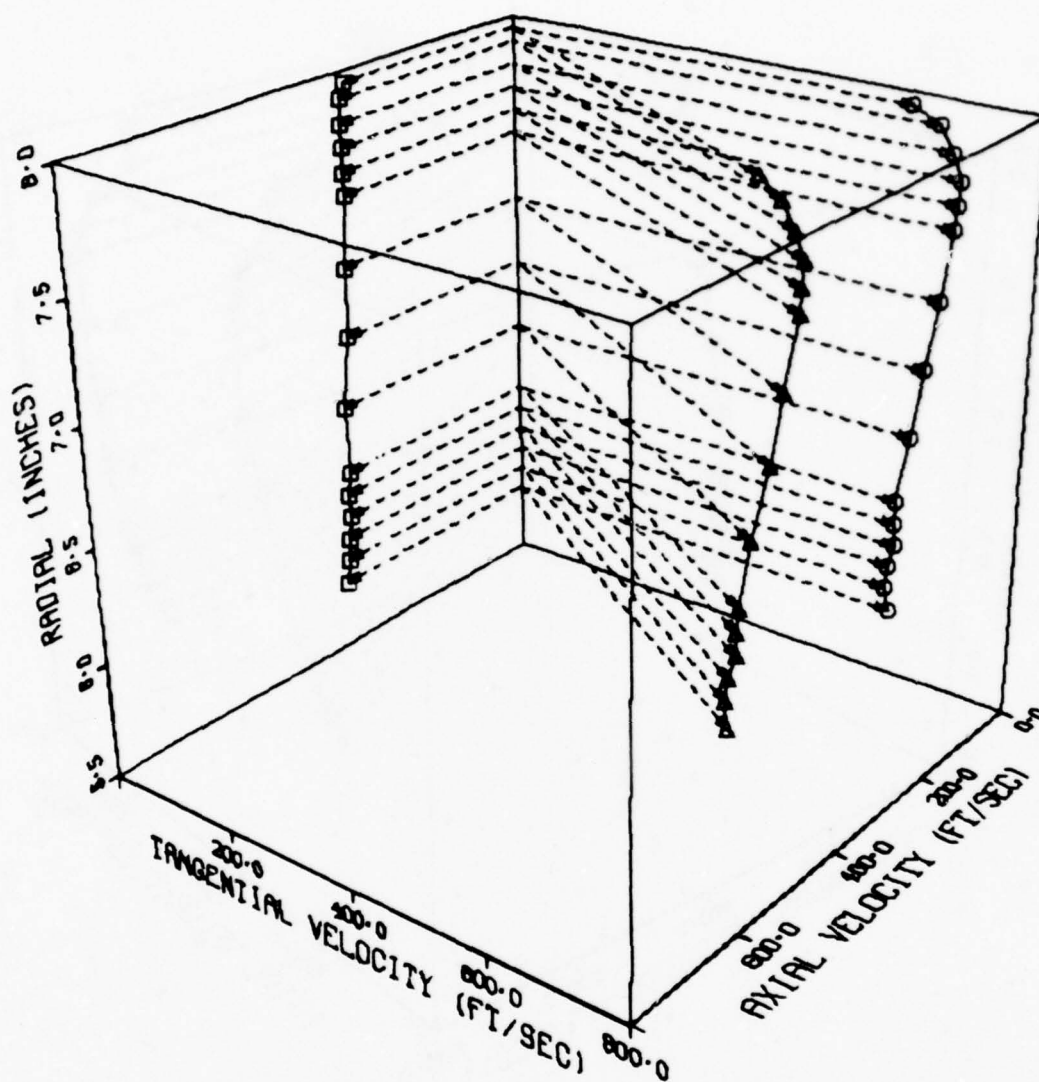
19.5° Right of T.E.
69.7° Blades
Station 1

Figure 78 Velocity Vectors & Components
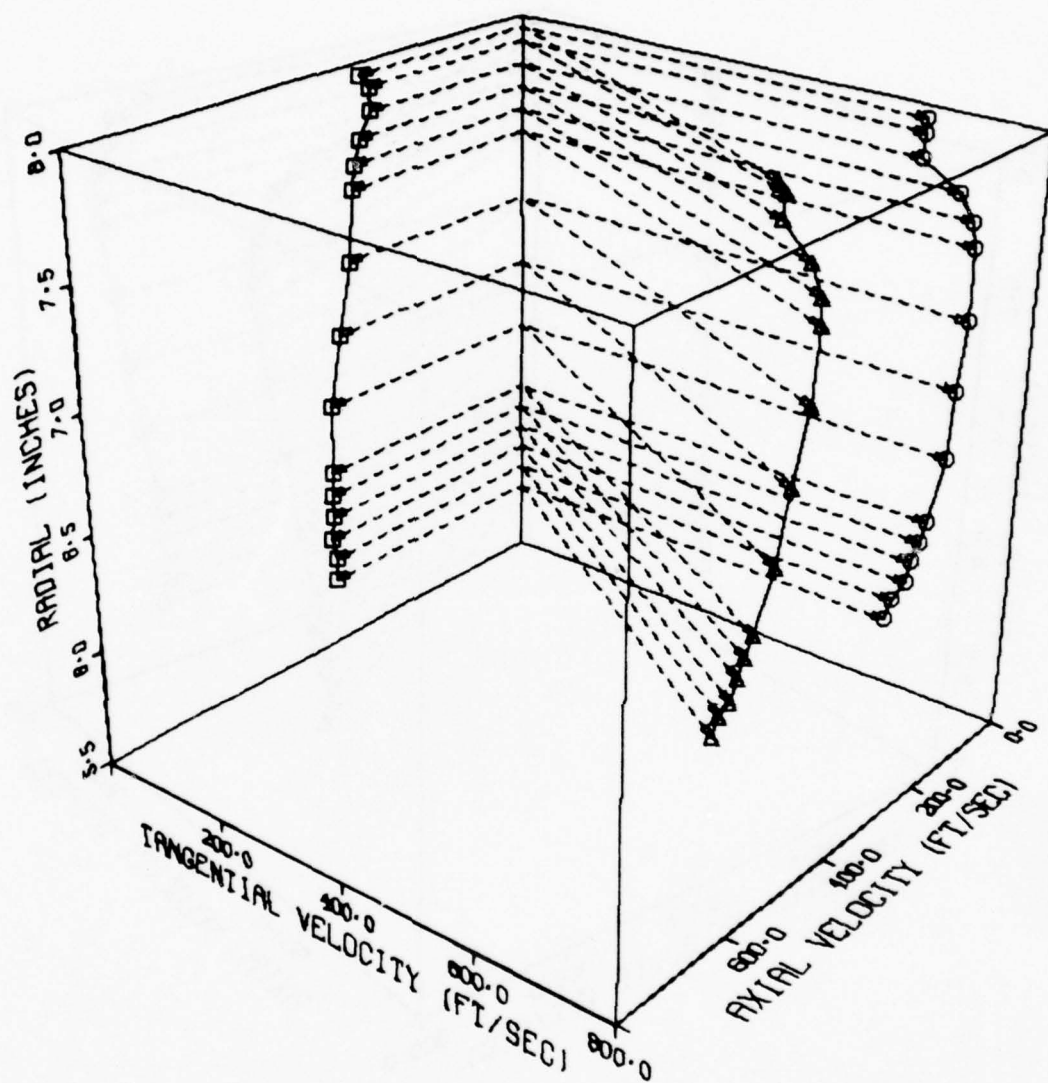
21.5° RIGHT OF T.E.
69.7° BLADES
STATION 1

Figure 79   Velocity Vectors & Components

110
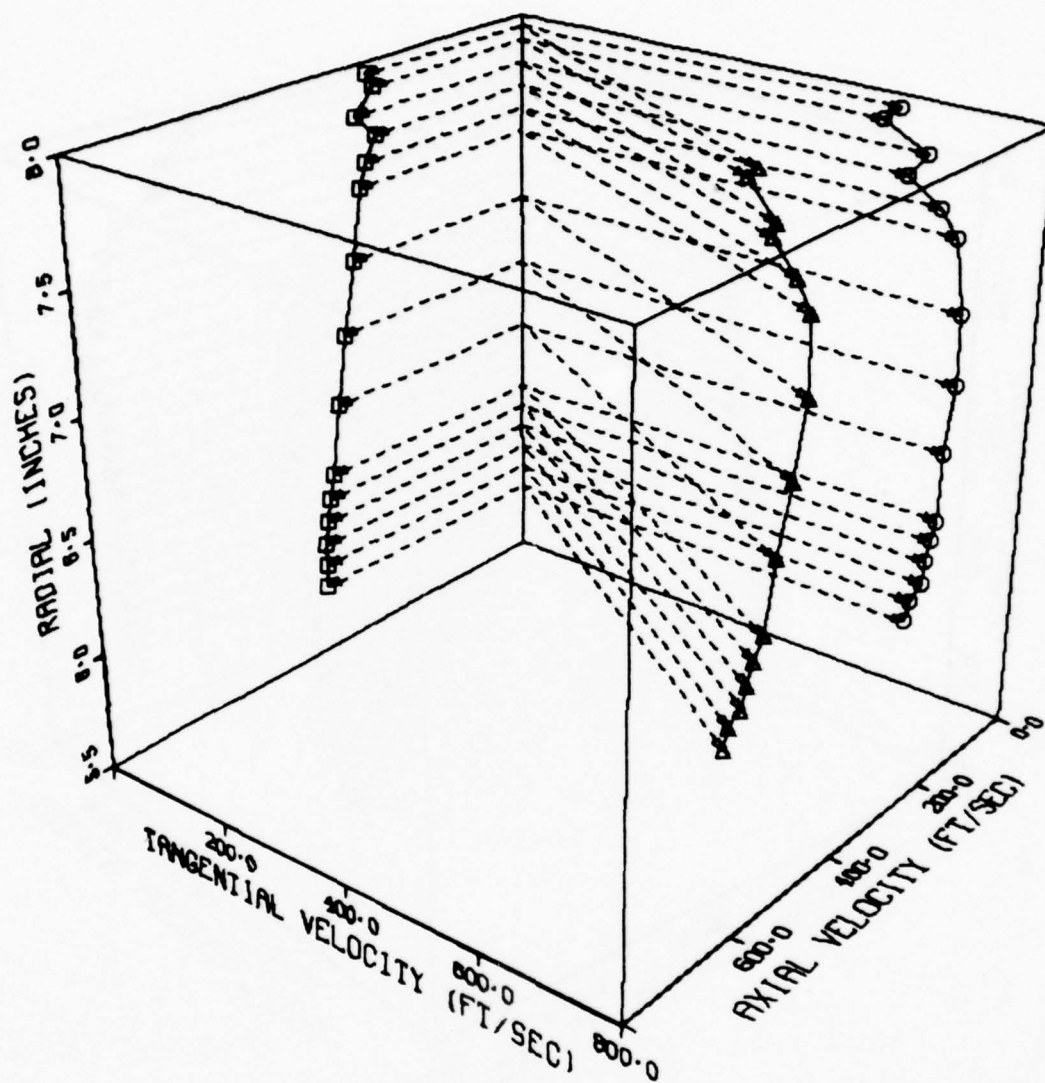
23.5° Right of T.E.
69.7° Blades
Station 1

Figure 80   Velocity Vectors & Components

111
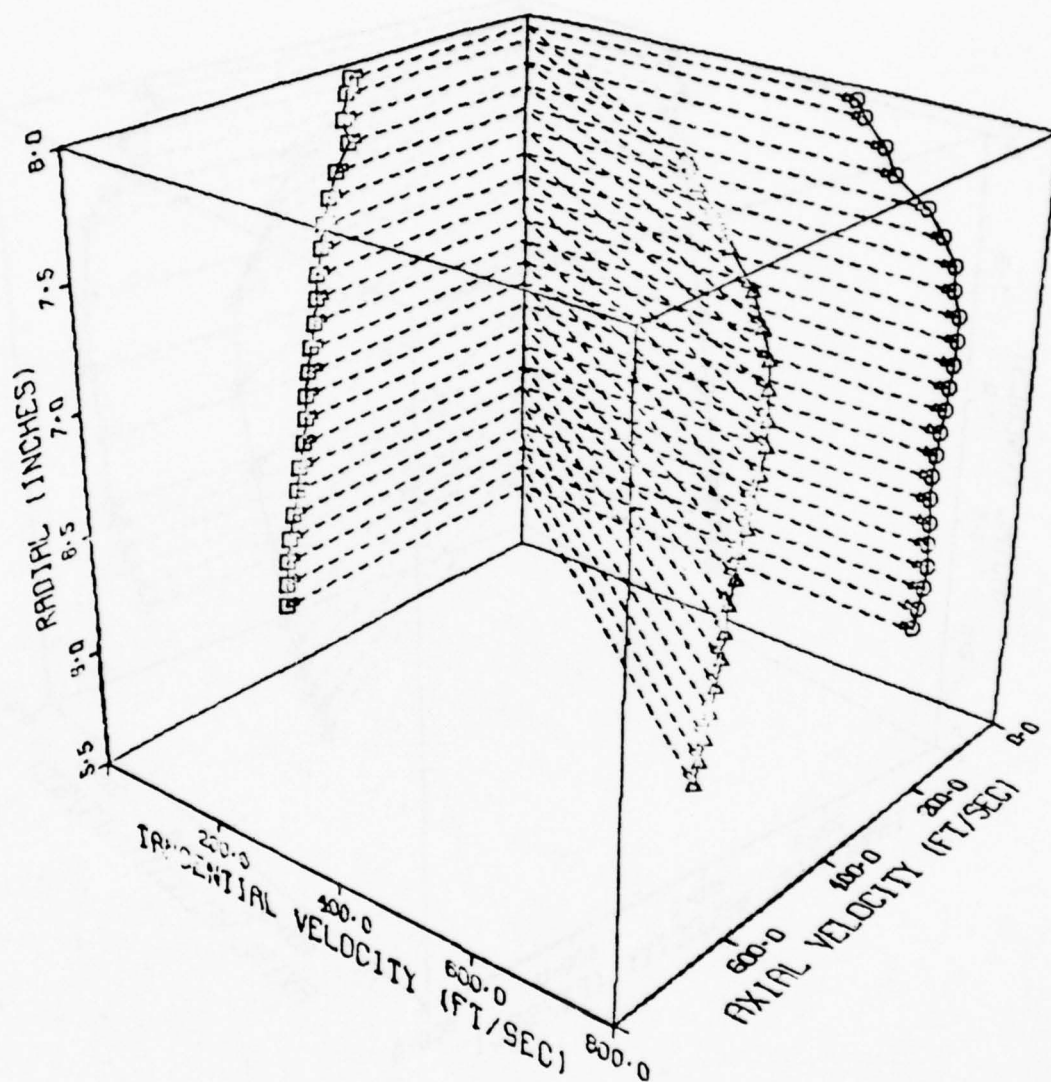
10° RIGHT OF T.E.
65° BLADES
STATION 1

Figure 81 Velocity Vectors & Components

112
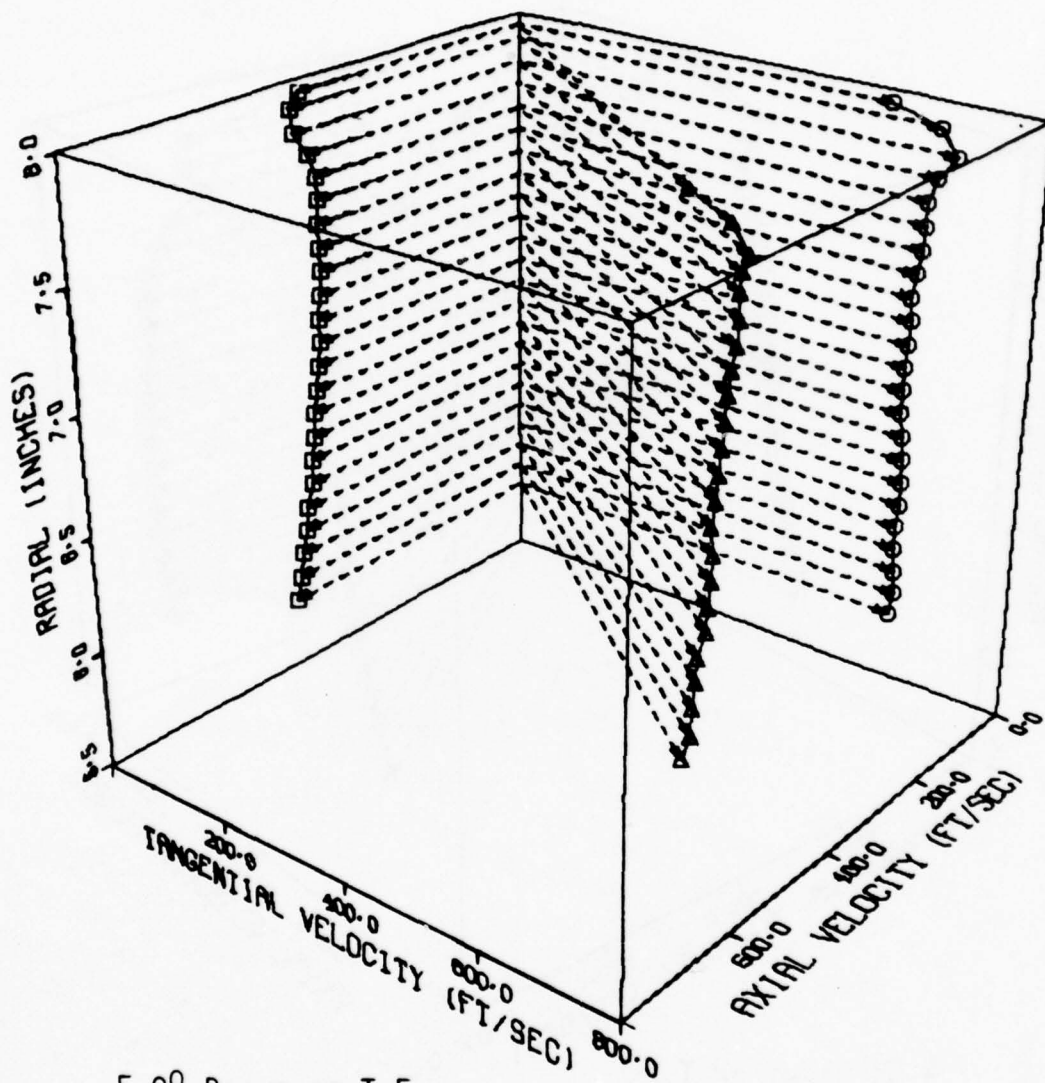
5.0° RIGHT OF T.E.
65° BLADES
STATION 1

Figure 82   Velocity Vectors & Components

113
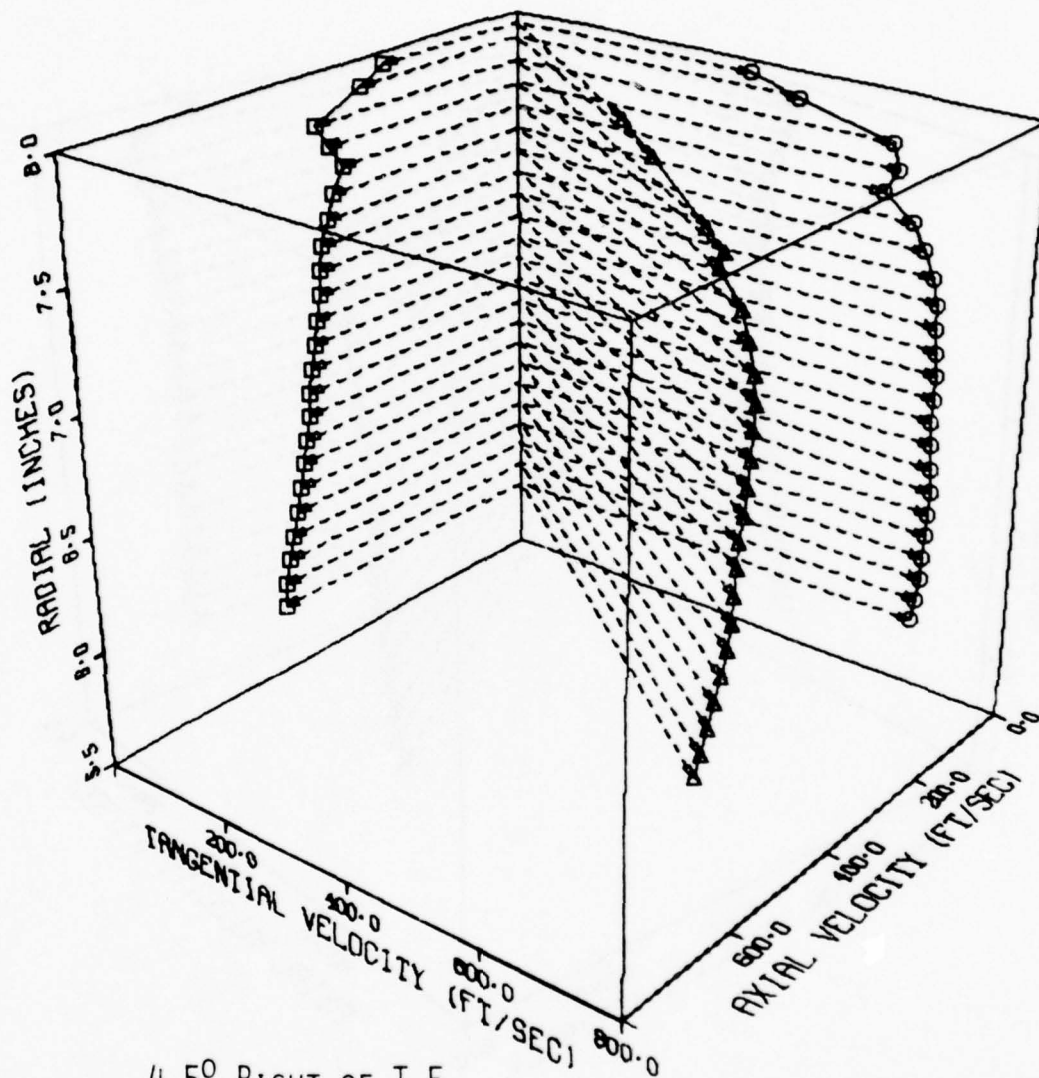
4.5° RIGHT OF T.E.
65° BLADES
STATION 1

Figure 83 Velocity Vectors & Components

114

RADIAL (INCHES)

TANGENTIAL VELOCITY (FT/SEC)

AXIAL VELOCITY (FT/SEC)
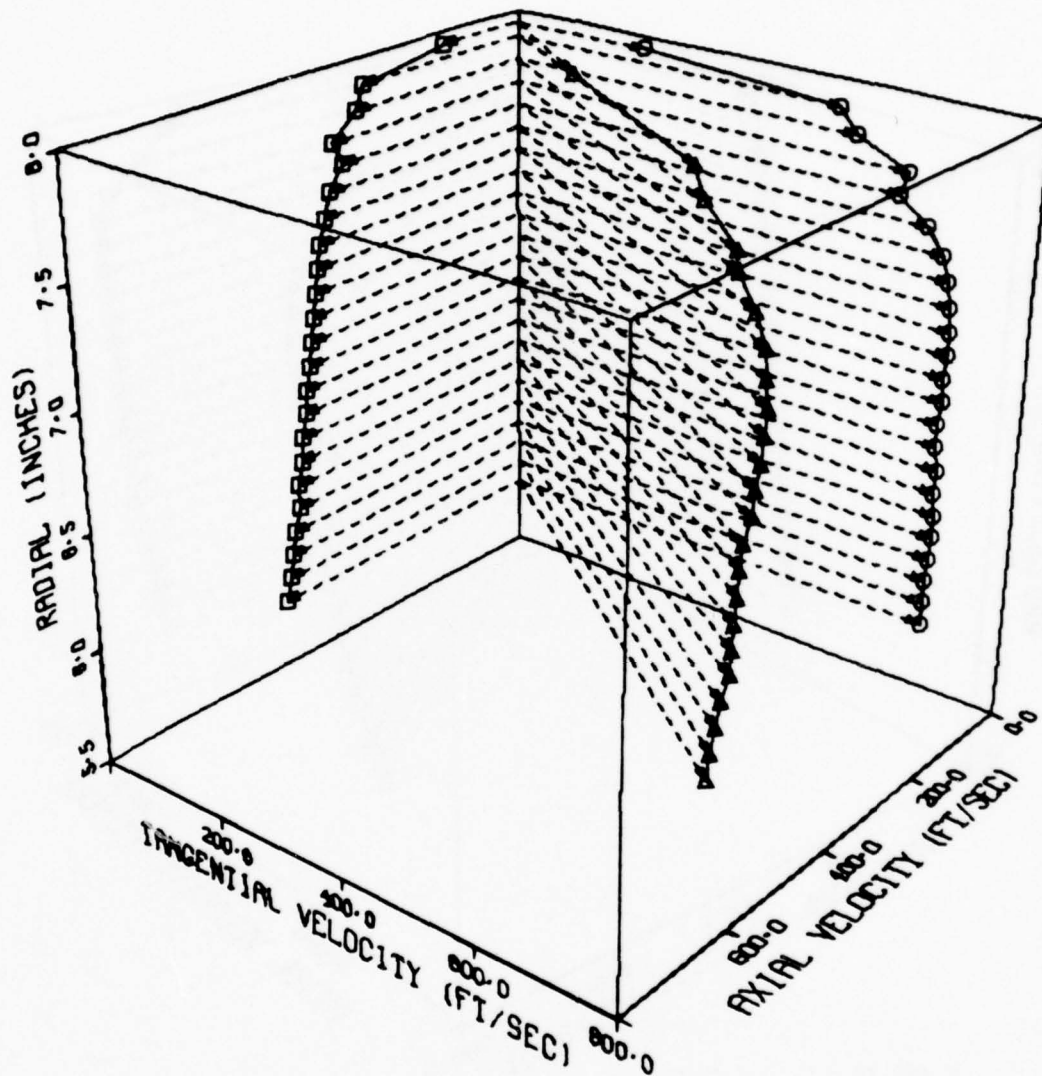
2.5° RIGHT OF T.E.
65° BLADES
STATION 1

Figure 84   Velocity Vectors & Components

115
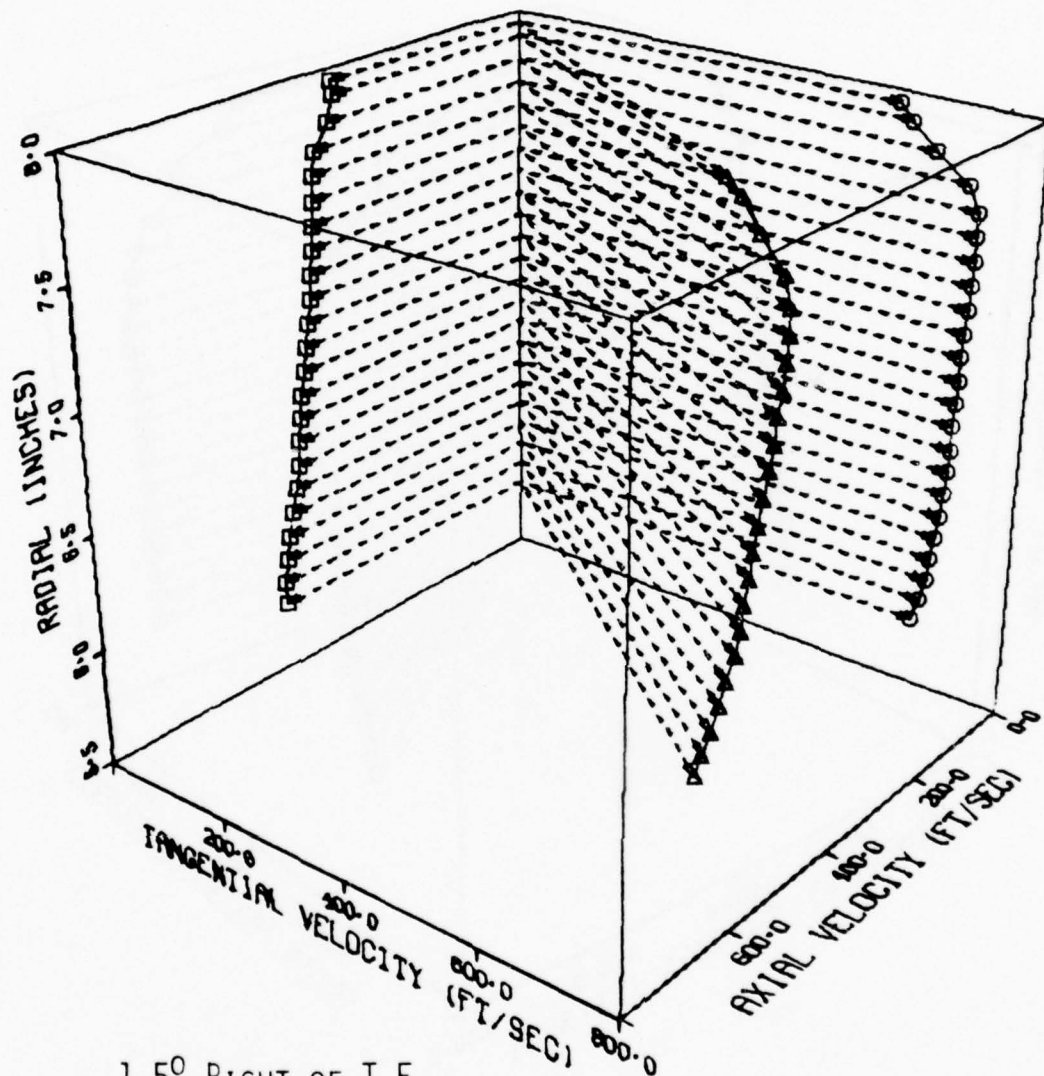
1.5° RIGHT OF T.E.
65° BLADES
STATION 1

Figure 85 Velocity Vectors & Components

116
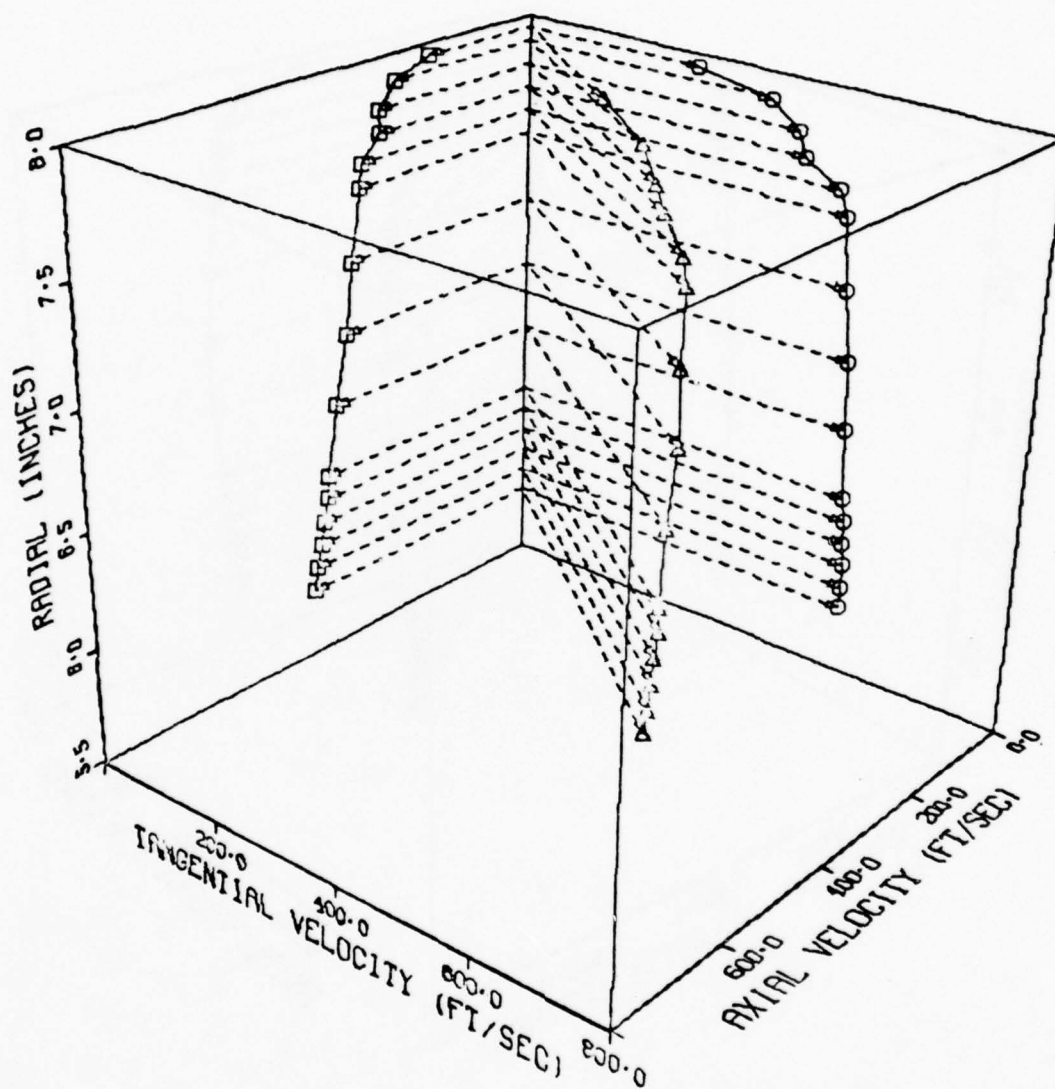
2.5° RIGHT OF T.E.
60° BLADES
STATION 1

Figure 86 Velocity Vectors & Components

117
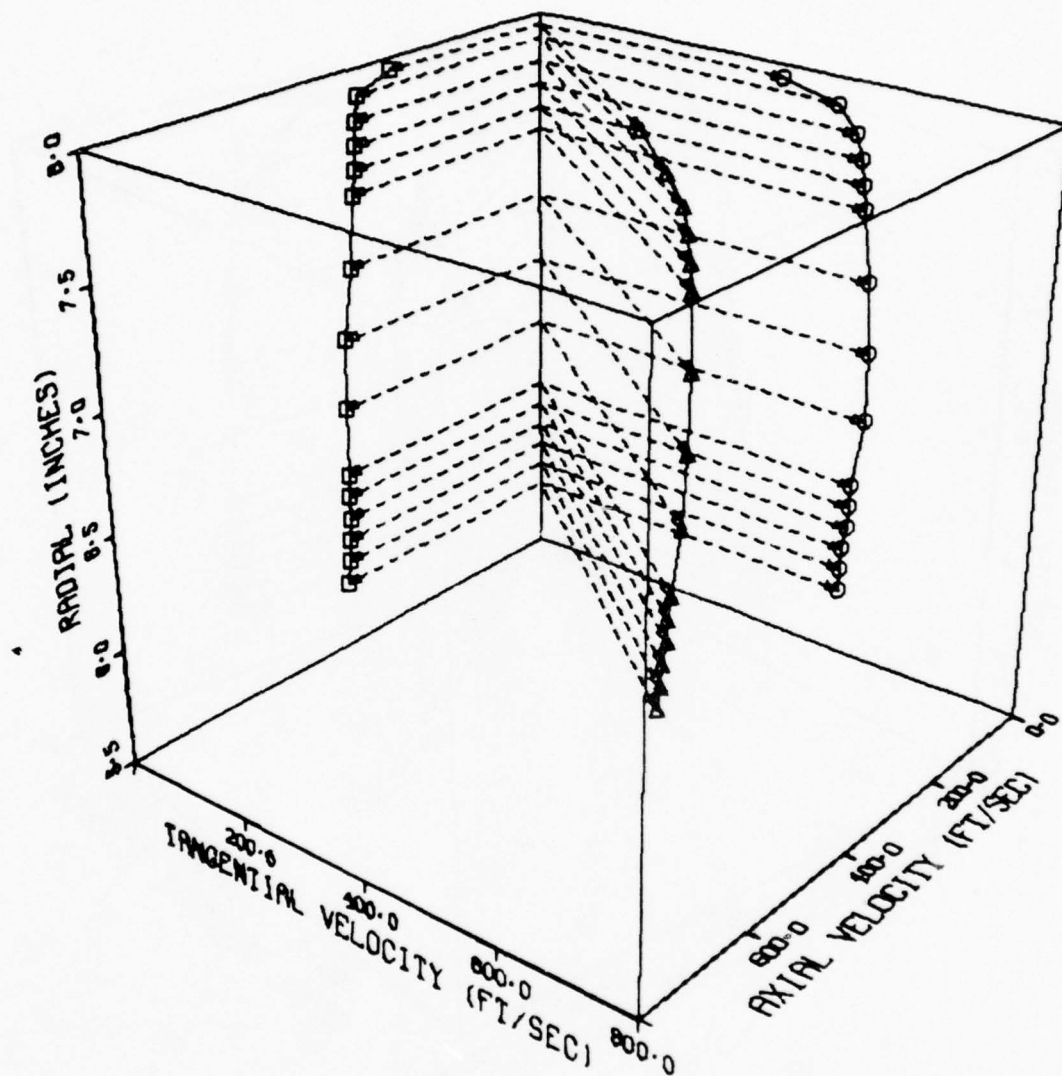
0° RIGHT OF T.E.
60° BLADES
STATION 1

Figure 87 Velocity Vectors & Components

118
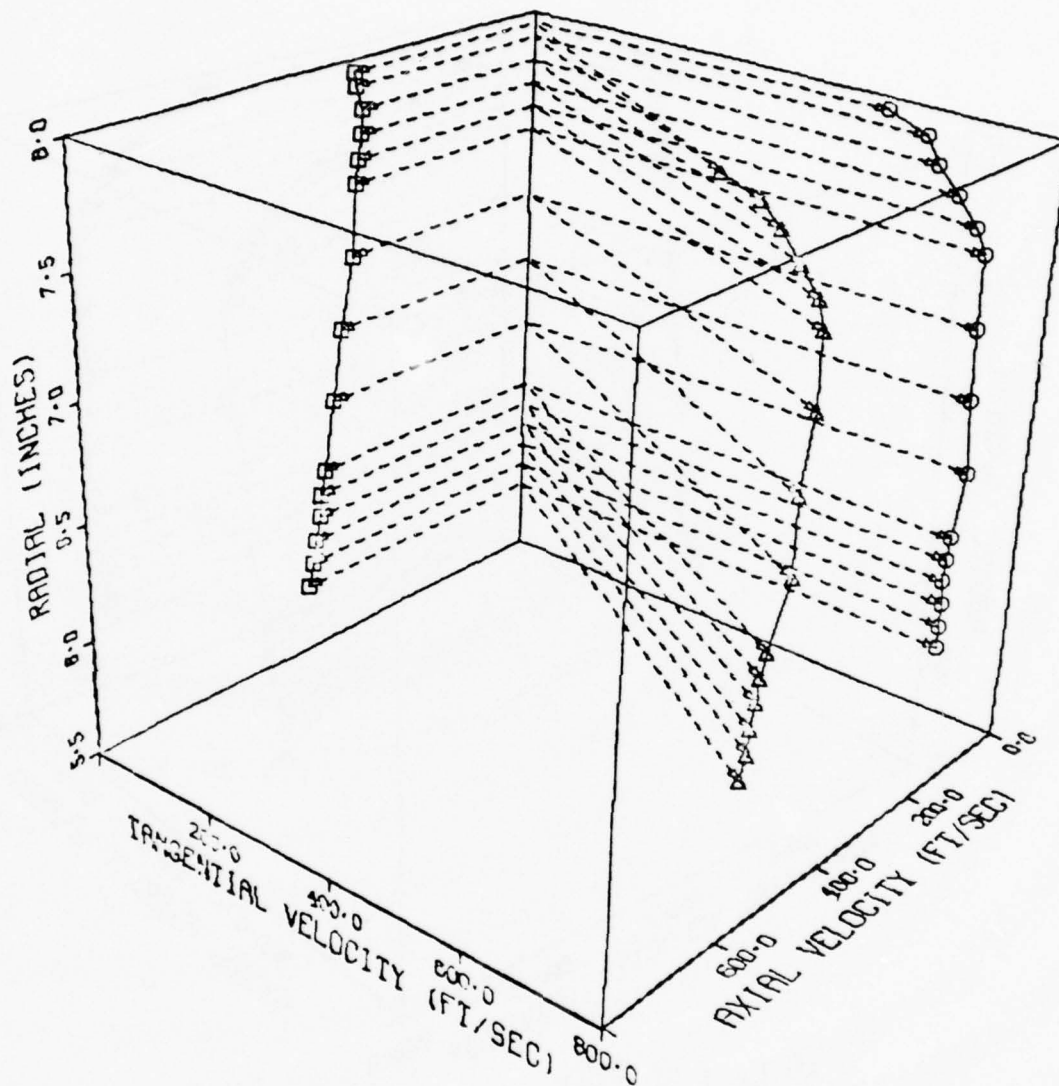
O° RIGHT OF T.F.
69.7° BLADES
STATION 3

Figure 88   Velocity Vectors & Components
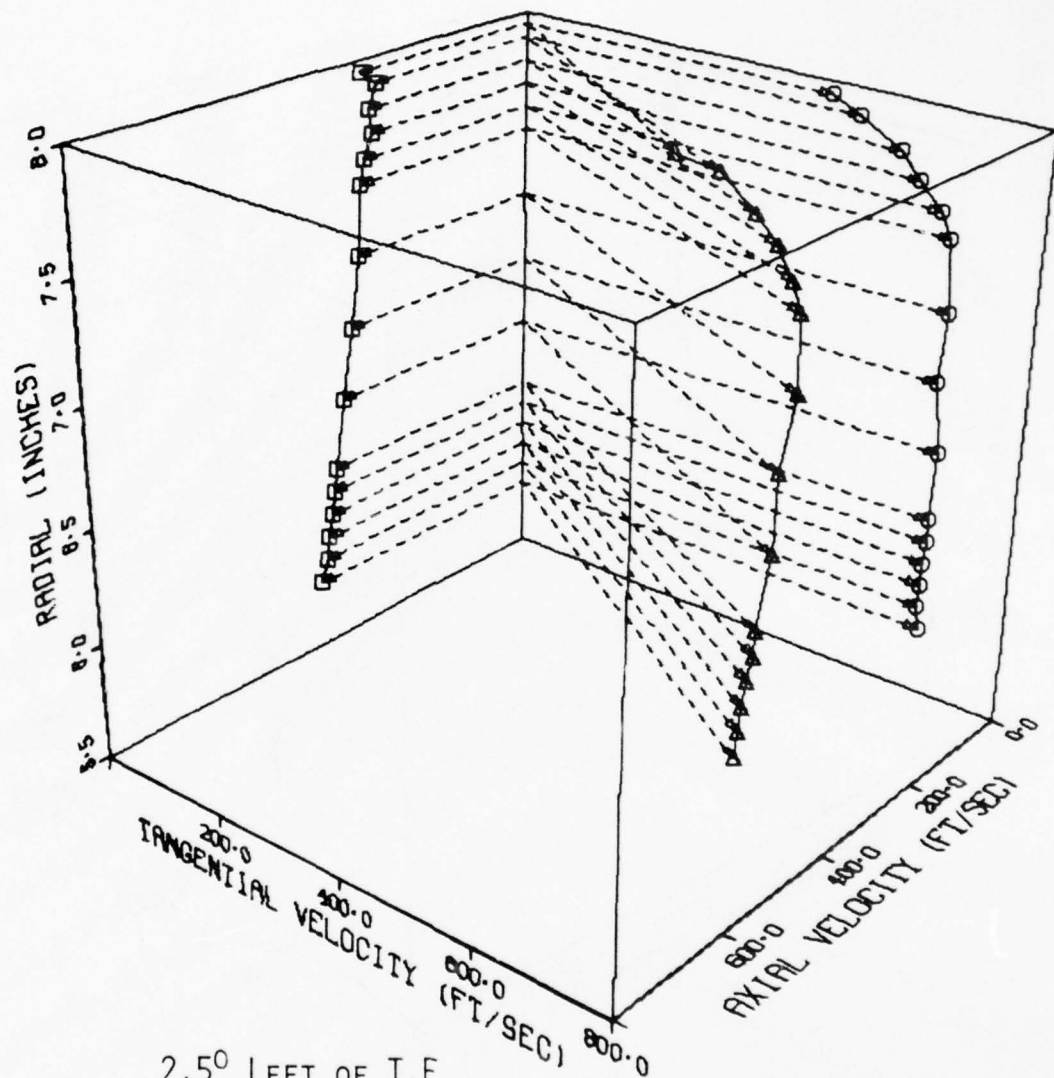
2.5° LEFT OF T.E.
69.7° BLADES
STATION 3

Figure 89   Velocity Vectors & Components

120
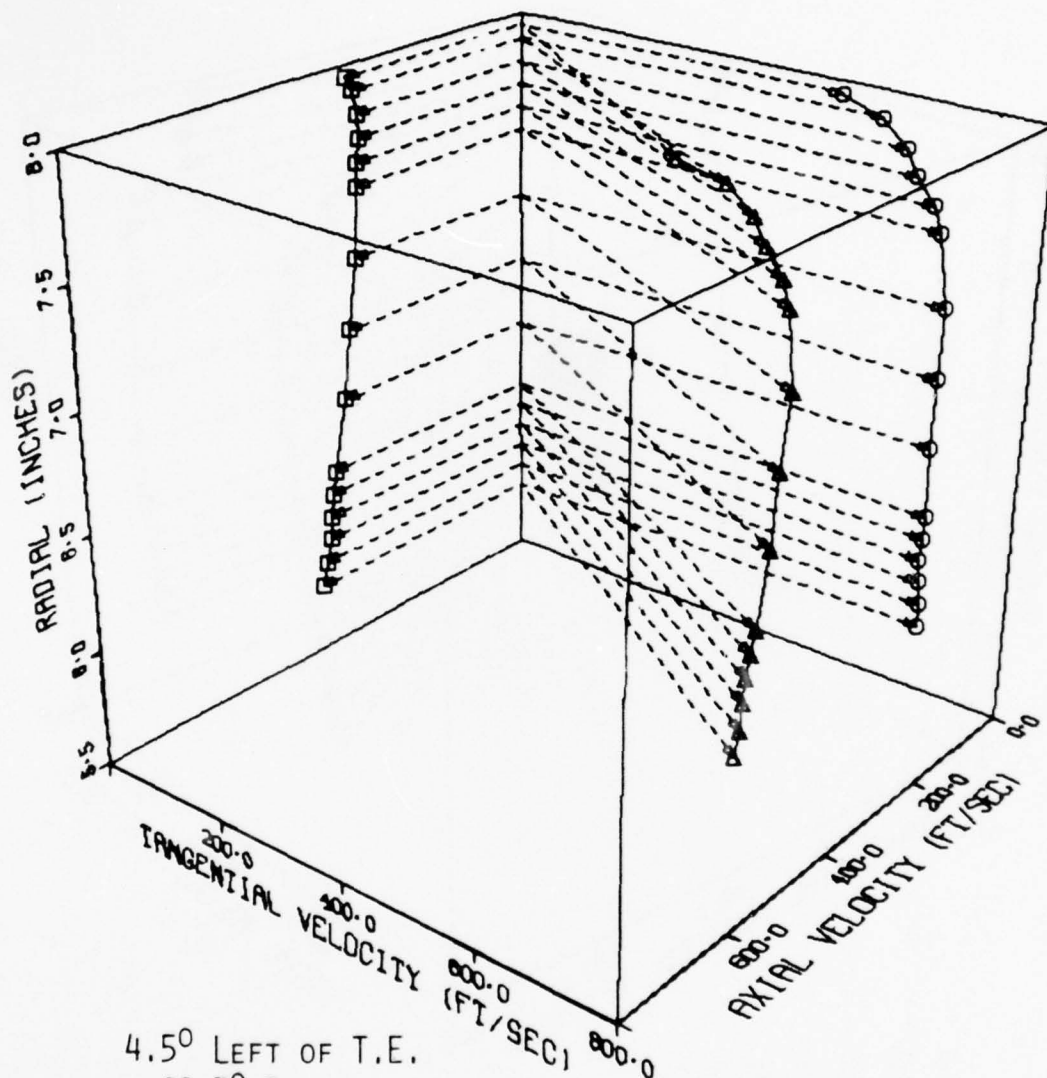
4.5° LEFT OF T.E.
69.7° BLADES
STATION 3

Figure 90   Velocity Vectors & Components

121
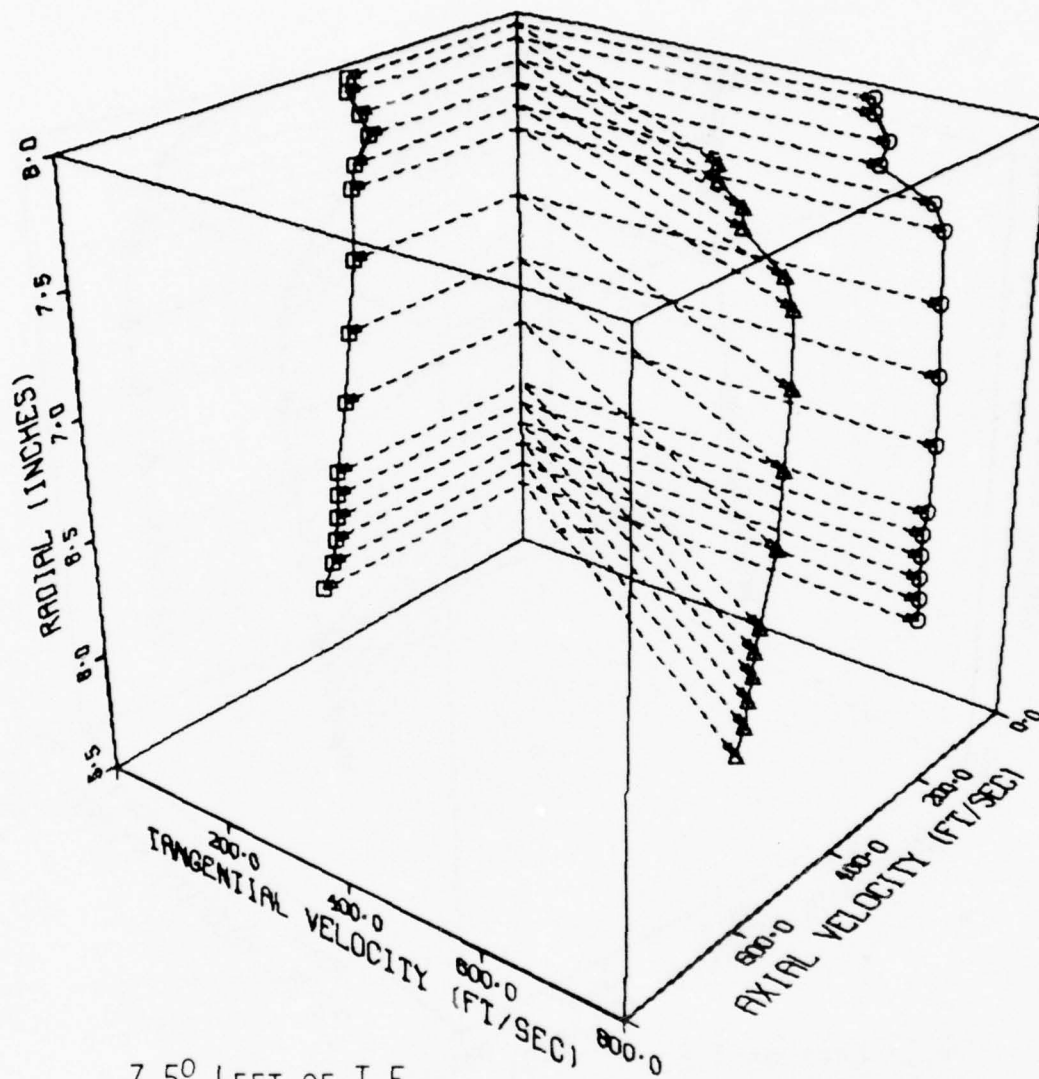
7.5° LEFT OF T.E.
69.7° BLADES
STATION 3

Figure 91   Velocity Vectors & Components

122
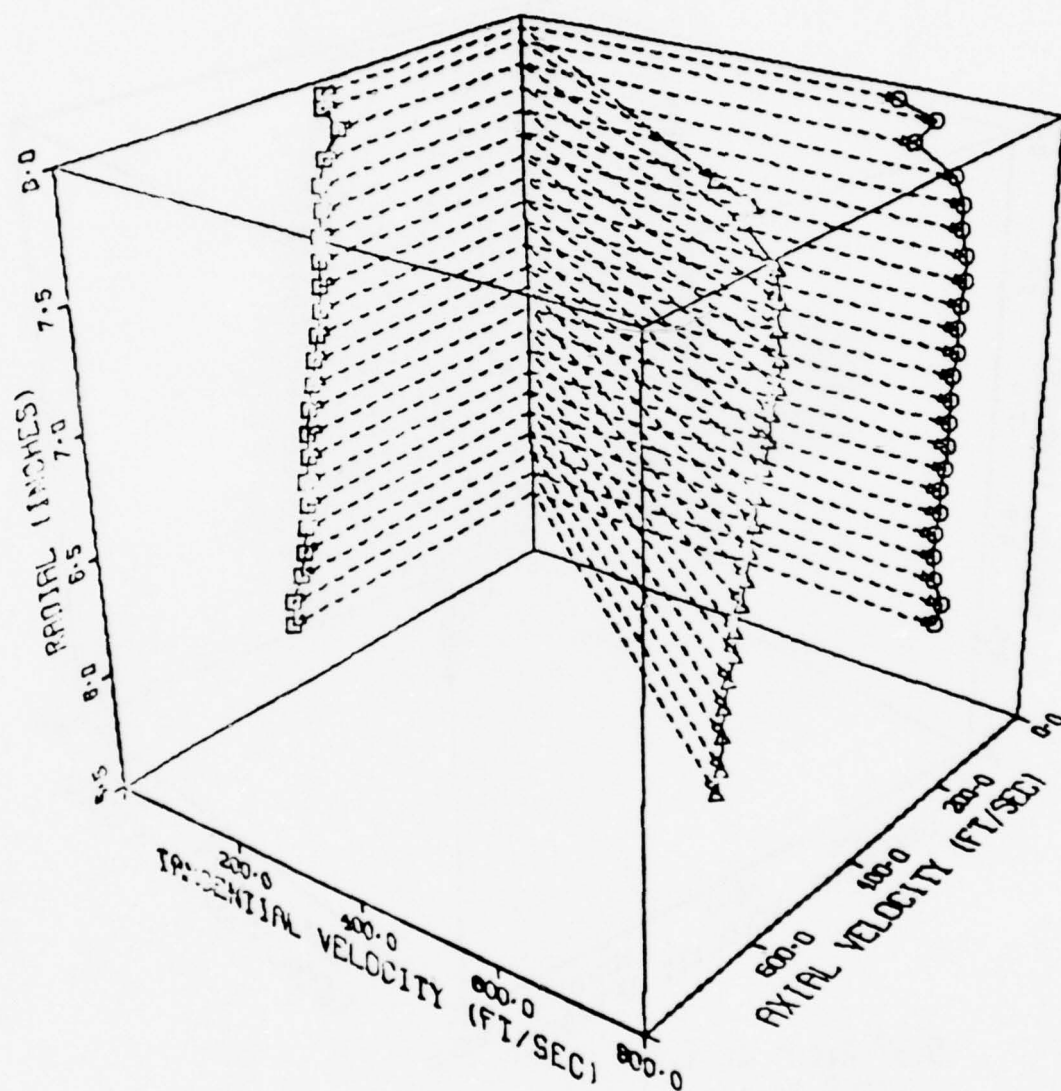
7.5° Right of T.E.
65° Blades
Station 3

Figure 92 Velocity Vectors & Components

123

5.5° RIGHT OF T.E.
60° BLADES
STATION 3
LOW FLOW
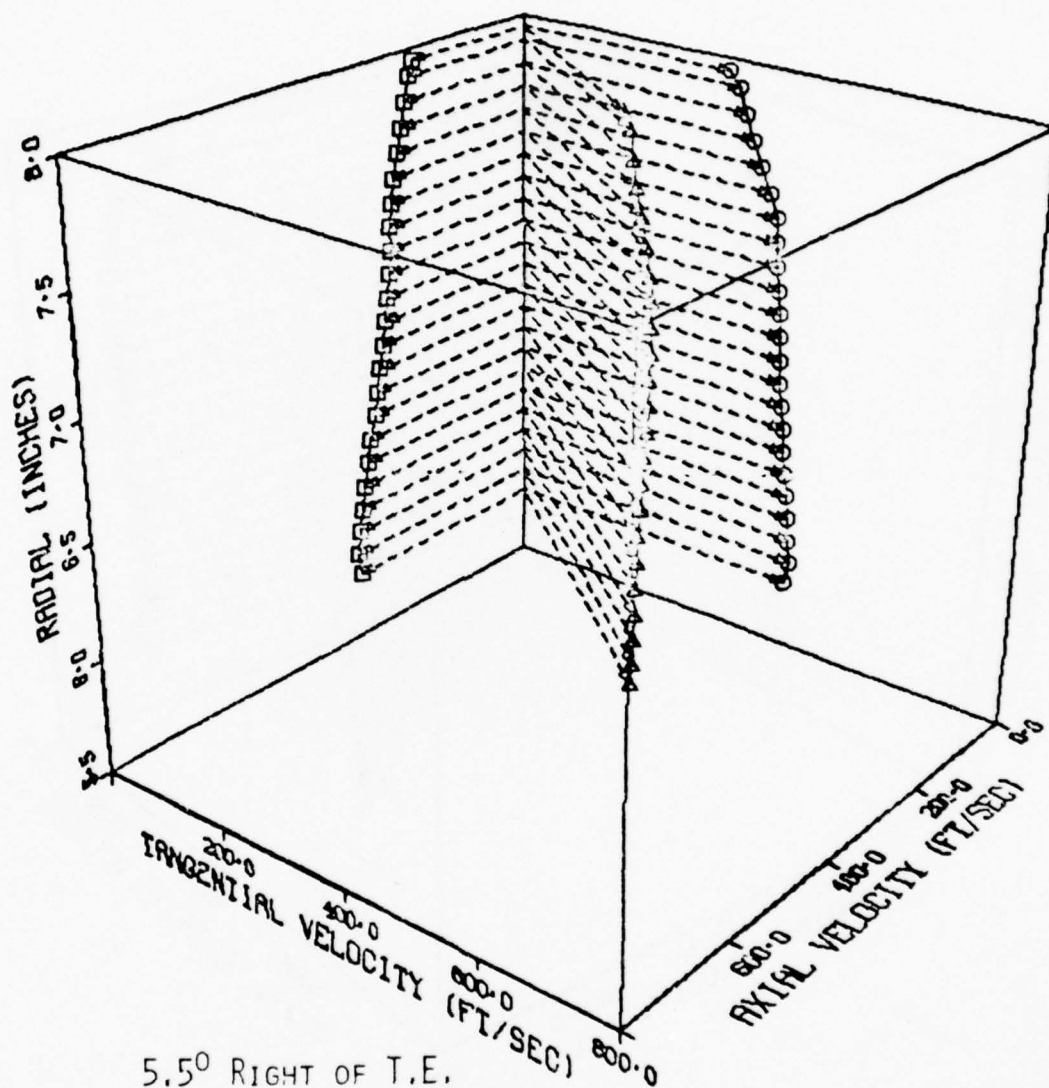
Figure 93 Velocity Vectors & Components
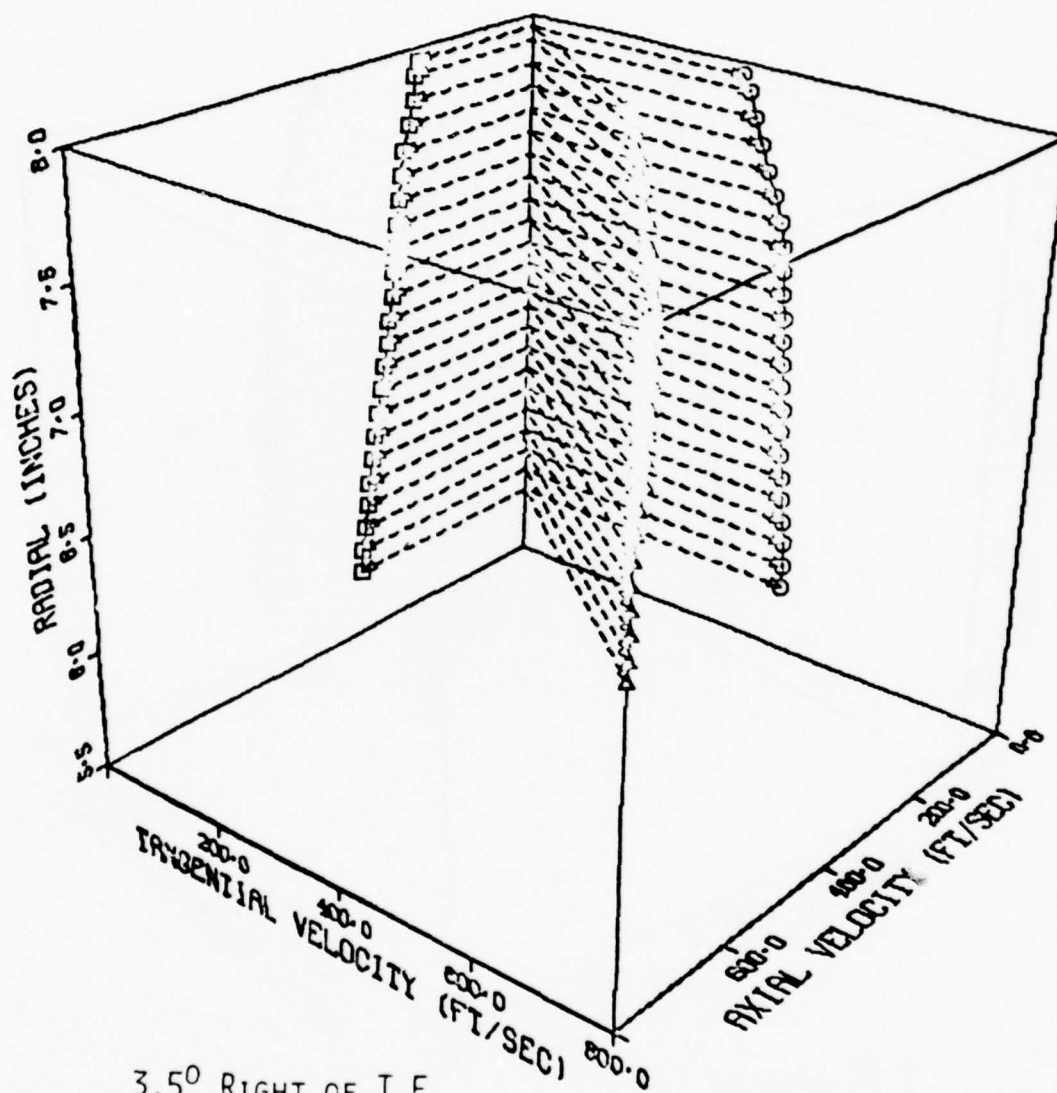
3.5° RIGHT OF T.E.
60° BLADES
STATION 3
LOW FLOW

Figure 94 Velocity Vectors & Components

125

2.5° LEFT OF T.E.
60° BLADES
STATION 3
LOW FLOW
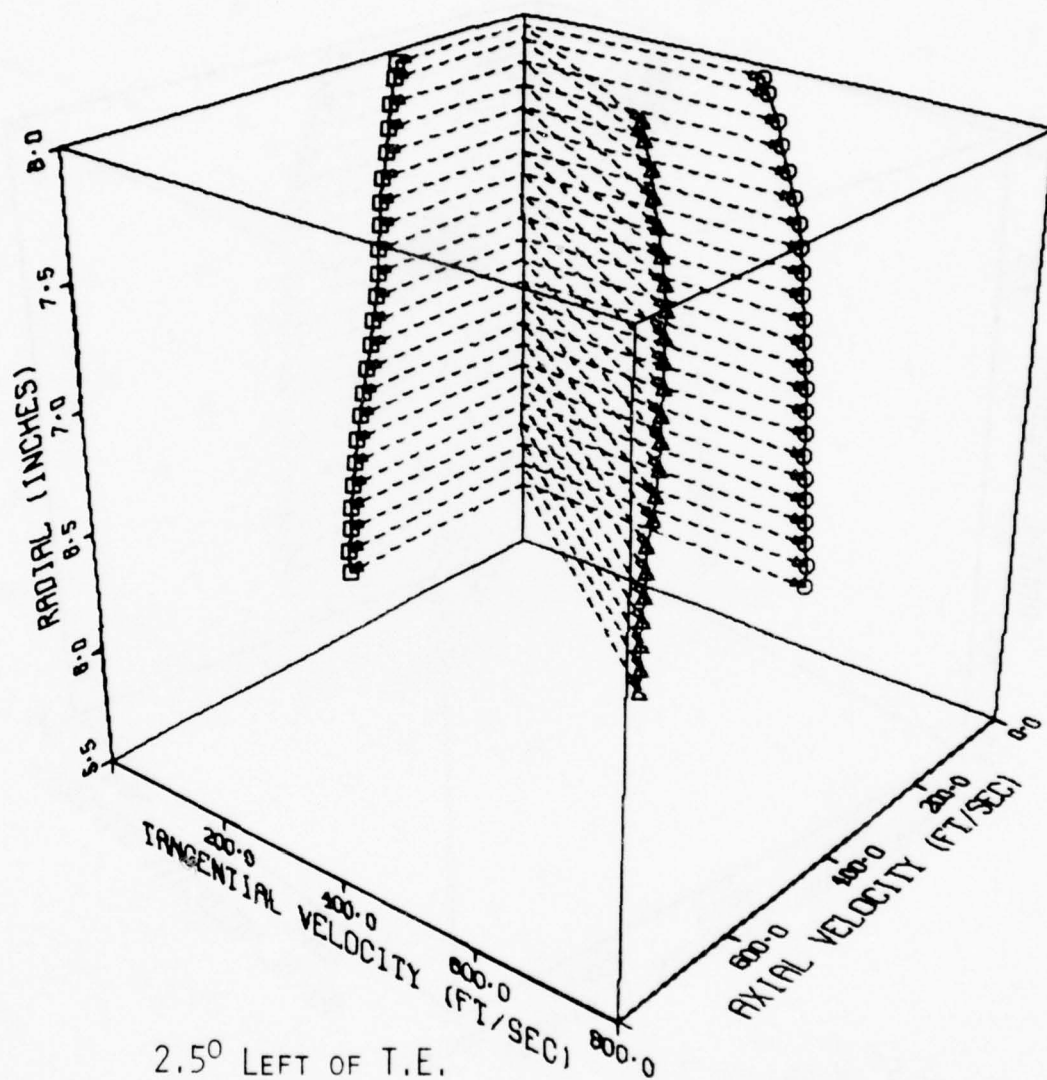
Figure 95   Velocity Vectors & Components

126
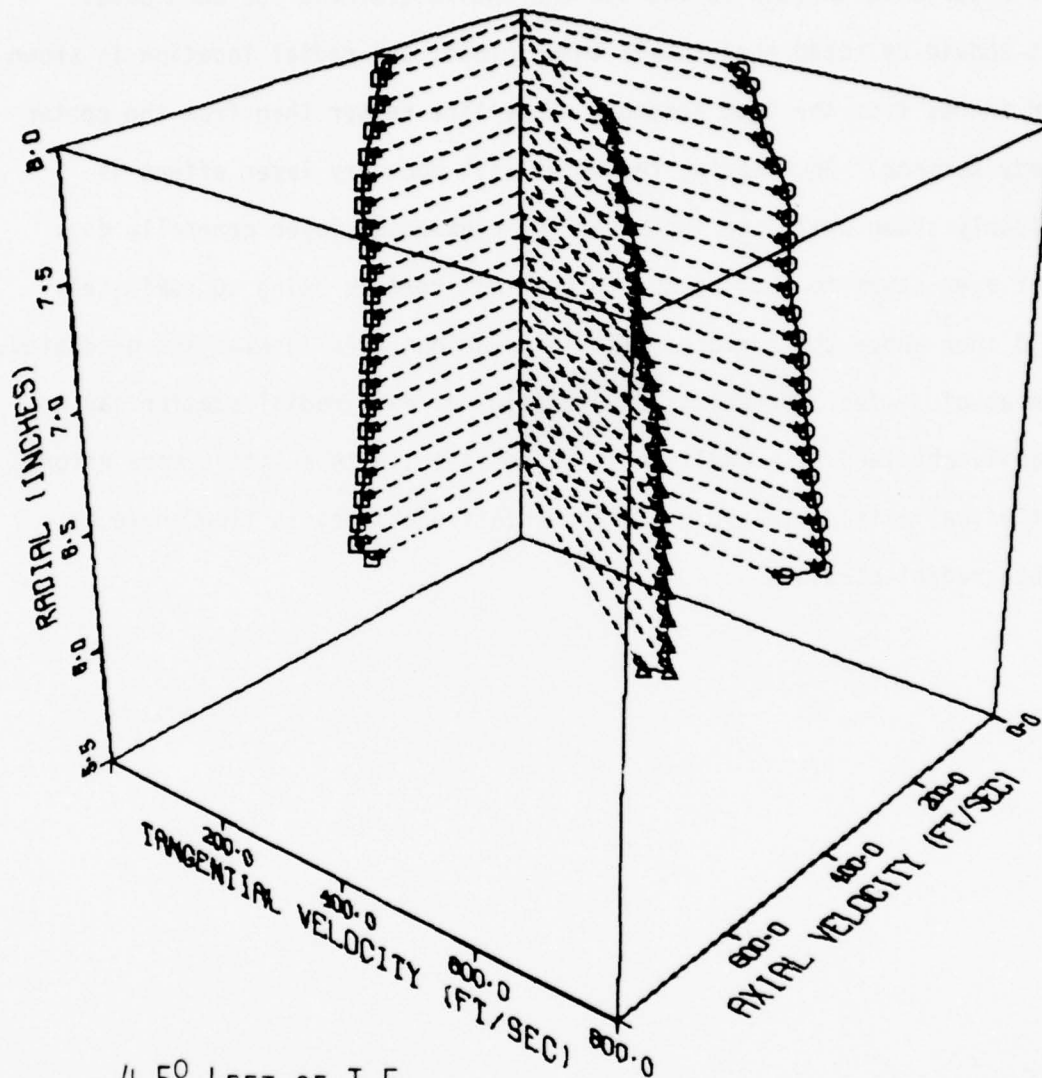
4.5° LEFT OF T.E.
60° BLADES
STATION 3
LOW FLOW

Figure 96 Velocity Vectors & Components

127

The velocity vectors and their axial and tangential components plotted in Figures 70 through 96 include the entire traverse for each case. It should be noted that in all these plots, the radial location is shown in inches from the test assembly centerline rather than from the centerbody surface. Once again, the outer wall boundary layer effect is clearly shown while the inner wall or centerbody layer generally does not even start to show up due to the last reading being approximately 0.3 inch above the surface. With the various axes labeled and graduated, an absolute feel for relative velocities at each radial station can be easily obtained. In addition it is possible, with a little more effort at visualization, to ascertain the relative changes in flow angle at each radial station.

Station 1 - 21 Traverses
69.7° Blade Angle
High Flow
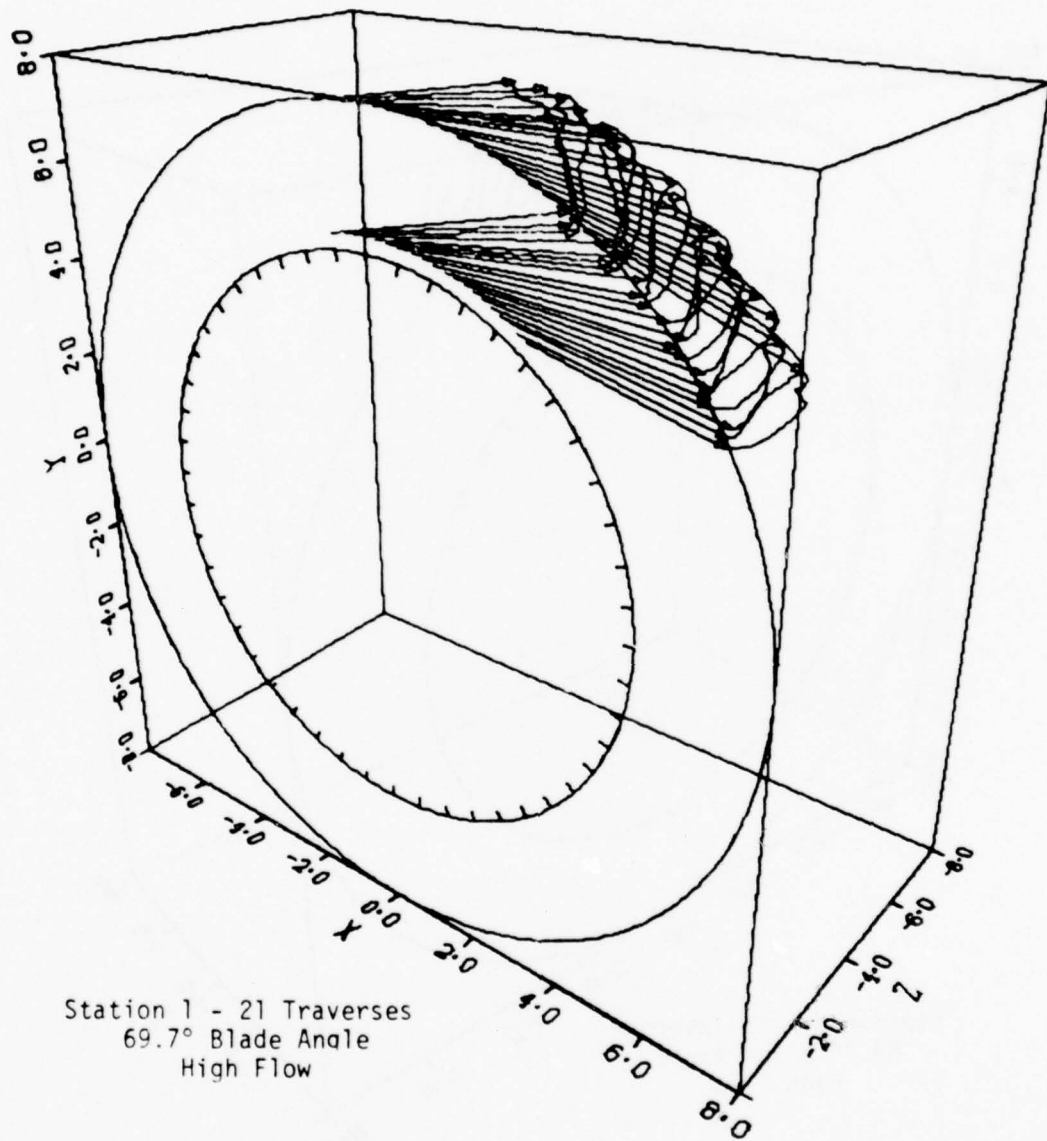
Figure 97 3D Composite of Velocity Profiles

Station 3 - 8 Traverses
69.7° Blade Angle
High Flow
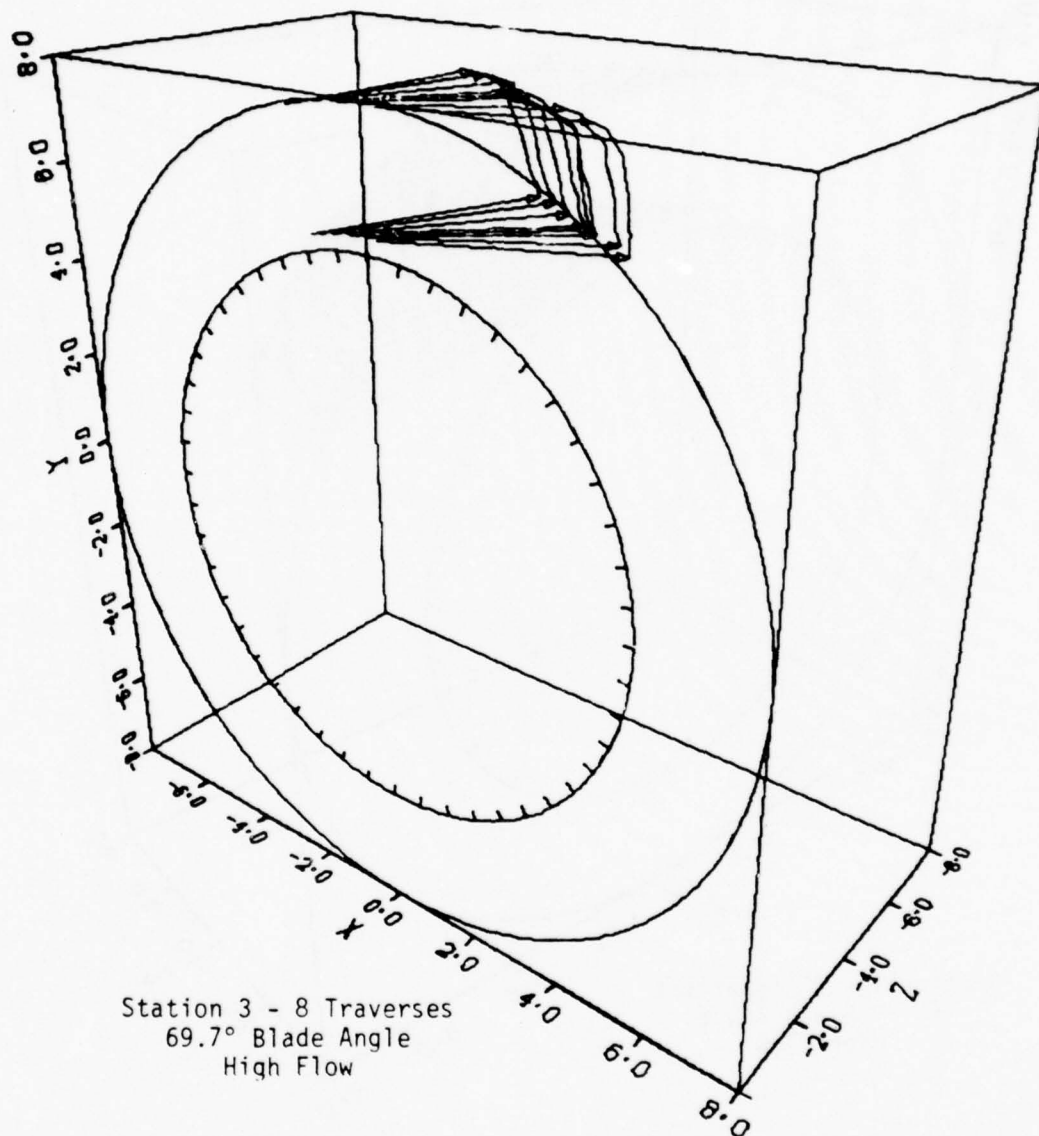
Figure 98   3D Composite of Velocity Profiles

130

Station 1 - 16 Traverses
65° Blade Angle
High Flow
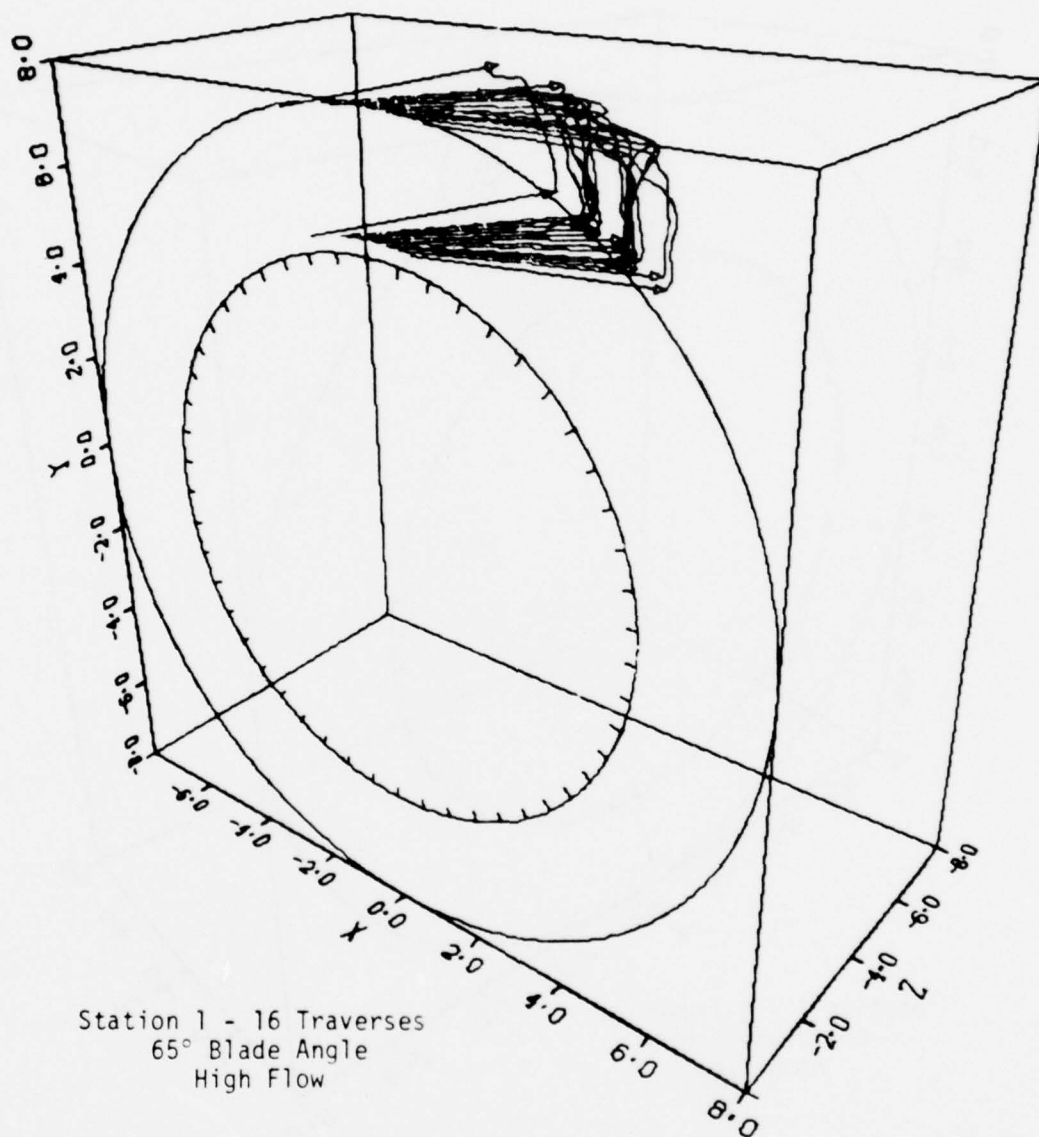
Figure 99 3D Composite of Velocity Profiles

131

Station 1 - 5 Traverses
60° Blade Angle
High Flow
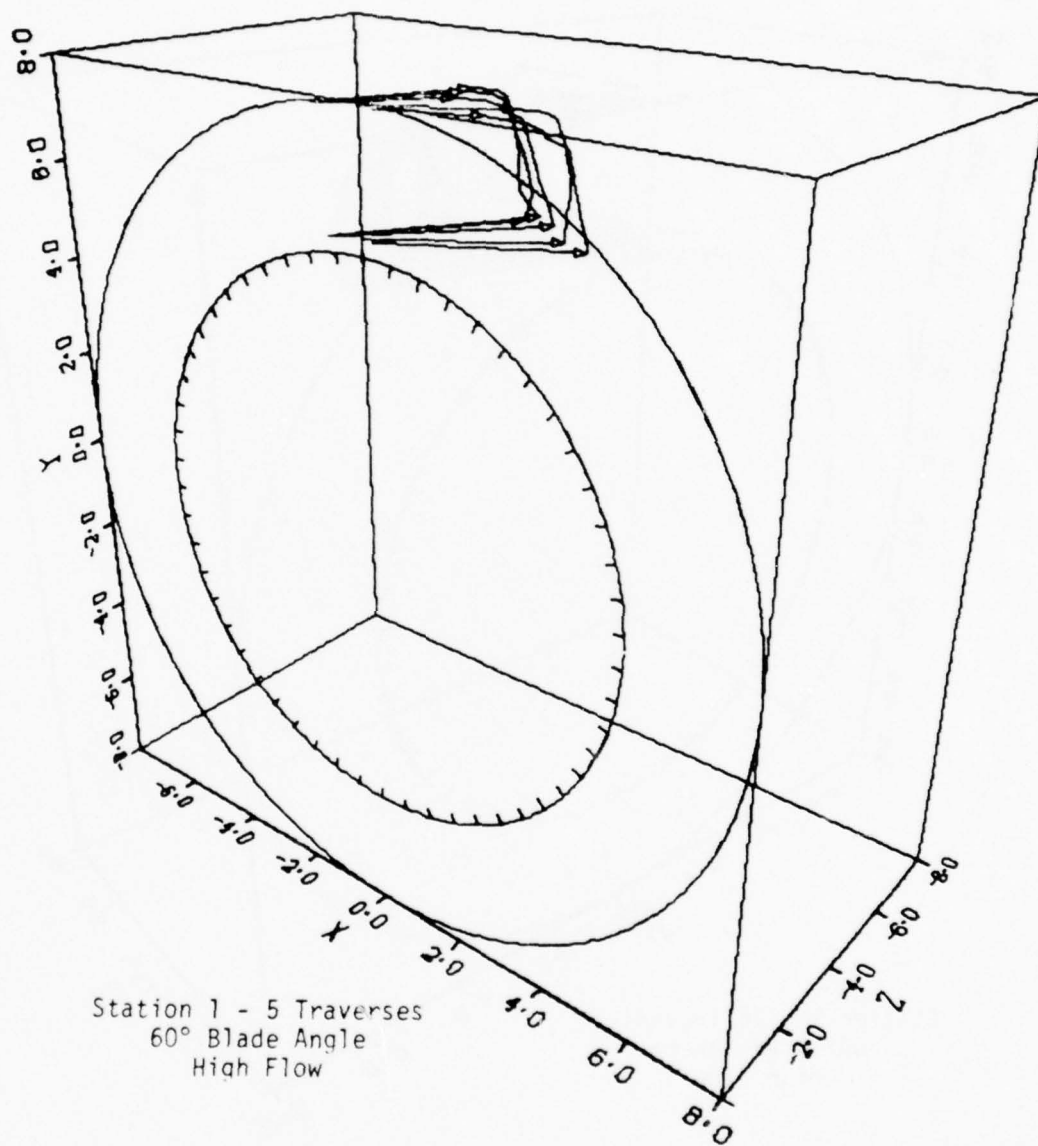
Figure 100 3D Composite of Velocity Profiles

Station 3 - 7 Traverses
60° Blade Angle
Low Flow
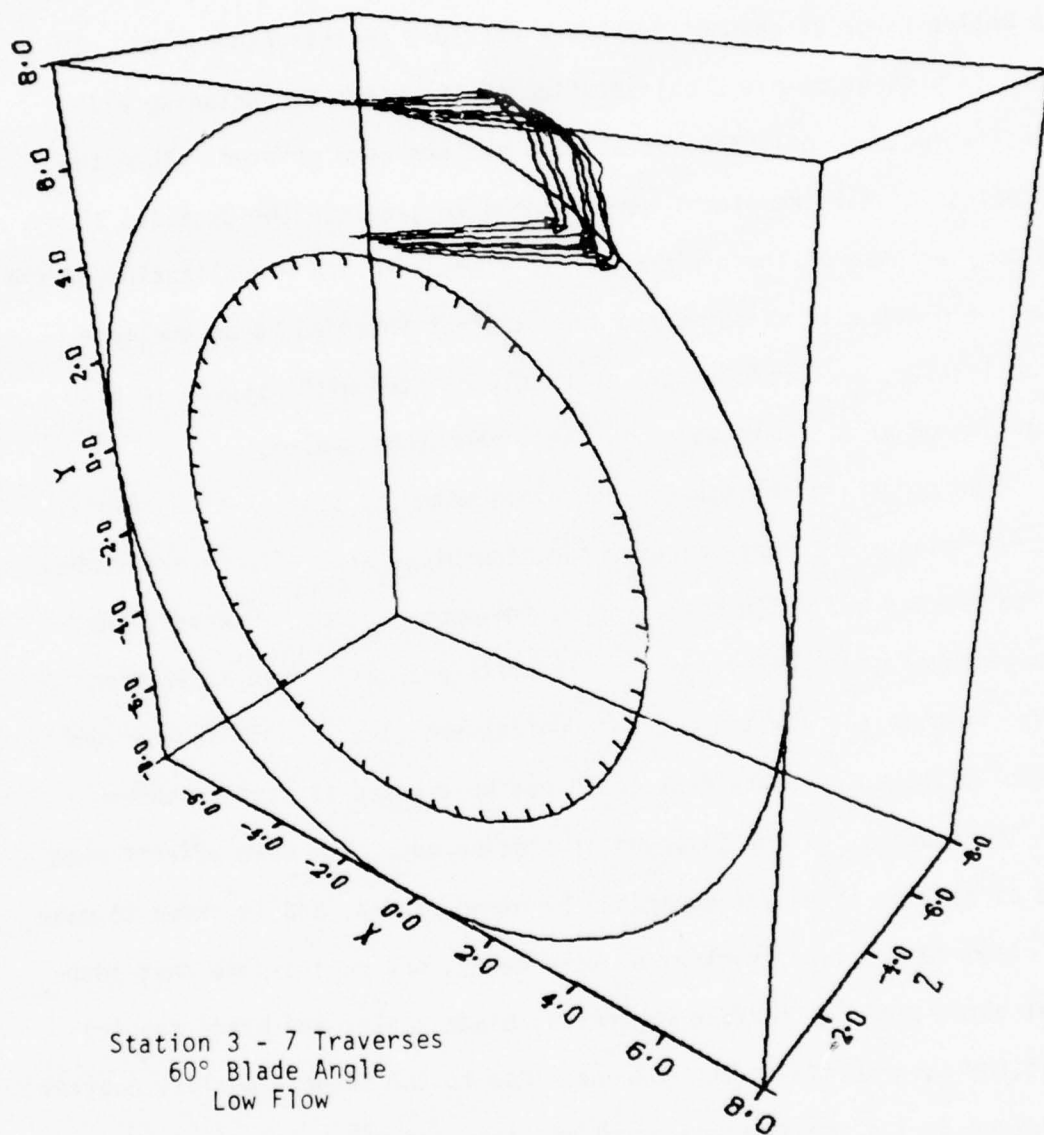
Figure 101 3D Composite of Velocity Profiles

133

The three-dimensional composites of velocity profiles plotted in Figures 97 through 101 incorporate representative runs in each case over the entire range of channel traverses recorded in this experiment. In order to prevent complete obliteration of the views by including all velocity vectors, only the hub and tip vectors were printed. Then the end points of all the others were printed to generate the profiles shown. The only purpose of these plots was to attempt to aid visualization of the flow field actually measured and they are not intended to be scalable directly; i.e. the profiles are correctly plotted with respect to each other but on an absolute velocity basis cannot be scaled.

When comparing the station-one plots with the station-three plots, it becomes apparent that, as expected, the blade wake effects are starting to mix out and while still there, are much reduced. However, any assumption of truly wake free flow is still not valid even at station three. Due to the limited circumferential travel available in the test assembly, the actual wake flow could not be tracked at station three from the specific blades surveyed at station one. The wake effects seen here at station three are generated by other blades, and in order to make any claim to absolute tracking of wake decay, one must assume that identical blade profile, surface roughness, blade angle, and blade spacing exist for every blade in the cascade. Due to the intense quality control exercised during the fabrication of the test assembly, this is considered a reasonable approach with errors induced from these sources to be less than any flow measurement errors.

134
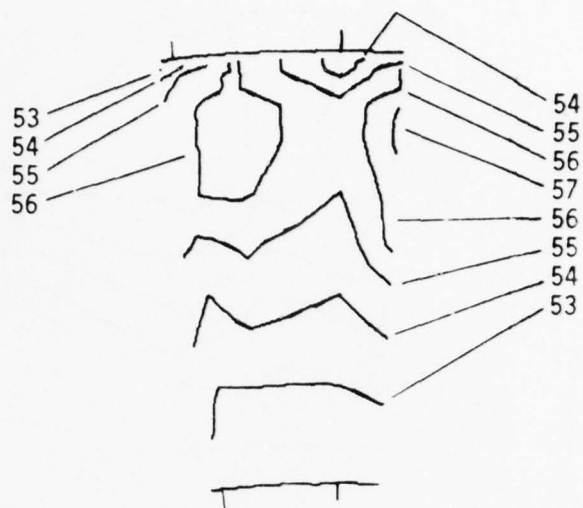
Figure 102 60° Blades, Sta 1

Constant Flow Angle Lines
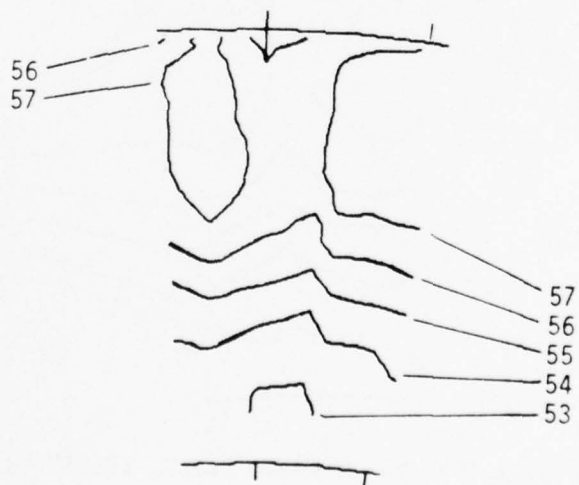
Figure 103 60° Blades, Sta 3, 18.10" Hg

Constant Flow Angle Lines

135
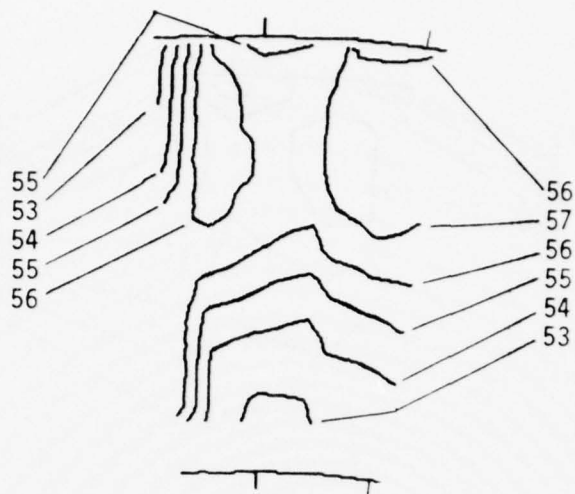
Figure 104 60° Blades, Sta 3, 16.10" Hg

Constant Flow Angle Lines
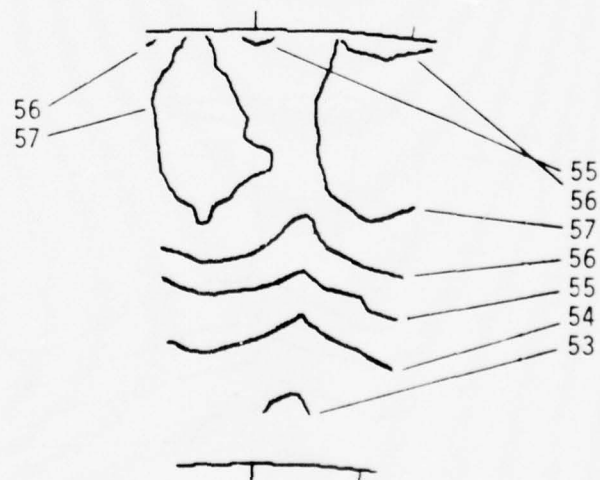
Figure 105 60° Blades, Sta 3, 12.05" Hg

Constant Flow Angle Lines
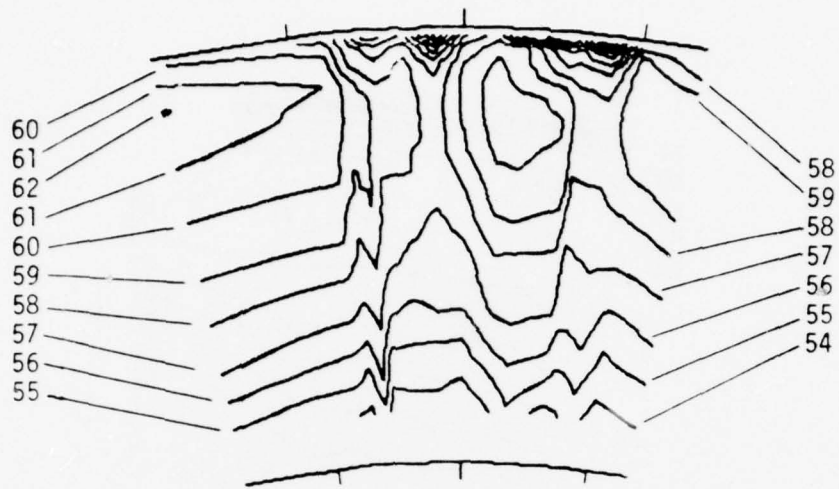
Figure 106 65° Blades, Sta 1

Constant Flow Angle Lines
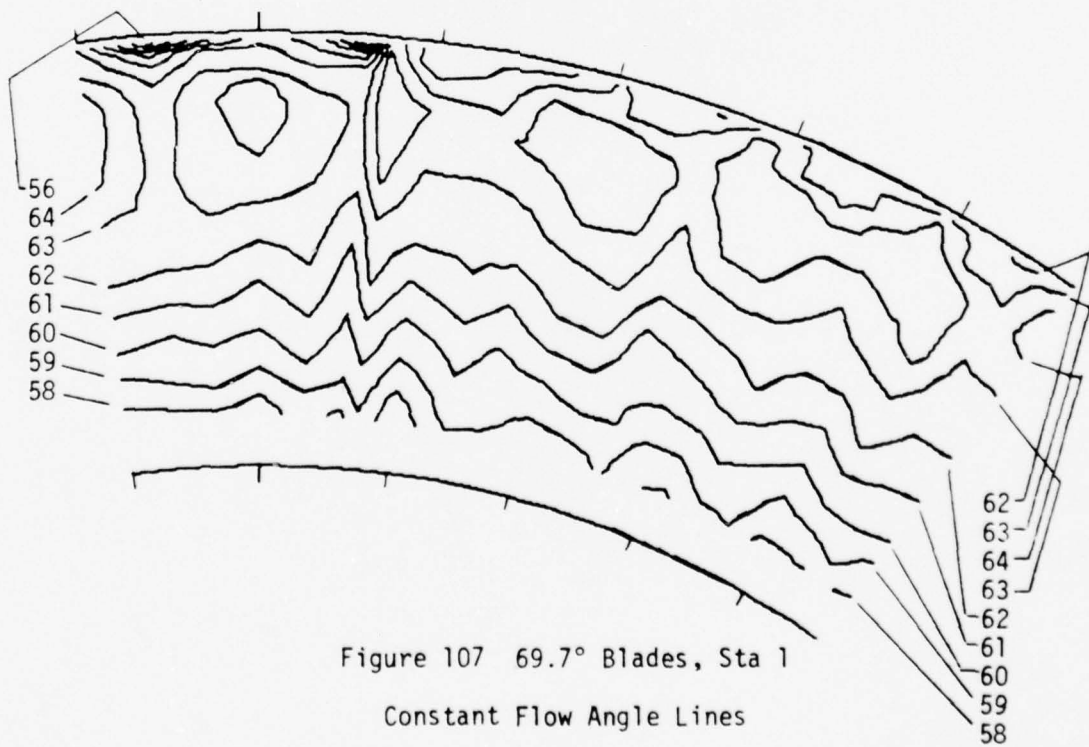
Figure 107 69.7° Blades, Sta 1

Constant Flow Angle Lines

137
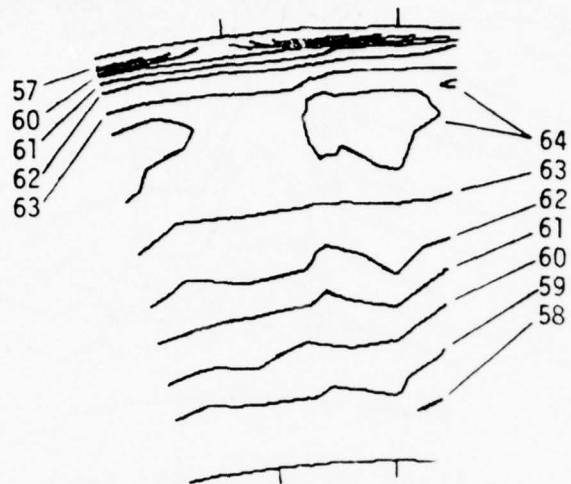
Figure 108   69.7° Blades, Sta 3

Constant Flow Angle Lines

Lines of constant flow angle across the annulus are plotted in Figures 102 through 108. These plots make use of all data taken and the circumferential range surveyed in each case is clear. For reference to the blade row, the tick marks at the hub and tip lines represent blade trailing edges. The pressure readings shown in the titles of Figures 103, 104, and 105 are the receiver pressures and indicate less than maximum flow conditions; i.e. what, in general, were called "low flow" runs during the course of this investigation. These runs were made to gather comparative data to test the notion discussed throughout this dissertation relative to the free vortex being most valid at lower Mach numbers while the Engelman analysis would be most valid at high Mach numbers. In general, the "high flow" runs were conducted with a receiver pressure of 11 inches of Hg absolute or less.

In these plots, the general blade effects can be seen as well as the variation in effect across the channel. The lines are labeled in degrees and, to prevent clutter, several interior islands and lines were not specifically marked. However, simply note that all lines were indexed one degree apart so that any unmarked line can be identified by referring to a nearby marked one. One word of caution in interpreting the plots is in order; i.e. due to the nature of the plotting program, if no data exist in an interval, it merely draws a straight line between the points available. Therefore, these effects must be evaluated accordingly when using the plots, but the presentation in this fashion was considered worthwhile as still another way to gain insight.

A final observation which can be made by comparing the plots for station three with those for station one is that there is very little reduction in flow angle. The axial distance between stations one and

139

three is four inches or approximately 3.2 chords.

In particular, when comparing the 69.7° data shown in Figures 107 and 108, the central channel flow shows no real change at all, and the outer wall boundary layer appears to be growing very slowly.

This growth is evidenced by the reduction in radius at which the flow angle starts to be reduced by the wall boundary layer effect.

In summary, by referring to one or more of these graphical presentation schemes, it is possible to get a clear visualization of the measured flowfield, including a reasonable feel for the absolute value of the flow angles and velocities.

The Reynolds numbers were calculated for representative high and low flow runs over the entire flow range investigated with each set of blades and these results recorded in Appendix I. In each case, both the highest and lowest number achieved are shown. The flow ranges investigated were as shown in Table 14 and the corresponding Reynolds numbers are included for reference. The characteristic dimension used to calculate these Reynolds numbers was twice the channel height (blade span).

Table 14

Flow Ranges Investigated

Blade Angle	Flow Rate Range lb/sec	Reynolds No Range (10^{-6})
69.7°	11.6 - 14.4	1.416 - 1.957
65°	12.8 - 15.5	1.312 - 1.911
60°	13.5 - 16.0	1.151 - 1.566

These rates were calculated based on the traverse data collected, and typical sets of results are shown in Tables 6 through 11. The annulus division into strips for these calculations is shown in Figure 65.

Surface roughness measurements for all parts of the flow path were made with a portable profilometer and these results are recorded in Appendix H. The flow path boundaries are machined aluminum (annulus inner wall), epoxy-varnished mahogany (annulus outer wall) and extruded aluminum (blades). In the case of the blades, the extrusion die marks were, of course, perpendicular to the flow. In general, however, all parts of the flow path were quite smooth mechanically and based on the work of Bammert and Sandstede[25], can be considered hydraulically smooth at the Reynolds numbers achieved in this experiment.

Calculations were then made to compare these measured results with various theoretical treatments and the details of that phase are covered in Chapter IV.

CHAPTER IV
COMPARISON WITH THEORETICAL CALCULATIONS

Theoretical flow angle calculations were made in the following four ways to generate predictions which could be compared with the measured results from this experiment:

(1) Free vortex assumption

(2) Engelman analysis

(3) Two dimensional computer solution

(4) Three dimensional computer solution

All four schemes are discussed in detail below and the comparisons are made following the calculation descriptions. The comparative results are presented in graphical and tabular form as appropriate.

First, a computer program was written to find the theoretical flow angles as a function of pressure ratio and ϕ_*, as predicted by both the free vortex analysis and the Engelman analysis. The angle ϕ_* is defined as the flow angle where Mach number equals one.

The governing equation for angles as predicted by Engelman's analysis is:

$$\frac{\cos \phi_*}{\cos \phi} = M \left[\frac{k+1}{2 + (k-1)M^2} \right]^{\frac{k+1}{2(k-1)}} \tag{4.1}$$

142

This equation can be obtained by use of the following method:

Substituting the equation for the geometric relationship as defined by
Figure A-1 in Appendix A

$$V_z = V\cos\varphi \tag{4.2}$$

into the continuity equation

$$\rho V_z = \rho_\star V_{z_\star} \tag{4.3}$$

and rearranging

$$\frac{\cos \varphi_\star}{\cos \varphi} = \frac{\rho V}{\rho_\star V_\star} \tag{4.4}$$

Substituting the following isentropic relationships

$$V = M \sqrt{g_c\, k\, \frac{p}{\rho}} \tag{4.5}$$

$$\frac{\rho}{\rho_o} = \left(\frac{p}{p_o}\right)^{1/k} = P^{1/k} \tag{4.6}$$

into equation (4.4) and rearranging

$$\frac{\cos \varphi_\star}{\cos \varphi} = \frac{M}{M_\star} \left[\frac{P}{P_\star}\right]^{\left(\frac{k+1}{2k}\right)} \tag{4.7}$$

Substituting the following isentropic relationships

$$\frac{p_\star}{p_o} = \left[\frac{2}{k+1}\right]^{\left(\frac{k}{k-1}\right)} = P_\star \tag{4.8}$$

$$\frac{p}{p_o} = \left[1 + \left(\frac{k-1}{2}\right) M^2\right]^{\left(\frac{k}{1-k}\right)} = P \tag{4.9}$$

into equation (4.7) and evaluating at $M_\star = 1$, equation (4.1) is obtained.
In this equation M is the Mach number and φ is the predicted angle.

143

Then, assuming $k = 1.4$, and solving equation (4.1) for ϕ and equation (4.9) for M gives

$$\phi = \cos^{-1}\left[\frac{\cos \phi_\star}{M}\left(\frac{2 + 0.4\, M^2}{2.4}\right)^3\right] \tag{4.10}$$

$$M = \sqrt{5\left[\left(\frac{1}{P}\right)^{.2857} - 1\right]} \tag{4.11}$$

Finally, combining (4.10) and (4.11) gives

$$\phi = \cos^{-1}\left\{\frac{\cos \phi_\star}{\sqrt{5\left[\left(\frac{1}{P}\right)^{.2857} - 1\right]}}\left[\frac{2 + .4\left[5\left\{\left(\frac{1}{P}\right)^{.2857} - 1\right\}\right]}{2.4}\right]^3\right\} \tag{4.12}$$

FREE VORTEX ANALYSIS

For the Free Vortex Analysis, the governing equations for flow angles obtained in Appendix A are:

$$\phi = \sin^{-1}\left\{\frac{\sin \phi_\star}{\frac{r}{r_\star}\sqrt{\left[1 - P^{\left(\frac{k-1}{k}\right)}\right]\frac{k+1}{k-1}}}\right\} \tag{4.13}$$

where,

$$\frac{r}{r_\star} = \sqrt{\frac{1}{1 - \frac{(k+1)\, P^{\left(\frac{k-1}{k}\right)} - 2}{(k-1)\sin^2 \phi_\star}}} \tag{4.14}$$

144

Combining (4.13) with (4.14) for k = 1.4 gives:

$$\phi = \sin^{-1}\left\{\sqrt{1 - \frac{6P^{.2857} - 5}{\sin^2 \phi_\star}}\left[\frac{\sin \phi_\star}{\sqrt{6\left(1 - P^{0.2857}\right)}}\right]\right\}$$

(4.15)

Equations (4.12) and (4.15) are both functions of P and $\phi_\star$. In Figures 109 and 110, the flow angles are plotted as a function of channel position. A value of $\phi_\star$ was calculated and used as a constant parameter. Then the measured pressure ratio at a particular channel position was used to find the theoretical ϕ values for both the Free Vortex analysis and the Engelman analysis. The calculation of $\phi_\star$ for Figure 109 was made as follows:

continuity of axial mass flow requires,

$$\rho V_z = \rho_\star V_\star \cos \phi_\star$$

(A.32)

so that

$$\cos \phi_\star = \frac{\rho}{\rho_\star} \frac{V_z}{V_\star}$$

(4.16)

Using the mid-channel data obtained at this station and the isentropic compressible flow functions from Table 30 of the Gas Tables by Keenan and Kay[27, pp. 139, 140], a value for $\cos \phi_\star$ can be found as follows:

At

$$M = 1 \quad \frac{\rho_\star}{\rho_t} = 0.63394$$

and at

$$M = 0.7 \quad \frac{\rho}{\rho_t} = 0.79159$$

so

$$\frac{\rho}{\rho_\star} = \frac{.79159}{.63394} = 1.249$$

145

then

$$\frac{1.249\ V_z}{V_\star} = \cos \phi_\star$$

From the reduced data,

$$V_z = 362 \text{ ft/sec and } T_t = 542°R$$

Again, from the Gas Tables,

$$\text{at M} = 0.7 \ \frac{T}{T_t} = 0.91075$$

So

$$T = (0.91075)\ (542) = 493.6°R$$

Hence

$$V_\star = 49.02 \quad T = 493.6 \text{ (ref)} = 1089 \text{ ft/sec}$$

Substitution into eq (4.16) yields

$$\cos \phi_\star = \frac{(1.249)\ (362)}{1089} = 0.41519$$

thus

$$\phi_\star = 65.5°$$

A similar calculation for conditions of Figure (110) yields $\phi_\star = 70°$.

As can be seen from these plots, the Engelman solution more nearly approximates the measured real flow field at high Mach numbers than does the free vortex solution.

146
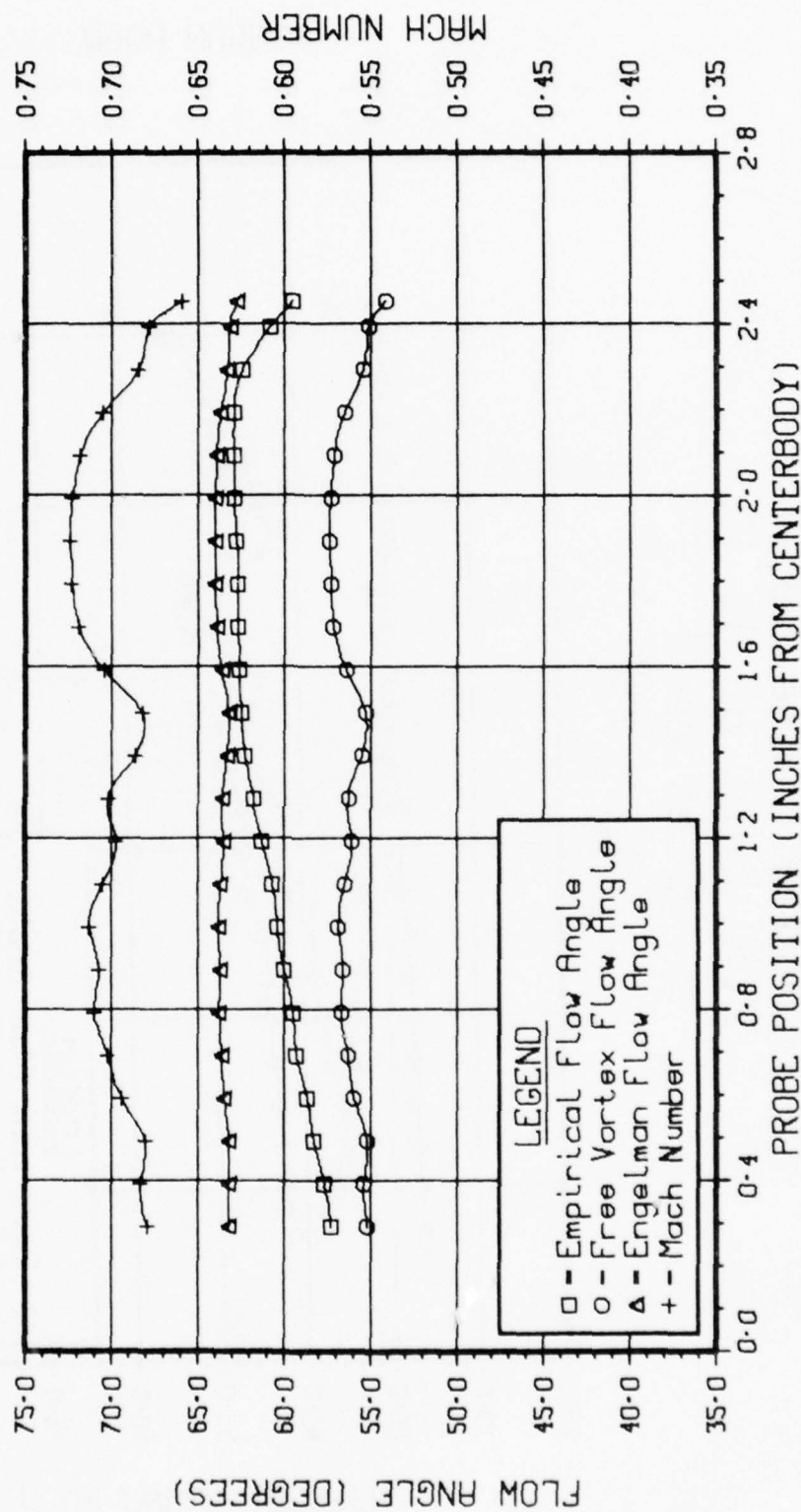
Figure 109 Flow Angle VS Probe Position

147

Blade Angle 69.7°
2.9° Left of T. E.
Station 1
$\phi_x = 70°$

LEGEND
□ − Empirical Flow Angle
○ − Free Vortex Flow Angle
▲ − Engelman Flow Angle
+ − Mach Number

PROBE POSITION (INCHES FROM CENTERBODY)

MACH NUMBER

FLOW ANGLE (DEGREES)
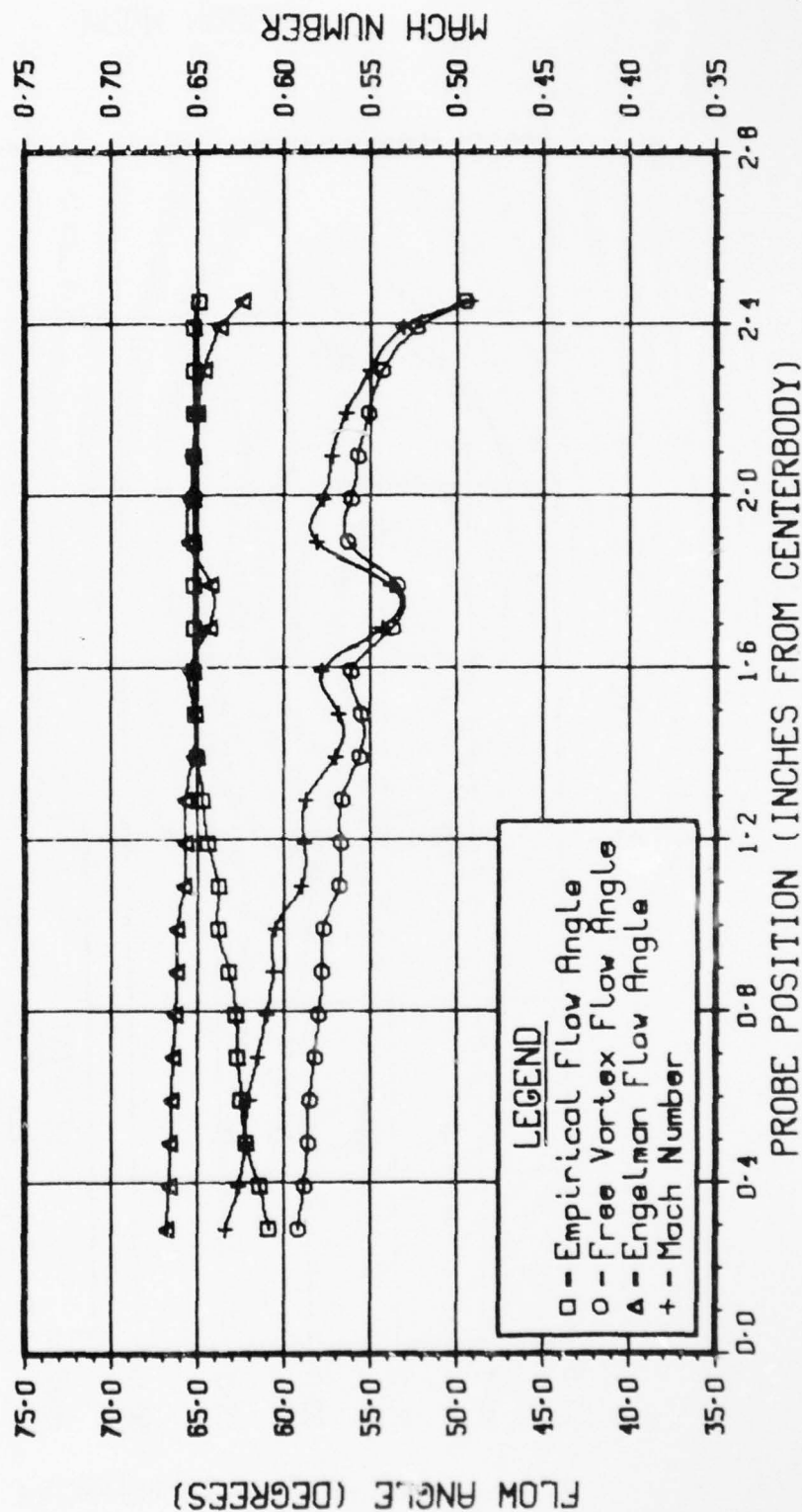
Figure 110   Flow Angle VS Probe Position

148

Next, in order to permit a comparison of the data resulting from
this experiment with current computerized analytical prediction techniques,
both two-dimensional and three-dimensional treatments were applied to the
cascade flow path. These programs were developed under contract to the
Air Force Aero Propulsion Laboratory Turbine Engine Division and are being
routinely applied to advanced design efforts. As with all analytical
schemes, certain assumptions must be made to permit the calculations to
proceed or to minimize computer time requirements. Therefore, the appli-
cation of these programs to this experimental work was an excellent addi-
tional opportunity to compare predictions with the measured data. The
two-dimensional program was prepared by Wysong[26] of the General Electric
Company and the three-dimensional program was prepared by Dodge[16] at the
Garrett Corporation. The results of this activity are presented
sequentially below.

The Turbine Design System (TDS) developed by Wysong[26] at the
General Electric Company includes various modules, each of which specifi-
cally addresses a major component of the overall design process. Its
primary overall purpose is to provide a preliminary design tool and is
set up as an interactive scheme intended for use on a terminal equipped
with a cathode ray tube and a hard-copy device. For the purpose of com-
parison with the data from this experiment the CASC Module was exercised
for two representative cases. The following description of the workings
of this module is quoted directly from Wysong[26]:

> "The CASC module performs a blade-to-blade flowfield analysis
> on a cascade of airfoil contours for the purpose of determining
> Mach number and pressure distributions on the airfoil surfaces.

149

These distributions provide the basic ingredients for evaluating blade section performance and for predicting blade heat flux rates.

"The streamline curvature technique (SLC) is used to solve the steady, compressible, inviscid flow equations. The calculation domain (Fig. 8) is a lamina of varying thickness conforming to the shape of an axisymmetric meridional stream surface which cuts the blade. Within this lamina, a number of confluent stream-tubes are bound together to obtain the total flow in the blade-to-blade passage. This binding of stream-tubes is accomplished by a grid of streamlines and orthogonal lines which provides the basic structure for the computing procedure. SLC has been found to be an accurate method even for coarse grids. The accuracy accrues from the SLC formulation, which is imbedded in a natural intrinsic coordinate system, and is enhanced by the fact that the cross-stream velocity distribution utilizes airfoil surface curvatures as boundary information.

"The CASC version of SLC employs "type-dependent differencing" to account for subsonic and supersonic flow regimes and a direct matrix solution for reliable convergence. Repeating boundary conditions are enforced outside of the "covered" blade-to-blade passage. The governing equations include centrifugal and Coriolis force terms, hence, both stationary and rotating blade rows can be treated.

"A brief description of the solution is as follows. An initial, approximate grid of streamlines and orthogonals is established.

150

Streamline curvature is evaluated at each grid point. The
Crocco form of the momentum equation is integrated along
orthogonals to obtain cross-stream velocity variations and the
continuity equation is integrated along orthogonals to determine
corrected streamline positions for the current curvature field.
Entropy and rothalpy are held constant in the streamwise
direction. Grid point adjustments are calculated by considering
the difference between computed and current streamline positions
and the effect of the implied curvature modification on the
integrated momentum equation. The streamlines are then reposi-
tioned according to the calculated adjustments. The process is
repeated until the maximum calculated point adjustment is less
than a prescribed tolerance.

"Since the movement of any one grid point alters the velocities
at nearby points through a change in curvatures, the point
adjustments throughout the field are made simultaneously through
a direct matrix solution. This departure from classical stream-
line curvature methods accounts for the rapid convergence
characteristics of SLC.

"Input to CASC falls into two categories. The first is geo-
metric data which include grid formation parameters, blade
section surface coordinates and slopes, and meridional surface
definition, all of which come from the BLDDES module results.
The second category is aerothermodynamic data which include gas
angles, inlet Mach number, inlet total pressure, inlet total
temperature, and downstream static pressure. All of these come

151

from the ATREC module results. They are part of the data extraction function of BDPREP and are passed along through the BLDDES file for availability to CASC.

"Execution of the module involves accessing one blade section at a time from the input file. Terminal queries and responses permit alteration of grid formation parameters when unusual circumstances dictate changes to the stereotyped data supplied from BLDDES. Other input items can also be changed to guide the course of the iterations. Output at the terminal includes plots of the grid structure and of the blade surface Mach number distributions (Fig. 9). Optional printouts of diagnostics and solution results are available. These results, coupled with the designer's expertise, are used to judge the aerodynamic performance of the blade section and, if deemed necessary, to determine where contour adjustments should be made when rerunning the section through the BLDDES module.

"This procedure continues until all blade sections of the input file have been evaluated. Then the BLDDES module is reactivated to create new versions of disputed sections and to produce a new input file for CASC. CASC is rigged to read the file selectively, so only the altered sections are treated. The final output file from CASC has data sets containing updated input variables and calculation results for at least one acceptable version of hub, pitch, and tip design sections. Multiple versions of one or more of these sections may be present."

Calculations were made for five sections along the span of the
blades at the following radii: 5.5 (Root), 6.125, 6.75 (Pitch), 7.375,
and 8.00 (Tip). The results of these calculations for the 69.7° blade
row (48 blades) are summarized in Table 15, while those for the 60° blade
row (54 blades) are shown in Table 16 .

Table 15

Flow Angle Comparison

(48 Blades) 69.7°

Radius (Inches)		Predicted Flow Angle @ Exit Plane (Degrees)	Measured Hub-to-Tip Range
Hub	5.5	71.53	58
	6.125	71.20	
Pitch	6.75	70.59	⬇
	7.375	69.92	
Tip	8.0	69.18	64

Table 16

Flow Angle Comparison

(54 Blades) 60°

Radius (Inches)		Predicted Flow Angle @ Exit Plane (Degrees)	Measured Hub-to-Tip Range
Hub	5.5	61.09	53
	6.125	59.71	
Pitch	6.75	59.95	⬇
	7.375	60.36	
Tip	8.0	58.90	57

153

Before making a comparison with the data collected in this experiment recall that:

(1) This analysis is based on a two dimensional, inviscid approach.

(2) The closest data available from this experiment was taken 0.75 inches (0.58 chord) behind the exit plane.

Now, the quickest way to compare results is to refer to Figure 107 for the 69.7° blade row and Figure 102 for the 60° blade row. Both these figures are in Chapter III, Results. To summarize such a comparison, it appears that the analysis is consistently predicting a flow angle several degrees higher than that measured. For the 69.7° blades, the hub-tip range measured was 58°-64° vs the prediction of 71.5°-69.2°. It is also considered significant that the prediction is inverted compared to the measurements; i.e., the angle was predicted to decrease from hub to tip while the measured values increased from hub to tip.

For the 60° blades the hub-tip range measured was 53°-57° vs the prediction of 61.09-58.90; again, the predictions were inverted compared to the measurements and several degrees too high in all cases.

A complete description of the theory and numerical procedures, used in the three-dimensional calculations, is included in the AFAPL-TR-77-64, "3-D Heat Transfer Analysis Program," October 1977 (Dodge[16]). This calculation scheme basically combines a relaxation solution technique with a marching solution in accordance with the logic diagram shown in Figure 111 taken from Dodge[16, p. 23]. To quote Dodge[16, p. 26] specifically on the algorithm:

"Three separate numerical algorithms are required. They are:

(a) the setup of the geometry and its conversion coefficients,

154
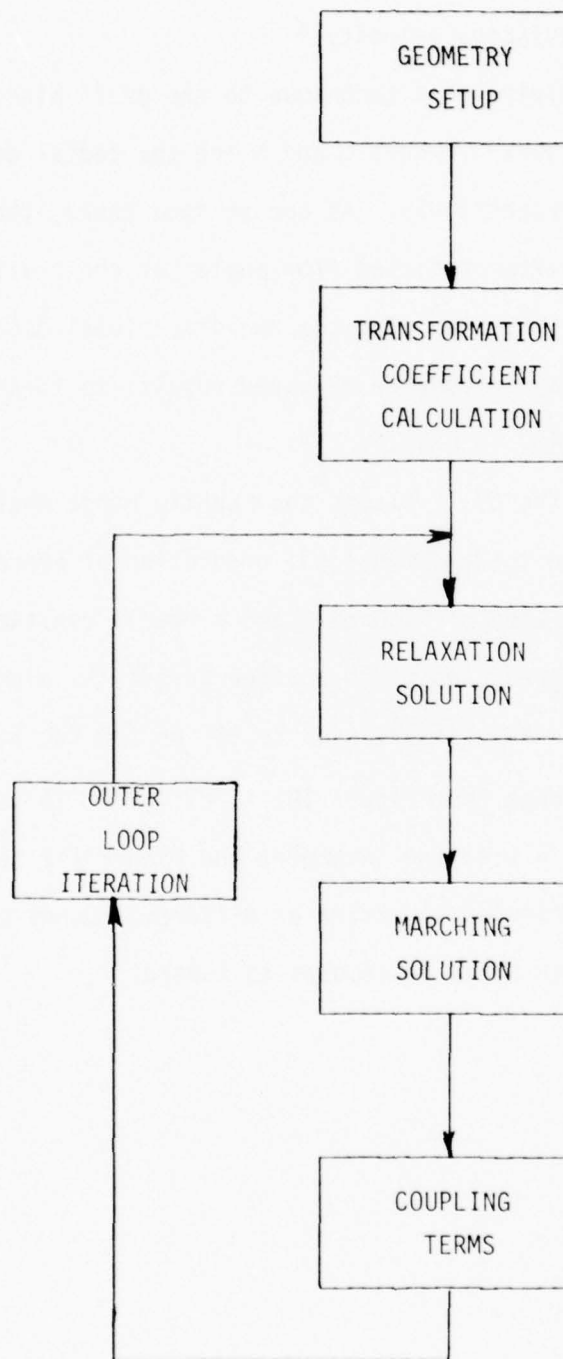
Figure 111   Program Logic Diagram

155

(b) a relaxation solution for potential, and

(c) a marching solution for temperature and the three components of viscous velocity."

The results of applying this technique to the 69.7° blade row (48 blades) are shown in Figure 112 where L and N are the radial and circumferential coordinates respectively. As can be seen there, the computer-generated output plot gives predicted flow angles at the trailing edge plane of the blade row. Now, as with the two-dimensional discussion, probably the quickest way to compare measured results to these predictions is to use Figure 107 in Chapter III.

In this case, for the 69.7° blades the hub-tip range measured was again 58°-64° versus the three-dimensional prediction of approximately 68°-72° on the pressure side of Figure 112 and a nearly constant 66° on the suction side. The predicted midspan range across the blade passage exit ranges from 70° on the pressure side to 66° on the suction side. The measured mid-span range from Figure 107 is 61°-63°. It is recognized that the reader can view and interpret the Figure 112 results at will, based on his experience, to arrive at different bounds on these ranges depending on which zones he chooses to ignore.
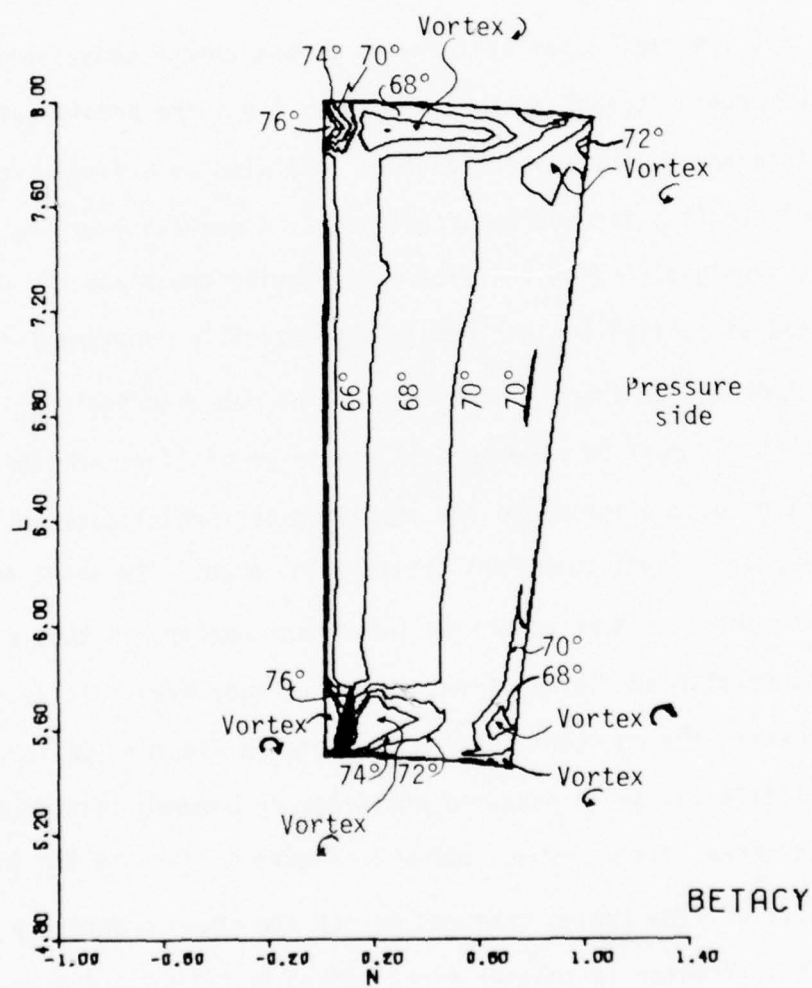
4B BLADE CASCADE

Figure 112 Tangential Flow Angles at TE

Now, to rationalize this apparent discrepancy of several degrees between predictions and measurements, two possible explanations are considered worthy of note here:

(1) The real blade exit angles are higher than the downstream measured angles at station one and that in 0.75 inch the flow "untwists" or straightens several degrees; i.e., the predictions are in fact correct and so are the measurements.

(2) The real blade exit angles do not change measurably at these Mach numbers in such a short distance; i.e., the predictions are actually in error by the several degrees indicated by a simple comparison.

To believe (1), it must be accepted that a mechanism exists to cause an instant straightening of the flow upon leaving the blade row which then was measured at station one and remained practically constant for at least another 4 inches (3.2 chords) downstream to be measured again at station three. Again, it must be remembered that the predictions are for the exact trailing edge plane while the nearest experimental data was 0.75 inch (0.58 chord) downstream from the trailing edge. The exact amount of flow straightening that occurs at these Mach numbers in that axial distance is debatable. In addition, it has already been pointed out, while discussing the constant flow angle plots in Figures 102 through 108, that little change in measured angle occurs between station one and station three. Furthermore, shown in Figure K-3 for the 65° blade row is a plot of flow angles measured across the channel during a check run at station 7 which is another eight inches (6.2 chords) downstream. As can be seen there, the hub-to-tip range of angles varies from approximately 52° to 58°. Now, referring to Figure 106 which plots constant flow angle lines for the 65° blades at station 1, it can be seen that the

158

measured hub-tip range is approximately 54°-62°. Therefore, even in a
distance of 12.75 inches (9.86 chords) downstream from the blade exit
plane there is only approximately 2 to 4 degrees of "untwist" in the flow.
This comparison clearly lends credence to the notion that little flow
straightening is occurring downstream at these Mach numbers. For reference,
the complete set of data taken and flow calculations made for this check
run are shown in Appendix K.

To believe (2), it must be accepted that the exit flow angles
produced at these Mach numbers will never exceed the metal angles and that
no effects other than boundary layer buildup exists to cause straightening
of the flow. This author subscribed to (2), and both the following con-
clusions about the three-dimensional predictions and the previous dis-
cussion of two-dimensional results were tempered by that opinion.

At this point, strictly on the basis of gross flow angle prediction,
it is difficult to make a case that the three-dimensional is considerably
better than the two-dimensional. If the two-dimensional procedure were
applied enough times across the span of the blades, one could expect to
generate a still better picture of the flow albeit still inverted. How-
ever, it would appear that the real strength of the three-dimensional
effort lies in the detail available with regard to secondary flows and
boundary effects which the two-dimensional approach will never yield no
matter how thin the spanwise slices become. The overall result pursued
by Dodge[16], after all, was a heat transfer analysis program applicable
to turbine design. Thus, the final conclusion regarding utility of the
three-dimensional scheme is that it certainly produces more detailed
results across the entire blade passage and, in the hands of an experienced

159

designer with access to adequate computer time, could eliminate the requirement for much experimental work. However, final testing and hardware iteration will likely always be required if maximum performance is the goal. As a matter of interest, the generation of Figure 112 required approximately one hour of computer time on a CDC 6600.

An interesting next step for this analytical effort would be to apply it to relatively very small gas turbine engines such as an Auxiliary Power Unit (APU) or a Jet Fuel Starter (JFS) where the secondary flows, leakage flows, etc. are a very significant portion of the total flow rate.

CHAPTER V

CONCLUSIONS

Several conclusions may be drawn from this activity and the results
produced:

1. At high subsonic flow conditions, the Engelman analysis of radial
equilibrium is indeed valid and such a model is more representative
of the real flow field than is the free vortex. This is due to com-
pressibility effects and, as stated by Hawthorne and Horlock[13, p. 789],
a free vortex turbomachine will have uniform axial mass flux distribution
providing the assumption of incompressibility is valid. Since a free
vortex design results in twisted blades, it is considered significant that
the nontwisted blades used here also resulted in uniform axial mass flux
distribution in a flow regime where the assumption of incompressibility
is certainly not valid. Hence, the conclusion is that the Engelman pre-
dictions were verified by this experimental evaluation effort.

2. The Engelman solution is best characterized as a synthesis tool to
guide machine designs rather than an absolute analytical technique. As
suggested by Hawthorne and Horlock[13, p. 790] the general turbomachinery
design problem "may be conceived as having a 'direct' and an 'indirect'
aspect. In the former, the configuration of the machine is given and it
is required to determine the behavior of the fluid. In the latter, a
particular fluid flow is specified and it is required to determine the

161

machine which will meet the specification." Thus, the Engelman technique is best suited and intended to be a basis for design to be used in much the same way as the basic free vortex ideas have been. As such, it is applicable to the so-called 'indirect' problem.

3. The overall rig performance and operational suitability were quite acceptable. All features functioned as designed and in general there were no significant problems with taking data anytime the facility air system could be made available. The hydraulic servo probe actuator was especially convenient and reliable. The only problem experienced with it was air entrainment in the fluid after any long period of inactivity. Bleeding the lines always solved this problem and caused no real hardship. The data produced by the test assembly and its instrumentation were demonstrated to be repeatable and consistent.

4. The two-dimensional stack solution technique developed by Wysong[26] produces flow angle predictions which are consistently several degrees too high and additionally are ordered in reverse to the measured data. At these flow Mach number conditions it appears that the combination of two-dimensional assumptions plus the lack of allowance for viscosity effects introduces significant error.

5. The three-dimensional viscous technique developed by Dodge[16] generates predictions of flow angle distribution which are generally ordered correctly compared to measured results but are still several degrees higher. While it is difficult to conclude that the three-dimensional effort produces results very close to measurements on the basis of gross flow angle comparisons, it does produce a detailed visualization of secondary flow effects and blade loss predictions. In addition,

162

the end purpose of this three-dimensional program is a heat transfer cal-
culation which has been proven in other test cases to be quite useful.
Due to the relative accuracy and completeness of the three-dimensional
analytical program, it is considered likely that small gas turbines
such as auxiliary power units could also benefit from such treatment,
and it is expected that such effort will evolve on future research
programs in that area.

APPENDIX A

DERIVATIONS AND SOLUTIONS

DERIVATION OF THE BASIC EQUATION

Consider an annulus utilizing cylindrical coordinates as follows:
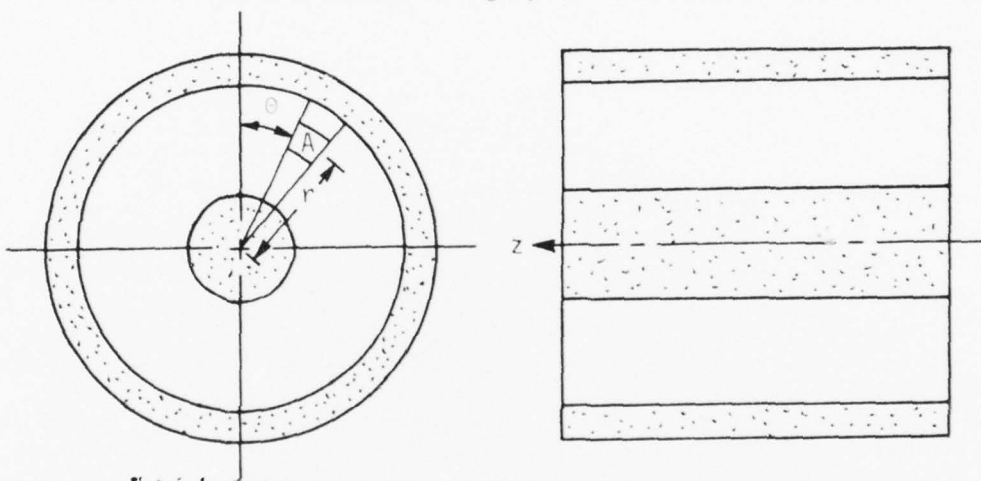
Differential Element A
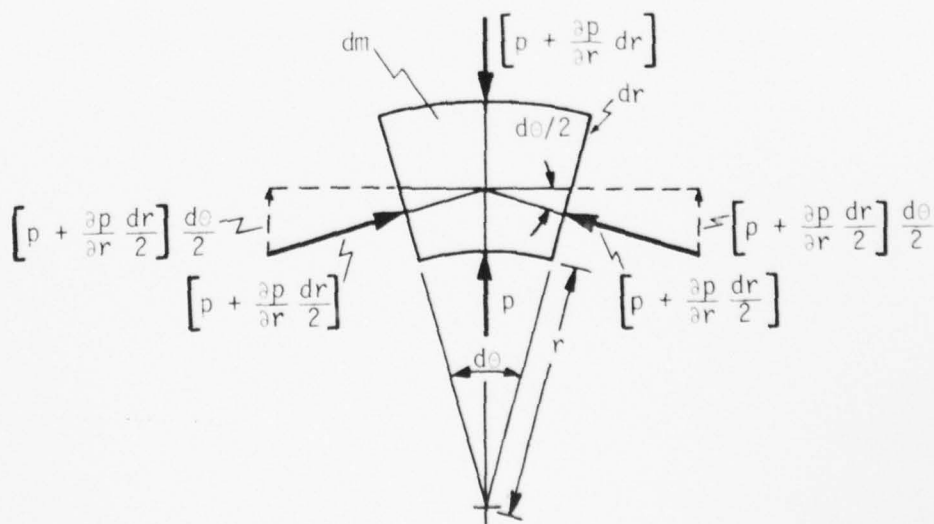
Figure A-1 Geometric Relationships

Then, after making the following assumptions, the pressure forces acting on differential element A may be calculated:

(i) Compressible, nonviscuous fluid.

(ii) Only a combined rotational and axial motion exist; i.e., there is no radial flow.

(iii) The effects of gravity and friction are neglected.

(iv) Flow is symmetric about the z-coordinate axis.

(v) Steady flow throughout the annulus.

(vi) $\sin(d\Theta) \simeq d\Theta$

r-direction:

$$F_r = \left[p + \frac{\partial p}{\partial r} \, dr \right] \left[r + dr \right] d\Theta \, dz - p \, r \, d\Theta \, dz$$

$$- \left[p + \frac{\partial p}{\partial r} \frac{dr}{2} \right] d\Theta \, dr \, dz \qquad (A.1)$$

$$F_r = \left[r \frac{\partial p}{\partial r} \, dr + \frac{1}{2} \frac{\partial p}{\partial r} \, dr^2 \right] d\Theta \, dz \qquad (A.2)$$

Neglecting the dr^2 term.

$$F_r = r \frac{\partial p}{\partial r} \, dr \, d\Theta \, dz \qquad (A.3)$$

Θ-direction:

$$F_\Theta = \left[p + \frac{\partial p}{\partial r} \frac{dr}{2} \right] \cos\left(\frac{d\Theta}{2}\right) - \left[p + \frac{\partial p}{\partial r} \frac{dr}{2} \right] \cos\left(\frac{d\Theta}{2}\right) \qquad (A.4)$$

$$F_\Theta = 0 \qquad (A.5)$$

z-direction:

$$F_z = \left[p + \frac{\partial p}{\partial z} \frac{dz}{2} \right] \left[\pi(r + dr)^2 - \pi r^2 \right] \frac{d\Theta}{2} \qquad (A.6)$$

$$- \left[p - \frac{\partial p}{\partial z} \frac{dz}{2} \right] \left[\pi(r + dr)^2 - \pi r^2 \right] \frac{d\Theta}{2}$$

$$F_z = \frac{\partial p}{\partial z} \, dz \left[2 \, r \, dr + dr^2 \right] \frac{d\Theta}{2} \qquad (A.7)$$

165

By neglecting the dr^2 term.

$$F_z = r \frac{\partial p}{\partial z} dr \, d\Theta \, dz \tag{A.8}$$

The mass of the differential element of fluid is found from:

$$dm = \text{density} \times \text{volume}$$

$$dm = \rho dz \left[\pi(r + dr)^2 - \pi r^2 \right] \frac{d\Theta}{2\pi} \tag{A.9}$$

$$dm = \frac{\rho dz \, d\Theta}{2} \left[2 \, r \, dr + dr^2 \right] \tag{A.10}$$

Neglecting the dr^2 term.

$$dm = \rho r \, dr \, d\Theta \, dz \tag{A.11}$$

Acceleration Equations

In cylindrical coordinates, the components of acceleration may be expressed as:

$$a_r = \frac{\partial V_r}{\partial \tau} + V_r \frac{\partial V_r}{\partial r} + \frac{V_\Theta}{r} \frac{\partial V_r}{\partial \Theta} + V_z \frac{\partial V_r}{\partial z} - \frac{V_\Theta^2}{r} \tag{A.12}$$

$$a_\Theta = \frac{\partial V_\Theta}{\partial \tau} + V_r \frac{\partial V_\Theta}{\partial r} + \frac{V_\Theta}{r} \frac{\partial V_\Theta}{\partial \Theta} + V_z \frac{\partial V_\Theta}{\partial z} + \frac{V_r V_\Theta}{r} \tag{A.13}$$

$$a_z = \frac{\partial V_z}{\partial \tau} + V_r \frac{\partial V_z}{\partial r} + \frac{V_\Theta}{r} \frac{\partial V_z}{\partial \Theta} + V_z \frac{\partial V_z}{\partial z} \tag{A.14}$$

Then using the previous assumptions, the components of acceleration may be reduced to:

$$a_r = - \frac{V_\Theta^2}{r} \tag{A.15}$$

$$a_\Theta = 0 \tag{A.16}$$

$$a_z = 0 \tag{A.17}$$

Equations of Motion

$$F = - \text{mass} \times \text{acceleration}$$

r-direction:

$$F_r = - dm \, a_r \tag{A.18}$$

166

$$r \frac{\partial p}{\partial r} dr \, d\Theta \, dz = \rho r \, dr \, dz \left\{ - \frac{v_\Theta^2}{r} \right\} \frac{1}{g_c} \tag{A.19}$$

$$\frac{\partial p}{\partial r} = \frac{\rho v_\Theta^2}{g_c \, r} \tag{A.20}$$

Θ-direction:

$$F_\Theta = - dm \, a_\Theta \tag{A.21}$$

$$o = o$$

z-direction:

$$F_z = - dm \, a_z \tag{A.22}$$

$$r \frac{\partial p}{\partial z} dr \, d\Theta \, dz = o \tag{A.23}$$

Finally, the partial differential equations of motion can be reduced to a single ordinary differential equation - the so-called "basic" equation of interest to this experiment.

$$\frac{dr}{r} = g_c \frac{dp}{\rho v_\Theta^2} \tag{A.24}$$

A SOLUTION TO THE BASIC EQUATION FOLLOWING ENGELMAN'S ANALYSIS

by making the following additional assumptions:

(i)   The flow has constant total enthalpy and constant entropy throughout the annulus.

(ii)   The fluid is a perfect gas

(iii)   There is a continuity of mass

Rearranging the geometric relationship

$$v^2 = v_\Theta^2 + v_z^2 \tag{A.25}$$

167

Where

$$V_z = \text{axial velocity}$$

$$V_\Theta = \text{tangential velocity}$$

$$V = \text{whirl velocity}$$

and substituting this into equation (A.24)

$$\frac{dr}{r} = g_c \frac{dp}{\rho V^2 - \rho V_z^2} \tag{A.26}$$

For a perfect gas with isentropic flow, the compressible Bernoulli equation results in:

$$\rho V^2 = 2 \ g_c \left(\frac{k}{k-1}\right) \ p_0 \left\{1 - \left[\frac{p}{p_0}\right]^{\left(\frac{k-1}{k}\right)}\right\} \frac{\rho}{\rho_0} \tag{A.27}$$

Substituting the isentropic relationship

$$\frac{\rho}{\rho_0} = \left(\frac{p}{p_0}\right)^{1/k} = p^{1/k} \tag{A.28}$$

into equation (A.27) and rearranging

$$\rho V^2 = 2 \ g_c \left(\frac{k}{k-1}\right) \ p_0 \left[p^{1/k} - p\right] \tag{A.29}$$

Evaluating the geometric relationship from Figure (A-1)

$$V_z = V \cos \phi \tag{A.30}$$

at the condition M = 1 and substituting this into the continuity equation

$$\rho V_z = \rho_\star \ V_{z\star} \tag{A.31}$$

the following equation is obtained:

$$\rho V_z = \rho_\star \ V_\star \cos \phi_\star \tag{A.32}$$

168

Multiplying the above equation by V_z

$$\rho V_z^2 = \frac{(\rho V_z)^2}{\rho} = \frac{\rho_\star^2 \, V_\star^2 \cos^2 \phi_\star}{\rho} \qquad (A.33)$$

Substituting equation (A.28) into the above equation

$$\rho V_z^2 = \frac{\rho_\star \, V_\star^2 \cos^2 \phi_\star \, p_\star^{1/k}}{p^{1/k}} \qquad (A.34)$$

Evaluating equation (A.29) at the condition M = 1, substituting into the above equation and rearranging

$$\rho V_z^2 = 2 \, g_c \left(\frac{k}{k-1} \right) p_0 \left[p_\star^{2/k} - P_\star^{\left(\frac{k+1}{k} \right)} \right] \frac{\cos^2 \phi_\star}{p^{1/k}} \qquad (A.35)$$

Substituting equations (A.29) and (A.35) into equation (A.26) and rearranging

$$\frac{dr}{r} = \frac{\left(\frac{k-1}{2k} \right) dP}{\left[p^{1/k} - p \right] - \left[p_\star^{2/k} - P_\star^{\left(\frac{k+1}{k} \right)} \right] \frac{\cos^2 \phi_\star}{p^{1/k}}} \qquad (A.36)$$

Substituting the isentropic relationship

$$\frac{p_\star}{p_0} = \left[\frac{2}{k+1} \right]^{\left(\frac{k}{k-1} \right)} = P_\star \qquad (A.37)$$

into equation (A.36) and rearranging

$$\frac{dr}{r} = \frac{C_1 \, dP}{C_2 \left[p^{1/k} - p \right] - \frac{\cos^2 \phi_\star}{p^{1/k}}} \qquad (A.38)$$

Where C_1 and C_2 are:

$$C_1 = \frac{1}{k} \left[\frac{k+1}{2} \right]^{\left(\frac{k+1}{k-1} \right)} \qquad (A.39)$$

169

$$C_2 = C_1 \left(\frac{2k}{k-1} \right) = \frac{2}{k-1} \left[\frac{k+1}{2} \right]^{\left(\frac{k+1}{k-1} \right)} \tag{A.40}$$

Integrating equation (A.38) from the condition $M = 1$ to a desired value

$$\int_{r_\star}^{r} \frac{dr}{r} = \int_{P_\star}^{P} f(P) \, dP \tag{A.41}$$

Evaluating and rearranging

$$\frac{r}{r_\star} = \exp \left[\int_{P_\star}^{P} f(P) \, dP \right] \tag{A.42}$$

The flow angle can be expressed by:

$$\phi = \tan^{-1} \left(\frac{V_\Theta}{V_z} \right) \tag{A.43}$$

Equating equation (A.24) and equation (A.38)

$$\frac{g_c}{\rho V_\Theta^2} = \frac{f(P)}{p_0} \tag{A.44}$$

Evaluating equation (A.43) at the condition $M = 1$, substituting into equation (A.33) and rearranging

$$\rho V_z^2 = \frac{(\rho_\star V_\star)^2}{\rho} = \frac{\rho_\star^2}{\rho} \frac{V_{\Theta\star}^2}{\tan^2 \phi_\star} \tag{A.45}$$

Rearranging equation (A.43), equating with equation (A.45) and rearranging

$$\rho V_\Theta^2 = \rho \left[\frac{\rho_\star V_{\Theta\star} \tan \phi}{\rho \tan \phi_\star} \right]^2 \tag{A.46}$$

170

Dividing g_c by the above equation and equating with equation (A.44)

$$\frac{f(P)}{P_0} = g_c \frac{\rho \tan^2 \phi_\star}{\rho_\star^2 V_{\Theta_\star}^2 \tan^2 \phi} \tag{A.47}$$

Substituting the geometric relationship from Figure (A-1)

$$V_\Theta = V \sin \phi \tag{A.48}$$

and the isentropic relationship

$$V = M \sqrt{g_c k \frac{P}{\rho}} \tag{A.49}$$

evaluated at the condition M = 1 into equation (A.47) gives

$$\frac{f(P)}{P_0} = \frac{\rho \tan^2 \phi_\star}{k \rho_\star P_\star \sin^2 \phi_\star \tan^2 \phi} \tag{A.50}$$

Substituting equation (A.28), (A.37), and (A.39) into equation (A.50), rearranging and solving for ϕ yields the following relationship:

$$\phi = \tan^{-1} \left[\frac{C_1 P^{1/k}}{\cos^2 \phi_\star f(P)} \right]^{1/2} \tag{A.51}$$

Thus, Engelman was able to determine that both the relative radius ratio, $r/r_\star$, and the flow angle, ϕ, are functions only of the pressure ratio, P, for a given $\phi_\star$ and k.

A simpler expression relating $\phi_\star$, the flow angle, ϕ, and the Mach number, M, can be derived by applying the previous assumptions.

$$\frac{\cos \phi_\star}{\cos \phi} = M \left[\frac{k+1}{2 + (k-1) M^2} \right]^{\frac{k+1}{2(k-1)}} \tag{A.52}$$

This equation was derived previously in Chapter III.

171

Assuming k = 1.4 and solving equation (A.52) to obtain:

$$\phi = \cos^{-1}\left[\frac{\cos\phi_*}{M}\left(\frac{2 + 0.4M^2}{2.4}\right)^3\right]$$

(A.53)

and since with k = 1.4

$$M = \sqrt{5\left[\left(\frac{1}{P}\right)^{.2857} - 1\right]}$$

(A.54)

And after combining equation (A.53) and equation (A.54) to obtain:

$$\phi = \cos^{-1}\left\{\frac{\cos\phi_*}{\sqrt{5\left[\left(\frac{1}{P}\right)^{.2857} - 1\right]}}\left[\frac{2 + .4\left[5\left(\frac{1}{P}\right)^{.2857} - 1\right]}{2.4}\right]^3\right\}$$

(A.55)

172

SOLUTION OF BASIC EQUATION FOR A
FREE VORTEX FLOW CONDITION

Consider again the basic equation

$$\frac{dr}{r} = g_c \frac{dp}{\rho V_\Theta^2} \tag{A.24}$$

The free vortex condition implies that:

$$r V_\Theta = r_\star V_{\Theta\star} \tag{A.56}$$

Where $r_\star$ and $V_{\Theta\star}$ are evaluated at the condition $M = 1$.

Substituting the equation of the isentropic relationship

$$V = M \sqrt{g_c k \frac{p}{\rho}} \tag{A.57}$$

into the equation of the geometric relationship as defined by Figure A-1 and the definition of flow angle ϕ

$$V_\Theta = V \sin \phi \tag{A.58}$$

and evaluating at the condition $M = 1$

$$V_{\Theta\star} = \sqrt{g_c k \frac{p_\star}{\rho_\star}} \sin \phi_\star \tag{A.59}$$

Substituting the above equation into equation (A-56) and

rearranging

$$V_\Theta = \frac{r_\star}{r} \sqrt{g_c k \frac{p_\star}{\rho_\star}} \sin \phi_\star \tag{A.60}$$

173

By taking the following equation of the isentropic relationship

$$\frac{\rho}{\rho_0} = \left(\frac{p}{p_0}\right)^{1/k} = p^{1/k} \tag{A.61}$$

and evaluating it at M = 1, the following relationships can be obtained:

$$\frac{\rho_\star}{\rho} = \frac{P_\star^{1/k}}{P^{1/k}} \tag{A.62}$$

$$\frac{dp}{p_\star} = \frac{dP}{P_\star} \tag{A.63}$$

Then by substituting the above two equations and (A.60) into equation (A.24) and rearranging

$$\frac{dr}{r^3} = \frac{P_\star^{\left(\frac{1-k}{k}\right)} dP}{k r_\star^2 \sin^2 \phi_\star \, p^{1/k}} \tag{A.64}$$

Substituting the isentropic relationship

$$\frac{p_\star}{p_0} = \left[\frac{2}{k+1}\right]^{\left(\frac{k}{k-1}\right)} = P_\star \tag{A.65}$$

into equation (A.66) and rearranging

$$\frac{dr}{r^3} = \frac{k+1}{2 k r_\star^2 \sin^2 \phi_\star} \frac{dP}{p^{1/k}} \tag{A.66}$$

Integrating from the condition M = 1 to a desired value

$$\int_{r_\star}^{r} \frac{dr}{r^3} = \frac{k+1}{2 k r_\star^2 \sin^2 \phi_\star} \int_{P_\star}^{P} \frac{dP}{p^{1/k}} \tag{A.67}$$

174

Integrating the above equation, substituting equation (A.65), and rearranging.

$$\frac{r}{r_\star} = \frac{1}{\sqrt{1 - \frac{(k+1) \; P^{\left(\frac{k-1}{k}\right)} - 2}{(k-1) \; \sin^2 \phi_\star}}} \tag{A.68}$$

The flow angle ϕ can be expressed as:

$$\phi = \sin^{-1} \left(\frac{V_\phi}{V} \right) \tag{A.69}$$

Substituting the isentropic relationship

$$\frac{p}{p_0} = \left[1 + \left(\frac{k-1}{2} \right) M^2 \right]^{\left(\frac{k}{1-k}\right)} = P \tag{A.70}$$

along with (A.57), (A.60), and (A.61) into equation (A.69) and rearranging

$$\phi = \sin^{-1} \left[\frac{\frac{r_\star}{r} \sqrt{\frac{P}{P_\star}}^{\left(\frac{1-k}{k}\right)} \sin \phi_\star}{\sqrt{\left\{ P^{\left(\frac{1-k}{k}\right)} - 1 \right\} \left(\frac{2}{k-1} \right)}} \right] \tag{A.71}$$

Substituting equation (A.65) into the above equation and rearranging

$$\phi = \sin^{-1} \left[\frac{\sin \phi_\star}{\frac{r}{r_\star} \sqrt{\left\{ 1 - P^{\left(\frac{k-1}{k}\right)} \right\} \left(\frac{k+1}{k-1} \right)}} \right] \tag{A.72}$$

175

Finally, continuing equation (A.68) and equation (A.72) for k = 1.4 we get:

$$\phi = \sin^{-1}\left\{ \sqrt{1 - \frac{6P^{.2857} - 5}{\sin^2 \phi_*} \left[\sqrt{\frac{\sin \phi_*}{6\left(1 - P^{.2857}\right)}} \right]} \right\} \qquad (A.73)$$

END
DATE
FILMED

9-79
DDC
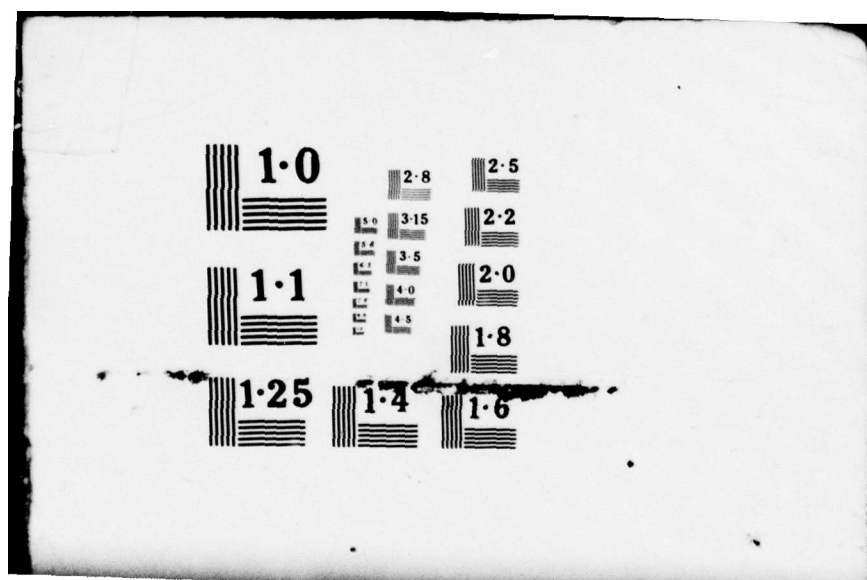
APPENDIX B

PROBE CHECKOUT PROCEDURE

Even though a quality wedge probe had been purchased from a well-known manufacturer, United Sensor and Control Corporation, there is always the possibility of a quality control error which could affect the indicated results. Since the flow angle was to be measured directly by nulling the wedge face pressures, it was considered worthwhile to set up some sort of checkout fixture which could verify the accuracy of such pressure indications. The plan was to establish an axial, uniform flow field with a probe mounting scheme located accurately with respect to it. Then, by making provision to accurately measure the probe rotation required to null, a calibration factor could be established and applied to any indicated flow angle on the rig.

The apparatus constructed is shown in Figures B-1, and B-2.

Since dial indicators were to be used against the face of the probe output head, the location of that face relative to the wedge faces had to be established accurately. The setup in the Air Force Aero Propulsion Laboratory machine shop to establish these relative locations using an optical dividing head is shown in Figures B-3, and B-4. For the probe used during all final data-taking runs, the output head face was determined to be exactly perpendicular to the centerline of the wedge itself so that no correction for that difference was necessary.
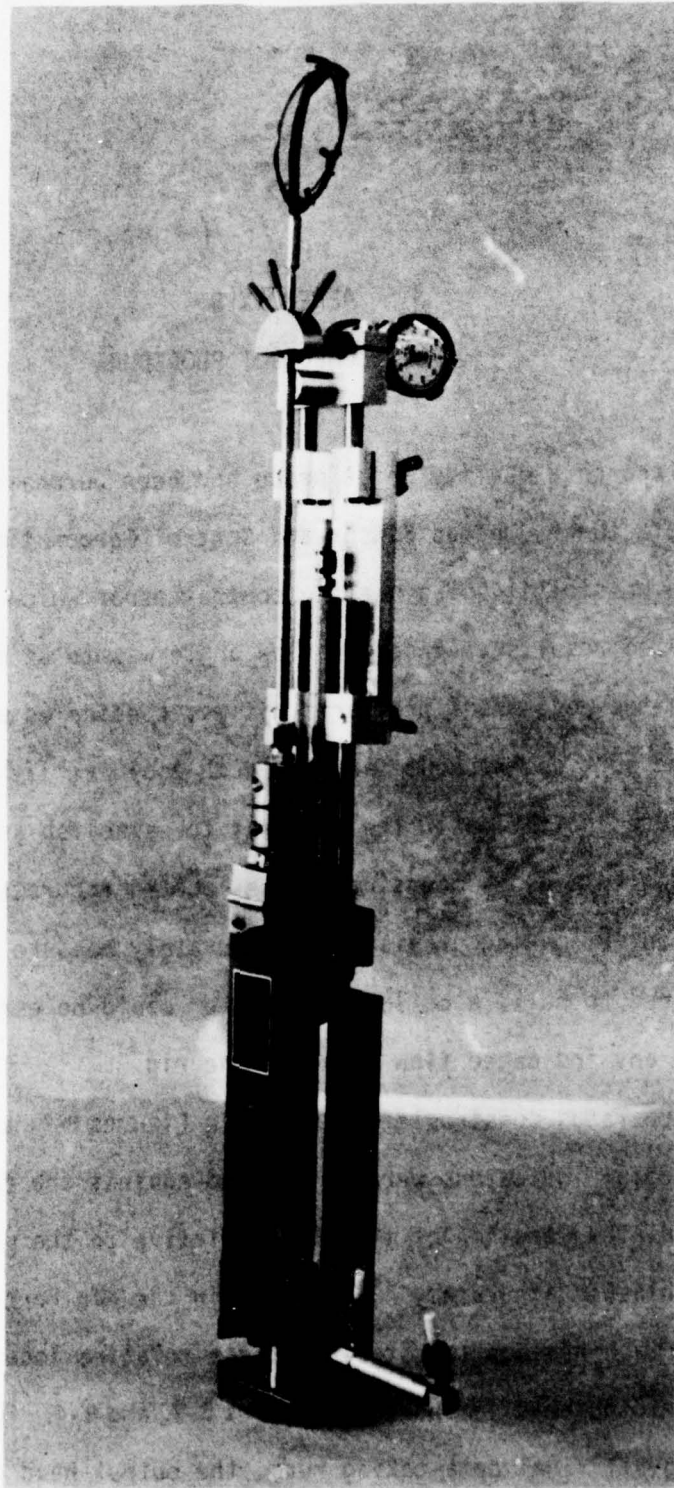
177

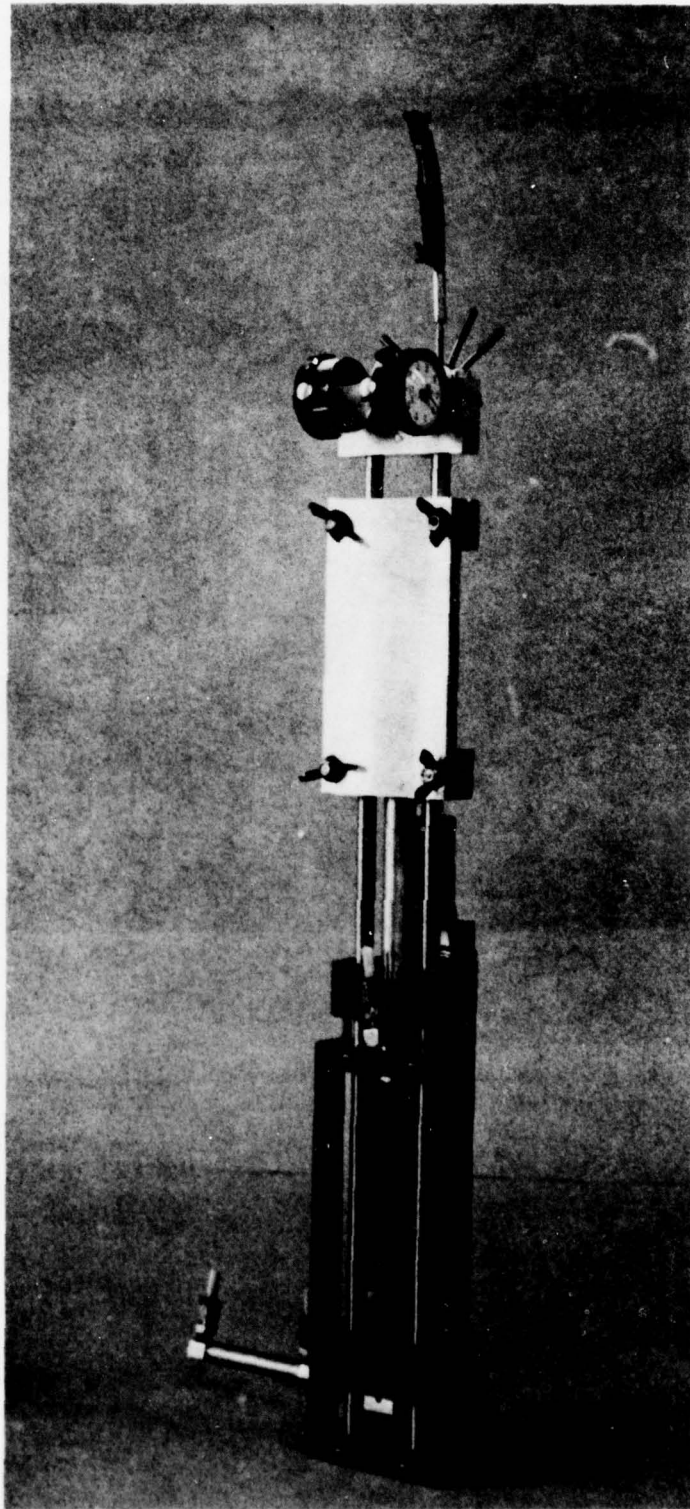Figure B-1   Probe Checkout Fixture - Front View

178

Figure B-2   Probe Checkout Fixture - Rear View
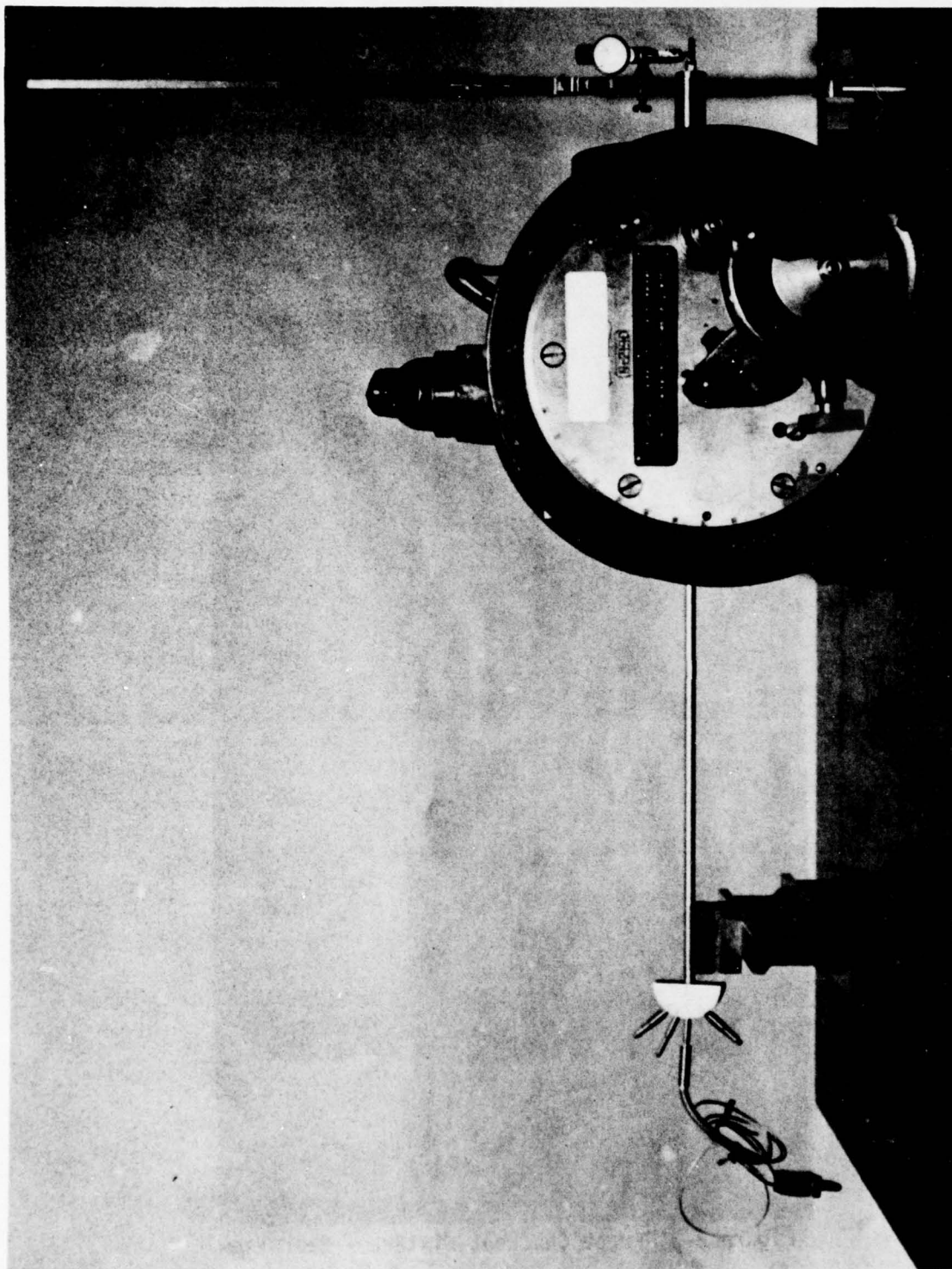
Figure B-3 Optical Dividing Head Probe Wedge Checkout
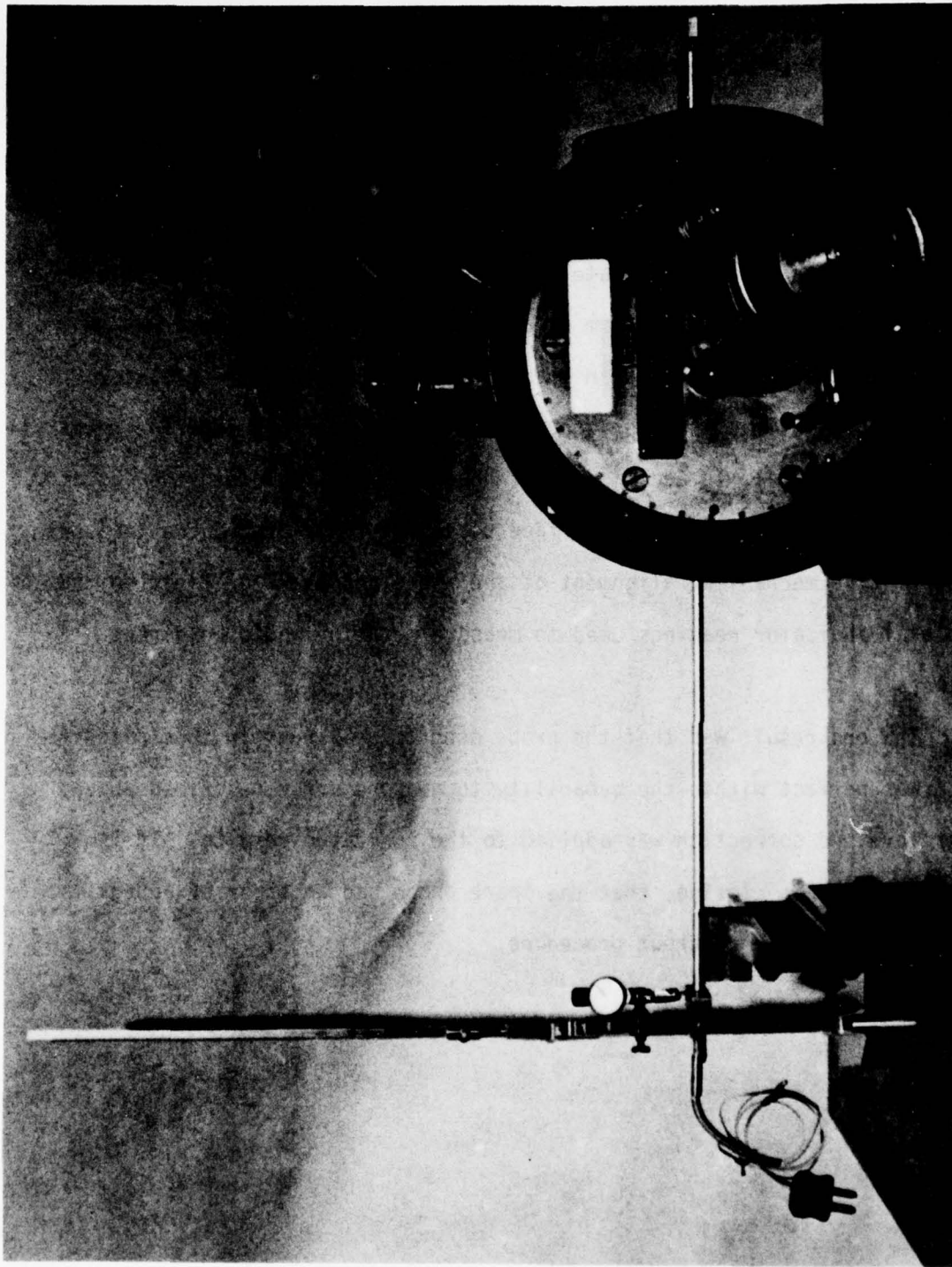
Figure B-4 Optical Dividing Head Probe Manifold Checkout

181

The final operational setup is shown in Figure B-5. As can be seen there, the apparatus was connected to the same altitude chamber used for the test apparatus receiver. An atmospheric inlet was provided to a plexiglass tube with an inside diameter of 3 1/2 inches. The probe was located 16 inches or approximately 4 1/2 tube diameters from the inlet to assure establishment of uniform axial flow. The probe actuator was operated to center the probe in the tube and, of course, the actuator mounting pad was machined very accurately to assure probe location relative to the flow field. In addition, the whole assembly, including the actuator, was checked by gage block and surface plate reference procedures to assure the relative mechanical alignment of the probe and the flow field so that the dial indicator readings used to measure rotation would be direct answers.

The end result was that the probe used for all runs in this dissertation was perfect within the capability to measure error described above. Therefore, no correction was applied to the indicated results. It is worth noting, in closing, that the spare probe had an error of approximately 3° using this same checkout procedure.

Figure B-5   Probe Checkout Flow Setup

APPENDIX C
ACTUATOR CALIBRATION

To make sure the probe would come as close to the centerbody as possible without damaging contact, a piece of 0.020" shim stock was ta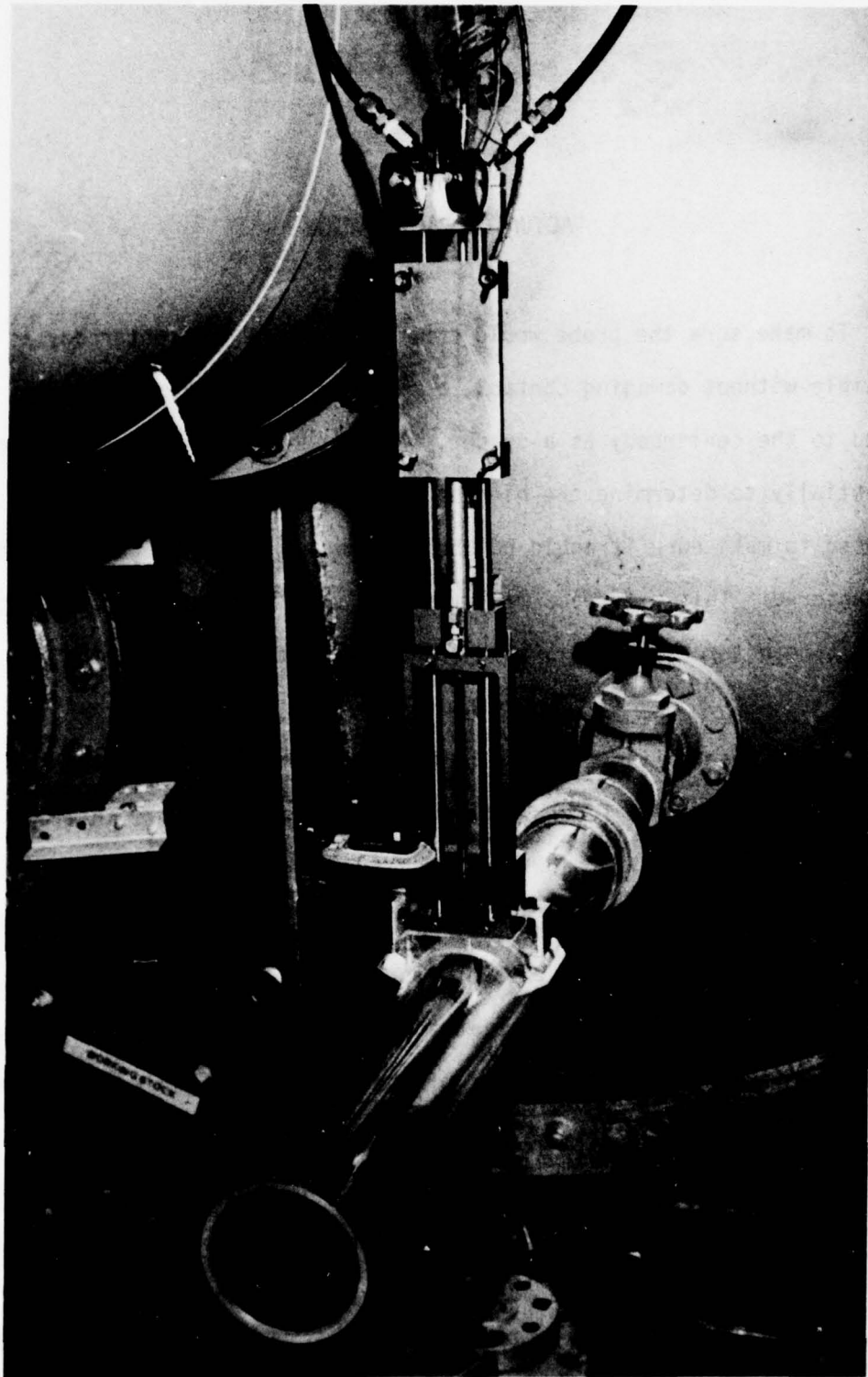ped to the centerbody as a spacer. The probe was then moved circumferentially to determine the highest point and the probe was then scribed to make sure it could not be set lower than the highest point encountered. This reference mark was then used to set the probe at the correct height for all calibrations and all installations in the rig itself.

The angular calibration of the probe was conducted by placing a round calibration disk (degree wheel) on the probe itself. This can be seen in Figure C-1. This disk was graduated in degrees and by use of the vernier, readings could be taken in 0.1 degree increments. The probe was hand turned relative to the actuator to read 50 degrees relative to the centerbody center line which would now be the lowest degree reading possible; i. e. the starting point of the rotary actuator travel range. Calibration was then started. One operator was stationed looking through a magnifying lamp at the disk and another turned the probe control until told to stop by the first operator. If the movement was too small or too large, iterative adjustments were made until the desired setting was obtained. The digital voltmeter reading was then recorded. This continued for every calibration point required. The next day, the

184
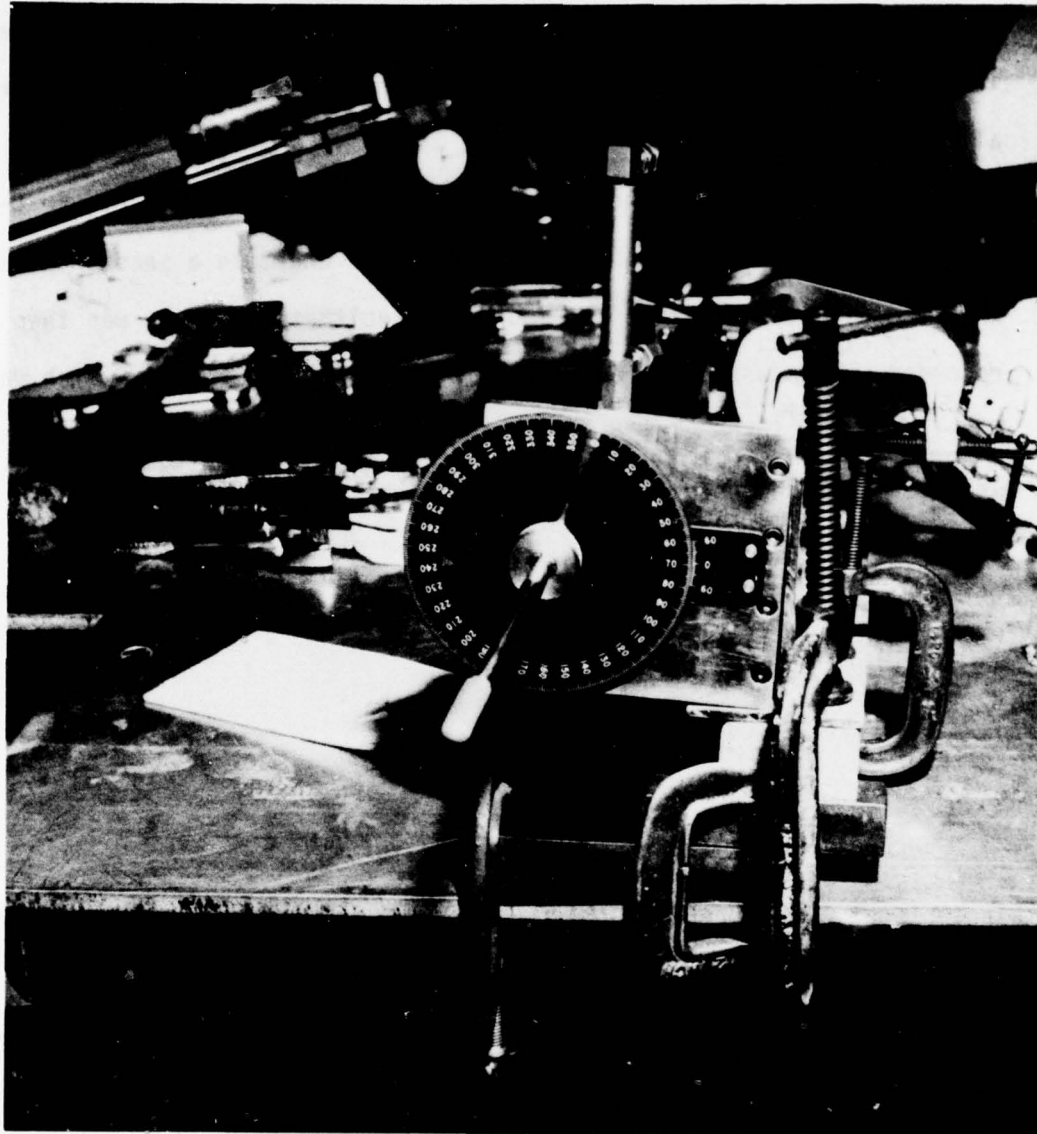
Figure C-1 Actuator Angular Calibration Setup

185

second operator positioned the probe by use of the voltmeter and the first operator observed the degree wheel reading, therefore checking the calibration. No significant differences were encountered and the readings were accepted. The calibration readings taken here and used for all tests are shown in Table C-1.

The linear calibration was done in the manner shown in Figure C-2 One operator looked through a magnifying lamp and told a second operator when the dial moved 1/10 of an inch. The voltmeter reading was then recorded. This was done for 22 readings and a final reading which was not 1/10 of an inch. These readings were all checked in the same manner used to check the angular calibration. They are also shown in Table C-1.
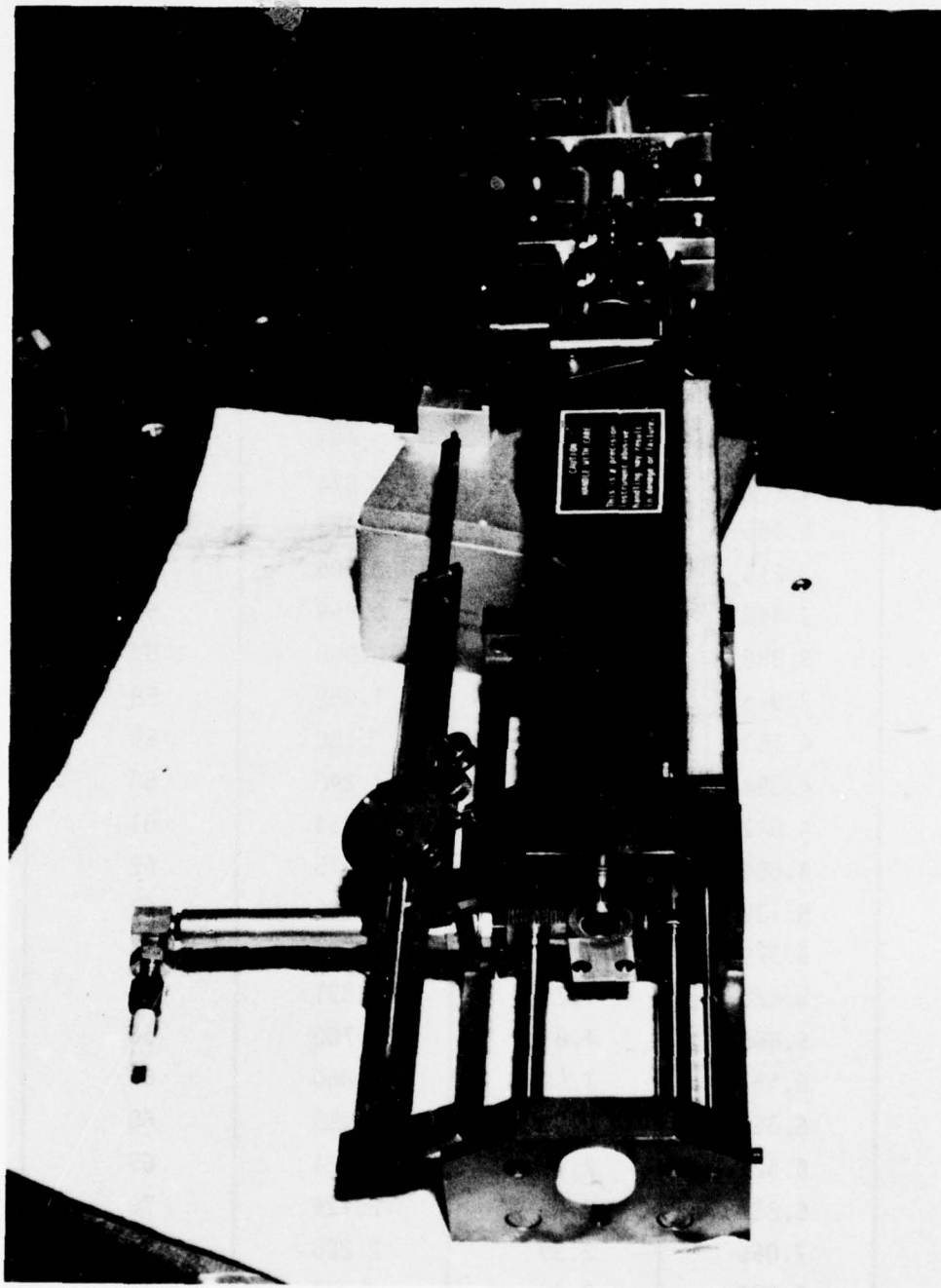
Figure C-2 Actuator Linear Calibration Setup

187

Table C-1

ACTUATOR CALIBRATION

LINEAR		ANGULAR	
VOLTMETER (VOLTS)	POSITION (INCHES)	VOLTMETER (VOLTS)	POSITION (DEGREES)
1.956	0.29	0.315	50
2.193	0.39	0.400	51
2.444	0.49	0.493	52
2.701	0.59	0.574	53
2.966	0.69	0.687	54
3.218	0.79	0.786	55
3.448	0.89	0.859	56
3.886	0.99	0.958	57
3.916	1.09	1.069	58
4.160	1.19	1.150	59
4.398	1.29	1.248	60
4.642	1.39	1.354	61
4.894	1.49	1.415	62
5.133	1.59	1.536	63
5.378	1.69	1.580	64
5.625	1.79	1.691	65
5.866	1.89	1.760	66
6.113	1.99	1.860	67
6.358	2.09	1.953	68
6.627	2.19	2.024	69
6.857	2.29	2.129	70
7.066	2.39	2.226	71
7.227	2.45	2.280	72

APPENDIX D

NUMERICAL INDEX OF TEST APPARATUS DRAWINGS

DWG. No	Date	Title
7552-04-2663	5 Jun 74	Blade Ass'y Installation
2664	5 Jun 74	Plate-Hold down
2665	5 Jun 74	Spacer
2666	10 Jun 74	Probe Drive Ass'y
2667	17 May 74	Drive Saddle
2668	24 May 74	Bar Screw Ass'y
2669	5 Jun 74	Plate-Actuator Mounting
2670	3 Jun 74	Motor Mount
2671	21 May 74	Angle-Roller Support
2672	24 May 74	Block-Roller Support
2673	3 Jun 74	Drive Pin
2674	3 Jun 74	Ball Bushing Pushrod
2675	28 May 74	Bracket
2676	7 Jun 74	Pointer
2677	7 Jun 74	Spacer-Pointer
2678	29 May 74	Ball Bushing Housing
2679	30 May 74	Ball Bushing Shaft Support
2680	21 May 74	Plate Ass'y Cylinder Lock
2681	10 Jun 74	Degree Rule
2682	5 Jun 74	Plug-Clamp
2683	5 Jun 74	Clamp
2684	5 Jun 74	Stud
2685	5 Jun 74	Nose Cone
2686	5 Jun 74	Blade Ass'y
2687	5 Jun 74	Blade Ass'y 69.7°
2688	5 Jun 74	Blade Ass'y 65°
2689	5 Jun 74	Blade Ass'y 60°
2690	5 Jun 74	Ring, Bellmouth Mounting
2691	5 Jun 74	Ring
2692	5 Jun 74	Liner
2693	5 Jun 74	Shell
2694	5 Jun 74	Cylinder
2695	5 Jun 74	Tube-Support
2696	5 Jun 74	Pressure Port Ass'y
2697	5 Jun 74	Support Ass'y Aft.
2698	5 Jun 74	Mounting Plate
2699	5 Jun 74	Mounting Saddle
2860	3 Sep 74	Motor Support Plate
2861	3 Sep 74	Motor Mounting Plate
2862	3 Sep 74	Motor Support Angle
2863	4 Sep 74	Ass'y Bar Screw
2864	4 Sep 74	Support Angle

APPENDIX E

SAMPLE DATA SHEETS

Table E-1   2 1/2° Right of T.E.

Table E-2 0° – Probe on Vertical ℄

BAROMETER 29.040 1005
29.045 0710 IN Hg
374.4467 IN H₂O

REQ'D TO CHOKE 15.3457 IN H₂
BLADE ANGLE 68.7 DEG

START 0830
STOP

ANNULAR FLOW RIG RM 24
SADDLE STATION 3
BACKFLOW PLATE BORE 14.625 IN
NET FLOW AREA 0.50638 FT²
SADDLE CIRCUMFERENTIAL LOCATION — Probe on Vertical ℄
(7½° LEFT OF ZERO)

DATE BOJANETT
OPERATOR(S) GODBIN
WEBER
(REPEAT OF 23 AUG 76 & 3 SEPT 76)

APPENDIX F

LONG VS SHORT TRAVERSE COMPARATIVE PLOTS

Presented in this appendix are plots of data taken at station three using the 69.7° cascade. The circumferential location was 2.5 degrees right of the reference blade trailing edge and, for comparison, both "long" and "short" traverses were made. The radial positions included in these traverses was shown previously as Table 4 in Chapter II.

As can be seen in Figures F-1 through F-3, the short traverse produces data which is quite comparable to that produced by the long traverse. Hence, in order to conserve energy and generate the maximum results in the minimum time, much of the data produced during this experiment was taken with a short traverse.
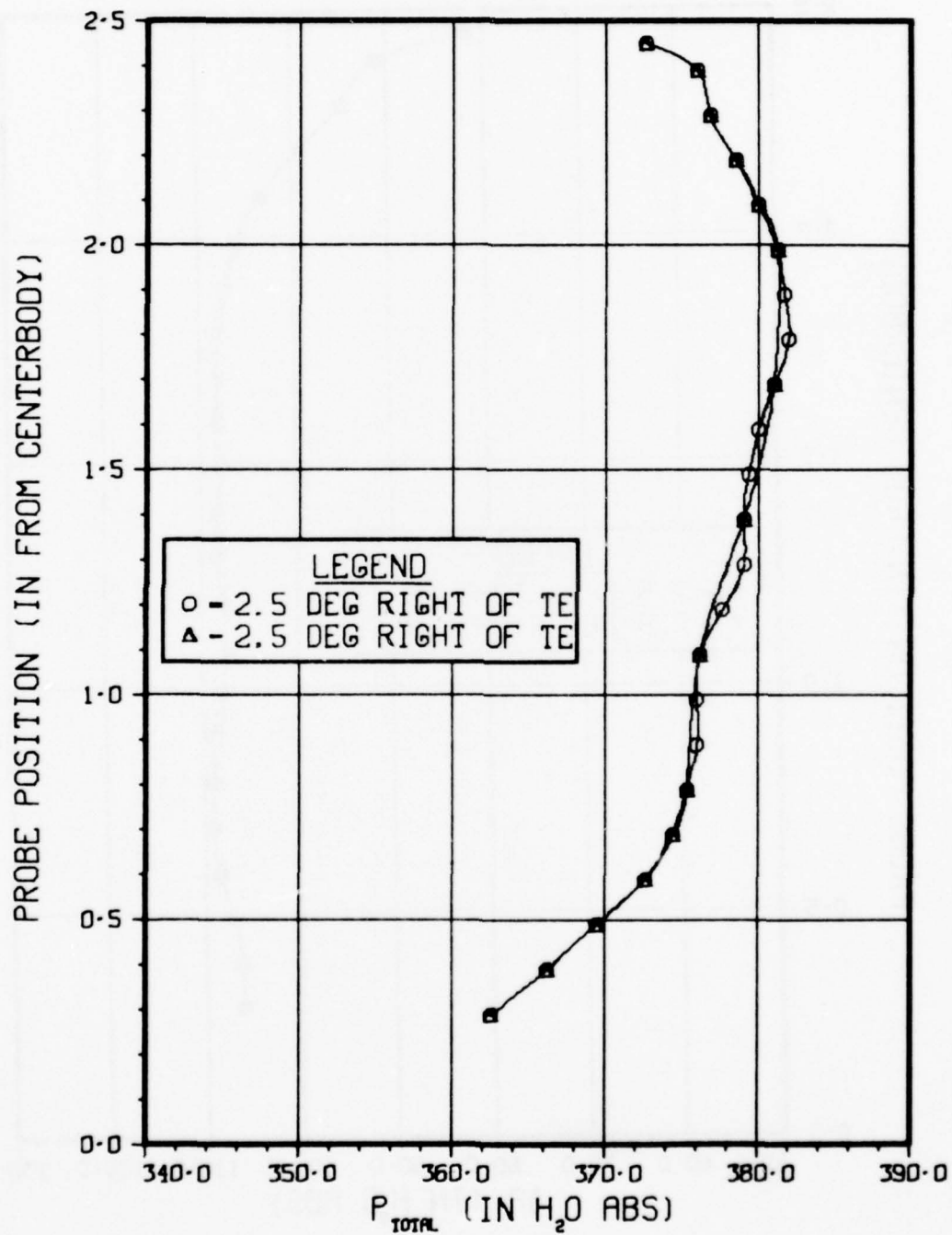
Figure F-1   P$_{total}$ VS Probe Position

Blade Angle 69.7°
Station 3
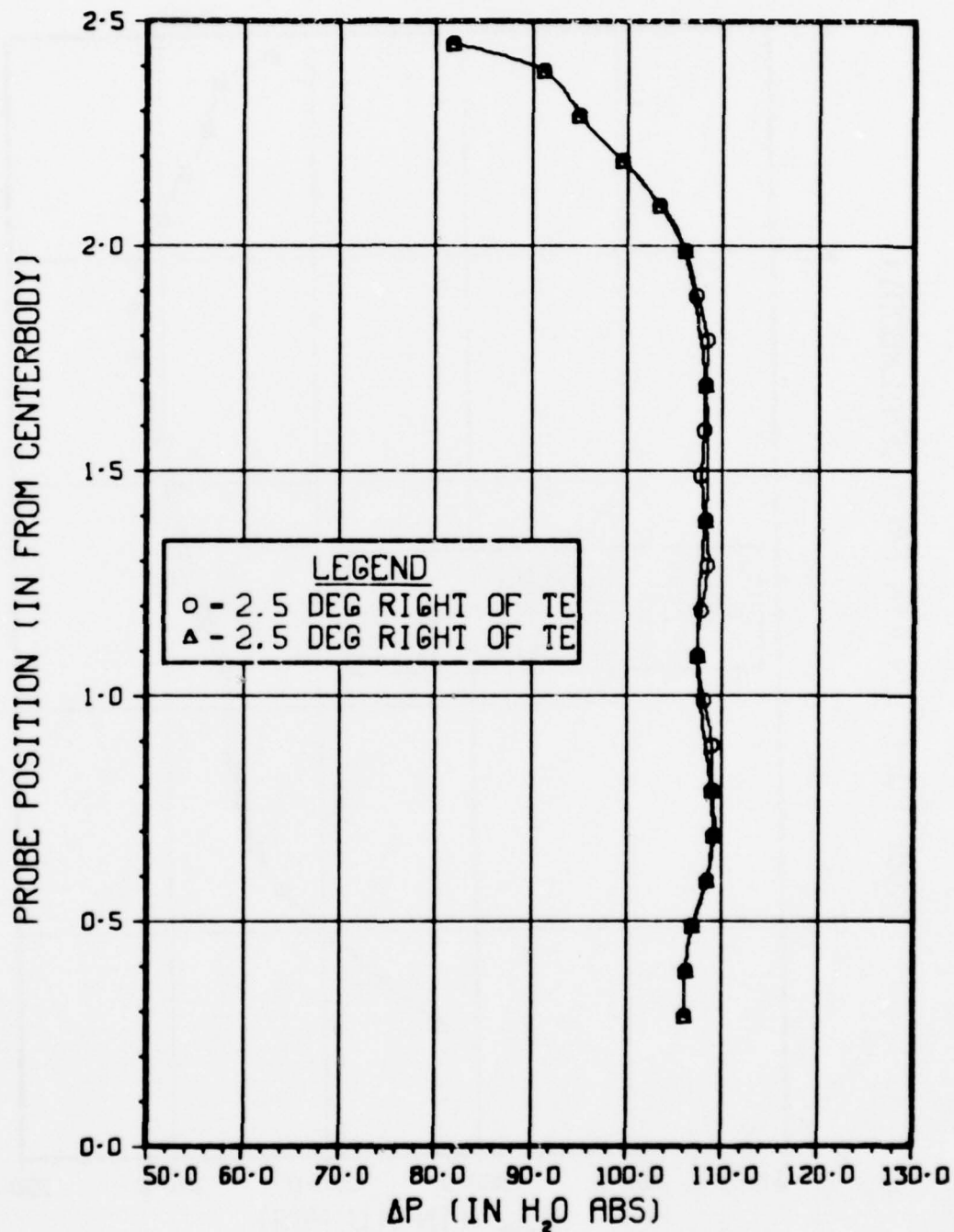
Figure F-2 ΔP VS Probe Position

194

Blade Angle 69.7°
Station 3
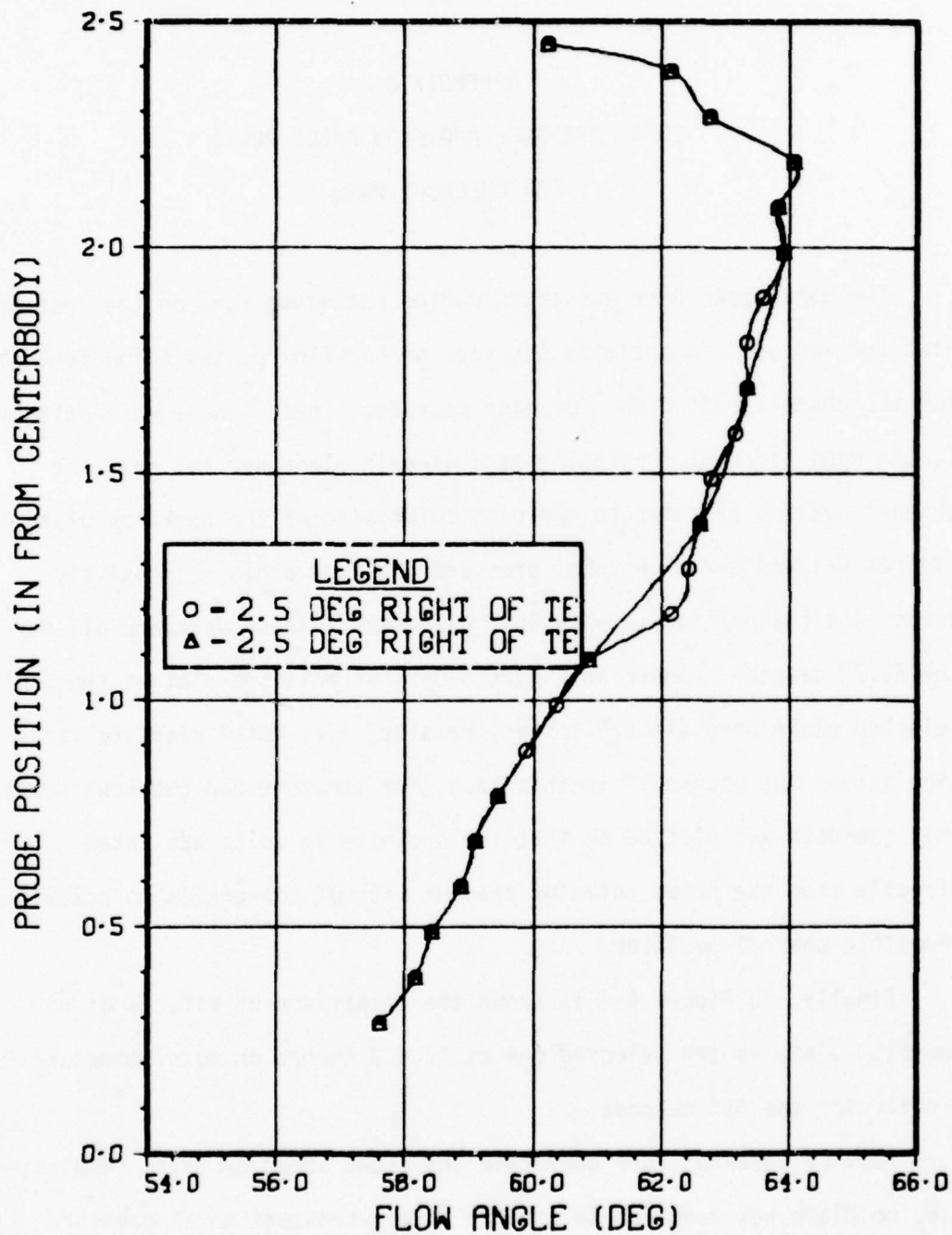
Figure F-3   Flow Angle VS Probe Position

APPENDIX G

TOTAL PRESSURE AND FLOW ANGLE PLOTS

FOR CHECKOUT RUNS

The data shown here was taken during shakedown runs on the test apparatus and was used to optimize the size of backflow plates (flow fences) for the channel exit plane for each cascade. These fences were attached to the wood liner at the test apparatus exit plane and cut down the channel outside diameter to the particular size of the backflow plate bore. Figures G-1 and G-2 show total pressure and flow angle respectively across the channel for varying exit diameters. These data are all for the 69.7° cascade. Shown in Figure G-3 is an enlarged plot of the selected plate bore (14.625 inches) results; i.e. total pressure variation across the channel. In this case, for the intended checkout purpose, only raw data was plotted so that the ordinate in volts was taken directly from the probe actuator readout without conversion to actual geometric channel position.

Finally, in Figure G-4 is shown the comparison of effects of no backflow plate vs the selected one at 15.403 inches on total pressure profile for the 65° cascade.

Further checkout runs confirmed the trend shown by these results; i.e. no plate was required to produce a very constant total pressure profile across the channel when the 60° cascade was installed.

196
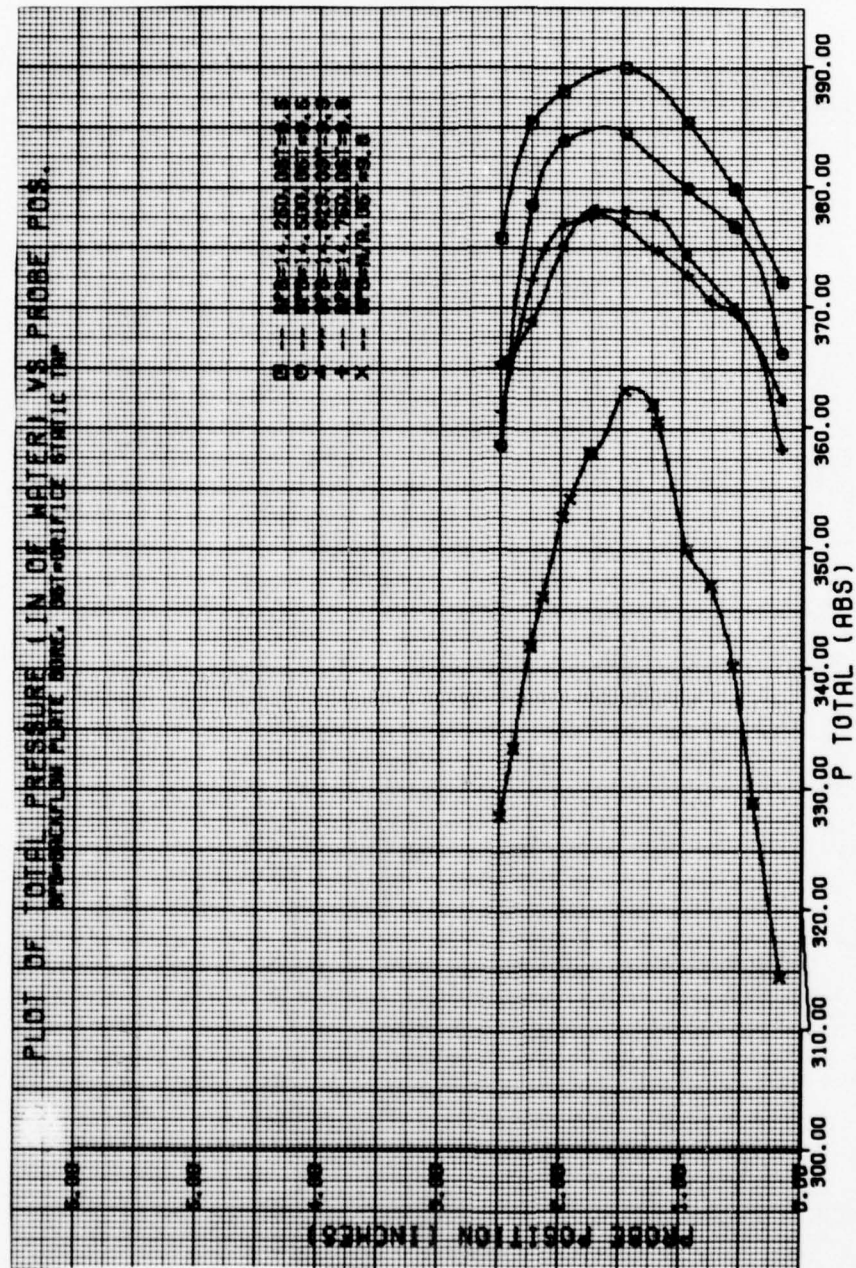
Figure G-1 Total Pressure VS Probe Position - 69.7° Cascade

197
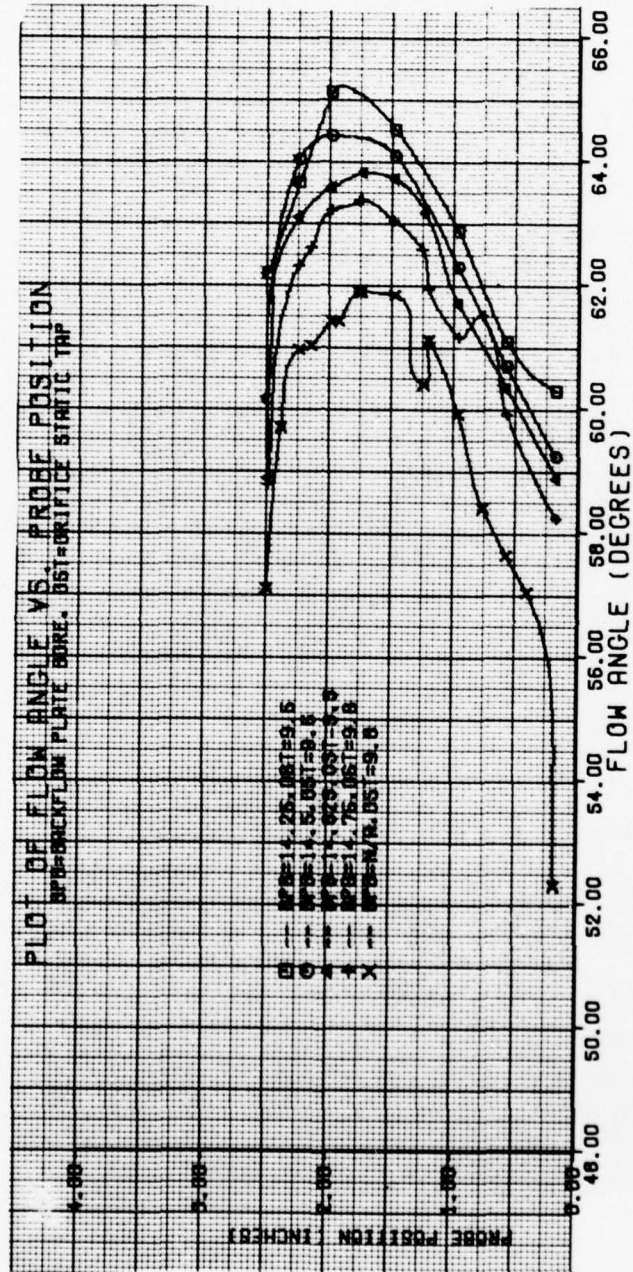
Figure G-2 Flow Angle VS Probe Position - 69.7° Cascade
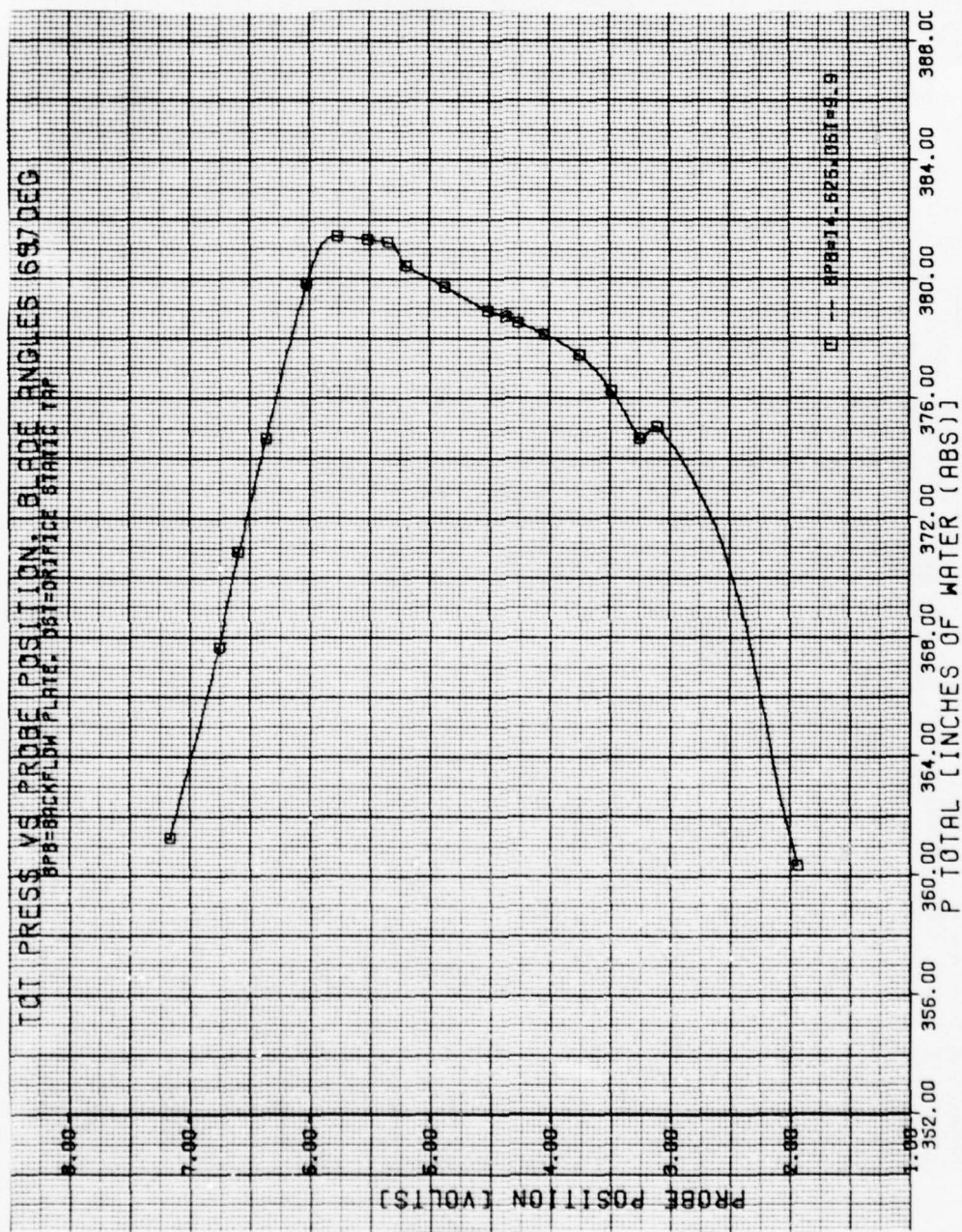
Figure G-3 Total Pressure VS Probe Position - 69.7° Cascade

Figure G-4 Total Pressure VS Probe Position - 65° Cascade

200

Shown in Figure G-5 is a typical flow fence made of wood, while in Figure G-6 one made of aluminum is shown installed in the rig. The "14.25" stamped into the wood is the inside diameter of the fence. The original plan was to use wooden ones while sizing the exit area and then make aluminum ones which would be durable enough for unlimited running. However, experience proved that the wooden ones were quite durable and they were used for most runs.
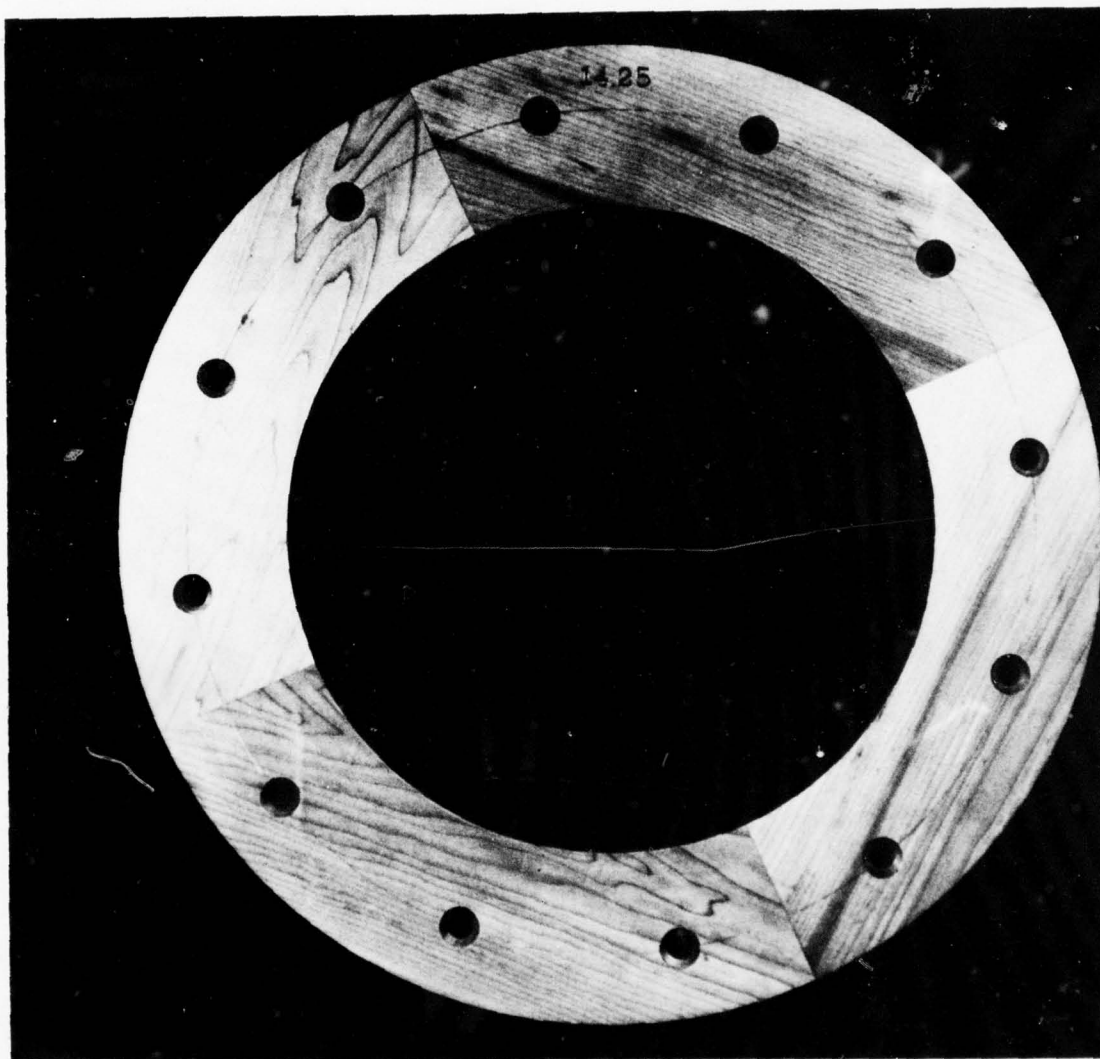
Figure G-5   Typical Wooden Flow Fence
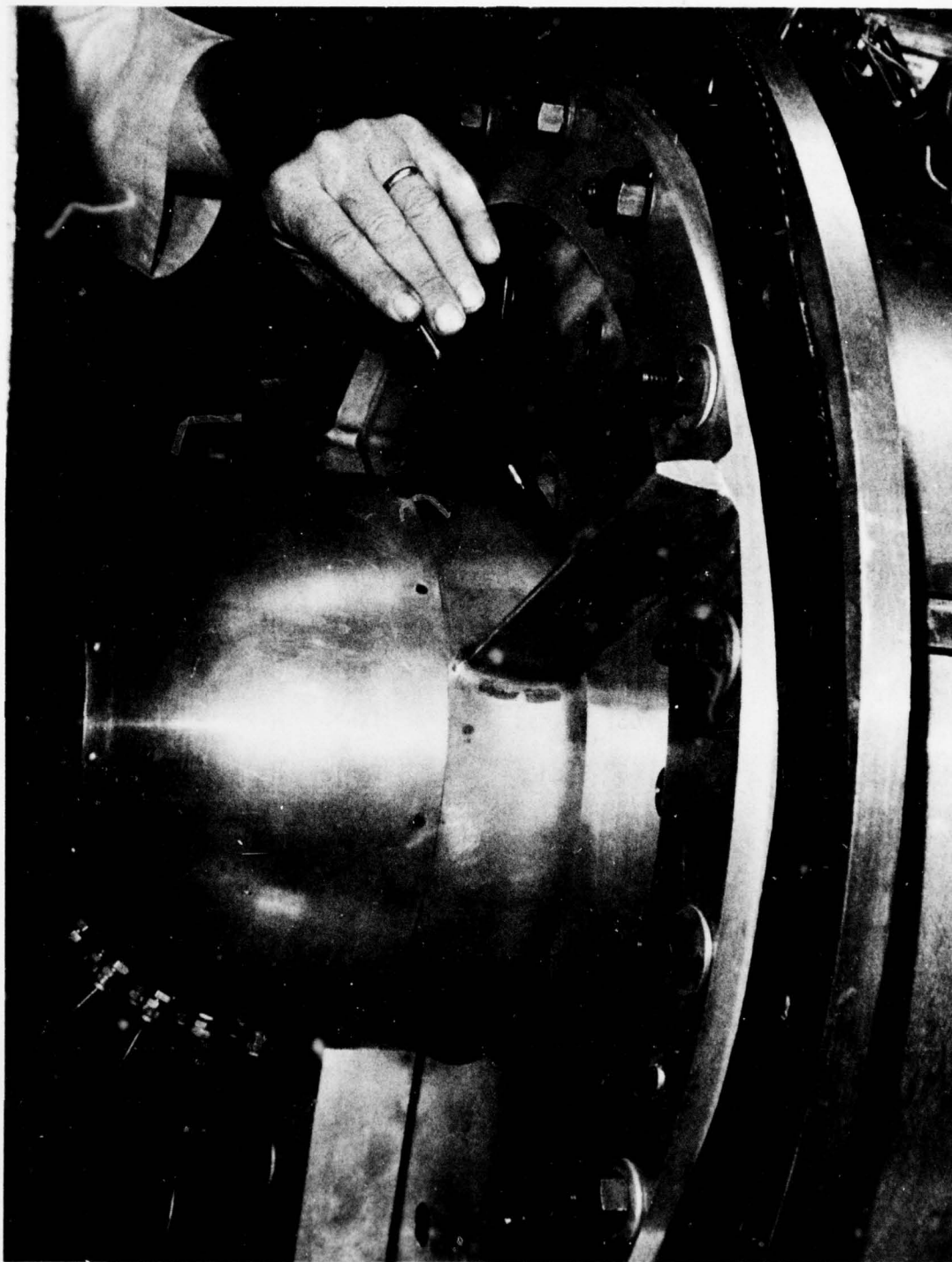
Figure G-6 Flow Fence Installation

203

APPENDIX H

SURFACE ROUGHNESS MEASUREMENTS

Measurements of surface roughness were made on representative sections of all parts of the rig flowpath. The measurement locations and results are shown as follows:
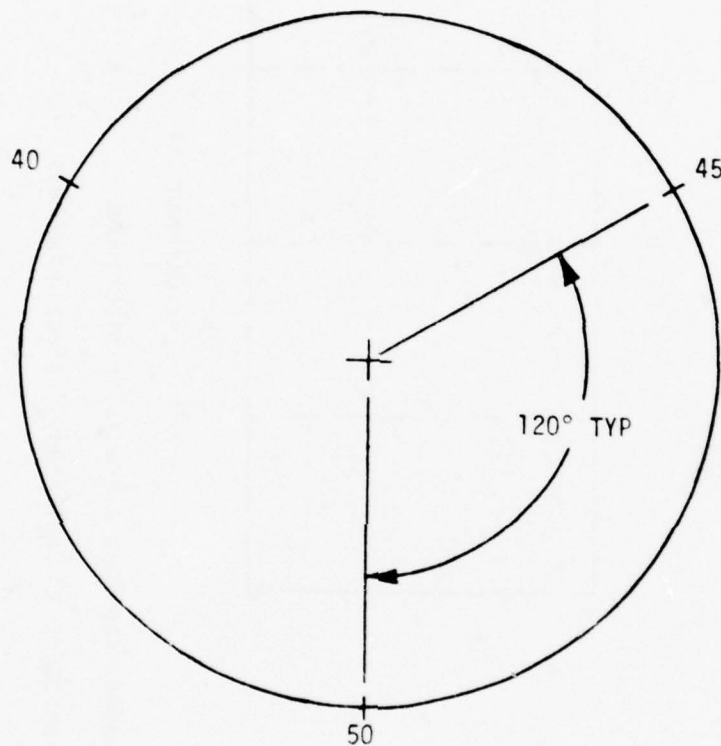
Note: All readings shown as averages in microinches

Figure H-1 Longitudinal Measurement of Inner Liner Surface Roughness

Circumferential

Longitudinal
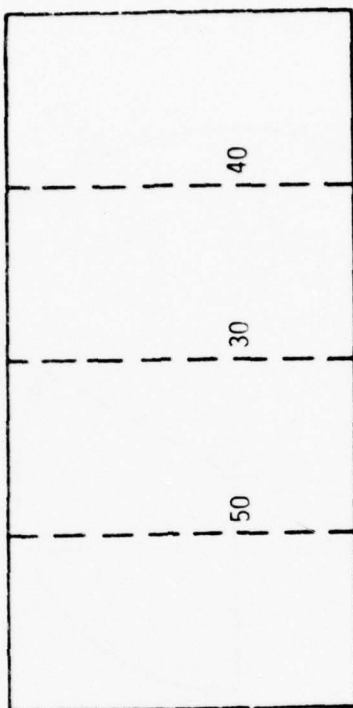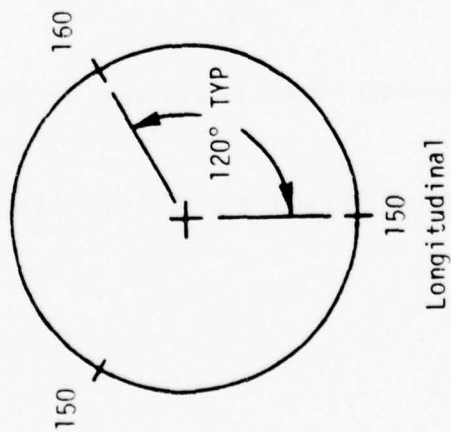
Note: All readings shown as averages in microinches

Figure H-2 Measurement of Centerbody Surface Roughness

206

Table H-1

Surface Roughness - 69.7° Blades
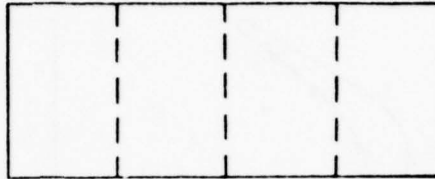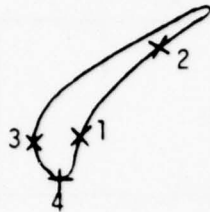
BLADE NUMBER 1

DATA SETS	READING POSITION (measured in RMS)[#]			
	1	2	3	4
1	130	140	140	150
2	130	200	150	190
3	130	160	150	190

BLADE NUMBER 17

DATA SETS	READING POSITION (measured in RMS)[#]			
	1	2	3	4
1	100	90	130	120
2	80	140	120	140
3	110	140	130	150

BLADE NUMBER 33

DATA SETS	READING POSITION (measured in RMS)[#]			
	1	2	3	4
1	90	80	110	130
2	80	110	110	110
3	90	90	110	130

[#]All surface roughness measurements are in microinches.

207

Table H-2

Surface Roughness - 65° Blades
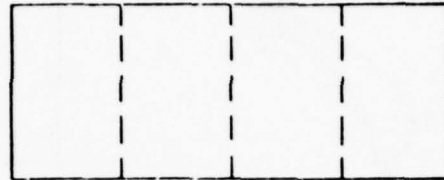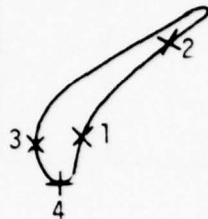
BLADE NUMBER 1

DATA SETS	READING POSITION (measured in RMS)[#]			
	1	2	3	4
1	45	70	70	140
2	40	65	70	135
3	40	65	75	120

BLADE NUMBER 17

DATA SETS	READING POSITION (measured in RMS)[#]			
	1	2	3	4
1	65	165	80	140
2	70	130	90	150
3	65	135	80	130

BLADE NUMBER 33

DATA SETS	READING POSITION (measured in RMS)[#]			
	1	2	3	4
1	70	90	80	150
2	70	95	100	130
3	80	100	90	120

[#]All surface roughness measurements are in microinches.

208

Table H-3

Surface Roughness - 60° Blades
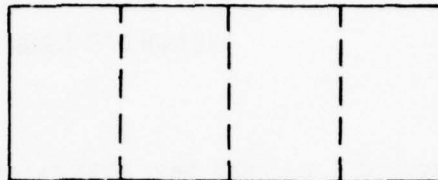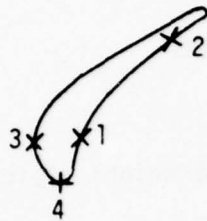
BLADE NUMBER 1

DATA SETS	READING POSITION (measured in RMS)[#]			
	1	2	3	4
1	60	110	60	130
2	70	120	70	110
3	80	130	80	100

BLADE NUMBER 18

DATA SETS	READING POSITION (measured in RMS)[#]			
	1	2	3	4
1	60	120	80	130
2	50	130	70	130
3	70	140	70	110

BLADE NUMBER 35

DATA SETS	READING POSITION (measured in RMS)[#]			
	1	2	3	4
1	60	110	70	130
2	55	135	75	120
3	50	125	75	95

[#]All surface roughness measurements are in microinches.

209

APPENDIX I

REYNOLD'S NUMBER CALCULATIONS

Reynold's numbers based on twice the channel height (twice the blade span) were calculated over the entire range of flow rates investigated. Table I-1 summarizes these results and the actual calculations follow. In the first set of calculations the extreme cases of velocities achieved, both high and low, were used and in the second set average values were used. The velocities were, of course, determined from the wedge probe pressure data and are in the measured direction of whirling flow. The summary table is based on the second set of calculations and the first set is included here for extreme bounding information only.

Table I-1

Flow Ranges Investigated

Blade Angle	Flow Rate Range lb/sec	Reynolds No Range $(\times 10^{-6})$
69.7°	11 - 12.5	1.416 - 1.957
65°	12 - 13.5	1.312 - 1.911
60°	13 - 15	1.151 - 1.566

210

Reynold's Number Calculations - Extreme Cases

60° Blades Low Flow

$$Re = \frac{(698 \text{ ft/sec}) \ (0.071 \text{ lbm/ft}^3) \ (5/12 \text{ ft})}{1.285 \times 10^{-5} \text{ lbm/ft sec}} = 1.607 \times 10^6$$

$$Re = \frac{(383.6) \ (0.071) \ (5/12)}{1.285 \times 10^{-5}} = 8.83 \times 10^5$$

65° Blades Low Flow

$$Re = \frac{(416.5) \ (0.071) \ (5/12)}{1.285 \times 10^{-5}} = 9.59 \times 10^5$$

$$Re = \frac{(648.45) \ (0.071) \ (5/12)}{1.285 \times 10^{-5}} = 1.493 \times 10^6$$

65° Blades Low Flow

$$Re = \frac{(473.24) \ (0.071) \ (5/12)}{1.285 \times 10^{-5}} = 1.089 \times 10^6$$

$$Re = \frac{(719.9) \ (0.071) \ (5/12)}{1.285 \times 10^{-5}} = 1.657 \times 10^6$$

60° Blades High Flow

$$Re = \frac{(494.2) \ (0.071) \ (5/12)}{1.285 \times 10^{-5}} = 1.138 \times 10^6$$

$$Re = \frac{(701.9) \ (0.071) \ (5/12)}{1.285 \times 10^{-5}} = 1.616 \times 10^6$$

65° Blades High Flow

$$Re = \frac{(465)\ (0.071)\ (5/12)}{1.285 \times 10^{-5}} = 1.07 \times 10^{6}$$

$$Re = \frac{(844.51)\ (0.071)\ (5/12)}{1.285 \times 10^{-5}} = 1.944 \times 10^{6}$$

69.7° Blades High Flow

$$Re = \frac{(701.26)\ (0.071)\ (5/12)}{1.285 \times 10^{-5}} = 1.614 \times 10^{6}$$

$$Re = \frac{(828.9)\ (0.071)\ (5/12)}{1.285 \times 10^{-5}} = 1.908 \times 10^{6}$$

Reynold's Number Calculations - Average Cases

60° Blades

$$Re = \frac{(680\ ft/sec)\ (.071\ lbm/ft^3)\ (5/12\ ft)}{1.285 \times 10^{-5}\ lbm/ft\text{-}sec} = 1.5655 \times 10^{6}$$

$$Re = \frac{(500\ ft/sec)\ (.071\ lbm/ft^3)\ (5/12\ ft)}{1.285 \times 10^{-5}\ lbm/ft\text{-}sec} = 1.1511 \times 10^{6}$$

$$\text{Range} \rightarrow Re = \frac{1.5655 \times 10^{6}}{1.1511 \times 10^{6}}$$

65° Blades

$$Re = \frac{(830)\ (.071\ lbm/ft^3)\ (5/12\ ft)}{1.285 \times 10^{-5}\ lbm/ft\text{-}sec} = 1.9108 \times 10^{6}$$

$$Re = \frac{(570\ ft/sec)\ (.071\ lbm/ft^3)\ (5/12\ ft)}{1.285 \times 10^{-5}\ lbm/ft\text{-}sec} = 1.3123 \times 10^{6}$$

$$\text{Range} \rightarrow Re \approx \frac{1.9108 \times 10^{6}}{1.3123 \times 10^{6}}$$

69.7° Blades

$$Re = \frac{(850 \text{ ft/sec}) \, (.071 \text{ lbm/ft}^3) \, (5/12 \text{ ft})}{1.285 \times 10^{-5} \text{ lbm/ft-sec}} = 1.9569 \times 10^6$$

$$Re = \frac{(615 \text{ ft/sec}) \, (.071 \text{ lbm/ft}^3) \, (5/12 \text{ ft})}{1.285 \times 10^{-5} \text{ lbm/ft-sec}} = 1.41586 \times 10^6$$

$$\text{Range} \rightarrow Re = \frac{1.9569 \times 10^6}{1.41586 \times 10^6}$$

APPENDIX J

MASS FLOW CALCULATION PROCEDURE

A computer program was written which calculated the mass flow as a function of probe position and then summed to get the total mass flow in the channel. While calculating the mass flow, other useful information was generated and printed for each case as follows: Measured Mach number, Axial Mach number and velocity (ft/sec), Density (lb/ft^3), and Pressure ratio PS/PT.

The information input to the computer was the area slice, total pressure, pressure difference, flow temperature and flow angle. The complete program is listed in Table J-1, and the line numbers referred to in the following description of operation are shown there. The program first forms the pressure ratio, (lines 14, 27, and 28),

$$\text{Pressure Ratio} = PCC = \frac{PS}{PT}$$

and from this calculates the Mach number (line 29),

$$\text{Mach Number} = A = \left\{ \left[\left(\frac{1}{PCC} \right)^{\gamma-1/\gamma} - 1 \right] \times 5 \right\}^{1/2} = \left[5 \left(\frac{1}{PCC}^{.2857} - 1 \right) \right]^{1/2}$$

Since for mass flow purposes, the axial velocity is desired, first the axial Mach number is found (line 30),

Axial Mach Number = $AX = A \cos \theta$

and then the axial velocity is computed (lines 25 and 31),

214

Axial Velocity = $A \cos \Theta \sqrt{\gamma R g_c TE}$

$$= AX \sqrt{1.4(53.4) \ (32.2) \ TE}$$

The density is then calculated (line 33) assuming an ideal gas,

$$P = \rho RT$$

or

$$\rho = \frac{P}{RT} = \frac{PS(5.198)}{53.4(TE)} = RHO$$

Mass flow rate (line 35) can now be calculated,

$$\text{mass flow rate} = FLOW = \rho AV = RHO(AR)V$$

Flow rate/area is calculated by line 37 ,

$$\text{Flow rate/area} = \rho AV/A = FLOW/AR = ARF$$

The total mass flow then comes from adding the various contributions from the individual slices of area and is done on line 39,

$$\text{Total mass flow} = FLOWS = (FLOW)_1 + (FLOW)_2 + \ldots + (FLOW)_{23}$$

The remaining cards transform the various parameters into proper units or introduce various constants or are logic and control cards. The program can handle N sets of data that consist of 23 data points.

215

Flow Rate Calculation Program

```
1              PROGRAM INTP(INPUT,OUTPUT,TAPE5=INPUT,TAPE6=OUTPUT)
               READ(5,12)N
               J=1
            51 READ(5,8)SA,SB,SC,SD,SE,SF,SG
5              WRITE(6,11)SA,SB,SC,SD,SE
               WRITE(6,19)SF,SG
               FLOWS=0
       C       WRITE THE HEADINGS
               WRITE(6,21)
10             WRITE(6,23)
               I=1
         1     READ(5,10)AR,FT,PO,T,THETA
       C       READ THE AREA, TEMP., AND THE FLOW ANGLE FOR THE CALCULATIONS
               PS=FT-PO
15     C       CONSTANTS
               GAM=1.4
               GAS=53.4
               GRA=32.2
       C       CONVERSION OF T TO DEGREES R
20             TE=T+459.67
       C       CONVERSION FACTOR
               TTHETA=THETA*3.141592694/180.
       C       TTHETA IS RADS
               CTHETA=COS(TTHETA)
25             ROOT=SQRT(GAM*GAS*GRA*TE)
       C       CALCULATION OF VELOCITY-AXIAL
               PC=(PT/PS)
               PCC=1/PC
               A=SQRT((((PC**.2857)-1)*5)
30             AX=A*CTHETA
               V=A*ROOT*CTHETA
       C       CALCULATION OF DENSITY
               RHO=PS*5.196/(GAS*TE)
       C       CALCULATION OF MASS FLOW RATE
35             FLOW=RHO*AR*V
       C       CALCULATION OF FLOW RATE/ UNIT AREA
               ARF=FLOW/AR
       C       TOTAL MASS FLOW RATES
               FLOWS=FLOWS+FLOW
40             WRITE(6,22)AR,THETA,A,AX,RHO,FLOW,ARF,V,PCC
               IF(I.EQ.23) GO TO 999
               I=I+1
               GO TO 1
           999 WRITE(6,24)FLOWS
45         200 IF(J.EQ.N)GOTO201
               J=J+1
               GO TO 51
           201 STOP
            10 FORMAT(5F10.6)
50          12 FORMAT(I2)
            15 FORMAT(" X NOT CALIBRATED FOR THIS NUMBER   ",F10.5)
             8 FORMAT(3I2,F5.2,I2,F5.2,F4.1)
            11 FORMAT(1H,///,9X,"DATE",2X,I2,"/",I2,"/",I2,5X,"POSITION: ",F5.2,
              1" DEGREES LEFT OF ZERO",5X,"SADDLE STATION ",I2)
55          19 FORMAT(28X,"CHAMBER PRESSURE ",F5.2," IN HG",5X,"BLADE ANGLE ",
              1F5.2," DEGREES")
            21 FORMAT(1H,///,9X,"AREA",4X,"FLOW ANGLE",2X,"MACH NUMBER-",2X,
              1"MACH NUMBER-",2X,"DENSITY",3X,"FLOW RATE",3X,"FLOW RATE/AREA",2X,
              1"VELOCITY-AXIAL",2X,"PS/PT")
60          24 FORMAT(9X,"TOTAL FLOW RATE IS ",F12.6," LB/SEC")
            22 FORMAT(8X,F7.6,2X,F5.2,7X,F10.8,  4X,F10.8,4X,F7.6,3X,F8.6,4X,F11.8
              1,4X,F9.4,7X,F7.6)
            23 FORMAT(9X,"FT**2",3X,"DEGREES",5X,"BLADE EXIT",4X,"AXIAL", 9X,
              1"LB/FT**3",2X,"LB/SEC",6X,"LB/SEC/FT**2",4X,"FT/SEC")
65             END
```

APPENDIX K

CHECK RUN AT STATION SEVEN

Presented in this appendix are the results from a traverse made at station seven for the purpose of pursuing further the general observation that relatively little flow straightening was occurring between stations one and three. As discussed in Chapter IV, these results do indeed verify that relatively little flow straightening occurs in several chord lengths downstream from the cascade.

217

Blade Angle 65.0°
Station 7
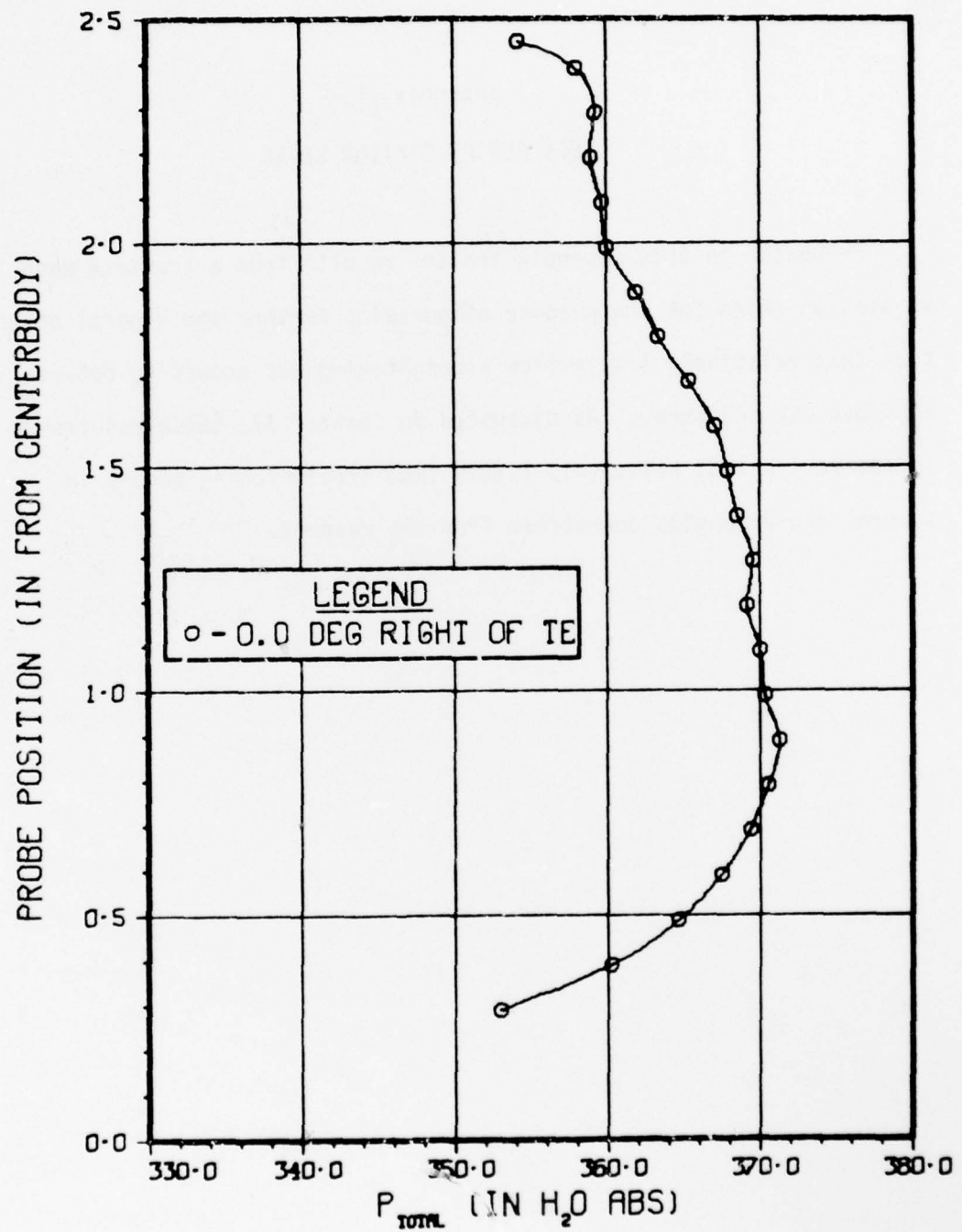
Figure K-1 P_{total} VS Probe Position

218

Blade Angle 65.0°
Station 7
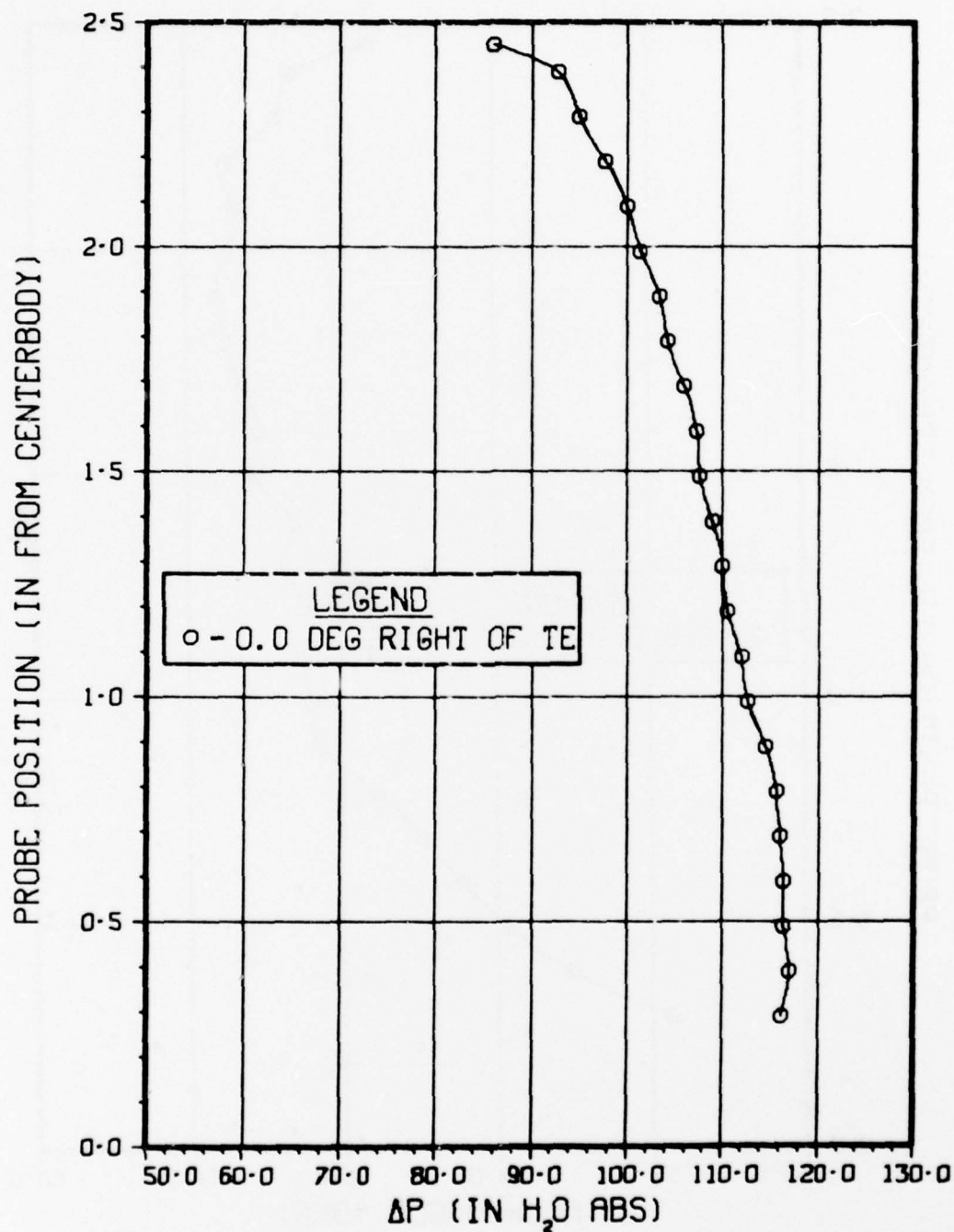
Figure K-2   ΔP VS Probe Position

219

Blade Angle 65.0°
Station 7
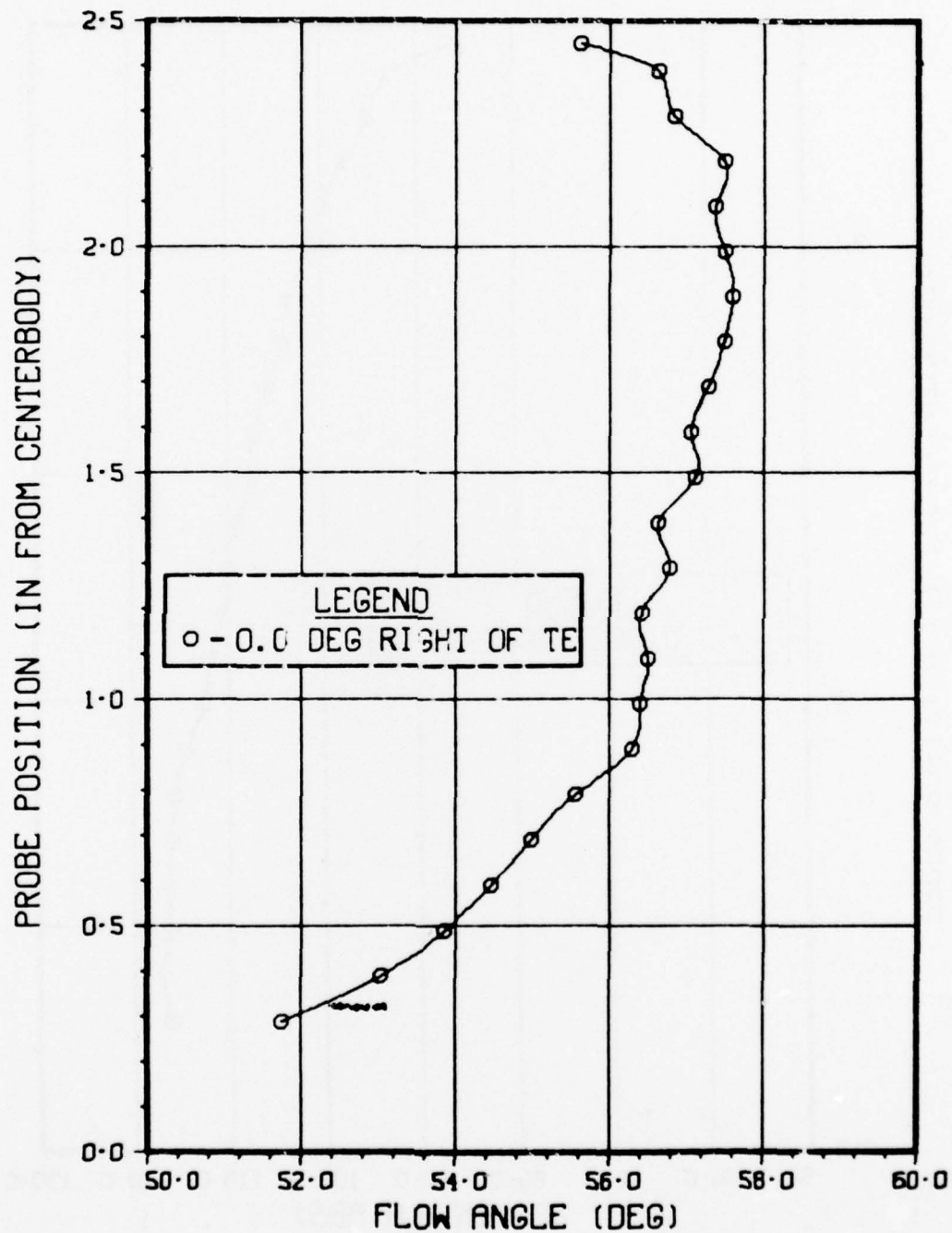
Figure K-3 Flow Angle VS Probe Position

220

Table K-1

Mass Flow Calculation – Station 7, 65°

DATE   7/ 4/77   POSITION: 7.50 DEGREES LEFT OF ZERO   SADDLE STATION 7
CHAMBER PRESSURE 9.85 IN HG   BLADE ANGLE 65.00 DEGREES
ACTUAL PROBE POSITION: 0° PROBE DIRECTLY BEHIND T.E.

AREA FT**2	FLOW ANGLE DEGREES	MACH NUMBER- BLADE EXIT	MACH NUMBER- AXIAL	DENSITY LB/FT**3	FLOW RATE LB/SEC	FLOW RATE/AREA LB/SEC/FT**2	VELOCITY-AXIAL FT/SEC	PS/PT
.024116	51.76	.77740276	.48139189	.045207	2.027630	24.10516370	533.2193	.670728
.025700	53.03	.77056593	.46341586	.046448	.612746	23.84226603	513.3080	.675190
.026136	53.85	.76201550	.44951398	.047496	.517481	23.62563569	497.4206	.684746
.026573	54.46	.75327575	.44076383	.048032	.622529	23.42713624	487.7380	.683179
.027009	54.98	.75410396	.43275185	.048472	.626934	23.21205887	478.8722	.685892
.027445	55.56	.75087832	.42465390	.048875	.629702	22.94414080	469.4490	.687989
.027882	56.29	.74541207	.41369596	.049220	.527622	22.50992219	457.3352	.691541
.028318	56.40	.73866757	.40877017	.049509	.632923	22.35057684	451.4445	.695922
.028754	56.51	.73612747	.40618893	.049586	.639601	22.24390250	448.5937	.697568
.029190	56.41	.73141485	.40465245	.049682	.643097	22.20269573	446.8969	.700623
.029633	56.78	.72882633	.39929134	.049757	.650833	21.96312374	441.4111	.702300
.030058	56.64	.72545448	.39893125	.049776	.659826	21.95177251	441.0130	.704478
.030499	57.12	.72074847	.39128988	.049910	.658439	21.58856990	432.5556	.707529
.030936	57.05	.72059353	.39183028	.049795	.667269	21.56933690	433.1630	.707629
.031373	57.28	.71676997	.38743855	.049737	.568337	21.30294551	428.3080	.710101
.031808	57.60	.71199580	.38265986	.049582	.667815	20.99519224	423.4416	.713185
.032245	57.60	.71029974	.38059227	.049467	.571773	20.83339476	421.1537	.714286
.032682	57.49	.70461151	.37836873	.049487	.577161	20.71969190	418.6932	.718333
.033117	57.37	.69844999	.37661248	.049580	.684957	20.68294901	417.1592	.721913
.033554	57.49	.68931732	.37047138	.049886	.686887	20.47108695	410.3569	.727779
.033990	56.84	.67721977	.37042493	.050360	.703026	20.58332938	410.7073	.735523
.027507	56.63	.66953629	.36772406	.050471	.566585	20.59785131	408.1122	.741061
.027785	55.62	.64350258	.36337235	.050904	.570950	20.54834149	403.6765	.756917

TOTAL FLOW RATE IS   16.219124 LB/SEC

221

Blade Angle 65.0°
Station 7
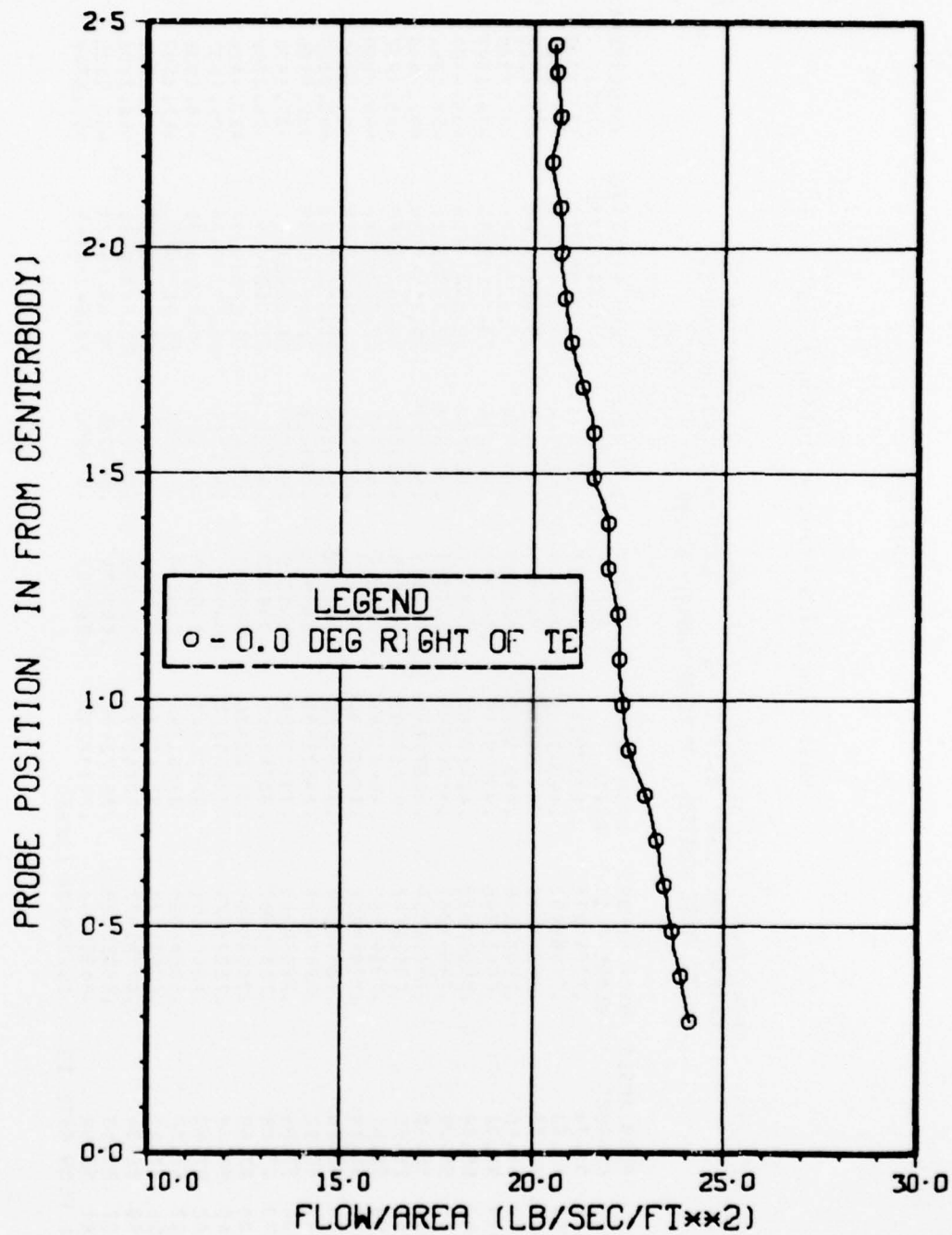
Figure K-4   Flow VS Probe Position

APPENDIX L

ERROR ANALYSIS

All pressure, temperature and flow angle measurements in this experiment were set up in accordance with the data and recommendations reported by Dean[24] and applied as closely as possible to this particular experimental apparatus. Other references used were John[28, pp. 330-338] and United Sensor and Control Corporation[29]. A standard, commercially-available wedge probe manufactured by United Sensor and Control Corporation was chosen as the traversing pressure and temperature sensor. It was identified by the manufacturer as part number WT 250-24-CD-C/C-36 and was configured with a wedge at the end of a tube 0.25 inches in outer diameter. Based on United Sensor and Control Corporation[29] experience and recommendations, the effect of probe size as a function of channel area can be determined as follows:

"For round probes perpendicular to the flow, the drop in static
pressure at the probe cross-section and downstream from it is
approximately:"

$$\frac{P_{s_2} - P_{s_2}}{P_t - P_{s_1}} = 1.2 \frac{a}{A}$$

Where: P_{s_1} and P_{s_2} are the original and modified static
pressures respectively

223

P_t = Total pressure

a = Cross sectional area of probe

A = Channel area

For a probe diameter of 0.25 inches, a = .04906 in^2 and the annulus area A = 105.98 in^2 therefore,

$$\frac{a}{A} = .00046$$

and

$$\frac{P_{s_1} - P_{s_2}}{P_t - P_{s_1}} = .00056$$

Hence, the conclusion that the disturbance effect of the probe on static pressure readings may be neglected is reasonable.

Based on the work of Keast[30], if the location of the direction-measuring taps in the wedge faces is such that:

$$\frac{p_i - p_s}{\frac{\rho}{2g_c}V^2} = 0$$

Where:

P_i = Indicated Static Pressure

P_s = Actual Static Pressure

ρ = Density

V = Velocity

g_c = Gravitational Constant

then the static pressure can be read directly. For this relationship to be satisfied, Keast's data shows that the ratio of the distance of the taps from the leading edge of the wedge to the overall length of the wedge face must equal 0.375. Measurement of the probe used in this experiment

224

indicated that this relationship was satisfied.

It is recognized (see John[28, p. 331]) that the most ideal static pressure probe would have a considerably longer and conical nose section with the measuring tap located 10 to 20 probe diameters downstream from the nose. However, such a probe would be totally impractical for use in this experiment and, the use of a wedge-type probe was considered a very reasonable compromise. The probe manufacturer, United Sensor and Control Corporation, has stated in their catalog that this probe, TYPE WT, is usable up to Mach 0.7 and in general, that value was not exceeded by more than 5% in any of the traverses made in this experiment. However, as a final observation, Keast[3, p. 687] reports that his wedge probe "measures the average static pressure to within 1.5 per cent when used for a wake traverse of a turbine cascade at an outlet Mach number of 0.8 and was even closer at lower Mach numbers."

The calibration data bulletin[29] supplied by the manufacturer of the wedge probe discusses several sources of error in static pressure measurement. These are:

  Mach number effects

  Pitch Angle

  Yaw Angle

  Immersion Depth

The yaw angle error is declared by the manufacturer to be zero when the probe has been rotated such that the wedge face taps indicate equal pressure. Specific calibration data was supplied on Mach number effects and pitch angle effects. For the probe used in this experiment, the pitch angle effects cancelled the Mach number effects almost completely in the

range of Mach numbers of greatest interest; i.e. 0.6 and above. The remaining effect of immersion depth is presented as "due to effects of boundaries of the passage and the secondary flow along the upstream edge of the probe which in turn is influenced by the total pressure gradient in the passage." For probes cantilevered out from one side of a passage (the case for this experiment), it is stated that the probe will read true static pressure "when the holes (taps) are ten probe diameters away from the boundary they project through and the probe tip is at least one diameter from the opposite wall." The specific data supplied on that source of error shows, for the size channel used in this experiment, a maximum error of 1.5% of indicated static pressure for the range of static pressures measured.

The readout of probe pressure indications was accomplished by visual observation of Kollsman aneroid gages graduated in inches of water. These were calibrated by the Precision Measuring Equipment Laboratory in accordance with the provisions of Technical Order (TO) 00-20-14, Air Force Metrology and Calibration Program. Specifically, the Kollsman gages are category 3 items. The standards used are directly traceable to the National Bureau of Standards (NBS) through the Directorate of Metrology, Newark Air Force Station, Air Force Measurement Standards Laboratory, and the Wright-Patterson Air Force Base Precision Measurement Equipment Laboratory (PMEL).

The inner wall (centerbody) static pressures were read from single tube vertical mercury manometers graduated in tenths of an inch, and the scales were "zeroed" prior to each run.

The outer wall static pressures were read from Kollsman aneroid gages identical to those used for the wedge probe. Therefore, the accuracy

226

discussion presented for the wedge probe gages is directly applicable and will not be repeated here.

Both stream total temperature and air inlet temperature were measured with thermocouples. The total temperature thermocouple was built into the wedge probe while the air inlet thermocouple was suspended approximately 5 feet in front of and 4 feet above the bellmouth centerline.

These were copper-constantan thermocouples and Dean[24, p. 52] reports a standard limit of error range of $\pm$ 1 1/2°F for the temperature range of -75 to +200°F. Dean[24, p. 43] classifies all common temperature measuring situations into three ranges as follows:

Range 1: Measurements in low velocity streams with negligible radiation.

Range 2: Measurement in high velocity streams with negligible radiation.

Range 3: Measurements under conditions specified in 1 or 2 but with significant radiation effects.

For the two temperatures required by this experiment, Range 1 covers the air inlet measurement, and Range 2 covers the stagnation temperature measurement at each traverse position.

Measurements within Range 1 are reported to be achievable with bare thermocouples or mercury thermometers with negligible error. In the absence of radiation effects, measurements within Range 2 are reported to be achievable over a wide range of subsonic and supersonic Mach numbers with a correction factor as high as 0.99. This is accomplished by various designs of vented, diffusion-type containers for the thermocouple inside the probe, and the United Sensor Type WT probe used in this experiment fits

227

these specifications suitably for the Mach number range explored here. Hence, the conclusion that correction of the raw temperature data is not required is considered reasonable.

Calibration of the entire temperature instrumentation subsystem was conducted by the Air Force Aero Propulsion Laboratory Instrumentation Shop. The Brown recorder is a category 2 item and was calibrated using a PMEL-calibrated 32°F reference junction and a PMEL-calibrated precision potentiometer. International Practical Temperature Scale of 1968 (IPTS-68) conversion tables were used to convert the thermocouple readings to actual temperature values. Thus, system traceability is established back to NBS just as for the pressure gages.

Measurement of both the radial location of the probe in the flow channel and the flow angle by use of a hydraulic servoactuator system was selected due to the convenience and proven repeatability of such devices. The calibration of this system in both linear and angular modes is covered in detail in Appendix C. In addition, determination of the so-called "zero reference" for the particular wedge probe used is presented in Appendix B. Selection of the "null method" rather than the "fixed method" as described by Dean[24, p. 101] was made to eliminate the requirement for any compressibility correction on flow angle indications from the wedge.

In summary, it is estimated that the accumulated total error on each parameter is bounded as follows:

Flow Angle	$\pm 0.25°$
Stream Total Pressure	1% of indicated pressure
Stream Static Pressure	2% of indicated pressure

228

Outer Wall Static Pressure	±0.5 inches of water
Inner Wall Static Pressure	±0.1 inch of mercury
Total Temperature	$\pm1\ 1/2°F$
Air Inlet Temperature	$\pm1\ 1/2°F$
Circumferential Position	$\pm1/4°$
Radial Position	$\pm.005$ inches

The equations and computer prediction models governing the results and conclusions presented in this Dissertation are such that the most critical measurement is clearly the flow angle. Accurate determination of flow angle was a primary objective from the outset and, it is considered reasonable to conclude that very acceptable accuracy was achieved. The next critical measurement was pressure and within the limits of resources available for this experiment, the error is considered acceptable to support the conclusions drawn. The error bounds established for the temperature measurements will result in no significant change to the conclusions drawn here.

Finally, with respect to the circumferential location in the channel and the radial traverse points, the errors here have the least possible effect on the conclusions. However, as presented in the main body of the Dissertation, repeatability of results was verified several times during the course of the experimental phase and was proven to be quite satisfactory. This verification required returning to a given circumferential location and repeating a radial traverse.

229

BIBLIOGRAPHY

1. Wu, Chung-Hua, Wolfenstein, L., "Application of Radial-Equilibrium Condition to Axial-Flow Compressor and Turbine Design," NACA Report 955, 1950.

2. Wu, Chung-Hua, "A General Theory of Three-Dimensional Flow in Subsonic and Supersonic Turbomachines of Axial-, Radial-, and Mixed-Flow Types," NACA Technical Note 2604, 1952.

3. Wu, Chung-Hua, "A General Through-Flow Theory of Fluid Flow with Subsonic or Supersonic Velocity in Turbomachines of Arbitrary Hub and Casing Shapes," NACA Technical Note 2302, 1951.

4. Stanitz, J. D., "Approximate Design Method for High-Solidity Blade Elements in Compressors and Turbines," NACA Technical Note 2408, 1951.

5. Wu, Chung-Hua, Brown, C. A., "Method of Analysis for Compressible Flow Past Arbitrary Turbomachine Blades on General Surface of Revolution," NACA Technical Note 2407, 1951.

6. Huppert, M. C., MacGregor, C., "Comparison Between Predicted and Observed Performance of Gas-Turbine Stator Blade Designed for Free-Vortex Flow," NACA Technical Note 1810, 1949.

7. Smith, L. H., Jr., Traugott, S. C., Wislicenus, G. G., "A Practical Solution of a Three-Dimensional Flow Problem of Axial-Flow Turbomachinery," ASME Transactions, Vol. 75, July 1953, pp. 789-803.

8. Shepherd, D. G., Principles of Turbomachinery, The MacMillan Company, New York, 1956.

9. Giamati, C. C., Jr., Finger, H. B., "Design Velocity Distribution in Meridional Plane," NACA Special Publication 36, 1965, pp. 255-278.

10. Mereiros, A. A., Hood, B. J., "Chart Procedures for Design Velocity Distribution," NACA Special Publication 36, 1965, pp. 279-295.

11. Herzig, H. Z., Hansen, A. G., "Three-Dimensional Compressor Flow Theory and Real Flow Effects," NACA Special Publication 36, 1965, pp. 365-384.

12. Smith, L. H. Jr., "The Radial Equilibrium Equation of Turbomachinery," ASME Journal of Engineering for Power, January 1966, pp. 1-12.

13. Hawthorne, W. R., and Horlock, J. H., "Actuator Disk Theory of the Incompressible Flow in Axial Compressors," Procedure of the Institution of Mechanical Engineers, Volume 176, Number 30, 1962.

14. Hawthorne, W. R., and Ringrose, J., "Actuator Disk Theory of the Compressible Flow in Free-Vortex Turbomachinery," Thermodynamics and Fluid Mechanics Convention of Institution of Mechanical Engineers, Cambridge 9-10 April 1964.

15. Marble, Frank E., "Three-Dimensional Flow in Turbomachines," Section C of Aerodynamics of Turbines and Compressors, Princeton University Press, 1964.

16. Dodge, P. R., "Three-Dimensional Heat Transfer Analysis Program," AiResearch Manufacturing Company, AFAPL-TR-77-64.

17. Binder, R. C., Advanced Fluid Dynamics and Fluid Machinery, Prentice-Hall, Incorporated, New York, 1951.

18. Velkoff, Henry R., "Notes on Elements of Turbomachinery," The Ohio State University, 1969.

19. Engelman, H. W., "Unpublished Lecture Notes on 'Advanced Principles of Energy Conversion in Turbomachinery,'" Department of Mechanical Engineering of the Ohio State University, Spring Quarter, 1969.

20. Bogus, A. S., "The Problem of Vortex Flow in an Annulus," M. S. Thesis, The Ohio State University, 1970.

21. Due, H. F., Rogo, C., "Advanced Small Axial Turbine Technology Program, Phase II Test Report," Contract DAAJ02-72-C-0117, February 1974.

22. Due, H. F., Rogo, C., Kosier, C. L., Jasas, G. B., "Advanced Small Axial Turbine Technology," Final Report USAAMRDL-TR-77-1, Contract DAAJ02-72-C-0117, May 1977.

23. Rayle, R. E., "An Investigation of the Influence of Orifice Geometry on Static Pressure Measurements," MIT S. M. Thesis, Department of Mechanical Engineering, 1949.

24. Dean, Robert C. Jr. et al, Aerodynamic Measurements, Gas Turbine Laboratory, Massachusetts Institute of Technology, 1953.

25. Bammert, K. and Sandstede, H., Influences of Manufacturing Tolerances and Surface Roughness of Blades on the Performance of Turbines, Journal of Engineering for Power - Transactions of the ASME, January 1976, pp. 29-36.

26. Wysong, R., et al, "Turbine Design System," General Electric, AFAPL-TR-78-92.

27. Keenan, Joseph H., and Kaye, Joseph, Gas Tables, John Wiley & Sons, Incorporated, 1948.

28. John, James E. A., Gas Dynamics, Allyn and Bacon, 1969.

29. United Sensor and Control Corporation, 85 School Street, Watertown, Massachusetts, Calibration Data - Bulletin W, WT

30. Keast, F. H. "High Speed Cascade Testing Techniques," Transactions of the ASME, Volume 74, Number 5, Page 685, July 1952.